Technische Universität München
TUM School of Natural Sciences

Development and evaluation of an adsorption-based dehumidification system for energy efficient air conditioning in electric vehicles

Dipl.-Ing. Christoph Futter

Vollständiger Abdruck der von der TUM School of Natural Sciences der Technischen Universität München zur Erlangung des akademischen Grades eines

Doktors der Ingenieurwissenschaften

genehmigten Dissertation.

Vorsitz:	Prof. Dr.-Ing. Kai-Olaf M. Hinrichsen
Prüfer der Dissertation:	
	1. Prof. Dr. Ulrich Stimming
	2. Prof. Dr.-Ing. Hartmut Spliethoff

Die Dissertation wurde am 15.07.2022 bei der Technischen Universität München eingereicht und durch die TUM School of Natural Sciences am 16.10.2023 angenommen.

ACKNOWLEDGEMENTS

A few words of appreciation go out to the following people who have in many different ways contributed to the successful completion of this thesis. Without any ranking order, i would like to express my sincere gratitude to

- My adviser, Prof. Dr. Stimming, who introduced me to the scientific environment at Technische Universität München (TUM) and beyond, and who provided direction and guidance, on both professional and personal issues along the entire way,
- The TUM itself, for offering the opportunities from with this research project arose, especially the possibility of what became a quite extensive research stay in Singapore,
- Prof. Dr. Oliver Schneider for the support during my teaching duties,
- The fantastic corporate team at TUM CREATE for taking great care of the administrative part that comes as an integral part of a research program,
- My colleague Witono Halim for his help with the assembly of test stands, but also for the photographic documentation of the progress - many of his photos went into the final version of the thesis at hand,
- Jan Geder, for his help with the thermal analysis, numerous fruitful discussions and some interesting side projects,
- The Teams of RP6 and RP9 for the extraordinary experience that it has been to be involved in the *EVA*-project,
- The ZAE Bayern in Garching for their time and support with advice, materials and equipment during my research visit in Summer 2014,
- Especially Fabian Fischer for his patient tutoring on the vapor deposition experiments,
- Dr. Matthias Wiener from the ZAE's facility in Würzburg for the fantastic SEM images,
- Dr. Miriam Keppeler for providing the *SBA-15* samples and plenty of insight into the world of materials synthesis,
- The SMART-MIT Innovation Program for the research grant and the associated mentorship programs,
- The TUM Graduate School, for facilitating many administrative issues and providing plenty of fruitful workshops and training courses,
- and finally, but especially my Family and Theresa, for their continued support, their patience, sometimes financial aid, but most of all for always having an open ear during the ups and downs that are inherent to the accomplishment of a doctoral thesis.

Acknowledgements

ABSTRACT

Until now, the design of the air conditioning (A/C)-system follows the concept established by combustion-engine driven vehicles. Although the use of an A/C-system leads to a rise in fuel consumption, the loss in range is not significant and generally accepted by drivers. In an electric vehicle however, the A/C system reduces the range drastically - especially under tropical conditions. Taking into account the limited battery capacity, it becomes clear that optimization of the A/C-system is an important design factor.

Usual conditions in Singapore, where the TUM CREATE program is located, are about 30 °C at 85 % relative humidity. A/C-systems are omnipresent, and in automobiles, operate constantly. This work therefor starts with an extensive literature study on the topic of thermal comfort, to establish the boundary conditions for required temperature, humidity and air exchange rates. In today's A/C-systems, moisture is removed by decreasing the temperature below the dew point and discarding the liquid water. This process is particularly energy consuming, as the so-called latent heat, i.e. the enthalpy of condensation, makes up a large part of the cooling requirement. If, however, the air was dehumidified by a separate device before entering the cooling system, the required cooling energy could be reduced substantially. To estimate the benefit of an additional dehumidification device, simulations have been carried out based on TUM CREATE's own electric vehicle *EVA*. This black-box approach predicts a significant reduction in energy consumption with the use of a dehumidification device. Such an apparatus will constitute an unknown energy sink and introduce extra mass, thereby increasing the energy consumption of the vehicle. This effect is therefor quantified, and a simple method to assess the usefulness of a dehumidification system is suggested.

An actual implementation can be realized through different types of air-drying measures, which are compared and discussed. In order to be energetically beneficial, the process should run on waste heat - the main challenge in electric vehicles is that they don't generate a lot, and only at rather low temperatures. From the possible options, a thermochemical process known as adsorption is deemed the most suitable choice for automotive applications. A brief introduction into the theory thereof is then given and different adsorbents and their preparation are introduced. Specific requirements are formulated for suitable desiccant materials and process designs.

In the experimental section, different desiccant materials are investigated with regard to their microscopic properties and their application in an adsorption-based dehumidification device. These properties (for example pore structure, surface area, heat of adsorption, specific heat capacity and sorption isotherms) are investigated by N_2-adsorption, thermal analysis and H_2O-isotherm measurements. Their thorough understanding supports the assessment of desiccants even in cases where not enough material is available to conduct experiments in the open-system test stand. The latter consists of a true-to-scale laboratory setup of the desiccant dehumidification system, keeping the restrictions imposed by the electric vehicle in mind. A series of adsorption- and regeneration experiments is conducted under conditions similar to the expected real-world use case, with several desiccant materials.

Overall, the results show the feasibility and suitability of the suggested process. Even as a laboratory test setup, the dehumidification performance is sufficient and thus reaches savings that could justify the addition to an electric vehicle. A critical discussion, followed by implications and suggestions for future work conclude the thesis.

Abstract

ZUSAMMENFASSUNG (GERMAN ABSTRACT)

Bisher entspricht der Aufbau der Klimanlage in Elektrofahrzeugen dem Konzept von Fahrzeugen mit Verbrennungsmotor. Obwohl ihr Gebrauch zu einem Anstieg des Kraftstoffverbrauchs führt, ist der Reichweitenverlust in Letzteren nicht signifikant und wird daher vom Fahrer meist in Kauf genommen. In einem Elektrofahrzeug reduziert das Klimasystem jedoch die Reichweite drastisch - insbesondere in tropischem Klima. Unter Berücksichtigung der begrenzten Batteriekapazität wird deutlich, dass hier jede Verbesserung einen wichtigen Konstruktionsfaktor darstellt.
Übliche Bedingungen in Singapur, dem Hauptstandort des TUM CREATE-Programms, liegen bei ca. 30 °C mit 85 % relativer Luftfeuchtigkeit. Klimaanlagen sind allgegenwärtig, im stationären sowie automobilen Bereich. Diese Arbeit beginnt daher mit einer umfangreichen Literaturstudie zum Thema thermische Behaglichkeit, um die Randbedingungen für erforderliche Temperatur- und Feuchtigkeitsbereiche sowie Luftaustauschraten festzulegen. In heutigen KfZ-Klimaanlagen wird Feuchtigkeit entfernt, indem die Temperatur unter den Taupunkt gesenkt und kondensiertes Wasser verworfen wird. Dieser Prozess ist besonders energieaufwendig, da die sogenannte latente Wärme, d.h. die Kondensationsenthalpie, einen großen Teil des Kühlbedarfs ausmacht. Würde jedoch die Luft vor dem Eintritt in das Kühlsystem durch eine separate Vorrichtung entfeuchtet, könnte die zur Kühlung erforderliche Energie erheblich reduziert werden. Um den Nutzen eines zusätzlichen Entfeuchtungsgeräts abzuschätzen, wurden Simulationen auf der Grundlage des Konzeptfahrzeugs *EVA* durchgeführt. Dieser Black-Box-Ansatz sagt eine signifikante Senkung des Energieverbrauchs voraus. Ein solcher Apparat stellt aber eine unbekannte Energiesenke dar: durch Zusatzgeräte, sowie das Eigengewicht der erforderlichen Komponenten, erhöht sich der Energieverbrauch des Fahrzeugs. Dieser Effekt wird quantifiziert, und es wird eine einfache Methode zur Bewertung des Nutzens eines Entfeuchtungssystems vorgeschlagen.
Eine tatsächliche Umsetzung lässt sich durch verschiedene Arten von Lufttrocknungsmaßnahmen erreichen, welche verglichen und diskutiert werden. Für einen energetisch vorteilhaften Betrieb sollte der Prozess mit Abwärme funktionieren - die größte Herausforderung bei Elektrofahrzeugen besteht hierbei darin, dass diese nur in geringem Umfang und bei relativ niedrigen Temperaturen anfällt. Aus den möglichen Optionen wird ein als Adsorption bekanntes, thermochemisches Verfahren als für Automobilanwendungen am besten geeignet angesehen. Der folgende Teil gibt eine kurze Einführung in die theoretischen Grundlagen der Adsorption und formuliert spezifische Anforderungen an geeignete Trockenmittel und Prozesse.
Im experimentellen Teil werden verschiedene Adsorbentien hinsichtlich ihrer mikroskopischen Eigenschaften und ihrer Anwendbarkeit untersucht. Die Charakterisierung Ersterer (z.B. Porenstruktur, Oberfläche, Adsorptionswärme, spezifische Wärmekapazität und Sorptionsisothermen) erfolgt durch N_2-Adsorption, thermische Analyseverfahren und H_2O-Isothermenmessungen. Ein gründliches Verständnis der so gefundenen Merkmale erlaubt die Bewertung von Trockenmitteln, selbst wenn nicht genügend Material zur Verfügung steht, um Experimente im Prüfstand mit offenem System durchzuführen. Letzteres besteht aus einem maßstabsgetreuen Laboraufbau des Entfeuchtungssystems unter Berücksichtigung der zuvor formulierten Randbedingungen. Eine Reihe von Adsorptions- und Regenerationsexperimenten wird unter Bedingungen durchgeführt, die dem erwarteten realen Anwendungsfall nachempfunden sind.
Insgesamt zeigen die Ergebnisse die Machbarkeit und Eignung des vorgeschlagenen Verfahrens. Bereits im Laboraufbau kann eine ausreichende Entfeuchtungsleistung, und somit potentielle Energieeinsparung erzielt werden, die den Einsatz in Elektrofahrzeugen rechtfertigen könnten. Eine kritische Diskussion, gefolgt von Schlußfolgerungen und einem Ausblick auf mögliche zukünftige Forschungsgegenstände, schließen die Arbeit ab.

Zusammenfassung (German Abstract)

ACRONYMS AND SYMBOLS

SYMBOLS

χ_i mole fraction of component i

Δh_{ads} enthalpy of adsorption

Δh_{vap} enthalpy of vaporization

η dynamic viscosity

γ surface tension

Φ_{LJ} Lennard-Jones potential

π_0 Poynting correction factor

ρ_l bulk liquid density

σ_{ads} cross-sectional area of the adsorptive

ε porosity

φ relative humidity

ϑ Celsius temperature

ϑ_{dp} dew point temperature

A_p pore surface area

C coverage of adsorbent

c_p specific heat capacity at constant pressure

c_v specific heat capacity at constant volume

c_{BET} BET constant

d_p pore diameter

d_h hydraulic diameter

d_{pt} particle diameter

E_c enthalpy of condensation

E_i enthalpy of adsorption in the i-th layer

E_s enthalpy of adsorption on the surface

h specific enthalpy

k_{ads} rate of adsorption

k_{des} rate of desorption

k_{DSC} DSC heating rate

M molar mass

m mass

N_i number of adsorption sites covered by i layers

N_s total number of adsorption sites on the surface

N_A Avogadro constant

p pressure

p_0 equilibrium vapor pressure

p_c critical pressure

p_s saturation pressure

q_{st} isosteric enthalpy of adsorption

R universal gas constant

R_i individual gas constant of component i

r_K kelvin radius

s_{BET} specific surface area calculated from the BET method

S_{BET} total surface area calculated from the BET method

t statistical thickness of adsorbed multilayer

T absolute temperature

T_c critical temperature

T_T triple point temperature

V_p pore volume

v_s superficial velocity

V_{ads} adsorbed volume of adsorptive

V_{dd} dead volume

V_{eq} volume adsorbed at equilibrium conditions

V_{md} manifold volume

V_{mono} adsorbed volume needed to form a complete monolayer

V_m molar volume

V_{pt} volume of solid particles

V_v void volume

x water content

z ion charge

ACRONYMS

LN_2 liquid nitrogen

A/C air conditioning

ACH air changes per hour

BEV battery electric vehicle

CAD computer aided design

COE Certificate of Entitlement

COP coefficient of performance

DAQ data acquisition

DFT density functional theory

DSC differential scanning calorimetry

EGA evolved gas analysis

EV electric vehicle

FCEV fuel cell electric vehicle

GWP global warming potential

HVAC heating, ventilation and air conditioning

MS mass spectrometry

NBR nitrile butadiene rubber

NTU Nanyang Technological University

PEO poly(ethylene oxide)

PHEV plug-in hybrid electric vehicle

PMV predicted mean vote

PPO poly(propylene oxide)

PSA pressure swing adsorption

PWM pulse width modulation

SEM scanning electron microscopy

STDC Singapore taxi driving cycle

STP standard conditions for temperature and pressure

TEOS tetraethoxysilane

TGA thermogravimetric analysis

TMOS tetramethoxysilane

TSA temperature swing adsorption

TUM Technische Universität München

CONTENTS

1

INTRODUCTION

1.1 THE TUM CREATE PROGRAM

The joint research program TUM CREATE was launched in 2011 by TUM and Nanyang Technological University (NTU) as a dedicated electromobility research institute. Both universities share a commitment to excellence in research and teaching, as well as an internationalist mindset. TUM is one of Europe's leading universities and continuously rated among Germany's top institutions. In addition to interdisciplinary education and the active promotion of promising young scientists, the university forges strong links with companies and scientific institutions across the world. In 2003, TUM became the first German university to establish an international campus, *TUM Asia*, in Singapore. TUM has around 35000 students, of which 18 % are international. NTU is a young and research-intensive, global university on a rapid rise. Steadily advancing in the rankings of the world's top universities, NTU has about 33000 students in the colleges of engineering, science, business, education, humanities, arts and social sciences. A melting pot of international award-winning scientists, young talents and eminent global partners, NTU is also home to several world-class research institutes and builds on its strengths in interdisciplinary research. Their collaborative venture, TUM CREATE, is part of the *Campus for Research Excellence And Technological Enterprise (CREATE)* program, funded by the National Research Foundation (NRF), an agency of the Prime Minister's Office in Singapore. Its ambition is to bring together the expertise and knowledge of Germany and Singapore, and together drive innovation to shape the future of sustainable mobility. The goal is to make positive contributions to the fields of both industrial capital and intellectual capital. This is achieved through the development of innovative transportation concepts and the application of electric vehicle (EV) to match the challenging mobility requirements of fast-growing tropical megacities. Within the research program, over 100 scientists and engineers are working in ten research areas including new battery materials, energy storage systems, EV design, computer models and simulations, and transportation systems design. The unofficial slogan thus quickly became *"from the molecule to the megacity"*. On top of these factors, Singapore's tropical weather also poses unique challenges for electromobility and forms the core of TUM CREATE's research.
Probably the most palpable result so far is TUM CREATE's own electric taxi concept, *EVA*. The decision to focus on the electrification of taxis arose from the expected leverage effect: although only 3 % of all vehicles registered in Singapore are Taxis, they account for 15 % of the total mileage. Thus, electrifying a comparably small number of vehicles would allow to harvest many benefits, like noise reduction and locally emission-free transportation, in amplified form. However, it also comes with challenges enforced by the taxi market, like the impossibility of downtime and other restrictions. The technology presented in *EVA* can of course also be applied to other EV platforms. The main purpose of *EVA* is to showcase some of the cutting-edge research and to demonstrate innovations developed within TUM CREATE in a drivable prototype. It also serves as a research-, testing-, and data collection platform for students, PhD candidates, researchers and the local industry. With this in mind, *EVA* was designed and built in Singapore by a team of researchers and engineers. About 30 research associates and young professionals from different disciplines have been working on *EVA*, with nearly 40 students supporting the project throughout its duration. It was completed in

only two years and unveiled at the Tokyo Motor Show in 2013, the biggest automotive show in the region and the key motor show for presenting prototype vehicles. *EVA* is a showcase of TUM CREATE's innovations and developments, and a reflection of the successful partnership between TUM and NTU. Many insights gained during the work on *EVA* have contributed to the scope of this thesis.

1.2 SINGAPORE AND THE TROPICAL CLIMATE CONDITIONS

Singapore is an island city state at the southern tip of the Malayan peninsula in South East Asia. The country, as we know it today, was founded after declaring its independence from Malaysia in 1965. The city itself however dates back a lot longer - modern Singapore was born in 1819 as a British trading post, later becoming a part of the Straits Settlements. This formative period in history is key to understanding Singapore's multi-ethnic demography and has left marks in all parts of public, political and economic life. As of today, a population of over 5.6 million people live on a total area of 712.4 km^2. A noteworthy aspect is that only 62 % are citizens, the rest consists of foreign workers and expatriates. Approximately 74 % of the population are of Chinese origin, the rest mainly has Malay or Indian roots. Singapore has a highly developed, trade-oriented market economy. The main industry sector is the electronics industry, followed by manufacturing and financial services. Altogether, Singapore is definitely one of the most fascinating cities on the planet today, therefor this section could easily fill an entire book on its own. To stay in line with the focus of the research project discussed within this thesis, the reader is kindly referred to the numerous publications on Singapore's rich history and cultural heritage, and its more recent growth into one of the most highly developed countries on the planet. For the scope of the thesis at hand, two main aspects shall be presented in more detail: climate and traffic conditions.
Singapore's employment rates are high, and the daily commuter traffic is obvious all over the island. The major form of public transportation is rail, with Mass Rapid Transit (MRT) and Light Rail Transit (LRT) forming the system's backbone. They are complemented by an extensive public bus network. Taxis are considered a part of the public transportation system. At the time the TUM CREATE program was launched, 27707 taxis were on the road in Singapore, 88 % of them running on diesel [1]. The rest operate on Compressed Natural Gas (CNG), or are powered by a hybrid petrol-electric power train. By that time, EVs in Singapore had only been registered under an EV test bed for research purposes [2]. Private cars in Singapore are relatively expensive due to high taxes and fees imposed on them. A large part of the vehicle fees comes from the Certificate of Entitlement (COE), which every car owner must purchase in an auction before being able to register a car in their name. This is a control instrument used to limit the number of vehicles, in order to keep the overall traffic conditions favorable. After adding up all the fees, it is not unusual for new cars to be three times more expensive than in Europe.
The location of the TUM CREATE program in Singapore makes for an excellent, representative foundation for most settlements within the tropical regions of our planet. Singapore is situated in the heart of the tropics at 1 °17 'N, 103 °50 'E. It's climatic classification according to the Köppen-Geiger system is *Af* [3], meaning all 12 months have an average precipitation of at least 60 mm. No distinct natural seasons, in terms of thermal and moisture changes, exist, and daylight hours are almost identical over the course of the year. Weather data for Singapore is well documented an readily available from the local authorities. For this project, a set of data recorded at a measurement station near Singapore's Changi Airport was obtained from the *Meteorological Service Singapore*. They were recorded over 13 years, from 2000 to 2012.

In Table 1, key values for temperature and humidity are compiled. Given are the median, maximum and minimum values. These values are plotted in Fig. 2, for illustrative purposes, the raw measurement data for the year 2000 is singled out in Fig. 1. In addition to the tabulated data, these diagrams contain both the average and the interval in which 90 % of all measurements can be found. It becomes evident that the climatic conditions can be assumed to be rather constant all year

Table 1: Yearly weather data as measured at Singapore's Changi airport. Given are the median (med) as well as maximum (max) and minimum (min) values.

	Temperature [°C]			Rel. humidity [%]			Pressure [mbar]		
Year	med	max	min	med	max	min	med	max	min
2000	27.0	34.0	21.3	88.7	100.0	46.5	1008.1	1012.9	1003.1
2001	27.0	34.0	22.0	87.2	100.0	49.5	1009.1	1014.9	1004.1
2002	28.0	34.1	22.0	83.8	100.0	43.8	1010.2	1016.9	1003.1
2003	27.7	34.0	22.9	85.7	100.0	41.1	1010.2	1014.9	1004.1
2004	27.8	35.0	22.0	83.9	100.0	45.8	1010.2	1014.9	1004.1
2005	28.0	35.0	22.0	84.1	100.0	44.3	1010.2	1018.0	1003.1
2006	27.4	34.2	22.5	88.3	100.0	48.0	1010.2	1015.9	1003.1
2007	27.0	34.0	22.0	87.0	100.0	49.5	1009.1	1015.9	1003.1
2008	27.0	34.0	22.0	83.9	100.0	47.0	1009.1	1013.9	1004.1
2009	28.0	35.0	22.6	83.8	100.0	41.4	1009.1	1015.9	1003.1
2010	28.0	35.1	22.5	83.9	100.0	44.0	1009.1	1015.9	1002.0
2011	27.2	34.1	22.0	87.7	100.0	38.9	1009.1	1014.9	1003.1
2012	27.5	33.3	21.4	83.8	100.0	49.2	1009.1	1014.9	1003.1

round. Considering the geographical location close to the equator, this is expected from the general properties of this climate zone. The uniformity of the conditions is reflected by two properties in the presented climate charts: The small difference between the average and the median value, as well as the narrowness of the 90 % interval. In addition to the recorded weather data, the effect of solar irradiation and cloud coverage is of great interest. Within the TUM CREATE program, measurement datasets were obtained and own experiments conducted as part of a Master's thesis project on solar roofs [4]. This data proved very useful during the thermal load simulations on the vehicle, which are introduced in Section 1.3.

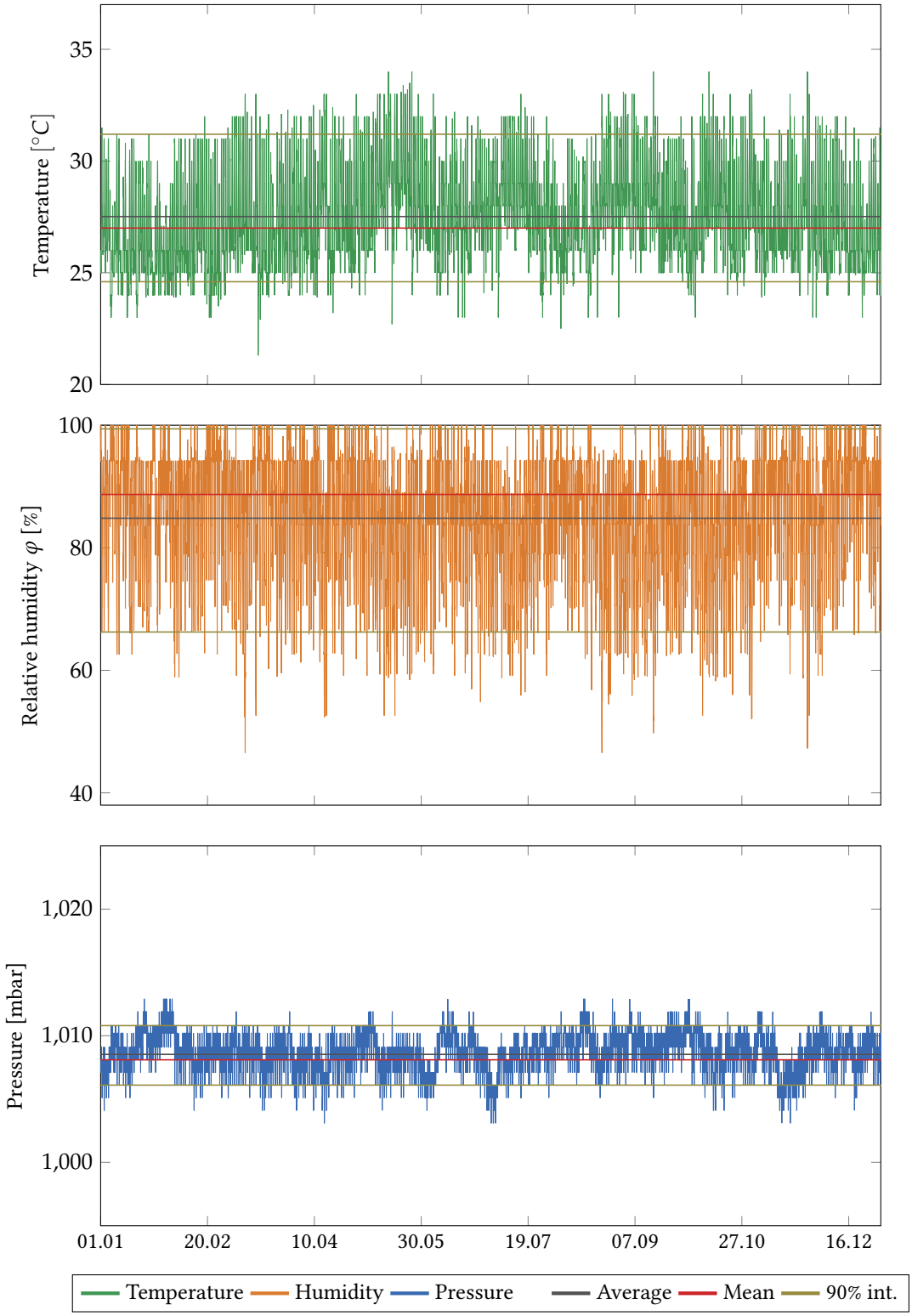

Figure 1: The temperature, relative humidity and pressure profiles during the year 2000, measured at Changi Airport. Highlighted are the maximum and minimum values, as well as the interval inside which 90 % of the measured values can be found.

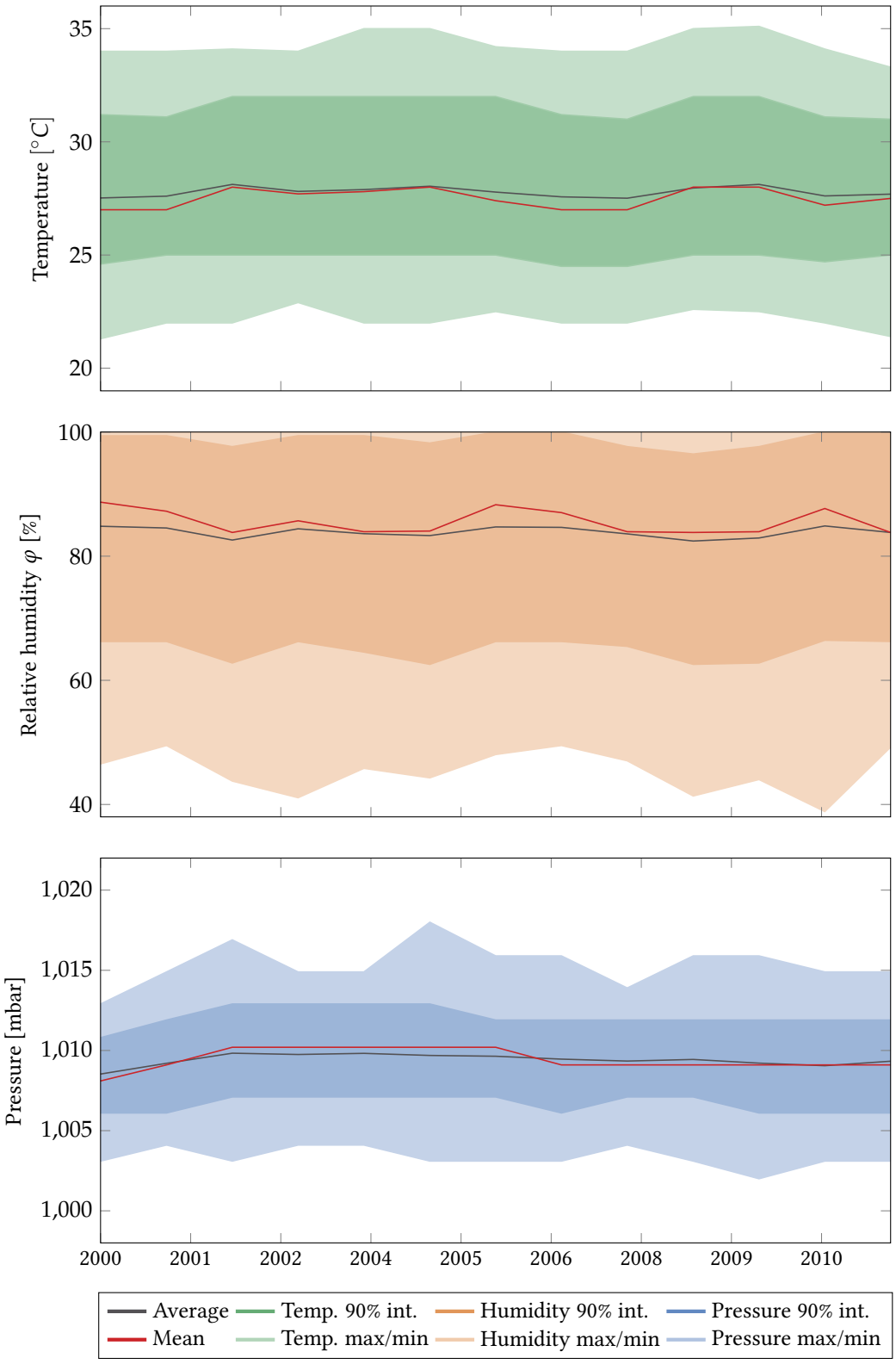

Figure 2: The annual indicators for temperature, humidity and pressure during the period between Jan. 1st, 2000 and Nov. 5th, 2012, measured at Changi Airport. Plotted are average and mean, as well as the interval inside which 90 % of the measured values can be found.

1.3 MOTIVATION

The ever increasing demand for personal mobility is accelerated by a rise in urbanization. There are currently 23 mega-cities in the world [5], and the United Nations predict that there will be more than 30 by 2025. The need to seek more efficient and cleaner (urban) mobility solutions is increasing. Together with an overall growth in population, the need to address mobility challenges is becoming more pressing. This trend is accompanied by increasingly strict regulations on CO_2 emissions and the urge to become less dependent on fossil fuels. TUM CREATE is striving to decrease the reliance on fossil fuels to propel vehicles by innovating new technologies, as well as to explore concepts in transportation and infrastructure engineering. Especially the electrification of personal mobility has proven to be more than a trend or a niche application: with the development of high energy density battery systems and the transition to renewable energy production, electromobility is steadily on the rise. This is reflected in the ever increasing variety of electric vehicle models by manufacturers all over the world, and the rising adoption by customers, as Fig. 3 shows.

While the term *electric vehicle* often triggers the association with the purely battery-powered car, there are actually several concepts which exist simultaneously. It is yet to be determined if either one of those will prevail over the others, or if they will complement each other and tend to their own specific market segment. The different concepts encompass the source of electric energy as well as the level of power train electrification. Many forms can be distinguished, from hybrid vehicles and chargeable hybrids (plug-in hybrid electric vehicle (PHEV)) that carry both an internal combustion engine and an electric driveline, to the pure battery electric vehicle (BEV) or the hydrogen-based fuel cell electric vehicle (FCEV). The necessity to reduce of CO_2 emissions and concerns about air quality in cities both drive the development and market adoption. However, certain downsides are associated with the transition, most notably range anxiety and the rather long charging times. Especially in the here considered use case as a taxi, both factors are vastly important: A taxi in Singapore runs practically 24 hours - two shifts of almost 12 hours each are separated by only a short break when the vehicle is handed over from one driver to another. This means that there is no opportunity for extended charging breaks, and the taxi must provide both a very short charging time but also a battery capacity to energy consumption ratio that allows to complete multiple trips before having to find a charging station. Every improvement on either of those factors have the potential to increase the attractiveness of a transition even in this very demanding market. Since the battery capacity itself can only be enlarged to a certain extent because the vehicles curb weight is limited, optimizations in energy consumption are a very promising approach.
At the time of this thesis, several, mutually complementary research projects concerning the energy consumption of electric vehicles were conducted concurrently at TUM CREATE. Results from the projects that I have in any way contributed to, are in turn used and cited in this section. The scope of these projects was to provide a representation of an electric vehicle under the conditions of the Singapore taxi driving cycle. This is a driving cycle based on recorded driving patterns from actual taxis in Singapore. It was developed in-house at TUM CREATE and serves as a reference case during vehicle simulations. A vehicle model was then set up as a 1-D simulation in *MATLAB/Simulink*, and complemented by a 3D simulation in the specialized thermal simulation software *Theseus-FE*. Details to these approaches and their results have been published, for example, in [7]. The boundary conditions were chosen in a way to represent the demands of the Singapore taxi driving cycle, but the principles can be generally applied to electric vehicles in tropical mega cities. The pre-investigations that led to the scope of the presented research project were conducted as follows: In a first step, the total impact of the auxiliary components of an electric vehicle were assessed under a set of boundary conditions, summarized in Table 2a. This was done as part of a Bachelor's Thesis project by Agua [7], the results are reproduced in Fig. 4a. The A/C-system was identified as the single largest consumer, and hence the obvious target for the largest reduction potential. Therefore, in a second step, it's energy demand was broken down to different sources, which are represented in Fig. 4b. As mentioned before, special attention was given to a precise understanding of the boundary

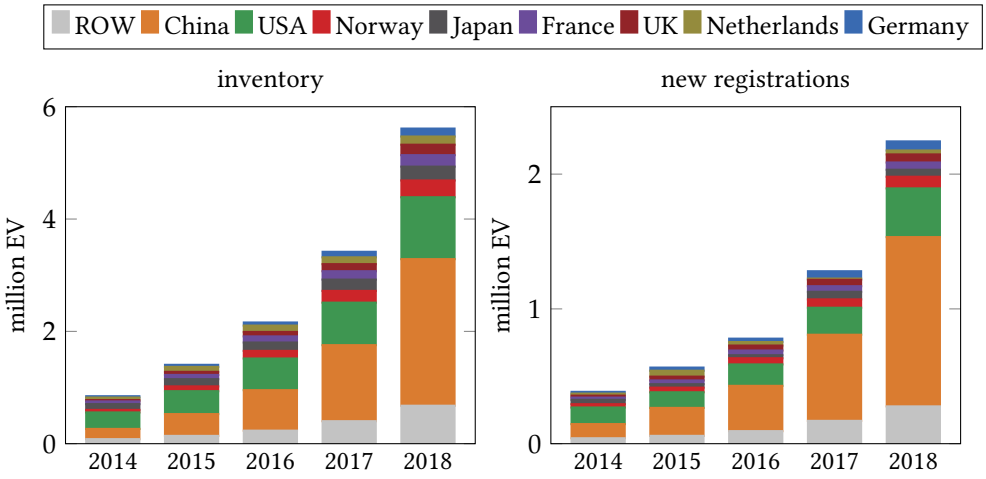

Figure 3: Development of inventory and new registrations of EVs (battery electric vehicle (BEV) & plug-in hybrid electric vehicle (PHEV)) by country [6].

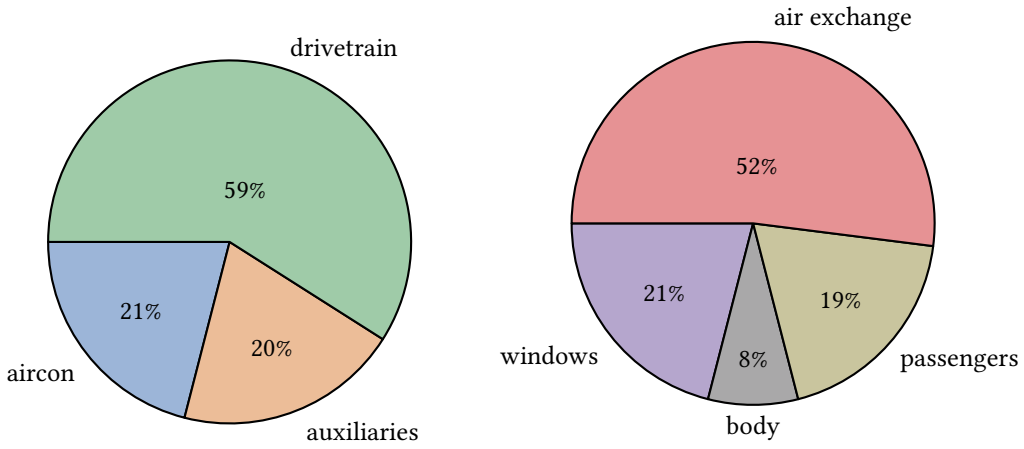

(a) Breakdown of the energy consumption

(b) Breakdown of the A/C-fraction

Figure 4: Distribution of the simulated energy consumption of an EV following the STDC. Reproduced from [7].

conditions that contribute to the A/Cs energy consumption. With the exception of the heat emitted by passengers, they can all be summarized as environmental factors. The third step thus consisted of investigating methods to mitigate the root causes. These methods were, for instance, variations in paint, interior color and materials as well as different window angles and glass tint to reduce the impact of solar irradiation. Insights from this stage were later adopted in the design of TUM CREATE's own vehicle *EVA*. The largest fraction, labeled *air exchange*, was investigated separately. This part forms the foundation of this research and is introduced in more depth in Section 2.2.

Table 2: Parameters and simulation results for the energy consumption of different A/C components, from [7]

(a) Input parameters for the vehicle simulation used to quantify the A/C consumption.

Parameter	Value	Unit
STDC length	7.759	km
STDC time	1,310	s
ambient temperature	31	°C
ambient humidity	85	%
cabin temperature	23	°C
cabin humidity	60	%
ambient air density	1.225	kg/m^3
cabin volume	5	m^3
air change rate	10	h^{-1}
number of passengers	2	-

(b) Breakdown of relevant energy consumption values for the Singapore taxi driving cycle.

Component	Energy [Wh]
vehicle total	1,189
per 100 km	15,324
A/C system total	253
air change	128
windows	54
body	20
passengers	46

1.4 AUTOMOTIVE AIR CONDITIONING

The fundamental examination of the air conditioning system's impact on the energy consumption of the electric vehicle clearly identifies the importance of optimization measures associated with it. This section introduces the development and technical principles of heating, ventilation and air conditioning with the focus on the special case of automotive systems, but covers also the underlying, general concepts behind the main functions.

1.4.1 *Short History of Automotive HVAC Systems*

The necessity of ventilation became apparent when automobiles received closed carriages. First, this was simply accomplished by hinged windows, later complemented by active ventilation with fans. Heaters followed shortly after, as the internal combustion engines provide excess thermal energy which can easily be utilized in cabin heating. Automotive A/C units haven't been around until the late 1930's, when they started to appear first on American-made cars. They became available as standard equipment from 1953. Depending on the geographic region where vehicles are sold, different shares of these individual HVAC functions dominate. In Europe for example, heaters were always common, in fact, they became mandatory for type approval of the vehicle since the 1960's (Germany 1963, USA 1969). The reason was that laws required cars to be equipped with windshield defrosting units. A/C units however were not common outside the luxury class segment in European cars, and even there they were often considered an optional upgrade. It is noteworthy that many Taxis in Central and Northern Europe belong to this vehicle class, and passengers have high expectations towards comfort. The adoption in private-owned vehicles has been rising steadily, presumably because of a rising demand in comfort in general, but also out of necessity: the change to more aerodynamic designs leads to an increase in window area, which in turn causes more solar irradiation into the vehicle [8]. But even today, only about 80 % of passenger vehicles sold in Europe are equipped with A/C units, whereas in North America, almost every car is [9]. An illustrated and complete history of automotive comfort systems can be found in the two-part series by Bhatti [10, 11]. Today, development work focuses automation with the help of modern sensor- and control systems and more optimized thermal units. Other important aspects are the constantly changing legislative requirements put on refrigerants used in the vapor compression cycle. Starting

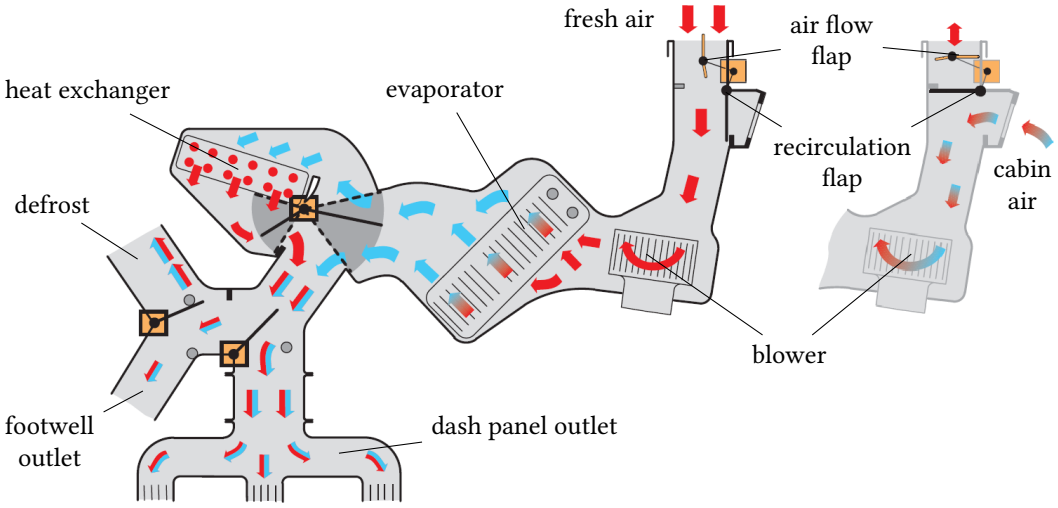

Figure 5: Illustration of an HVAC module as used in Volkswagen vehicles (from [12]). The main image to the left shows operation in fresh air mode, the lighter section on the right depicts the recirculation flap closed, i.e. air is taken from the cabin.

with the ban on chlorofluorocarbons according to the *Montreal Protocol on Substances that Deplete the Ozone Layer*, environmental aspects have gained importance. This is reflected in the planned phase-out of the most common refrigerant used in A/C units, Tetrafluoroethane (R134a), because of it's high global warming potential (GWP). As of the writing of this thesis, no definitive successor has emerged. Finally, the adoption of electric vehicles requires a new approach to heating, since electric cars produce neither hot exhaust gases nor do their electrical components transfer sufficient waste heat to the cooling circuit, which would allow to heat the cabin. Many concepts are being researched, from the obvious electric heater to heat pumps and fuel burners. The EV sector also drives the development of purely electric A/C units with high-voltage compressor systems.

1.4.2 *Technical Principles*

In both building- and transportation technology, four elementary functions are available to achieve a comfortable atmosphere. These are Heating, Ventilation and Air Conditioning, often abbreviated as HVAC. The last part, A/C, can be further divided into cooling, dehumidifying and humidifying. In the everyday definition however, *Air Conditioning* refers to only the former two - active humidification is only found in very specialized systems. Within this thesis, the terms *Air Conditioning* and its abbreviation *A/C* are used accordingly. The proper design of HVAC systems is a science in its own right, hence this introduction only covers the very basics that are needed to put the research project in context. The basics of an automotive air conditioning system are identical to any vapor-compression based A/C system. But where residential devices rely simply on a moving duct which distributes cold air, the automotive HVAC module is more complex. Especially in recent years, sophisticated designs with several climate zones and electronic control systems have been introduced in mid- to luxury segment models. All of those still have some basic principles in common, which are illustrated in Fig. 5.

As for the actual refrigeration system, the method of choice for cold generation in the automotive setting is the vapor compression cycle. Several other ways to put air conditioning in practice exist - adsorption and absorption- based solutions can sometimes be found in building technology, air-cycle systems that achieve cooling by subjecting the supply air to various pressure changes are common on commercial aircraft and were even tested on passenger trains. None of those are applied in automotive air conditioning, the simple reason being the relatively high

efficiency of vapor compression refrigeration, and the rather beneficial power-to-weight ratio of the required devices. The fundamental functions are the same for every vapor-compression refrigerant cycle - Fig. 6 gives an overview of the major components: The section between compressor and (thermostatic) expansion valve is called high-pressure part, whereas the part between expansion valve and compressor is usually referred to as the low-pressure side. The individual components of the refrigerant cycle are connected through hoses or rigid pipes - in automotive applications, rubber hoses are common at least in parts of the system for the sake of vibration absorption. In conventional, combustion-engine powered vehicles, the compressor is connected to the engine through a belt drive, and engaged through a magnetic clutch. In electric vehicles, hermetically sealed compressors with electric motors are common. Regardless of the specific architecture, the general principle is the same: the compressor compresses the refrigerant vapor and, together with oil for lubrication, pumps it through the refrigerant cycle. After compression, the pressurized and superheated refrigerant enters the condenser, where it is cooled, and ultimately liquified. Here, it enters the filter dryer, a unit combining several important functions: impurities, trapped gas bubbles, and residual water that may have entered the refrigeration system during assembly, are removed. It also acts as a reservoir and compensator to equalize pressure fluctuations. The expansion valve forms the interface between high- and low-pressure section. The liquid refrigerant is injected into the evaporator, where it provides the desired cooling effect through evaporation. In older vehicles, capillary tubes or fixed orifice devices were used to reduce the pressure and atomize the refrigerant. However, modern vehicles usually employ a thermostatically regulated valve, which regulates the refrigerant flow depending on the temperature at the evaporator exit. The aforementioned efficiency of the vapor compression cycle, as well as other types of refrigeration processes, is defined as the ratio of heat removed from the system to the work required by the considered refrigeration process. In vapor compression cycles, this is the energy required to drive the compressor. The theoretical limit would be set by a device working at Carnot efficiency, thus given by the lower (T_L) and upper (T_U) temperature limits between which it operates [13]:

$$COP = \frac{Q}{|W_{comp}|} \quad , \quad COP_{max} = \frac{T_L}{T_U - T_L} \tag{1.4.1}$$

In reality, the attainable coefficient of performance (COP) is considerably less than the theoretical value. The reasons are inherent losses in the refrigeration device, like compressor efficiency, pressure drop in pipes and varying environmental conditions. Although not part of the COP, possible additional power consumption arising from the necessity of auxiliary devices like fans and control units are to be considered. All these effects are even more prominent in mobile applications, where space restrictions often lead to thermodynamically poor system designs. While stationary devices reach coefficients of performance of 2.4 to 5 [14], COP values for automotive A/C-units are quoted between 1.2 to 3.6 [15, 16] - the actual values are most likely on the lower end of this spectrum. This is due to the operating conditions inside the engine compartment, where condenser temperatures are rather high. Between service intervals, a significant refrigerant loss due to leakages is common, resulting in deviations from the nominal system design pressures.
Within the scope of this thesis, the focus is mostly on the air flow at the evaporator. Here, a very important aspect of automotive air conditioning comes into play, which is the option to recirculate air. In Singaporean taxis, this is the usual operating method. Two principle advantages of air recirculation inside a vehicle can be identified: The first being energy efficiency - fresh, outside air has to be constantly cooled and dehumidified, whereas in the recirculated air only the heat and moisture added by the passengers has to be removed. The second advantage is that contaminants, at least to a large extent, are barred from entering the vehicle. The implementation of these functions into a passenger vehicle is shown in Fig. 5.

There are, however, also some downsides to recirculating air inside an enclosed volume. Besides the accumulation of odor, the most notable is the accumulation of germs and their cultivation in the filter mat [17]. The effects of recirculation are quantified with the help of air exchange rates.

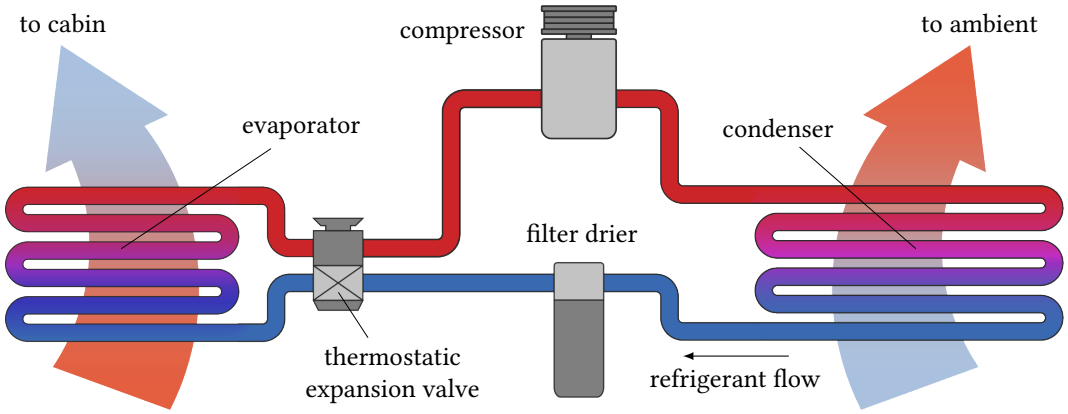

Figure 6: Contemporary automotive air conditioning refrigeration cycle design.

Since this is crucial for the scope of this thesis, it is discussed in Section 2.2 in more detail. A final noteworthy aspect is that, under certain ambient conditions, fogging of the windows can occur as a consequence of condensation. This can be prevented through the A/C, since it not only cools the air, but also removes moisture - in this sense, it acts as an active safety system. A more detailed discussion of dehumidification and other thermodynamic aspects will be conducted in Section 2.2.

1.4.3 *Health and Comfort Aspects*

Climatic physiology, by definition according to the standard DIN1946, is a combination of different factors that exert an effect on the driver and passengers of a vehicle. Examples include the temperature of both air and the enclosing surfaces, the air velocity, humidity, sunlight and others. These environmental conditions, when taken to extremes, can pose a significant risk to human health - either directly by causing adverse reactions like heat stroke etc., or indirectly by influencing the capability to safely operate a vehicle. The extreme conditions that could cause direct damage on a person's health are usually not found in vehicles, and in those rare cases where they are, they can easily be mitigated to a non-hazardous level. For example, a parked car can heat up by up to 35 K above ambient, reaching inside temperatures of more than 75 °C [18]. Although it can easily be ventilated to reach a harmless temperature before entering, the driving experience will most likely still be an uncomfortable one if no further measures are taken. The reason is that certain combinations of the above mentioned environmental factors are generally perceived as less *comfortable* than others. This phenomenon has been studied extensively with regard to building technology, and there are many methods to quantify this thermal comfort. Most notable is the formalized expression of comfort according to the equation introduced by Fanger [19, 20]. His method predicts comfort as the predicted mean vote (PMV), a numerical value representing thermal sensation of test subjects on a scale of -3 (cold) to +3 (hot), with 0 being neutral. Together with the PPD (percentage of persons dissatisfied), which predicts the amount of persons that are not pleased with the conditions, it has been incorporated in several national standards (e.g. DIN EN ISO 7730, ASHRAE Standard 55). Although some restrictions have been identified, it is still the most widely used thermal comfort model today [21]. A number of newer models also exist, some of which are also based on Fanger's methodology. An elaborate comparison, specifically for vehicular thermal comfort, has been compiled by Alahmer et al. in [22]. The above mentioned studies and standards take humidity into account to varying extent. From the data available, Frank [23] has compiled a visual representation of conditions that are perceived as comfortable. The plot is reproduced in Fig. 7. In general, insights gained from the building sector are also valid for automotive use cases, however, due to the restricted space, some differences exist that have to be accounted for. These are,

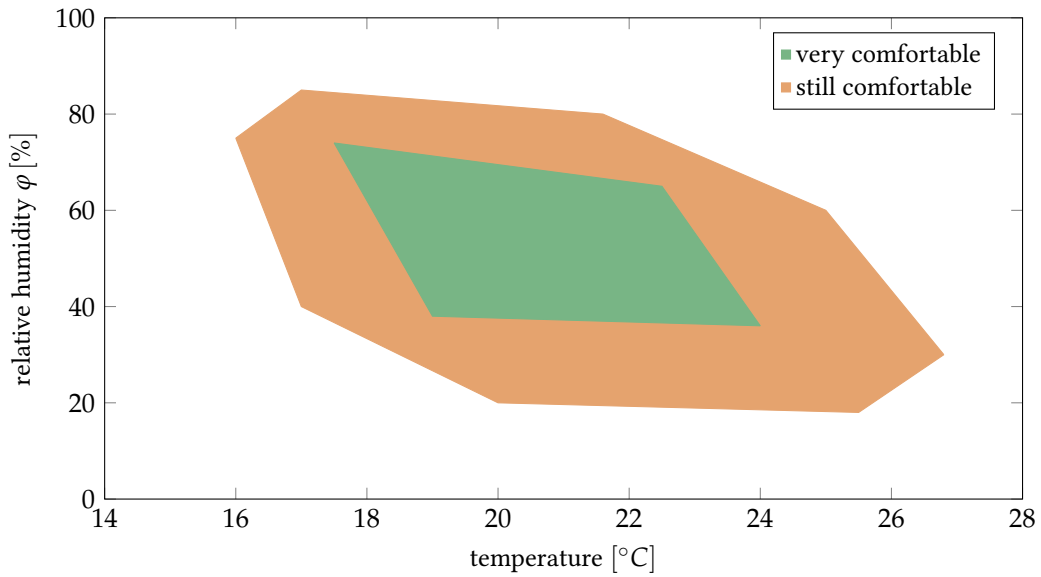

Figure 7: Representation of comfortable conditions with regard to temperature and relative humidity. Compiled from literature values by Frank [23].

for example, the close proximity of passengers to the windows and, hence, the stronger exposure to direct sunlight. Another aspect is the air velocity from the vents, and again, the passenger's proximity to them. Owing to the complexity of this topic, and also the difference in preferences among individuals, thermal comfort is ultimately validated by subjective experiments with test drivers [8]. Within this thesis, these definitions and standards are used as interpretation of the term *comfortable*. As briefly mentioned before, the interior climate of a vehicle plays an important role not only for comfort, but also for the performance of the driver. Outside a certain comfort zone, not only the travel experience in the vehicle is negatively affected. Basic body functions are influenced [24], concentration and reaction time are impaired [25]. The application of an air conditioning system thus contributes once more to an increase in active safety by keeping the driver in a more vigilant state. Especially in Singapore, an automotive air conditioning system (A/C) is not considered a luxury upgrade, but instead a necessity. Here, practically no car is sold without an A/C unit. In reference to the increase in people's performance, the importance of air conditioning was famously recognized by Singapore's founding father and first prime minister, Lee Kuan Yew. In a 2009 interview, he named air conditioning "*...one of the signal inventions in history*" and an enabler for Singapore's success [26].

1.5 PRIOR ART

Humidity has long been recognized as one of the key factors in the performance of HVAC systems, and the idea of dehumidifying intake air entering an air conditioning system is thus not new. Especially for building technology, although not widespread, several approaches exist and are in operation at numerous locations all over the world. For automotive applications, literature is scarce. This can probably be attributed to the general considerations already mentioned in Section 1.3, meaning that the energy efficiency of the A/C system does not constitute a major concern for most owners of motor vehicles. A few sources on dehumidifying devices for cars could, however, be found. The basic principles have usually been presented in form of patents [27–29], or theorized in journal articles. Most of the relevant materials which have come up during a prior art search rely on presenting the concept on a very fundamental level, without any details on practicability or

design details - especially when it comes to suitable desiccants. Some even show inherent design flaws, as for example, the enthalpy of adsorption and the consequential, additional heat exchanger are simply ignored [30]. Others describe very sophisticated devices that give much consideration to the design restrictions arising from the application in an automobile, but again, do not discuss the properties of the necessary adsorbent. Although it must be said that the principles can in general be used for every type of vehicle, most come from the age of internal combustion engines and do not take into account the characteristics of electric vehicles. Therefor, a systematic approach to desiccant selection and process design with a defined set of operating parameters is considered a novelty. The unique use case of an electric taxi, which is purposely designed for tropical mega-cities, constitutes a great case to approach this topic in a scientific manner.

1.6 THESIS OUTLINE

The introduction describes the TUM CREATE program as a scientific approach reaching *from the molecule to the megacity*. The structure of this thesis is laid out in the opposite way - the macroscopic context is introduced in the beginning, starting with the geographical conditions and the overall project background. The approach is refined to the automotive level, where the special conditions of electric vehicles operating in tropical environments are defined as the framework in which this thesis project has been conducted. Requirements on A/C systems and thermal comfort are then presented, and results from previous simulations with the findings therefrom are discussed. Subsequently, chapter two moves on to the microscopic level, outlining the basic thermodynamics of humid air and principles of air drying. The benefits of a dehumidification device and the reasoning behind the decision in favor of an adsorption-based system is discussed. This is followed by a comprehensive introduction to adsorption theory. Different adsorption materials and their respective characteristics are presented. The chapter concludes with a brief overview of adsorption process design. Chapter three explains the experiments that were conducted. They are grouped in closed system measurements, open system measurements and microscopic investigations. The corresponding results are presented in chapter four and discussed in the following chapter five. The last chapter closes with a summarizing conclusion and provides an outlook on further developments as well as issues to be resolved. An appendix compiles plots that have been excluded from the main chapter to improve readability. Computer programs created for automated evaluation of measurement data are also documented here along with relevant literature values.

2

THEORY AND CONCEPTS

2.1 BASIC THERMODYNAMICS OF HUMID AIR

It has been outlined in Chapter 1 that humidity poses a huge challenge for air conditioning systems in tropical environments, but the reason for this and the quantification of this effect have not been elaborated on. This section comprises a brief recap of the underlying thermodynamics of humid air and shall serve to introduce the terminology, symbols and diagrams that are used throughout this thesis. In order to keep it as comprehensive as possible, the fundamental theory and derivations of widely used equations are omitted. A basic knowledge of technical thermodynamics is presupposed, but several excellent textbooks are referenced for further reading. The topics that are necessary for the scope of the research presented, however, are explained in detail.

2.1.1 *Definitions of Humidity*

The term *humid air* describes a mixture of dry air and water. If water is present as vapor only, we refer to the mixture as unsaturated air. After saturation is reached, water is present in a second phase in form of droplets or ice crystals. Air itself is a mixture of several gases, composed of nitrogen (78 %) oxygen (21 %) and argon (1 %). Other gases appear in traces, and under natural conditions, water vapor is always present to a varying extent. For all following calculations humid air will be treated as a mixture of two compounds with defined thermodynamic properties, dry air and water. There exist several types of measures to quantify humidity, which one is used depends largely on the application.

RELATIVE HUMIDITY is probably the most widely used definition of humidity, owing to it's presence in meteorological reports. It is defined as the ratio of the partial pressure of water vapor p_w to the *saturation pressure* p_s. The latter represents the partial pressure of water at which the air package cannot take up any more water. p_s can be calculated from the *equilibrium vapor pressure* p_0 and the Poynting correction factor π_0

$$p_s(p,T) = p_0(T)\,\pi_0(p,T) \tag{2.1.1}$$

Through the Poynting correction factor, the saturation pressure is slightly dependent on the system pressure. However, all experiments in this thesis are conducted at ambient pressure, where the influence of the Poynting factor is negligible [31]. Therefor, both *saturation pressure* and *equilibrium vapor pressure* are used synonymously within this thesis and referred to as p_0. Hence, the definition of relative humidity φ becomes:

$$\varphi = \frac{p_w}{p_0} \tag{2.1.2}$$

From this definition, it becomes apparent that the relative humidity is a measure for the water uptake capability of dry air that reaches a limit at $\varphi = 1$, or 100 %. Once this point is reached, the

water condenses as water droplets (if the temperature T of the humid air is higher than the triple point temperature of water, $T > T_{T,H_2O}$) or ice crystals (for $T < T_{T,H_2O}$). In rare cases, if there are no nucleation sites where droplets or crystals can begin to form, more water can be taken up even after the relative humidity reaches 100 %. Under environmental conditions, as covered in this thesis, this is not the case. Even in a laboratory atmosphere, enough nucleation sites are present to prevent such supersaturated conditions. The equilibrium vapor pressure p_0 is temperature dependent, it can be calculated from various widely accepted methods. The approach used within this thesis is presented in Section 3.3.3.

ABSOLUTE HUMIDITY refers to the mass of water present in a unit volume of humid air V_{ha}:

$$ah = \frac{m_w}{V_{ha}} \tag{2.1.3}$$

The volumetric uptake capability is highly dependent on pressure and temperature, as is the density of air and water vapor. The absolute humidity is therefor not a very meaningful measure for engineering purposes and thus rarely used.

SPECIFIC HUMIDITY refers to the mass of water vapor m_w present in a specific mass of humid air m_{ha}. The latter is the sum of the vapor mass and the dry air mass m_{air}.

$$\chi = \frac{m_w}{m_{ha}} = \frac{m_w}{m_{air} + m_w} \tag{2.1.4}$$

This quantity is not very useful for process design, since it uses the total mass of humid air as a reference. If processes are considered, in which changes in water content occur (such as dehumidification or evaporation), the reference quantity also changes and comparing two process steps becomes unnecessarily inconvenient.

WATER CONTENT also frequently termed *mass mixing ratio* or *humidity ratio*, its definition is similar to the one of the specific humidity given above. The difference is that that reference quantity is only the mass of dry air m_{air}, instead of the total mass of the air package:

$$x = \frac{m_w}{m_{air}} \tag{2.1.5}$$

Especially in chemical engineering, the water content is sometimes called *absolute humidity*, which is inaccurate because another quantity is already defined under this name. The water content x is the basis of the graphical representation of humid air, the psychrometric charts. One of the most important, the Mollier h,x-diagram, is introduced later in this section.
Both *water content* and *relative humidity* are used throughout this thesis. They can be converted into one another using Dalton's law [1] for both water vapor ($p_w V = m_w R_{H_2O} T$) and dry air ($p_{air} V = m_{air} R_{air} T$) to find:

$$x = 621.98 \frac{\varphi p_0}{p - \varphi p_0} \tag{2.1.6}$$

The factor 621.98 is an approximation of the molar mass ratio of water (M_{H_2O} = 18.015268 g/mol [32]) and dry air (M_{air} = 28.9644 g/mol [33]); multiplied by 1000 to obtain the water content in g_{H_2O}/kg_{air}. Unlike the relative humidity, the water content x remains constant when temperature and/or pressure changes occur - even if the water uptake capability of the air is reached. This

[1] Dalton's law is often cited in the formulation: "In any ideal mixture, the partial pressure of component i is the same as it would be, if this component would occupy the mixtures' volume by itself." However, it can be expressed in a more general way: "The total pressure of the mixture is the sum of all partial pressures, according to their definition of $p_i = \chi_i p$", with $\chi_i = n_i/n$ as the molar fraction, to apply to all mixtures. This definition is used within this thesis, and the partial pressure of water p_w is calculated from p_0 to account for the non-ideal behavior of water vapor.

is distinctive from the other measurements of humidity, which are only defined until saturation. Another advantage of the water content x is that the reference quantity m_{air} remains unchanged when m_w is varied through condensation, addition of vapor, or mixing. An equivalent way of expressing the water content is the dew point temperature (ϑ_{dp}): as the name suggests, it refers to the temperature at which condensation occurs. These properties make the water content x the most useful of the mentioned measures of humidity when describing the adsorption process.
For engineering purposes, it is also imperative to quantify the energetic properties of humid air. The most essential quantities are outlined hereafter.

2.1.2 *Heat Capacity*

Heat capacity refers to the amount of energy required to raise the temperature of a certain system by a defined interval. The SI unit is J/K. *Specific heat capacity* refers to the heat capacity per unit mass of a material, given in J/kgK. There are several ways of expression for the specific heat capacity depending on the process conditions, the most common being at constant volume (c_v) and at constant pressure (c_p):

$$c_v = \left(\frac{\partial u}{\partial T}\right)_v \qquad c_p = \left(\frac{\partial h}{\partial T}\right)_p \tag{2.1.7}$$

Since the designs investigated within the scope of this thesis are open systems, the specific heat capacity at constant pressure, c_p, is the one predominantly used. From the definition of the specific heat capacity, it is noteworthy that this quantity is dependent on temperature, i.e. $c_p = c_p(T)$. Within the rather small temperature range considered during the described experiments, this effect is negligible [31], and the c_p values for pure substances are assumed constant.
In a mixture of more than one gas, the heat capacity is simply the sum of the individual heat capacities multiplied by their respective mass fraction x_i - in the case of a binary mixture of air and water vapor, the mass fraction of water is identical to the water content x, and for the air, it can be expressed as $1 - x$. With the specific heat capacity of water vapor $c_{p,w(g)}$, the specific heat capacity of humid air $c_{p,ha}$ becomes therefor:

$$c_{p,ha} = (1 - x)\ c_{p,air} + x\, c_{p,w(g)}. \tag{2.1.8}$$

While it might seem convenient to use this combined quantity to calculate thermodynamic state changes in humid air, care has to be taken that those do not involve phase transitions. If this is the case, the enthalpy of vaporization has to be accounted for. In the context of air conditioning, it is therefor more practicable to directly resort to the *enthalpy* of humid air instead.

2.1.3 *Specific Enthalpy of Humid Air*

To accurately design any cooling or dehumidification process, it is important to quantify the enthalpy of the humid air. As the section's heading suggests, it is often given as the enthalpy per unit mass. The reference unit is 1 kg of dry air, or in other words, $(1 + x)$ kg of humid air; it is expressed in kJ/kg. The specific enthalpy is calculated as follows:

$$h = \underbrace{c_{p,air}\,\vartheta + x\, c_{p,w(g)}\,\vartheta}_{\textit{sensible heat}} + \underbrace{x\,\Delta h_{vap}}_{\textit{latent heat}}. \tag{2.1.9}$$

Due to the appearance of the enthalpy of vaporization Δh_{vap}, the specific enthalpy requires a reference temperature. It can be arbitrarily chosen, so it is often set to the triple point temperature (T_T) of water at $T_{T,H_2O} = 273.16\,K$. In engineering, a common reference is the standard state temperature of $T_{STP} = 273.15\,K$ and for most practical applications, the difference between those two

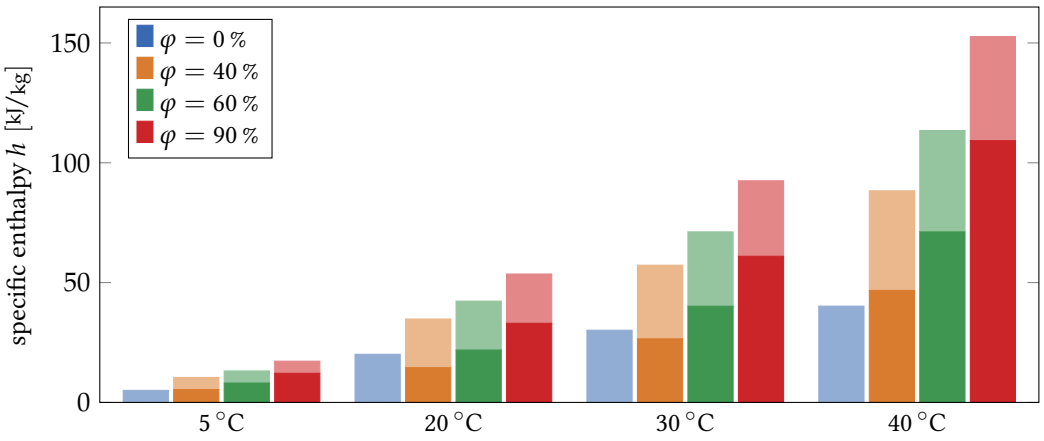

Figure 8: Specific enthalpy of moist air at different states. Light parts denote the fraction of sensible, bold parts of latent heat.

is negligible. Throughout this thesis, the latter reference point is chosen, as it allows for convenient replacement of the absolute temperature T by the Celsius temperature ϑ. The specific enthalpy is arguably the most tangible quantity for the purpose of air conditioning: The two parts of Eq. (2.1.9) are often referred to as *sensible heat* and *latent heat*. As long as the water vapor remains in a gaseous state, any temperature change affects only the first, the sensible, term. Here, the impact of x on the air conditioning process is not that severe, as the heat capacities (and therefor, the enthalpy change) are rather small - but when condensation occurs, the energy consumption of an air conditioning system increases drastically, due to the water's high enthalpy of condensation. A small example in Fig. 8 illustrates the magnitude. The increase in total specific enthalpy with increasing temperature is accelerated at higher relative humidity. The cause is also visible from this plot - it is owing almost entirely to the increase in latent heat. For such applications, the aforementioned *dew point temperature* ϑ_{dp}, or simply dew point, is regularly used. It refers to the temperature that corresponds to the saturation point at a given water content x. If any temperature within the cooling system is below this dew point, condensation will occur. From this point of view, the significance of a distinction between sensible and latent heat is evident: at the same total enthalpy, different air packages may have vastly different dew points. The next paragraph introduces a practical visualization diagram that illustrates this phenomenon.

2.1.4 *The h-x-Diagram*

One of the most common graphical representations of the caloric properties of humid air is the h-x-diagram, introduced by Mollier in 1923 [34]. The reason for its continued popularity, especially in engineering, is that state changes can be simply sketched into the diagram and provide all relevant thermodynamic quantities without further calculations. Even additive processes, where water or steam are added can be directly assessed. An especially convenient application is the mixing of given volumes of humid air at different conditions: the resulting state of a mixing process can be found on a straight line connecting the initial states, its exact position simply determined by the mass ratio of the initial air flows [13]. The Mollier-diagram is used within the scope of this thesis to illustrate relevant psychrometric process steps. Its basic layout is as follows: for a given pressure, the specific enthalpy of humid air h is plotted as a function of the water content x. The enthalpy axis is slanted at an angle so that the $\vartheta = 0\,°\mathrm{C}$ isotherm is horizontal. Other isotherms exhibit a slope, which corresponds to the increase in enthalpy caused by an increase in water content (see Eq. (2.1.9)). The lines of constant relative humidity are also drawn; the saturation line at $\varphi = 1$, or 100 %, represents the dew points at the given water content x.

An example of how to apply the Mollier-diagram to practical problems is shown in Fig. 9a: Humid air at an initial state Z_I shall be conditioned to a final state Z_{IV}. The characteristic values at these state points Z_i are given in Table 3. Z_I represents common outdoor conditions in Singapore (see Fig. 2, Table 1), with a temperature of 28 °C and a relative humidity of 90 %. At the end of the conditioning process, Z_{IV} is a desirable climate for humans (Fig. 7). Two alternative paths between these points are shown in the h-x-diagram. They represent alternative thermodynamic processes - the one plotted in orange can be understood as sorption-based; the one plotted in blue is a classical, refrigeration-based approach. The former will be discussed in later sections. For now, let's take a look at the refrigeration process first, as this is the usual method found in all automotive air conditioning systems, as well as in virtually all household A/C devices. The intake air is passed over the cold surface of the evaporator, which is thermostatically set to a value just above 0 °C. Common dew point temperatures at the evaporator range from 2 °C to 6 °C, although variations can occur [17]. The higher the evaporator temperature is set, the more energy efficient the refrigeration process due to the increased COP (see Section 2.2). While passing the evaporator, the air is cooled at constant water content (Z_I to Z_{II}). When it reaches the dew line ($\varphi = 1$), condensation occurs on the evaporator and thus water is removed from the air (Z_{II} to Z_{III}). The air is then heated at constant water content to the desired temperature (Z_{III} to Z_{IV}). In modern automotive units, this is can be achieved by passing a fraction (or all) over the heat exchanger, as shown in Fig. 5. In most residential units, the cold, saturated air (Z_{III}) is simply mixed with the indoor air (Z_I) to reach the desired conditions. This works especially well if the intake air is hot, but not too moist. For the sketched conditions, the mixing point will be found somewhere on the yellow line. It is noteworthy that parts of it are located below the saturation line, in the two-phase region. If the mixing point lies somewhere in this part, the observed result is fog, forming from droplets of liquid water in the vicinity of the cold air duct. The values obtained from the Mollier-diagram are the ones for pure thermodynamic state changes. The actual energy consumption of a device implementing either of the paths will vary due to their efficiency. For example, component efficiencies need to be accounted for as well as auxiliary consumption due to e.g. compressor, fans or blowers. These can be summarized into a combined COP value for the entire process, as introduced in Section 1.4.3. The following sections make use of this diagram for reference and further explanations of the cooling and dehumidification processes considered.

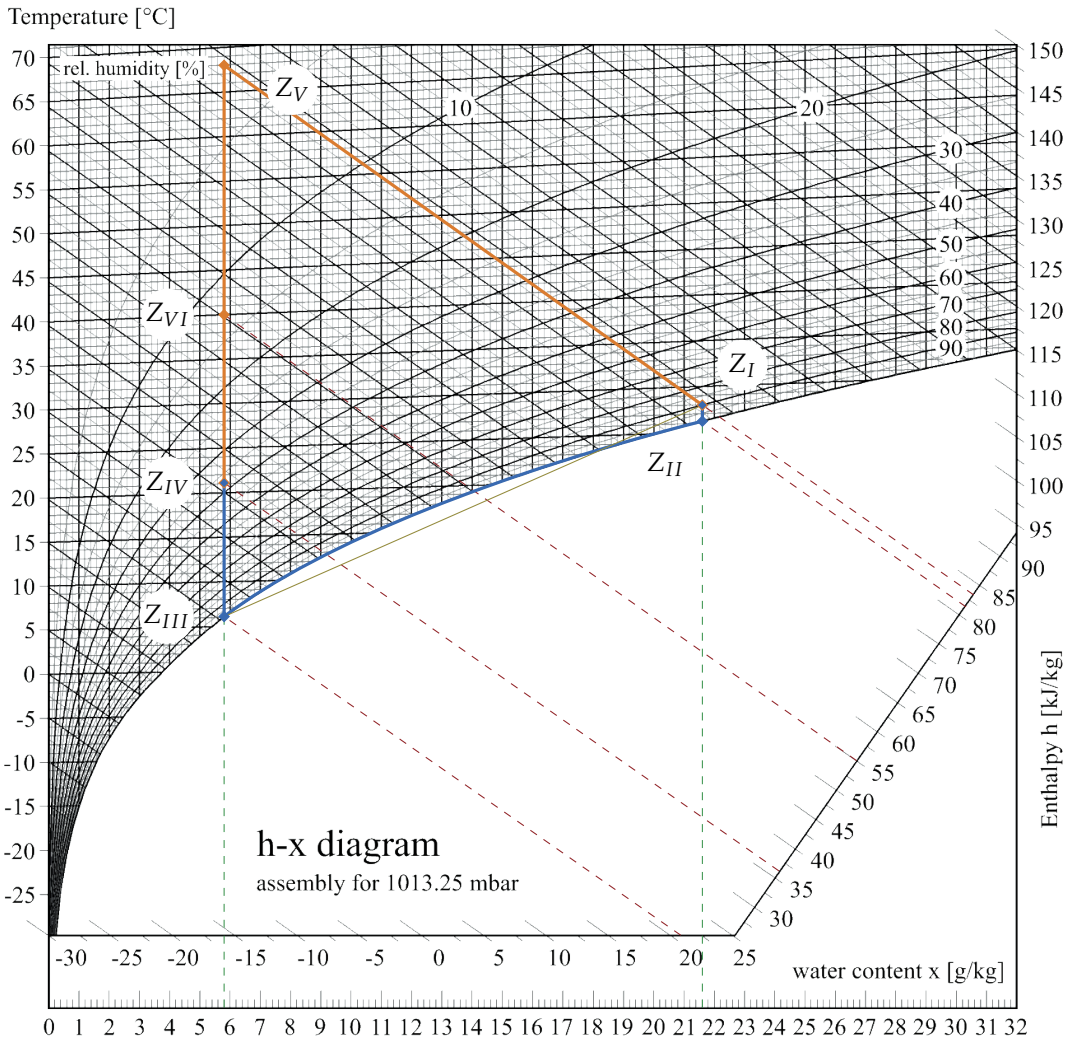

(a) A common plot of the Mollier h-x-diagram for standard pressure (p = 1013.25 mbar).

State Z_i	ϑ_i [°C]	x_i [g/kg]	h_i [kJ/kg]	φ_i [%]
Z_I	28.0	21.6	83.5	90
Z_{II}	26.2	21.6	81.5	100
Z_{III}	6.0	5.8	20.5	100
Z_{IV}	21.0	5.8	36.0	38
Z_V	40.0	5.8	55.0	13
Z_{VI}	68.0	5.8	83.5	3.3

(b) Thermodynamic states of air as depicted in Fig. 9a, specific enthalpy values rounded to 0.5 kJ/kg.

Figure 9 & Table 3: Mollier-diagram and thermodynamic states for an adsorption-supported cooling cycle.

2.2 EFFECT OF AIR DRYING IN AUTOMOTIVE AIR CONDITIONING

It can be concluded from Section 1.3, that the dominant factor in A/C-energy consumption is the enthalpy introduced into the vehicle by air exchange. If the vehicle was perfectly airtight, the thermal load would only arise from solar radiation through the windows, conduction through the body, and heat generated by the passengers. However, a vehicle is never hermetically sealed and even under stationary conditions, leakage causes a certain influx of ambient air into the vehicle cabin. Moreover, it has already been pointed out that an operation strategy using recirculated air only, has significant disadvantages. Necessary ventilation rates were therefor taken into account, according to thermal comfort studies. In order to quantify the air flow through a vehicle, the use of the unit *air changes per hour (ACH)* has become an established concept. It can be interpreted as the ventilation rate in m^3/h divided by the vehicle's volume in m^3. It is a normalized quantity, thus independent of type and size of the vehicle considered. Often used in the assessment of the evolution of contaminant concentrations in cabin air, within this project, its main application is to determine the thermal load caused by intrusion of fresh ambient air. There are numerous studies that investigate the air changes per hour under different aspects. As a starting point, a literature review of those was conducted to get a good estimate of the ACH values which are to be expected. One major challenge lies in the accurate determination of the vehicle's interior volume: when no CAD-data is available, which would allow for computerized calculation, own measurements have to be conducted. Two methods are used within the reviewed studies, sometimes both within the same one. The first, rather obvious approach consists of geometrical measurements, where lengths of void volumes and furnishings inside the vehicle are measured and the volume is then calculated therefrom. Other approaches employ a tracer gas, either to fill the vehicle up to an equilibrium concentration while measuring the gas flow, or by releasing a known amount of gas inside the vehicle and measuring the decay. Both methods are described in detail in the study conducted by Ott et al. [35]. The air changes per hour itself was measured at several different vehicle operating conditions. Variables are the vehicle's velocity, the position of the vents, the blower setting, and in some studies, also the position of the windows. The latter is obviously not relevant for the scope of this project: when the A/C is running, the windows must be closed, and ventilation is only conducted through the designated channels. The results for all relevant operating conditions are compiled in Table 35. In addition to these experimental results, Fletcher and Saunders [36] gave a functional correlation between wind speed and the air change rate, which coincides well with the other results from Ott et al. and is even used there to describe the air changes per hour for vehicle C [35]. Based on the air change rates found from the cited studies, a vehicle with a volume of 3.5 m^3 can be considered average, representative size. For TUM CREATE's own vehicle *EVA*, an initial, coarse assumption was made by Agua [7], who estimated a cabin volume of 5 m^3 for his simulations. At a later stage in the design process, the interior volume was recalculated from *EVA*'s geometry. It amounts to 3.82 m^3, to which the passenger compartment contributes 3.08 m^3 and the remaining 0.74 m^3 are allotted to the luggage compartment. Furnishing, such as driver and passenger seat as well as the center console have been accounted for. Since the compartments are not physically separated, the entire interior volume is used for the calculation of the air change rate. Again, this fits very well with the values found from literature cited in Table 35. These volumes will later be used to calculate actual air flow rates, and subsequently, the enthalpy that constitutes the load on the A/C unit. For now, a simplistic approach is taken, where the energy consumption is extrapolated from the findings in [7]. In his work, Agua used a rather high ACH value of 10 as the baseline, to account for *EVA*'s intended use case as a taxi - here, beside the leakage effects, the opening and closing of doors during passenger changes cause additional air changes as compared to a regular car. Based on this method, we will take a deeper look into the potential of an air-drying device. Also, the assumed COP value of 2.5 is more on the optimistic side, but still justifiable for a well-designed, brand new prototype vehicle. For the time being, the proposed dehumidification system shall be further investigated through a *black box* approach: the inner working principle is not yet considered,

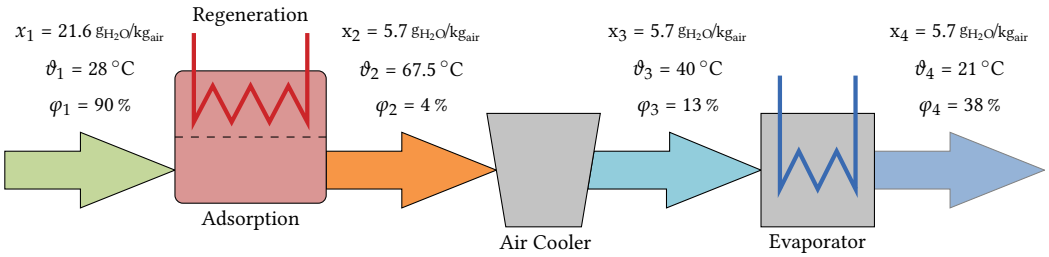

Figure 10: Illustration of the dehumidification process using the state changes from Fig. 9a.

instead only the input- and output-parameters are important: moist, ambient air is passed through the dehumidifier, where it undergoes an adiabatic drying reaction. It is subsequently cooled in an air cooler and then passed to the evaporative cooler of the regular A/C system. Simultaneously, another dehumidifier is regenerated. This concept is illustrated in Fig. 10 with the thermodynamic states from Fig. 9a.

To simplify the approach even further, we will assume an open system which operates at constant, ambient pressure. The parameters *humidity* and *temperature* can then be summarized under *specific enthalpy*. The relation of these parameters can conveniently been read from the Mollier-chart, introduced earlier. This chart also provides a simple way to estimate the maximum energy saving potential of a dehumidifying device: With the values highlighted in Fig. 9a, we can make the following estimation: If intake air from at a state Z_I is dehumidified to a state Z_V and subsequently cooled to a state Z_{VI}, the specific enthalpy changes accordingly. For the described state change, it is reduced by $\Delta h_{I-VI} = 28\,\mathrm{kJ/kg}$ - from $h_I = 83\,\mathrm{kJ/kg}$ to $h_{IV} = 55\,\mathrm{kJ/kg}$. The remaining $\Delta h_{VI-IV} = 19\,\mathrm{kJ/kg}$ has to be supplied by the refrigeration cycle. If the same state change was to be achieved without dehumidification, the entire enthalpy change of $\Delta h_{I-III} = 62\,\mathrm{kJ/kg}$ would have to be borne by the A/C. The re-heating from state Z_{III} to state Z_{IV} can usually be done with waste heat, so this part can be omitted. In this example, the difference between the two described processes would be $43\,\mathrm{kJ/kg}$ - a reduction of 69 %. Although this is an idealized example, the savings potential justifies further investigation. First and foremost, one aspect has only been implicitly stated so far: the key to such a process is the regeneration of the desiccant - only if this part can be achieved with waste heat, at least to a significant portion, can the overall system be energetically beneficial. At this point, a major issue of the electric vehicle concept comes into play - due to the high efficiency of modern electric machines and power electronics, much less waste heat is available compared to combustion engine powered cars. Furthermore, the vehicle's components operate at much lower temperatures than combustion engines. These two factors constitute drastic limitations on the design of a suitable dehumidification system, and their consequences are thus at the very core of this research project. For a preliminary assessment of the regeneration of the desiccant, estimations can be made for the available waste heat: the power needed for regeneration must be smaller or equal to the waste heat produced by the vehicle, otherwise an auxiliary heater would be necessary. Only the losses from the power train and the A/C shall be considered. Firstly, because they make up for the vast majority of all losses. But secondly, many other auxiliary devices that cause losses are not connected to the refrigeration- or water coolant circuit, so the waste heat produced by them is actually not available for desiccant regeneration. The available waste heat can be written as the sum of the waste heat generated by the power train, which is calculated directly from the initial power consumption P_{init} and the power train efficiency η_{pwr}. This heat is rejected through the water cooling circuit's radiator, which is stacked together with the condenser of the A/C in the front part of the vehicle. Adding to this is the thermal load on the A/C system, which consists of the thermal loads of the solar irradiation ΔP_{solar}, the passengers P_{pass}, the heat flow through the vehicles body P_{body}, and the residual enthalpy of the fresh air Δh_{rest}. The term Δh_{rest} corresponds to the state change from Z_{VI} to Z_{IV} in Fig. 9a. Finally, the heat generated by the compressor is added,

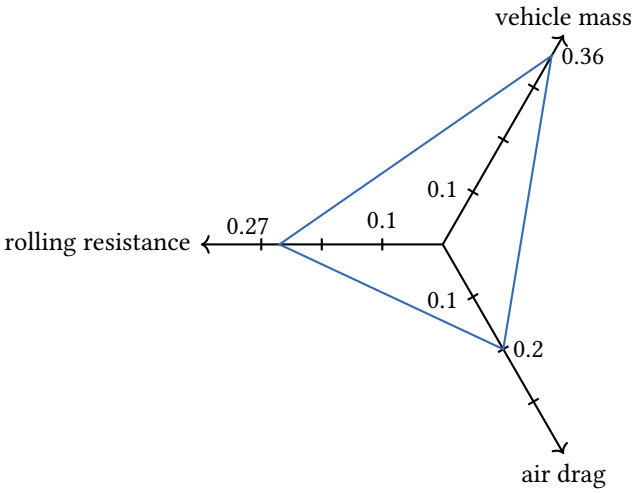

Figure 11: Sensitivity analysis of the influence of three parameters on the overall energy consumption of the vehicle, reproduced from [7]

which is simply the sum of the load on the A/C system, divided by the COP. The waste heat rejected through the thermal module, consisting of condenser and radiator, can then be calculated as

$$\dot{Q}_{waste} = \left(1 - \eta_{pwr}\right)\ P_{init} + \left(1 + \frac{1}{COP}\right)\ \left(P_{solar} + P_{pass} + P_{body} + \dot{m}\,\Delta h_{rest}\right). \tag{2.2.1}$$

In the world of automotive engineering, any proposed addition of mass to a vehicle design is met with great skepticism. Therefor, in a final step, the conflicting issue of additional mass in the vehicle is addressed by quantifying the impact of its implementation by means of a sensitivity analysis. Even in the first iteration, simulations showed that the electric vehicle is relatively insusceptible to the addition of mass: An increase of 1 % in total vehicle mass leads to a consumption increase of just 0.36 % (Fig. 11) in energy consumption. The proposed dehumidification device was represented as the sum of its estimated component masses. This was done in terms of a worst-case-analysis by assuming a low-performing desiccant, heavy heat exchangers and heavy auxiliaries. Several scenarios were sketched, but the following seemed a viable starting point: with 6 kg for desiccant units, an 8 kg air cooler, a 3 kg blower and 3 kg of auxiliary components, a rather pessimistic setup amounts to 20 kg. It is also assumed that an increase in blower power, or a second fan, of 50 W is required to overcome the pressure drop caused by the dehumidifer. It is very important to mention that this value is assumed to be independent of the air change rate. With a specific dehumidifier, the pressure drop, and hence the additional energy consumption, would strongly depend on the air flow rate - this correlation is discussed in detail in the following chapters. The model at hand can thus be understood as employing an optimized dehumidifier for each air flow rate.
With the additional mass, *EVA*'s energy consumption would increase by 0.81 $^{\mathrm{Wh}}/_{\mathrm{km}}$, and by another 2.39 $^{\mathrm{Wh}}/_{\mathrm{km}}$ from the additional electrical load. As underlined by the simulations (Fig. 12), this is offset by energy savings from the dehumidification device even at moderate air change rates. In spite of these very suboptimal design parameters, the addition of a dehumidification device is deemed advantageous. As the project progressed, the assumptions were continuously refined in order to reflect the more precise data on component dimensions. The beneficial effect becomes more pronounced, the lighter the device can be built, the less additional energy it requires and the larger the achievable enthalpy decrease. During the simplified, simulation based assessments in this chapter, the dehumidifier is not discussed in detail. As a measure for efficiency, the dehumidifier is simply characterized by its potential to reduce the intake air's enthalpy while achieving the target

water content x. Although this is a rough and reduced calculation, for the sake of correctness, it shall be highlighted that a dehumidifier can only lower the latent heat - the parts of the specific enthalpy that are caused by moisture (see Eq. (2.1.9)). The largest - theoretically - possible amount of enthalpy that can be removed by a dehumidifier is thus the difference between the enthalpy at ambient water content x_{amb}, and the enthalpy at the target water content - both at the original ambient temperature ϑ_{amb}. This is not achievable in practice, since heat transfer in the air cooler will diminish when approaching ϑ_{amb}, and this temperature will never be reached. It can be found from the Mollier chart at the intersection of the ϑ_{amb} isotherm with the target water content. For the example at hand, this is accounted for by limiting the maximum efficiency to 90 %. How well the dehumidifier actually performs at meeting the target moisture content will be addressed in later sections. With the described assumptions for the added mass and the auxiliary power, the total energy consumption was extrapolated from the baseline scenario. Fig. 12 shows the plotted results for up to 30 ACH. The method is quite straightforward: the simulation results for the A/C system's energy consumption $W_{A/C}$ and the breakdown into the different sources (see Fig. 4) at a given air change rate are defined as a reference scenario (index *ref* in Eqs. (2.2.2) and (2.2.3)). The dehumidification process is accounted for as a reduction in enthalpy ΔH of the intake air. Finally, the additional electrical load is introduced as power consumption P_{dh} over the duration of the simulated driving cycle's duration (here: STDC with 1310 s). The extrapolated energy consumption for the new scenario is then calculated as follows:

$$W_{A/C,new} = \left[\underbrace{\frac{H_{new}}{H_{ref}}}_{\substack{\text{enthalpy}\\ \text{decrease}}} \underbrace{\frac{ACH_{new}}{ACH_{ref}}}_{\substack{\text{air change}\\ \text{rate increase}}} \underbrace{\frac{W_{air,ref}}{W_{A/C,ref}}}_{\substack{\text{air change}\\ \text{contribution}}} + \underbrace{\left(1 - \frac{W_{air,ref}}{W_{A/C,ref}}\right)}_{\substack{\text{passenger, window \&}\\ \text{body contribution}}} \right] W_{A/C,ref} + P_{dh} \frac{1310\,\text{s}}{3600\,\text{s}} \tag{2.2.2}$$

which can be simplified to

$$W_{A/C,new} = W_{A/C,ref} + \left(\frac{H_{new}}{H_{ref}} \frac{ACH_{new}}{ACH_{ref}} - 1 \right) W_{air,ref} + 0.364\, P_{dh}. \tag{2.2.3}$$

The same reasoning applies to the extrapolation of the total energy consumption, which takes into account the consumption increase caused by adding the extra mass of the dehumidification system m_{dh} to the vehicle's mass m_{car}. From the sensitivity analysis, the effect of additional mass on the reference consumption is quantified by a factor of $\xi = 0.36\,\%/\%$. With Eq. (2.2.3), the extrapolated total energy consumption $W_{ttl,new}$ can thus be expressed as

$$W_{ttl,new} = \left(\frac{m_{dh}}{m_{car}} \xi + 1 \right) W_{ttl,ref} - W_{A/C,ref} + W_{A/C,new}. \tag{2.2.4}$$

Four scenarios are plotted in Fig. 12, representing different dehumidification efficiencies of 20 %, 50 %, 90 % and one with no dehumidifier at all. The graphs show the vehicle's absolute energy consumption, the fraction of the air conditioner's contribution, the remaining range and it's percent reduction. The bottom left plot shows the potential increase in available range with different dehumidification systems, as compared to a reference design without dehumidification. As expected, the energy consumption rises drastically with increased ACH, which leads to a reduction in the vehicle's available range. In this simplified approach, the A/C will eventually become the dominant energy consumer with ever increasing ACH. This leads to a behavior that seems counter-intuitive at first, which can be observed from the bottom-left plot: the range gain goes through a maximum and then remains constant (actually diminishes again slightly). A quick glimpse at the adjacent plot explains this phenomenon and reveals the inherent flaw of extrapolations to large air change rates: as the remaining range approaches 0 km, the corresponding range reduction gets close to 100 % - at some point, even with the best dehumidifier, all considered systems result in an infinite energy

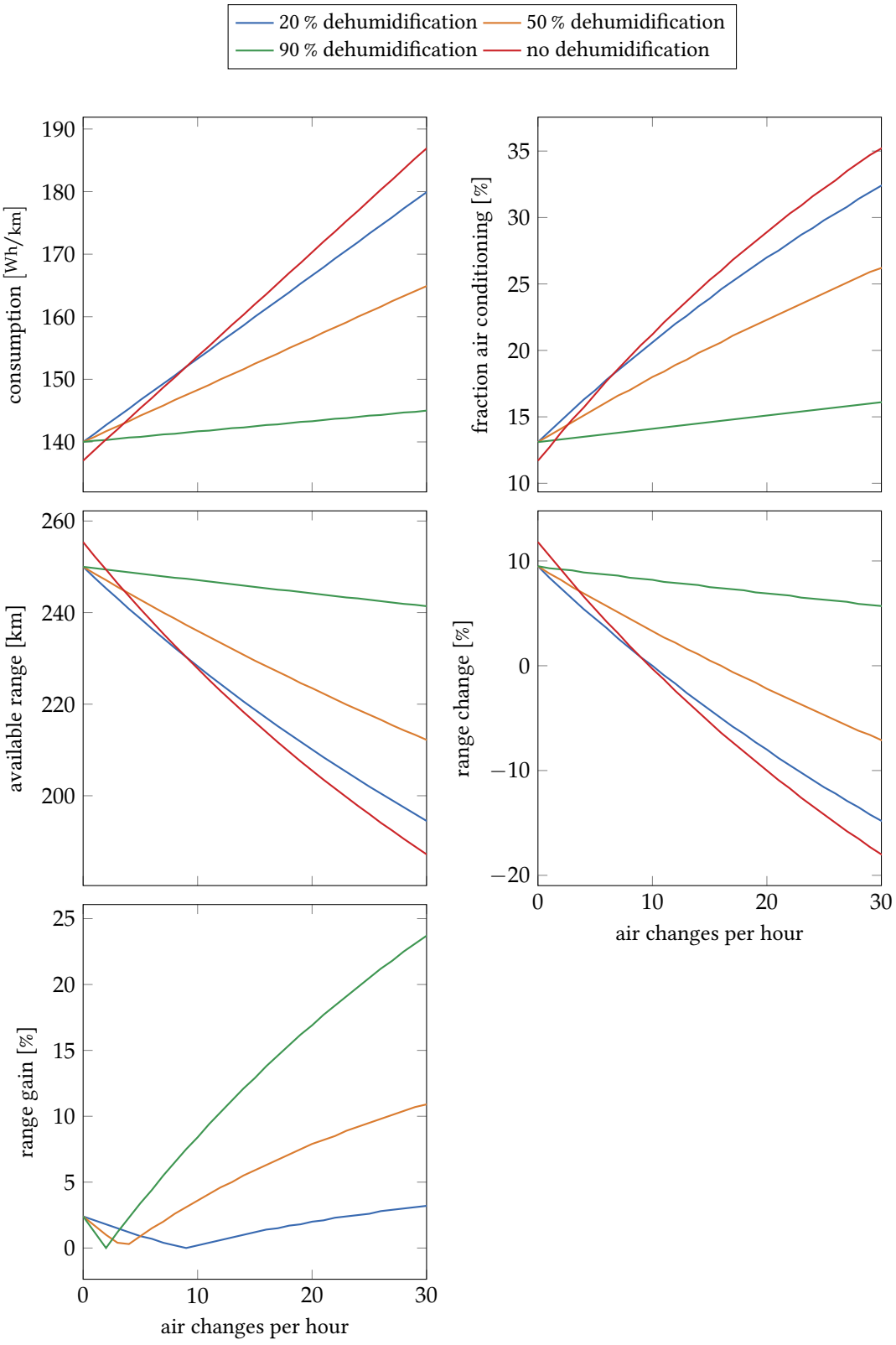

Figure 12: Range of an electric vehicle as a function of air changes per hour.

consumption and there would be no measurable added benefit. This underlines the importance to note that these extrapolations have limited significance, as they don't take into account that an actual A/C system is limited to a few kW of cooling power. Also, due to the nature of the ACH concept, it is hard to compare the results for different vehicles, as the absolute power consumption depends strongly on the interior volume of the vehicle. That said, in the range up to approximately 50 ACH, they provide a good qualitative indication of the systems behavior. Despite their limitations, the simulated values point towards an universal property of any A/C system: a dehumidification device does not provide an ever increasing benefit, instead, it exhibits a point of maximum effect, which in turn depends on the system's efficiency. Combining this insight with the results from research focusing on thermal comfort, the goal is now to balance a trade-off between comfortable ACH and a reasonable power consumption. It has been established in previous research that fractional recycling provides the best compromise between energy savings and comfort, as studied by Grady et al. [37] and Jaakkola et al. [38]. The ambition, however, should be to identify a scenario that provides optimum thermal comfort while consuming *less* energy than the reference system. Under the considered circumstances and boundary conditions, an air change rate between 10 ACH and 20 ACH is considered a good trade-off between an increase in consumption and elevated comfort. For example, even in the scenario of a moderate enthalpy reduction by 50 %, the air change rate could be increased from 10 ACH to 14 ACH, while maintaining the original range. In the scenario with 90 % reduction, this break-even point would be found at a value of 70 ACH!

The integration of the dehumidification system into a common automotive A/C unit is sketched in Fig. 13. Air enters the enhanced A/C system at ambient conditions (green), is then dried in a dehumidifier, cooled down passively and passed to the existing evaporative cooling system. The regeneration of the desiccant is done in parallel, with waste heat from the condenser and the vehicle's other thermal systems. Moisture leaves the system with the regeneration airflow back to the environment (orange).

The constant weather conditions in the tropics are a huge advantage when designing the dehumidification process. The operating point will most of the time lie within this quite narrow margin, therefor the apparatus does not have to be designed to cover other conditions. This leads to a lean and compact setup, which can potentially achieve high efficiencies at the target conditions. This assumption will be further discussed in the following sections. It should be emphasized that the reason for focusing on tropical conditions lies within the scope of the TUM CREATE project, which is focused on the mobility sector of Singapore. This doesn't mean that the concept presented in this thesis is not applicable to other climatic regions. The main difference between the tropics and all other climate zones is the absence of seasons: While, in another region, the device might be useful during a few hot and humid months annually, it might not be advantageous during other times of the year. In that case, it constitutes additional weight to the vehicle without any benefit, thus possibly offsetting the energy saving effect during its operation. Therefore, applications outside the tropics pose additional questions that need to be addressed separately in future works, most probably on a case-by-case basis. The results of this thesis will nevertheless provide a solid foundation for such projects. The conditions in Singapore on the other hand constitute an excellent reference scenario for other cities located in a tropical climate.

As a generalized approach, the usefulness of adding a system like the one described above can be estimated for other environmental conditions if some input parameters are known: a reference power consumption P_{ref} [W] of the vehicle at a given ACH number, which is extrapolated from a driving cycle simulation or a representative data recording. The corresponding sensitivity ξ of this consumption towards additional mass must be then be assessed from models or experiments. The average number of months per year $M_{A/C}$ that air conditioning is actually needed, and the vehicle volume V_{car} [m^3] need to be known. Reasonable assumptions are required for the additional mass m_{dh} [kg] and power consumption of the dehumidifier P_{dh} [W], as well as for the COP of the A/C unit. Lastly, the potential decrease in enthalpy that can be achieved through a dehumidifier, Δh_{dh} [kJ/kg], must be estimated. This can be done, for example, with the help of the Mollier-chart,

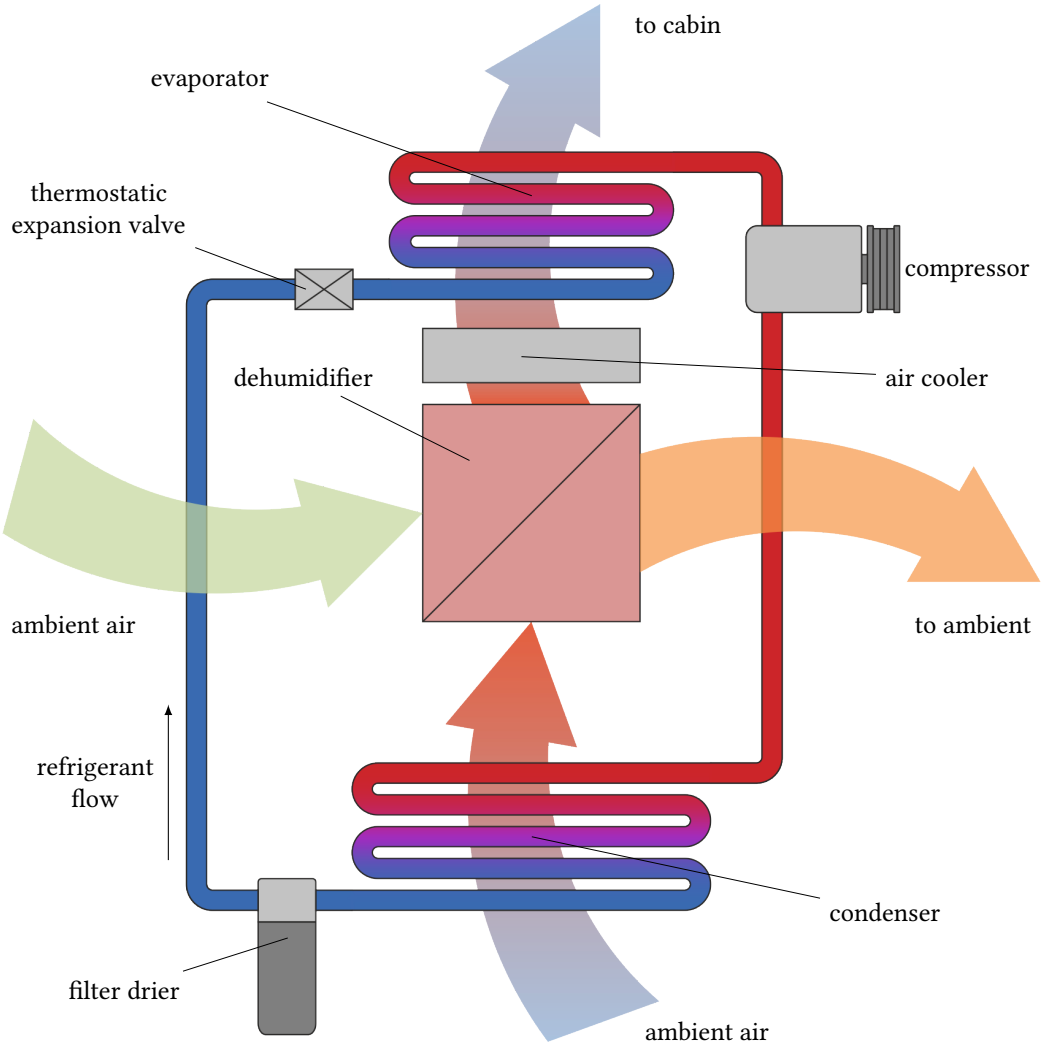

Figure 13: Automotive air conditioning refrigeration cycle with added dehumidifier and air cooler.

as described earlier. The following expression is then simply the ratio η_{dh} between potential energy savings and the expected increase in total power consumption - consequentially, for $\eta_{dh} > 1$, the dehumidification system can be considered beneficial.

$$\eta_{dh} = \frac{ACH \;\; V_{car} \;\; \rho_{air} \;\; |\Delta h_{dh}|}{\left(\frac{12}{M_{A/C}} \;\; \frac{m_{dh}}{m_{car}} \;\; \xi \;\; P_{ref} + P_{dh}\right) 3.6 \;\; COP} \tag{2.2.5}$$

The scaling factor 3.6 in the denominator is required to adjust between the different units.

2.3 DRYING METHODS

After the preliminary calculations on the effect of intake air drying on the vehicles energy consumption were deemed promising enough, an actual dehumidification process had to be designed. The process of air drying, or, more generally speaking, gas drying, is rather common in everyday applications. From treatment of high-purity laboratory gases to household air conditioning, several methods exist to dehumidify a given stream of gas. The method of choice depends a lot on the specific application's characteristics. The most commonly available gas drying methods are presented here.

2.3.1 *Cooling*

The most ubiquitous dehumidifying technique is cooling below the dew point of the moist intake air. This is accomplished by passing the airflow over a cooled surface, on which the water vapor condenses. The liquid water is then discarded and, depending on the application, the dry air must be warmed up again. A typical cooling-dehumidification process is shown in Fig. 9a. As discussed before, this is exactly the part that should be avoided as much as possible.

2.3.2 *Gas Separation*

Another method, often used for the drying of process gases, is the membrane dryer. By principle, this type of dryer can only be used if an already dry gas stream is available. The dry gas stream and the moist process gas are separated through a semipermeable membrane, through which water molecules can pass, but gas molecules are retained. The difference in partial pressure of the water vapor drives the molecules through a membrane, where they are swept away by the dry gas. This method is often used for drying compressed gases: a small fraction of the pressurized process gas can be expanded, thus enlarging it's water uptake capacity, and then be used as the sweep gas.

2.3.3 *Absorption*

Absorption, in the most general sense, refers to a process in which an atom, ion or molecule enters the volume of another bulk phase of any state (gaseous, solid or liquid). Many industrial absorption processes rely on a liquid-state absorbent. Especially in the field of gas treatment, wet scrubbers are commonly employed. The feed gas is brought into contact with an absorbing solution - this can be implemented as a trickle bed, through spraying or by forcing it through a vessel containing the absorbent solution or any other method that provides sufficient mass transfer of the substance to be absorbed. Absorption drying processes can be realized in the very same manner, here, water vapor represents the compound to be removed from the air stream. Absorbents used as liquid desiccants are usually salt solutions, common examples include lithium chloride, lithium bromide or calcium chloride solutions. More recently, ionic liquids have been investigated for this purpose [39], but questions around long-term stability and economic viability remain yet to be investigated. In the

special case of so-called deliquescent materials, which are also mostly salts, the desiccant is not initially a solution. Deliquescence refers to the property of an - initially solid - compound to absorb sufficient moisture to form an aqueous solution.
In any of the cases described above, the saturated solution (or dissolved deliquescent compound, respectively), needs to be regenerated if it is to be reused. The water is driven out of the solution through thermal separation methods. Depending on the type of installation, the process can be arbitrarily sophisticated, but the common denominator is the exposure of the saturated solution to increased temperature, possibly at reduced ambient pressure.

2.3.4 *Adsorption*

In an adsorption process the atoms or molecules that are to be removed from the fluid phase are bound to a surface, instead of being taken up into the volume. This process is the method of choice for automotive air conditioning. It is explained in greater detail in Section 2.4.4.

The decision-making process that led to the solution proposed and investigated in this thesis, on a high level of abstraction, is rather straightforward: To begin with, the design parameters of the dehumidification process must be considered. They are partly dictated by the boundary conditions of an electric vehicle, such as the low amount of waste heat due to the generally high efficiency, and the low operating temperatures (see Section 2.2). Since condensation is the part that shall be avoided, a sub-cooling process is ruled out immediately. The membrane-based gas separation process is not applicable either, since no dry sweep gas stream is available. The most promising candidates are thus the desiccant-based absorption- and adsorption processes. Considering the application environment, it quickly becomes obvious that absorption systems are not suitable in an automotive setting: The drying process would require the absorbent to be in contact with the humid air stream, which happens either through an atomized spray or a trickle bed. Both require complex pumping systems and carry the risk of spillover to other parts of the vehicle, in the worst case, to the passenger compartment. This poses a health concern, and is furthermore undesirable due to the corrosive nature of the halide anions often present in absorbent desiccants. Finally, any loss of desiccant should be avoided in order to keep the system's performance constant, but also for reasons of convenience - most electric vehicle owners will not take too kindly on an added necessity of regularly refilling the absorbent storage tank. This leaves the adsorption-based process with a solid-state desiccant as the likely solution of choice. It is at this point where the more detailed work begins - the design parameters of such a process can be varied endlessly, and the challenge is to identify the most suitable solution for the specific application. For the proposed dehumidification device in the electric vehicle, the key factors to consider are

- temperature of the air that is to be dried
- humidity of the air that is to be dried
- amount of air to be dried
- desired residual humidity
- desired target temperature
- cost of the drying process
- size and weight of the resulting process design.

These form the boundary conditions that determine the design of the process and the choice of a suitable desiccant. Those are the two key elements of the experimental part of this thesis. They are discussed in greater detail in their own respective parts, Section 2.5 and Section 2.6.2.

Table 4: Common nomenclature to describe the adsorption system.

Adsorbent	Solid phase whose surface interacts with molecules from the fluid phase
Adsorptive	Fluid phase whose molecules are able to adsorb on the surface
Adsorbate	Molecules from the fluid phase adsorbed on the surface, forming a separate phase

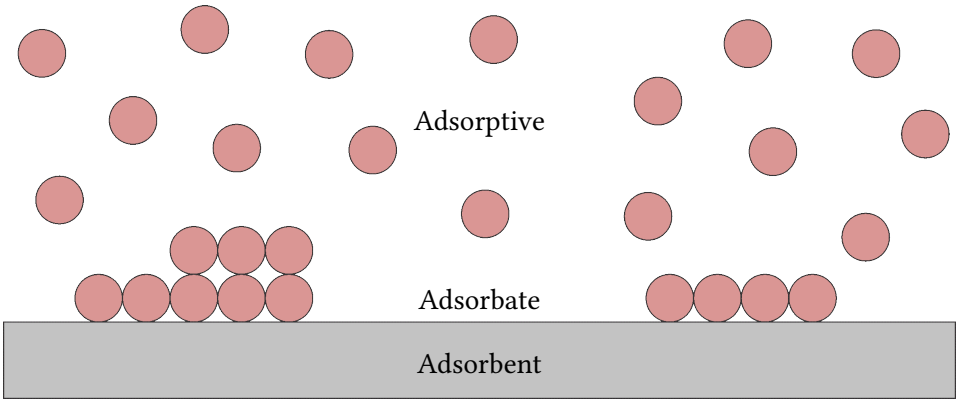

Figure 14: Illustration of adsorptive molecules in the fluid phase, adsorbate consisting of layers of molecules bound to the surface and adsorbent surface exposed to the fluid phase.

2.4 FUNDAMENTALS OF ADSORPTION

Adsorption as a means of separation has been known and applied since ancient times [40]. The first scientific experiments date back to the late 18$^{\text{th}}$ century, with Scheele being the first to describe the phenomenon as it is understood today [41]. The term *adsorption* was coined in the late 19$^{\text{th}}$ century by Kayser [42]. First industrial applications date back to the late 18$^{\text{th}}$ century, when charcoal was used in British sugar refineries [43]. However, large-scale industrial application did not begin until the early 20$^{\text{th}}$ century, when the patents by Ostrejko made the systematic production of activated charcoal possible [44]. During the second half of the 20$^{\text{th}}$ century, a vast amount of new adsorbents came into use, both natural and synthetic. An excellent overview of the historic development of adsorption in science and engineering can be found in [45] and [46], respectively.

As briefly mentioned before, adsorption refers to the enrichment of a species from a fluid phase on the interface of a condensed phase. It can further be distinguished between purely physical adsorption, also called physisorption, and adsorption involving the formation of chemical bonds, often referred to as chemisorption.
Physisorption involves only physical forces, which will be explained in more detail in Section 2.4.1, and is generally characterized by low enthalpies of adsorption. It is non-specific and more than one layer of adsorbed molecules can be formed, even to the point where condensation occurs and pores can be filled completely. In Physisorption, no activation enthalpy is required and adsorption equilibrium is usually reached quickly. Physical adsorption is fully reversible, the transfer of molecules from the surface to the fluid phase is called desorption.
Chemisorption on the other hand involves high enthalpies of adsorption, is highly specific and requires activation enthalpy. Since chemical bonds are formed between the surface and the adsorbed molecule, only the formation of a monolayer is possible and the process is irreversible.
Due to the nature of the application in this work, where adsorbents are used as desiccants, the term *adsorption* refers to physisorption only unless otherwise stated.
To describe the adsorption system, the nomenclature given in Table 4 and illustrated in Fig. 14, is established in literature and will be used throughout this work.

2.4.1 *Driving Forces during Adsorption*

Physical adsorption occurs due to van der Waals forces and electrostatic interactions. The latter can be subdivided into polarization, dipole- and quadrupole interactions between the molecules of the adsorbent and the molecules of the adsorptive. Electrostatic interactions, however, are significant only in adsorbents with an ionic structure, like Zeolites, especially in the presence of polar adsorptives [47]. They are largely temperature-dependent because the adsorbate molecules tend to orientate themselves differently according to their thermal motion. For non-ionic adsorbents, van der Waals forces form the dominant part. They can be described by the Lennard-Jones potential function [48] and are much less dependent on temperature.
The effects mentioned so far are strictly valid for a flat surface. In the case of porous adsorbents, more factors have to be considered to describe the adsorption potential. If the pores are sufficiently small in diameter, the potentials will overlap and different effects are observed. According to this behavior, the *International Union of Pure and Applied Chemistry* (IUPAC) proposed to classify pores by their internal pore width [49]. By definition, the pore width corresponds to the diameter in case of cylindrical pores and to the distance between opposite walls in case of slit pores. This classification is illustrated in Fig. 15, with the corresponding pore widths as follows:

- **Macropores - pore width > 50 nm**
  At macropore dimensions, the influence of the potential from the opposite wall is negligible, so that they behave like a free surface in the sense that condensation will only occur at relative pressures of approximately $p/p_0 = 1$.

- **Mesopores - pore width between 2 nm and 50 nm**
  In mesopores, potentials overlap partially and become small towards the center of the pore. While in the region closer to the wall the adsorption potential depends mostly on adsorbent-adsorptive attraction, towards the center interactions between adsorptive molecules become dominant. The combination of these effects can lead to the occurrence of capillary condensation, where condensation occurs at relative pressures far below $p/p_0 = 1$. This phenomenon will be further discussed in Section 2.4.4.

- **Micropores - pore width < 2 nm**
  The pore width lies already in the same order of magnitude as the diameter of the adsorptive molecules. Adsorption behaviour in this pore type is almost entirely dependent on adsorbent-adsorptive interactions.

2.4.2 *Adsorption Equilibria*

The most important way to understand and describe an adsorption process is the analysis of adsorption equilibria. For a single adsorptive, any adsorption equilibrium can be described by a function

$$F(p, T, C) = 0$$

with p and T being the pressure and absolute temperature of the adsorptive, respectively. C refers to the coverage of the adsorbent.
Consequently, there are three possibilities to express one variable as a function of the others:

$$p = f(T)_C \qquad C = f(T)_p \qquad C = f(p)_T$$

Depending on which parameter is kept constant, the adsorption equilibria are plotted as *isosteres* (lines of constant coverage C), *isobars* (lines of constant pressure p) or *isotherms* (lines of constant

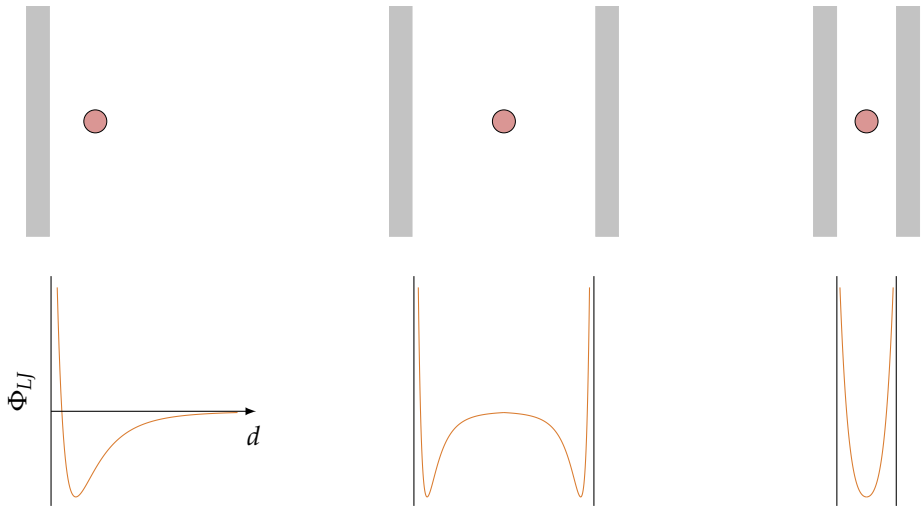

Figure 15: From left to right: Illustration of an adsorptive molecule in the vicinity of an open surface, a mesopore and a micropore. The bottom row shows their corresponding Lennard-Jones potentials Φ_{LJ} as a function of the distance d between adsorbent (grey) and adsorptive molecule (red). Drawing based on [50].

temperature T)[51]. While each representation has its own benefits, as discussed in [52], the most common way to publish adsorption data is in the form of isotherms. Since the processes investigated in this work are considered to be isothermal, this representation is used for the experimental data in the subsequent sections.

There exist a vast number of theoretical and semi-empirical theories to predict adsorption isotherms, giving all of them consideration would go far beyond the scope of this thesis. An extensive overview and description of established theories can be found in [53]. A short introduction, however, shall be given to the model proposed by Brunauer, Emmett and Teller [54]. Derived from the initials of the authors, it is commonly known as the *BET model*. It is valid for relative pressures between approximately 0.05 and 0.35. In this range, the amount of adsorbed fluid is considered proportional to surface area. At higher relative pressures, the pore filling process - especially in mesoporous materials - is often dominated by capillary condensation which is not described by the BET model. Within its range of validity however, it does not only predict adsorption behavior, but it also forms the basis for surface area measurements. On top of these factors comes its relative simplicity. For these reasons, the BET model still remains one of the most important equations today.
The BET theory is an extension of Langmuir's monolayer gas adsorption theory [55] to multilayer adsorption. It takes into consideration that it is not required for an adsorbed layer to be completed before an upper layer formation starts. In fact, a complete monolayer never forms in reality: with increasing surface coverage, the probability increases for an adsorptive molecule to strike an already covered adsorption site, thus being adsorbed in another layer. This principle is illustrated in Fig. 16. The BET theory provides the means to calculate the number of adsorptive molecules that would be necessary to form a closed monolayer. For the formation of the multilayer adsorbate, the BET model is based on three assumptions:

- All adsorption sites are energetically equivalent, with the enthalpy of adsorption $E_1 = E_s$ on the bare surface
- There is no lateral interaction between adsorbed molecules
- Adsorption energies in all higher layers are equal to the enthalpy of condensation of the adsorbate, i.e. $E_i = E_c \ \forall \ i > 1$

The following, short introduction shall illustrate the derivation of the BET-Equation. It follows largely the way found in literature [50].
We consider any equilibrated condition, meaning that at a certain relative pressure, the adsorbate is in equilibrium with the surrounding fluid phase. For the sake of simplicity, we will consider only a single species of adsorptive molecules in the fluid phase. At equilibrium conditions, the number of adsorption sites on the adsorbent surface covered by i layers (N_i) remains constant (Fig. 16). To formulate the equilibrium equations, the BET theory assumes that the uppermost layer is in dynamic equilibrium with the surrounding fluid phase.
The adsorbed layers are considered individually, starting with the first layer on the bare surface. Here, the number of unoccupied adsorption sites N_0 depends on two mechanisms: Adsorption of molecules on the surface and evaporation from the first layer to the fluid phase. In other words, N_0 decreases through adsorption, and increases through desorption. The rate of adsorption to the surface is

$$k_{ads} = a_1 \, p \, N_0 \tag{2.4.1}$$

and the rate of desorption is

$$k_{des} = b_1 \, N_1 \, e^{-E_1/RT} \tag{2.4.2}$$

where a_i is a constant derived from the kinetic gas theory [55] and p is the pressure of the adsorbate. b_i can be interpreted as the vibrational frequency of the adsorbate molecule normal to the surface and E_i is the enthalpy of adsorption. Since at equilibrium conditions N_0 remains constant, the adsorption rate must be equal to the desorption rate:

$$k_{ads} = k_{des} \tag{2.4.3}$$

$$a_1 \, p \, N_0 = b_1 \, N_1 \, e^{-E_1/RT} \tag{2.4.4}$$

If we look at the adsorption sites covered by one layer of adsorbate, we have to consider that the formation is governed by more mechanisms than the first one. N_1 increases through adsorption on the bare surface, but also through desorption from the second layer of adsorbate. It decreases when molecules desorb from the surface, as well as through adsorption of molecules into the second layer. At equilibrium conditions, the rates of formation and disappearance have to be equal:

$$a_1 \, p \, N_0 + b_2 \, N_2 \, e^{-E_2/RT} = a_2 \, p \, N_1 + b_1 \, N_1 \, e^{-E_1/RT} \tag{2.4.5}$$

by substituting Eq. (2.4.4), we obtain

$$a_2 \, p \, N_1 = b_2 \, N_2 \, e^{-E_2/RT} \tag{2.4.6}$$

With the assumptions made earlier, we can replace the enthalpy of adsorption for the second layer E_2 with the enthalpy of condensation E_c and generalize this equation for all higher layers ($i \geq 2$):

$$a_i \, p \, N_{i-1} = b_i \, N_i \, e^{-E_c/RT} \tag{2.4.7}$$

Also, we assume that the adsorption behavior in these higher layers is identical, i.e.

$$\frac{b_i}{a_i} = const. = g \;\; \forall \;\; i \geq 2 \tag{2.4.8}$$

and thus we can rewrite Eq. (2.4.7) in the following form:

$$N_i = \frac{p}{g} N_{i-1} e^{E_c/RT} \tag{2.4.9}$$

To find the relation between N_i and N_0, we start with defining

$$x = \frac{p}{g} e^{E_c/RT} \tag{2.4.10}$$

and substitute x into Eq. (2.4.9) to obtain

$$N_i = x\, N_{i-1} \;\; \forall \;\; i \geq 2 \tag{2.4.11}$$

from which one can immediately see the relation between N_i and N_1:

$$N_i = x\, N_{i-1} = x^2\, N_{i-2} = ... = x^{i-1}\, N_1. \tag{2.4.12}$$

By rearranging Eq. (2.4.4) to

$$N_1 = \frac{a_1}{b_1} p\, N_0\, e^{E_1/RT} \tag{2.4.13}$$

and substituting into Eq. (2.4.12), we find

$$N_i = x^{i-1} \frac{a_1}{b_1} p\, N_0\, e^{E_1/RT} = \frac{x^i}{x} \frac{a_1}{b_1} p\, N_0\, e^{E_1/RT}. \tag{2.4.14}$$

Recalling the definition of x in Eq. (2.4.10), and substituting into Eq. (2.4.14), the following relation is obtained:

$$N_i = x^i \frac{a_1}{b_1} g\, N_0\, e^{(E_1 - E_c)/RT} \tag{2.4.15}$$

At this point, the *BET constant* c_{BET} is introduced as follows

$$c_{BET} = \frac{a_1}{b_1} g\, e^{(E_1 - E_c)/RT} \tag{2.4.16}$$

and substituted into Eq. (2.4.15):

$$N_i = c_{BET}\, x^i\, N_0 \tag{2.4.17}$$

With these relations, the equations for the actual adsorbed amounts of fluid molecules can now be derived. The amount of adsorbed molecules at equilibrium, N_{eq} is the sum of all occupied adsorption sites, multiplied with their respective number of layers:

$$N_{eq} = \sum_{i=0}^{\infty} i\, N_i = \sum_{i=1}^{\infty} i\, N_i \tag{2.4.18}$$

The total number of adsorption sites on the surface N_s is simply the sum of all occupied and unoccupied adsorption sites. This number is identical to the number of molecules adsorbed at exactly one completed monolayer:

$$N_s = \sum_{i=0}^{\infty} N_i = N_0 + \sum_{i=1}^{\infty} N_i \tag{2.4.19}$$

By using Eq. (2.4.17), the ratio of adsorbed amount and available adsorption sites can be written as

$$\frac{N_{eq}}{N_s} = \frac{c_{BET}\, N_0 \sum_{i=1}^{\infty} i\, x^i}{N_0 + c_{BET}\, N_0 \sum_{i=1}^{\infty} x^i} \,. \tag{2.4.20}$$

Under the premise that $x < 1$, which will later be shown to be valid, the summations can be expressed as

$$\sum_{i=1}^{\infty} x^i = \frac{x}{1-x} \tag{2.4.21}$$

$$\sum_{i=1}^{\infty} i\, x^i = \frac{x}{(1-x)^2} \tag{2.4.22}$$

and substituted into Eq. (2.4.20):

$$\frac{N_{eq}}{N_s} = \frac{c_{BET}\, x}{(1-x)\,(1-x+c_{BET}\, x)} \tag{2.4.23}$$

The expression N_{eq}/N_s becomes infinite when x approaches unity. In the actual adsorption process, this is the case when the pressure of the adsorptive p approaches the saturation pressure p_0. This condition is inserted into the definition of x (Eq. (2.4.10)):

$$1 = \frac{p_0}{g}\, e^{Ec/RT} \tag{2.4.24}$$

Comparing this equation with Eq. (2.4.10) reveals the physical meaning of x as the partial pressure of the adsorptive:

$$x = \frac{p}{p_0} \tag{2.4.25}$$

This also justifies the above made assumption that $x < 1$.
At this point, the adsorbed amount N_{eq} and the number of adsorption N_s sites are replaced with the adsorbed volume and the monolayer volume according to the relation

$$\frac{N_{eq}}{N_s} = \frac{V_{eq}}{V_{mono}} \,. \tag{2.4.26}$$

Eq. (2.4.25) and Eq. (2.4.26) are then substituted into Eq. (2.4.23) to obtain the actual BET equation which describes the adsorption isotherm:

$$V_{eq} = \frac{V_{mono}\, c_{BET}\, p}{(p_0 - p)\left[1 + (c_{BET} - 1)\left(\frac{p}{p_0}\right)\right]} \tag{2.4.27}$$

Apart from providing an insight into the mechanisms of adsorption, this model is explained in such detail because it also constitutes a powerful tool for surface analysis. The importance of the BET equation in this context will be explained in Chapter 3.

2.4.3 *Enthalpy of Adsorption*

In the previous section, the energy E_i has been introduced as the amount of energy that is required to remove an adsorbed molecule from the adsorbed state. In a fully reversible process, this is the same amount that is released during the adsorption of one molecule onto the adsorbent. As it is impractical to consider the enthalpy for a single adsorbed molecule, a common way to derive an

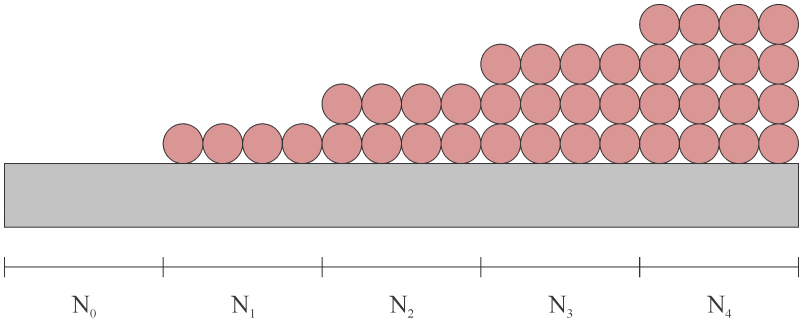

Figure 16: Multilayer formation of fluid molecules on an adsorbent surface. N_i denotes number of layers on the respective adsorption sites. At equilibrium conditions, all N_i remain constant.

expression for the enthalpy of adsorption is to consider the difference in enthalpy of the adsorbate before and after an infinitesimal amount is adsorbed - hence the widely used name *isosteric heat of adsorption* q_{st}. Today, the term "heat" is preferably replaced by *enthalpy of adsorption* to emphasize that this quantity is derived from an equation of state. The term "heat" should strictly be reserved for measured quantities [56]. It is noteworthy that q_{st} in literature usually bears the opposite sign as Δh_{ads}, meaning that

$$\Delta h_{ads} = -q_{st}. \tag{2.4.28}$$

The enthalpy of adsorption is of practical importance for several reasons. Firstly, as mentioned, it provides a measure for the strength of the interaction between adsorbent and adsorptive. In practical adsorption processes, this knowledge can be used to calculate the amount of energy necessary to regenerate a loaded adsorbent by means of desorption. Furthermore, one has to consider that the release of heat can also influence adsorption equilibria and kinetics in a process, because the heat is partially dissipated to the adsorbent.
The enthalpy of adsorption can be directly measured by using a microcalorimeter, or it can be obtained indirectly by using theoretical models. For the BET equation discussed in the previous section, the enthalpy can be calculated as follows [53]

$$\Delta H_{ads} = E_c + \zeta \frac{\left(1 - \frac{p}{p_0}\right)^2}{1 + (c_{BET} - 1)\left(\frac{p}{p_0}\right)^2} \tag{2.4.29}$$

with ζ defined as

$$\zeta = -R\,T^2 \left(\frac{\partial \ln c_{BET}}{\partial T}\right)_C \tag{2.4.30}$$

If we substitute Eq. (2.4.16), we can see that ζ becomes simply $E_1 - E_c$ and that at zero coverage ($p/p_0 = 0$), ΔH_{ads} is identical to E_1. As full coverage ($p/p_0 = 1$) is approached, ΔH_{ads} approaches the enthalpy of condensation of the adsorptive E_c.

This model requires the strict validity of the BET model. As discussed before, this may not always be the case for different adsorptive-adsorbent pairs or outside the range of applicability ($0.05 < p/p_0 < 0.35$). This is why in practice, a different method is widely implemented in laboratory software. It is an indirect approach that calculates the enthalpy of adsorption from at least two different isotherms, i.e. equilibrium data obtained at at least two different temperatures. This method is also used to calculate the enthalpy of adsorption in the later sections of this thesis. It applies the Clausius-Clapeyron equation for constant coverage

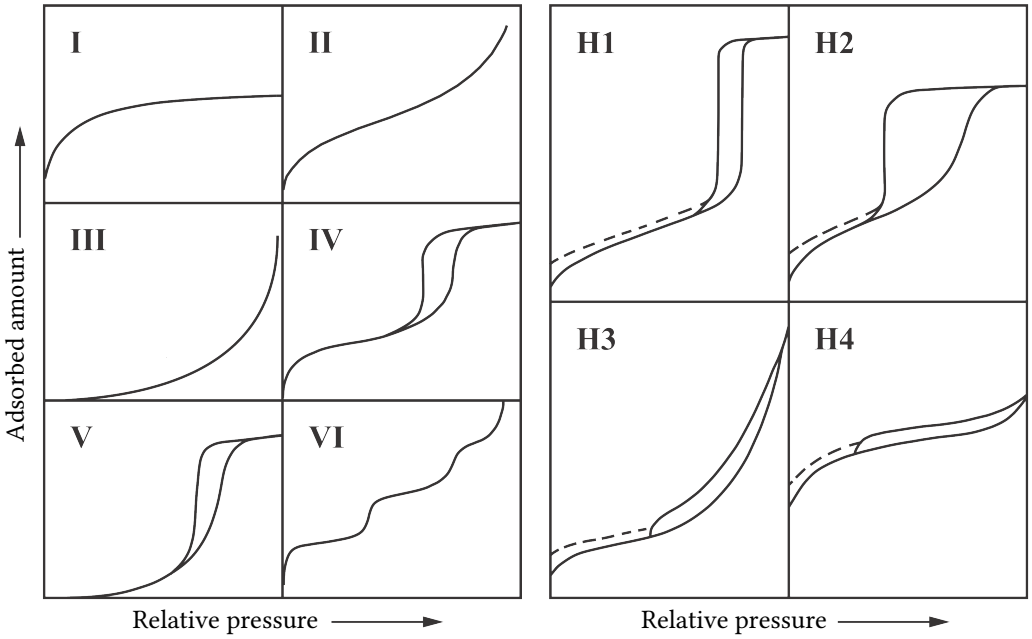

(a) Adsorption isotherm types

(b) Hysteresis types

Figure 17: The classification of adsorption isotherms and hysteresis as proposed by IUPAC [49].

$$\frac{q_{st}}{R\,T^2} = \left(\frac{\partial \ln p}{\partial T}\right)_C \tag{2.4.31}$$

in the integrated and rearranged form for two isotherms measured at T_1 and T_2, respectively:

$$q_{st} = \frac{R\,T_1\,T_2}{T_2 - T_1}\,(\ln p_2 - \ln p_1) \tag{2.4.32}$$

This quantity is often referred to as the *isosteric enthalpy of adsorption*, due to p_1 and p_2 being measured at the points of identical coverage in both isotherms.

2.4.4 *Capillary Condensation and Adsorption-Desorption-Hysteresis*

The validity of the BET isotherm finds its limit when the pore filling mechanism is not governed by adsorption on the surface and multilayer formation anymore, but instead condensation in pores occurs. The phenomenon is illustrated in Fig. 18. It is an important factor in the study of porous adsorbents for two main reasons.

First, the existence of a curved surface, a meniscus, inside the capillary delivers the explanation of isotherm hysteresis during reversible adsorption-desorption processes. The influence of this curvature on the vapor pressure of the adsorbent is quantified by the Kelvin equation [57]

$$\ln\left(\frac{p}{p_0}\right) = -\frac{2\,\sigma\,V_m}{r_K\,R\,T} \tag{2.4.33}$$

where σ is the surface tension and V_m the molar volume of the adsorbate. The meniscus radius r_{men}, as illustrated in Fig. 18, is often referred to as the Kelvin radius r_K . It should be noted that this model is only valid for pores that exhibit a diameter sufficiently larger than the molecular diameter of the adsorptive. If the pore diameter is smaller than a certain critical value, the concept

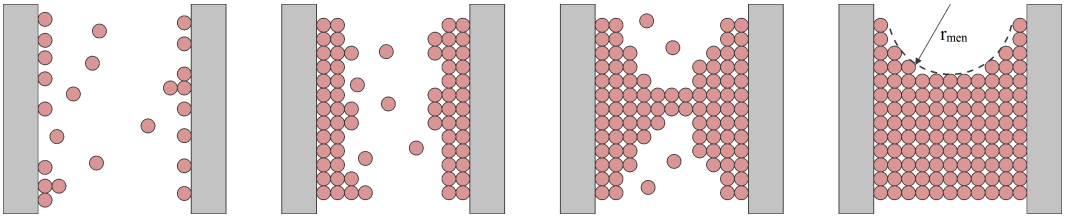

Figure 18: Formation of capillary condensation. From left to right: Adsorption on bare surface, Multilayer formation, beginning of capillary condensation, fully filled pore with characteristic meniscus radius r_{men}

of capillary condensation begins to fail. This is attributed to the occurrence of negative pressure in the condensed phase (p_l), as it is described by the Young-Laplace equation:

$$\Delta p = p_l - p_v = -\frac{2\,\gamma}{r_K} \tag{2.4.34}$$

If r_K reaches a certain value and the pressure in the gaseous phase p_v is sufficiently low, it is possible for p_l to assume negative values. The condensed phase is then in a metastable state, until the negative pressure exceeds the limiting tensile strength of the adsorbate. The condensed phase then becomes thermodynamically unstable and the concept of capillary condensation can no longer be applied [58]. The critical meniscus radius has been calculated by Kadlec and Dubinin [59] for various adsorptives and compared with experimental results, the values given here are in the range of $10.9\,\text{Å} < r_K < 16.8\,\text{Å}$, corresponding to pore diameters of $2.18\,\text{nm} < d_p < 3.36\,\text{nm}$. The actual critical pore diameters will be larger because the adsorption layer thickness t (see Fig. 28a) is neglected. As mentioned above, the critical radius varies for different adsorptives due to different molecular diameters, but it is independent of the adsorbent. These results are in good agreement with the findings in the studies by Harris [60], where a critical diameter of 3.6 nm is given. They also correspond roughly to the upper limit of the nanopore region as defined by IUPAC. In an isotherm plot, the point at which the critical diameter is reached can be found at the lower closure point of the hysteresis loop (the point between section B and C in Fig. 29). While there is no theoretical upper limit for the applicability of the Kelvin equation , it is in practice mostly dependent on the accuracy with which p/p_0 can be controlled. Modern devices suggest ranges from $p/p_0 = 0.93$ up to $p/p_0 = 0.995$, depending on the adsorptive [61, 62]. Due to p/p_0 appearing in logarithm in Eq. (2.4.33), this can mean huge differences as p/p_0 approaches unity. With nitrogen as the adsorptive, for example $p/p_0 = 0.93$ corresponds to a maximum meniscus diameter of 26 nm, whereas $p/p_0 = 0.995$ yields already a diameter of 374 nm. These constraints limit the applicability of the following Kelvin equation-based methods for pore size calculation to the mesopore and lower macropore region [63].

Second, the study of filled pores provides a means to calculate the pore size distribution of the material. Commonly used models were developed using a simplified model of simple cylindrical pores, which are either open to one or both sides and not interconnected. Several models based on the Kelvin equation have been described and are still widely used. The first one was published by Barrett, Joyner and Halenda [64] and is known as the BJH algorithm. Others include the ones published by Cranston and Inkley [65], Dollimore and Heal [66], and Broekhoff and de Boer [67, 68]. Methods based on the Kelvin equation are often considered *classical* models. More recent approaches rely on variants of density functional theory [69, 70], these are, however, not applied within this thesis and mentioned for the sake of completeness only.
Most modern laboratory devices provide at least some of these methods within their standard analysis software suite. However, analysis of pore size distribution has to be handled with extreme care if the structural properties of the material are not exactly known. The presence of non-ideal structures, for example dead-end-pores, bottleneck pores or narrow pore interconnections, can lead to evaporation phenomena like cavitation and percolation pore blocking - two mechanisms

which severely alter the physical meaning of the results obtained from the classical models [45]. Careful consideration has to be given to the presence of such effects if the isotherm data is used for pore size calculations. To avoid meaningless results, it is useful to have at least some information about the microscopic structure of the material that is analyzed. This can for example come from structural analysis, but also the classification of isotherms (Fig. 17a) can provide an indication of the applicability of a model. Any method that is based on the Kelvin equation can only be applied to type IV isotherms. Within the sub-classification of hysteresis loops (Fig. 17b), only types H1 and H2 exhibit a characteristic saturation plateau that can serve as a reference for completely filled pores. H1 isotherms are typical of ordered mesoporous materials, whereas H2 isotherms can be observed in materials with complex pore systems. All materials investigated within this thesis belong to one of theses two categories.
Even if the classical approach is found to be applicable, which method to apply can be a difficult choice. An evaluation of several methods for ordered mesoporous silica gels was done by Choma et. al. [71], [72]. From their results, the BJH method is deemed suitable for most of the materials used in this project.

2.5 ADSORPTION MATERIALS

Applicable materials for the design of an adsorption-based dehumidification process exist in tremendous varieties, but they can all be classified into just a few groups. This section gives an overview of these groups and provides more in-depth information on those that were ultimately selected and further investigated. Those that were rejected, and the respective reason for the decision against them, are also discussed. Decisive criteria for a suitable desiccant in the application at hand come from the process design parameters introduced in Section 2.3.4, and from general requirements towards materials that are in contact with respiratory air. They can be summarized as follows.

- low regeneration temperature, due to the restrictions in electric vehicles
- good heat conductivity - especially when larger desiccant particles are used, the interior should reach the regeneration temperature as quick as possible
- low specific heat, in order for the packed bed to cool down quickly after regeneration
- high adsorption capacity (gravimetric & volumetric), to keep the required desiccant mass low
- good long-term stability - to be in line with usual automotive service intervals, constant characteristics over several ten thousand cycles are desirable.
- good processibility for desired process - the adsorbent should be easy to handle and remain robust even in a mobile application
- sterile - microbial growth should not be possible on the adsorbent substrate
- cheap
- non-toxic - the adsorbent must not be harmful under any circumstances, to passengers, first responders and the environment

One noteworthy aspect of the major materials presented here is that they all fulfill one major criterion - if no additives are used, none of them is in any way toxic or environmentally harmful during disposal. In other characteristic features they show large discrepancies - for example the strength of the adsorption forces, the regeneration temperature, or the adsorption capacity to name a few. A comparison of typical adsorption behavior expressed by different materials, compiled from literature data, is shown in Fig. 19. The materials investigated in the respective studies were Sorbead R (silica gel), F-200 (activated alumina), Zeolite 13X and activated carbon BPL; the isotherms were measured at 25 °C, with the exception of the silica gel, which was measured at 27.85 °C.

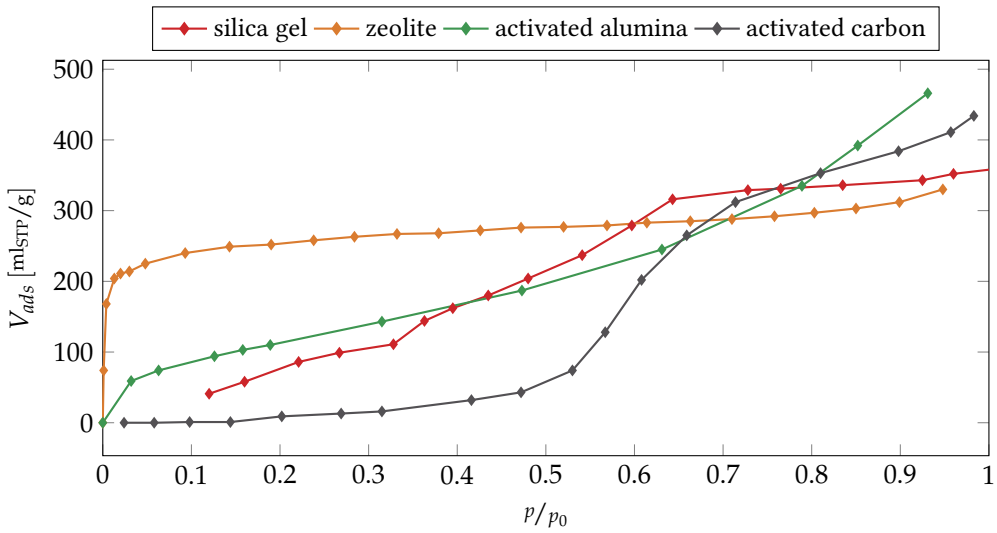

Figure 19: Typical water vapor adsorption isotherms for selected materials from different groups, compiled from [73–76]

.

ACTIVATED CARBON Arguably the most common adsorptive, activated carbons are used in many applications such as gas and water treatment, food and pharmaceutical purification needs, and even as medical products. Activated carbon is often derived from charcoal, but can also be produced from coal. The term *activation* refers to partial oxidation of the carbonaceous material, thereby greatly increasing its internal surface area. The activation process is done either by physical activation with heat and an oxidizing gas (often steam), or by chemical activation. The latter method uses oxidizing or dehydrating chemicals and heat, but at lower temperatures than the physical activation process. Both the specific surface area of activated carbon and the pore size distribution can vary greatly, they are often selectively synthesized to fit the desired application. Commercial products have surface areas in excess of 500 m^2/g, experimentally synthesized materials reach values of 2500 m^2/g [77]. Pore size distributions usually show a maximum in the micropore region, but extend well into the macroporous region. Due to the hydrophobic character of the material, these adsorbents are not suitable for application as desiccants, although they show some significant water uptake at high relative pressures [74]. Overall, the characteristics are still poor in comparison with other desiccants, and this group of adsorbents is thus not further investigated within this work.

ACTIVATED ALUMINA Activated alumina is a synthetically produced, highly porous form of aluminum oxide, Al_2O_3. Typical surface areas for commercial products are in the range of 300 m^2/g to 360 m^2/g. Its bulk density ranges from 690 m^3/kg to 785 m^3/kg, depending on pellet size. It is a polar adsorbent, thus molecules with a high polarity are preferentially adsorbed. It therefor exhibits excellent drying capabilities, and is widely used as a desiccant for process air in the chemical industry. Its low abrasion and high crush strength also make it an interesting candidate for mobile applications. Within this project, activated alumina is not considered because of its high regeneration temperature of 170 °C to 320 °C [78].

ZEOLITES The zeolites are a group of microporous, aluminosilicate minerals, which occur naturally but are also synthesized in large quantities. The term *molecular sieve* is often used synonymously, but this practice should be handled with care, since more colloquial definitions also refer to other substances as molecular sieves. According to the classical definition [79], zeolites are

crystalline, hydrated aluminosilicates with elements of group I and II, predominantly Na, K, Ca and Mg. They can be described through the following symbolic formula,

$$M_{2/n}O \cdot Al_2O_3 \cdot xSiO_2 \cdot yH_2O$$

wherein $x \geq 2$, n denotes the charge of the cation M, and y the number of adsorbed water molecules [80]. Many types of zeolites exist - around 200 are known today - of which 60 occur naturally [81]. Their crystalline structure causes a well defined pore size distribution, which promotes the application as molecular sieves for separation processes. The pore size can be controlled by the cation species M, most commercial materials exhibit pore diameters between 0.3 nm and 1 nm. Their specific surface area ranges from 500 m^2/g to more than 1000 m^2/g.
If the water is removed through heating, zeolites become strong adsorbents which can be used in both drying and energetic applications. Much research has been conducted on their application in thermal energy storage and adsorption-based air conditioning [82]. The water vapor adsorption behavior is different from the materials discussed so far. Zeolites generally show a lower specific capacity, but it is reached at much lower relative pressures and nearly constant (see Fig. 19). Together with their bulk density of 655 m^3/kg to 750 m^3/kg and their favorable crush strength, they seem well suited for the application at hand. Their high enthalpy of adsorption of ΔH_{ads} = 6800 kJ/kg [82] leads to stable adsorption characteristics at much higher temperatures than activated alumina or silica gel can provide. But consequently, it is also the adsorbent with the most demanding regeneration conditions - usual regeneration temperatures are between 200 °C and 450 °C. These temperatures are far from what is possible with waste heat of an electric vehicle, and thus the zeolites are not considered suitable.

CLAY MINERALS Also silicate minerals, clay minerals form a subgroup within the major group of *phyllosilicates*. As suggested by their name (*phyllon* being greek for "'leaf"'), this group is characterized by a structure made up of parallel sheets of silicate tetrahedra with a Si:O ratio of 2:5. Between these sheet layers, large cations or H_2O molecules can be intercalated, which makes them well suited as ion exchangers or catalyst supports [83]. The uptake processes show characteristics of both adsorption and absorption, and for some clays the desorption process causes irreversible structural changes. In fact, only one species of the clay mineral group is widely used as a desiccant - montmorillonite. As with the other desiccants discussed here, it is able to adsorb water from the gaseous phase and can be regenerated many times at moderate temperatures of around 150 ° C. Often it is not marketed in pure form, but instead as bentonite, where it forms the major constituent (60 - 80%). At low relative humidity of up to 30 %, its adsorption capacity is comparable to silica gel, in addition, it is resistant to liquid water. However, the adsorption capacity decreases already at temperatures exceeding 50 ° C, which limits its applicability to low-temperature drying applications.

SILICA GEL Silica gel is an amorphous form of silicon dioxide (silica). As the term *gel* suggests, it consists of a highly porous, irregular, tridimensional SiO_2 framework with voids in between, which may be filled with another fluid. Free-standing hydroxyl groups, called silanol groups, are also present, the overall chemical composition can therefor be expressed as $SiO_2 \cdot nH_2O$ [47]. The mechanism of adsorption to the surface arises from the formation of hydrogen bonds between these silanol groups and adsorptive molecules [84]. Due to the polarity of the surface groups, polar molecules are preferentially adsorbed.
Several methods for the preparation of silica gel can be found in literature, a common way is the acidification of alkaline metal silicates. Here, orthosilicic acid ($Si(OH)_4(aq)$) is produced in sufficient concentrations, in order for the polymerization process to start through intramolecular condensation. Through several steps, illustrated in Fig. 20, the final product is formed. After drying, silica gel becomes a hard, glassy substance that is clear to pale white in appearance. For many applications, indicators are added during the synthesis process which allow to visually estimate the

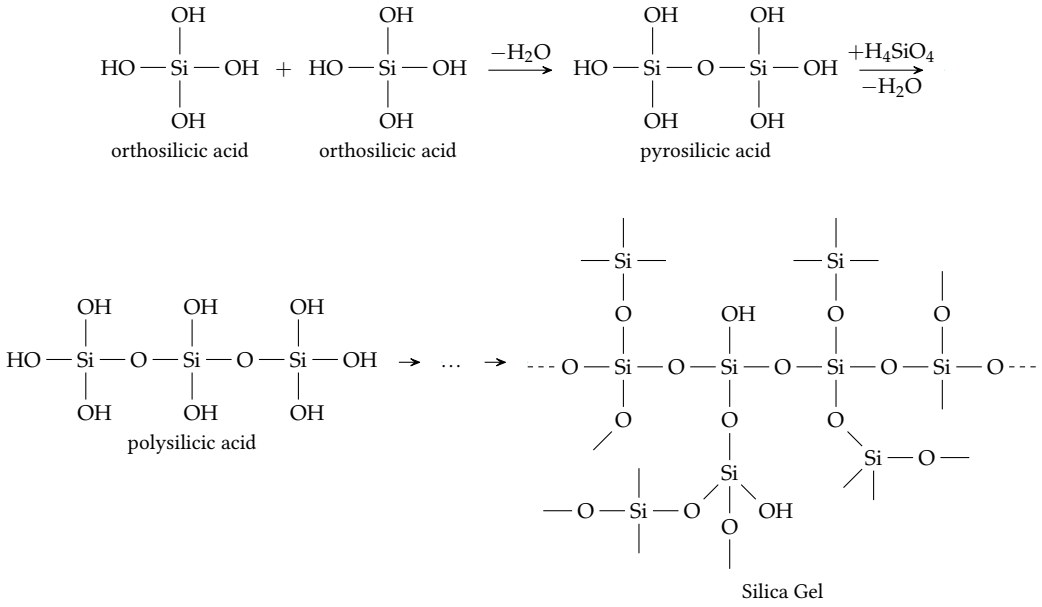

Figure 20: Formation of silica gel from waterglass [85].

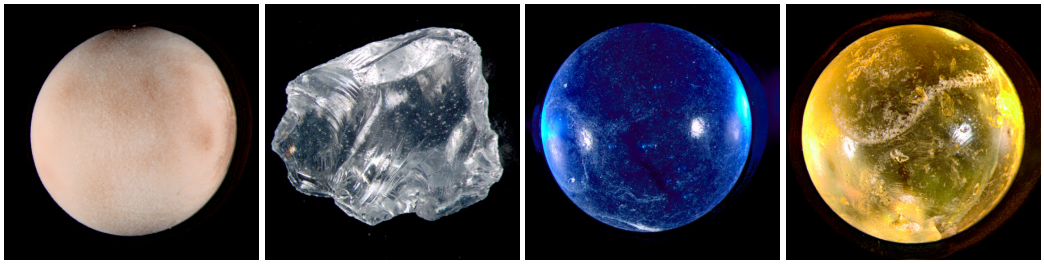

Figure 21: Examples of different shapes and colors of commercial Silica Gels, from left to right SB-WS, DT-G, QP-B and HD-O. Taken on an *Olympus SZX16* microscope with *Olympus DP25* camera module.

water loading of the silica gel. Commercial products may also be treated further to enhance certain properties, such as, for example, the resistance against liquid water. Some examples of various forms are shown in Fig. 21. By variation of the synthesis conditions, the internal surface area and the pore size distribution can be influenced. Typical values range from 250 m^2/g to 900 m^2/g, with pore size diameters of 1 nm to 12 nm [53]. Silica gel has been used extensively and for a long time, applications include chromatography and industrial-scale separation processes, but by far the most important use is as a desiccant. The adsorption capacity for water vapor is strongly dependent on the relative ambient humidity, but is independent of temperature up to approximately 65 °C. The enthalpy of adsorption is often cited as ΔH_{ads} = 4900 kJ/kg [82], but decreases with the amount of adsorbed water - as explained in Section 2.4.4. The stability of silica gel is promising, after 1300 regeneration cycles at 130 °C, the remaining capacity is reduced to 93 % [86]. Since the temperatures in the proposed application are much lower, it can be assumed that this value will be exceeded.

In recent years, novel types of silica gels have attracted much attention - the synthetic, hierarchically ordered nanostructured materials. Unlike the silica gels described above, their pore system is of defined size and follows a geometric order. First synthesized in 1992 as a catalyst support material for applications in the petrochemical industry [87], *MCM-41* is arguably the most well-known variety of these materials. The targeted synthesis procedure provides the possibility to accurately adjust a well-defined pore diameter within the mesopore range. Despite this ordered structure, they are not considered crystalline, as the SiO_2-network that forms the walls between the pores

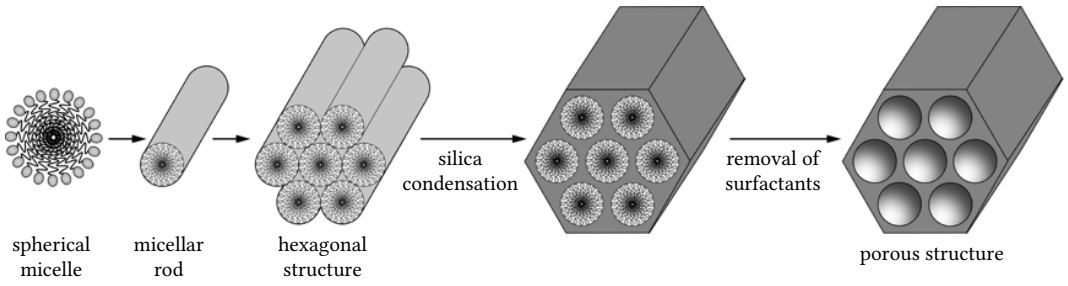

Figure 22: Illustration of the synthesis process for *SBA-15* type Silica Gels, from [88].

is still amorphous. The later introduced *SBA-15* belongs to the same class of structured materials, in fact it is very similar to *MCM-41* in many ways. The synthesis procedure of *SBA-15*-type silica gel varies from the one for *MCM-41*, as different surfactants are used as the template. This leads to some structural differences that are later discussed. *SBA-15*-type materials are also of high interest as catalyst carriers, and their application was also briefly considered within the TUM CREATE project as part of electrode materials for batteries. This approach was abandoned due to their poor electrical conductivity, among other issues. For adsorption drying however, *SBA-15*-type materials are very promising candidates due to their high surface area and well-defined pore size. This is enabled by the targeted synthesis process, where the pore diameter and arrangement of the pore network are determined. The synthesis was not part of the scope of this thesis, thus the description of the preparation process is kept brief - for more in-depth understanding of the field of mesoporous materials, the reader is kindly referred to the extensive literature on the topic.
In order to obtain materials with a defined nanostructure, template processes are a well established method. As the name suggests, the process involves the formation of a pattern structure, around which the desired material is then built up - in this case, a mesoporous network is arranged in a hexagonal configuration. The pattern, or template, is then removed, and its shape preserved in the final structure. For this purpose, sol-gel processes are widely used: in the most general description, a colloidal solution of finely dispersed precursor compound (the *sol*), forms a solid/liquid diphasic structure (the *gel*). This gel is then treated further to obtain the final product. For the synthesis of nanostructured materials, although variations can occur, four main steps can be identified - these are described here and illustrated in Fig. 22. First, the mesoporous structure is built up by using a block copolymer as the template, and a silica precursor. This is the main difference to the synthesis of *MCM-41* type materials, where quaternary ammonium surfactants are used. When in aqueous solution, they form liquid crystalline phases, just as the block copolymer does. The shape of this phase depends on temperature and concentration - cubic, hexagonal and lamellar mesophases are all found as well as isotropic and multiphase regions [89]. A common compound for template-based synthesis is P123, an amphiphilic PEO-PPO-PEO triblock copolymer, which forms micelles in aqueous solution. Spherical in shape at lower concentrations, it arranges in a cubic phase. At higher concentrations it forms a hexagonal phase with cylindrical micelles. It is also possible to obtain this arrangement at lower concentrations, if the silica precursor is already present [90]. At this stage, swelling agents can be added that increase the micelle diameter, and thus the resulting pore size. The silica precursor is then added to the solution. Well known compounds such as TMOS (tetramethoxysilane) or TEOS (tetraethoxysilane) can be used, but due to their low solubility and inherent property to release alcohols upon hydrolysis, which interact with the liquid crystalline phase, they are not a first choice. It is instead often preferred to first modify them with polyhydric alcohols, for example ethylene glycol, which mitigates both issues [91]. Alternatively, other silica precursors may be employed, which also do not show hydrophobic behavior - for example sodium metasilicate dissolved in dilute hydrochloric acid [88]. The second step is hydrothermal treatment at higher temperatures. Varying the temperature and treatment time also allows to influence the

resulting pore diameter. During this step, the template expands due to a decrease in hydrophilicity, and thus reduces the thickness of the silica walls. This increases the silica density, and as a side effect causes a reduction in microporosity of the wall material. After this treatment, filtration and washing of the samples are the third step, and the fourth step is removing the polymer by calcination at high temperatures. The template can also be extracted with many organic solvents, or through combinations of the described methods [92]. The method of choice also depends on the desired purpose of the resulting material, for example, if functional surface groups are introduced during the synthesis, or planned to be introduced afterward, some methods might be less suitable than others. Finally, the quality of template removal is also an important factor, the appearance of residual templating agent is not uncommon and also discussed in Chapter 4. An aspect that should be kept in mind about the *SBA-15*-type silica gels is their mechanical stability. The same properties that give them very favorable adsorption characteristics, namely the low ratio of wall thickness to pore size, makes them rather brittle. This is generally the case for all mesoporous silica gels, but *MCM-41* for example, shows a more favorable wall-to-pore ratio. The micropores that form in *SBA-15* walls as a result of the template removal further contribute to the low durability. However, at least this last part can to some extent be mitigated by adjusting synthesis parameters [93].
All silica gels, both unstructured and structured, are non-toxic and not harmful to the environment - as long as they do not contain additives like indicators. Their properties fulfill all the necessary criteria for a suitable desiccant, and they are thus considered the first choice for the investigated dehumidification device.

SPECIAL AND HYBRID MATERIALS Besides the major groups introduced above, some more specialized, even exotic types of adsorbents have emerged. Their availability varies from lab-scale synthesis to market-ready products. Functionalized polymers are commonly used in chromatography, are common in many industrial processes, and scientific research constantly produces new, innovative compounds [94]. In recent years, metal-organic frameworks (MOFs) have been investigated as adsorbents for many different applications, including water vapor adsorption [95]. Since these materials are usually tailored to very specialized applications, they are not considered within the scope of this thesis. If, however, they become readily available and fulfill the other criteria discussed, they may constitute viable improvements in future dehumidifier designs. *Hybrid Materials* refers to any combination of two or more materials in order to harness the advantages of several different compounds in one product. Here, the term refers to silica gels which have been impregnated with hygroscopic salts. These materials are sometimes referred to as *CSPM*s (composites 'salt in porous matrix') or *selective water sorbents*.

2.6 DESIGN OF ADSORPTION REACTORS

2.6.1 *Overview of Process Designs*

After focusing on the microscopic properties of the desiccant, this following section will give a brief introduction into the design of solid-state adsorption processes. They will be explained using adsorption of water vapor from an air stream as an example, since the main topic of this thesis is concerned with an air-drying process. The principles, however, can be applied to all sorts of processes in which a gaseous adsorptive is adsorbed onto a solid-state adsorbent. Herein, these processes are all considered to be perfectly adiabatic. The most obvious distinction can be made according to the system's boundaries. Adsorption systems can either be closed, or open to the environment. In a closed system, the adsorptive is stored in one container, the adsorbent in another. When brought in contact, for example by opening a valve, the adsorption process begins. During regeneration, the adsorbate is removed from the adsorbent, it can either directly return to its container and be stored for reuse, or be vented to the environment and the respective container refilled with fresh adsorptive. Since they are completely sealed, the system pressure can be arbitrarily

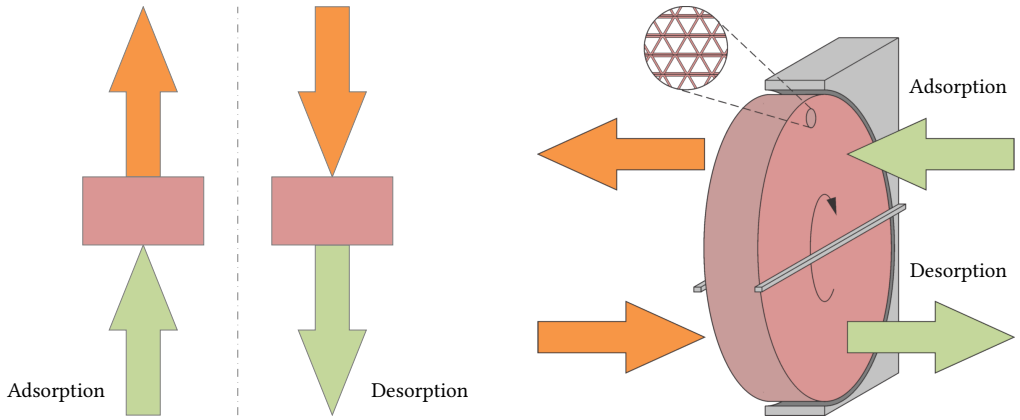

(a) Batch process (b) Continuous process

Figure 23: Illustration of a batch adsorption process (left) and a continuous adsorption process (right). Moist, cool air is shown in green, orange denotes hot, dry air. The adsorbent is shown in pink - as packed beds in the batch process, and as a desiccant-coated rotor in the continuous process. In a batch process, adsorption takes place until the desiccant is saturated. Then, desorption is carried out by passing hot air through the bed which removes and carries away the adsorptive, thereby regenerating the desiccant. The continuous adsorption process uses a desiccant coated rotor, where adsorption and desorption take place simultaneously in different sections.

chosen to fit the process requirements. Common examples include non-electric cooling devices that are often used for pharmaceutical, food- and beverage containers. Open systems on the other hand operate at ambient pressure and are in contact with the environment. Since the research interest of this project is the dehumidification of ambient air, only open systems are discussed herein. Another important distinction between adsorption systems can be made regarding their operation over time. A process can be described as either continuous, or as a batch process.

Batch refers to a process where adsorption takes place in a reactor until the saturation of the desiccant has reached a predefined value. The adsorbent bed is then regenerated by an appropriate method, both steps are sketched in Fig. 23a. In case of dehumidification, this is usually done by heating the bed to remove the adsorbed water molecules, which are then carried away by passing a stream of air through the packed bed. Often, the bed does not contain heaters itself, but instead hot air is passed through the bed. This type of regeneration is known as temperature swing adsorption (TSA). Other methods include pressure swing adsorption (PSA), where the pressure of the adsorptive is lowered to remove the adsorbate, purge gas stripping or displacement adsorption [47]. Those methods are generally not applied in desiccant dehumidification processes. After cooling down, the packed bed is ready for the next cycle. By their nature, the before mentioned closed systems are always batch processes.

In a *continuous* process, adsorption and regeneration take place simultaneously in different parts of the reactor, as shown in Fig. 23b.

Another distinction can be made taking into consideration the macroscopic shape of the desiccant. Here, we can differentiate between packed-bed reactors or flow-through support structures with a desiccant coating. For the sake of completeness it should be mentioned that the concept of the fluidized bed can also be applied to dehumidification processes [96], but this is neither common nor is it a suitable concept for mobile applications.

While theoretically both packed beds and coated substrate designs can be continuously operated, practical applications usually employ a flow-through support structure for this type of process. However, packed beds are sometimes also used in continuous processes in the form of rotating horizontal beds or multiple vertical beds [97].

Both the batch process and the continuous process concepts have their own respective strengths

Table 5: Comparison of batch reactor and continuous process.

Criterion	Batch process	Continuous process
drying capacity	+	++
pressure drop	-	-
desiccant change	+	-
continuity	-	+
design	+	-
weight	+	-
cost	+	-

and weaknesses, they are summarized in Table 5. Due to the overall simpler concept, the batch process is preferable in terms of weight, cost, and simplicity of mechanical design and maintenance. Both concepts add a pressure drop to the air path, that is within the same order of magnitude. While it is obvious that the continuous process provides uninterrupted operation, there is another inherent difference that is not immediately obvious: the adsorbing section of the desiccant rotor provides constant conditions of the desiccant bed, which is not the case in a batch reactor. Here, the adsorption characteristics of the packed bed are subject to change over the operating time. This is caused by the increased loading of the desiccant, and observed as a change of the conditions at the reactor outlet, even with the inlet conditions unchanged. Detailed descriptions on the fundamentals of adsorption packed bed reactors are found, for example, in the books by Ruthven [47] and Do [53]. With the conditions given in automotive operations, the dehumidification process must be designed with special regards to its compactness and light weight. For the latter, a desiccant rotor is well suited, since it has a rather low density of about 0.65 g/cm^3 [98], which is about 20 % less than that of a packed bed, see Table 9. For the principle stipulated in Chapter 1, the process must operate continuously. These properties would make the continuous process as described above the concept of choice. In real-world implementations however, there are some downsides which directly concern its suitability for automotive applications: Although in coated substrate rotors, it might seem that the airflow passes relatively unobstructed through the rotor's straight channels, the pressure drop in rotary dehumidification devices is still high. This is caused by the rather narrow geometry of these channels, which is required for sufficient interaction with the desiccant, thus providing the actual dehumidifying effect. Also, the elaborate ducting necessary to channel process- and regeneration air causes an additional pressure drop, that is present in packed bed reactors only to a much lesser extent. To overcome this pressure drop, powerful fans are necessary that add to energy consumption, weight and volume of the overall system. In order to achieve sufficient drying in a reasonably small segment of the rotor, an auxiliary heater (usually electric) is often employed. Finally, in order to operate at an optimum performance, the desiccant wheel must rotate at an optimum speed [99]. The necessary motor and gear further add to the overall system complexity. The packed bed system is therefor superior when it comes to dehumidifying performance versus design volume and overall system weight. As a reference, a few own measurements were conducted: A commercial desiccant rotor device with similar geometric dimensions as the proposed batch reactor was available at TUM CREATE: The *Dantherm AD120B* desiccant rotor was set up following the instructions. In addition to the principle sketched in Fig. 23b, this device also contains an electrical heater to provide hot regeneration air. The system was connected to a set of sensors and a *Graphtec GL-220* data logger. Temperatures and humidity of the dried airstream were logged, while the ambient humidity was monitored with a stationary hygrometer. The results are presented in Fig. 24. One of the most severe drawbacks of the continuous process can be observed here: the heat transfer between the regeneration zone and the adsorption zone. It is especially prominent through the pulsed operation

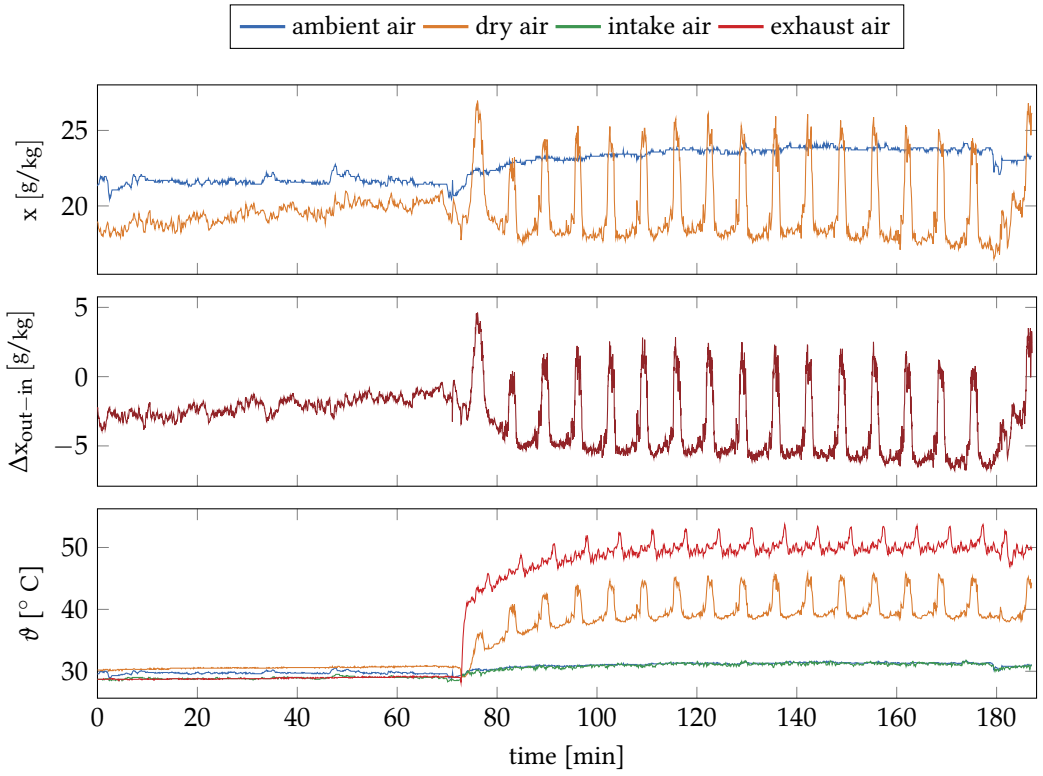

Figure 24: Results from the measurements with the *Dantherm* wheel

of the heater, indicated by the peaks in temperature. When the regeneration zone is heated, the wheel continues to rotate while it is still warm, transferring heat to the adsorption zone - which can be seen as peaks in the dry air temperature. Due to the increased temperature, the adsorption capacity is reduced - resulting in another peak, this time in the humidity of the dry air stream. The average dehumidification capacity is measured at around -3.81 g/kg. With the flow rate of 120 m^3/h, as specified by the manufacturer [100], and an air density of 1.2 kg/m^3, a total dehumidification capacity of 0.53 kg/h is calculated. This is even higher than the specified capacity of 0.45 kg/h, probably owing to the higher adsorption capacity of silica gel at higher specific humidities. However, the minimum achievable water content in this design was just 16.1 g/kg, with an average of 19.6 g/kg measured in the dried air flow. A quick look at Fig. 9a shows that the target value is around 6 g/kg for the final state. The mass of the entire device is given at 12 kg, from which the enclousre makes up for 5 kg. This does not include the gas cooler.

Other types of continuous processes, like multiple alternating batch, or rotating packed bed architectures, have to be ruled out due to their complexity at this stage. They might gain more interest if in the future the concept of automotive dehumidification is further pursued. Based on these considerations, a batch solution has been used for the experiments with the open system. This concept provides a clear advantage when it comes to the design of the packed bed, as it requires no additional treatment of the desiccant and no coating procedures. It allows for quick changing of the desiccant, and the reactor vessel can be reused many times. The design of the packed bed reactors and the auxiliary devices are described extensively in Section 3.4.

2.6.2 *The Packed Bed Reactor*

The process design used in the experimental section of this work corresponds to a batch-type packed bed reactor. Therefor, a short introduction into the characteristics of such a system is given here. The modeling of adsorption equilibria, mass transfer and heat transfer functions and other detailed characteristics is not discussed, as this is outside the scope of this thesis. These investigations would need to come at a potential later step, when one, or a small number, of systems are to be optimized and then compared with each other. Instead, the reactor that is to be used here should serve as a universal test system for all desiccants investigated. For laboratory scale experiments with the aim to quantify the parameters specified in Section 2.2 and Section 2.5, a general approach is sufficient. Should the system actually be employed in a specific environment, using a given desiccant, a more detailed design approach is justified.
The parameters considered in the design of the reactor are the amount of desiccant to be held, and the thickness of the bed. This last dimension is especially important, because it directly influences the pressure drop that has to be overcome by the blower system and should thus be as low as possible. On the other hand, the shorter the bed, the less mass transfer will take place, negatively affecting the dehumidification performance. This will be further explored in Section 3.4, for now, the theoretical concepts behind the calculations performed during the design process will be briefly explained.
Any flow through a packed bed will cause a pressure drop in the flow medium due to friction. This is measurable as the difference $\Delta p = p_2 - p_1$, as sketched in Fig. 25a. In process engineering applications, it can be beneficial to control the pressure drop over the packed bed to influence diffusivity of the adsorptive [101]. In this case however, the pressure drop is of interest to estimate the required power for the blower which will deliver the required airflow. To quantify this pressure drop mathematically, several models have been developed. Very basic ones include the well-known Carman-Kozeny equation [102], which is valid for laminar flow only. More sophisticated models, for example the ones introduced by Brauer [103], Brownell et. al. [104], Jeschar [105] or Stichlmair et. al. [106] are applicable to both laminar and turbulent conditions. However, the equation introduced by Ergun [107] remains one of the most commonly used methods today and is used for the calculations in this thesis.

The Ergun equation (Eq. (2.6.1)) is a semi-empirical relation to predict the pressure drop in a packed bed for both laminar and turbulent flow conditions. It expresses the pressure drop over a packed bed of particles as a function of the bed thickness l, the superficial velocity (v_s), particle diameter (d_{pt}) and the dynamic viscosity (η) of the fluid.

$$\Delta p = k_1 \, l \, \eta_f \, \frac{v_s}{d_{pt}^2} \, \frac{(1-\varepsilon)^2}{\varepsilon^3} + k_2 \, l \, \rho_f \, \frac{v_s^2}{d_{pt}} \, \frac{(1-\varepsilon)}{\varepsilon^3} \tag{2.6.1}$$

It is derived from the general approach from hydrodynamics to describe the pressure drop in pipes [107]. The values for the constants, k_1 = 150 and k_2 = 1.75, were originally obtained by Ergun from experimental data. It has been pointed out by several authors [108, 109], that in smaller reactors, these values should be recalculated to account for wall effects. For the application in this work however, they are deemed suitably accurate.
When comparing the Ergun equation to common models for flow in pipes or channels, we can find two quantities that are not used in these models: First, the porosity (ε) is introduced. The porosity is defined as the ratio of void volume (V_v) to the total volume of the packed bed (V_{tot}), which consists of the void volume and the volume of solid particles (V_{pt}), as shown in Fig. 25a.

$$\varepsilon = \frac{V_v}{V_{tot}} = \frac{V_v}{V_v + V_{pt}} \tag{2.6.2}$$

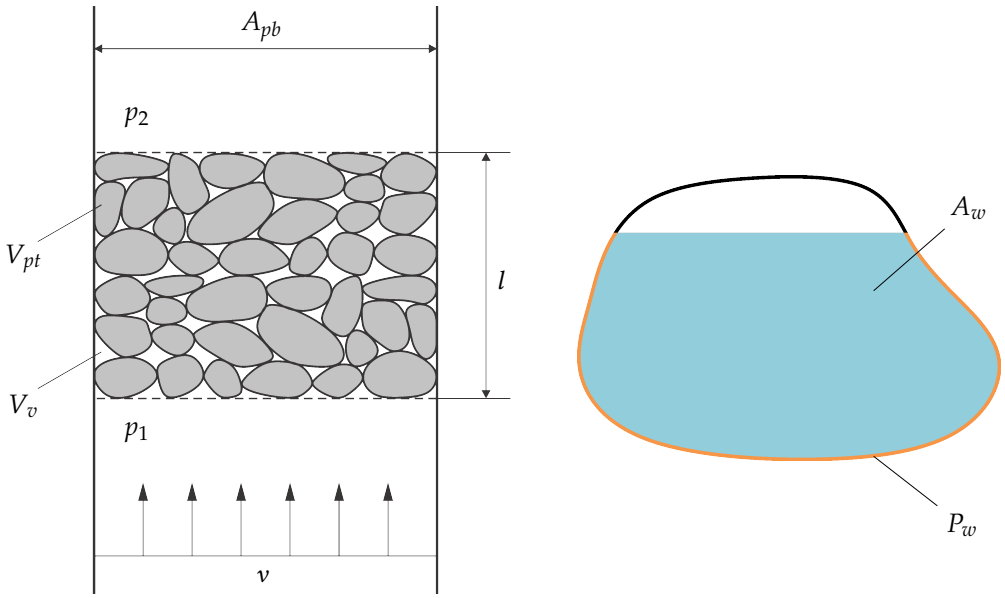

(a) Characteristic dimensions of a packed bed.

(b) The concept of the hydraulic diameter.

Figure 25: Left: Illustration of the quantities used in characterization of a packed bed process. Right: An arbitrary geometry is partially filled with a fluid (blue) of cross-sectional area A_w. The section which is in contact with the fluid (orange) is called the wetted perimeter P_w, from which the equivalent hydraulic diameter is calculated.

Second, the particle diameter has a huge influence on the pressure drop inside a packed bed, as is evident from its appearance in the Ergun equation. It is worth taking a closer look on how d_{pt} influences the hydrodynamics of the packed bed.
We start by recalling the hydraulic diameter, a concept well known from hydrodynamics. In its original definition, the hydraulic diameter is defined as the ratio of the cross-sectional area of fluid flow A_w, to the *wetted perimeter* P_w. The latter refers to the length of the surface in direct contact with the fluid. Both quantities are illustrated in Fig. 25b, the relation is therefor

$$d_h = \frac{4\,A_w}{P_w}. \tag{2.6.3}$$

The flow path in a packed bed assumes a very complex geometry, and thus it is not possible to determine A_w and P_w directly. This is why a simplified model is used. The void volume inside the bed is theoretically replaced by parallel, cylindrical channels of constant length and diameter. The total of these channels takes up the same volume as V_v, and their surface area is identical to the surface area of the particles that make up the packed bed. These simplifications enable us to find an expression for an equivalent hydraulic diameter as a function of the particle diameter.
We begin by considering the non-spherical shape of the particles by expressing their shape as the diameter of a spherical particle of the equivalent surface. The specific surface of a particle of arbitrary shape is defined as the ratio of its real surface area to its volume:

$$a_{sp} = \frac{A_{pt}}{V_{pt}} \tag{2.6.4}$$

and the diameter of a spherical particle of identical surface area can be expressed as

$$d_{pt} = \frac{6}{a_{sp}}. \tag{2.6.5}$$

With the assumptions described above and Eqs. (2.6.2) and (2.6.5), one can derive an expression for the specific surface area of the entire packed bed, i.e. the wetted area per unit volume of the imaginary channels:

$$a_w = a_{sp}\ (1-\varepsilon) = \frac{6}{d_{pt}}\ (1-\varepsilon) \tag{2.6.6}$$

From this relation it is evident that the active surface of a packed bed depends on both it's porosity ε and the specific area of the pellets. The former is determined by the shape, the latter by the size of the packing material.
We now apply the definition of the hydraulic diameter (Eq. (2.6.3)) and assume a length l_w for the imaginary cylindrical channels. We can now find a simple relation for the equivalent cross-sectional area of the channels as the ratio of the void volume to the length of the channels:

$$A_{eq} = \frac{V_v}{l_w} \tag{2.6.7}$$

or, by using Eq. (2.6.2)

$$A_{eq} = \frac{\varepsilon\, V_{tot}}{l_w} \tag{2.6.8}$$

The wetted perimeter can be found by dividing the total wetted area by the channel length:

$$P_w = \frac{V_{tot}\, a_w}{l_w} \tag{2.6.9}$$

Substituting Eqs. (2.6.8) and (2.6.9) into Eq. (2.6.3) yields

$$d_h = \frac{4\,\varepsilon}{a_w} \tag{2.6.10}$$

and with Eq. (2.6.6) we finally obtain the hydraulic diameter as a function of particle diameter

$$d_h = \frac{2}{3}\,\frac{\varepsilon}{(1-\varepsilon)}\,d_{pt} \tag{2.6.11}$$

The particle diameter is much easier to determine than the hydraulic diameter in practice. It is particularly useful when dealing with approximately spherical particles, since it can then be directly obtained from the sieve curves. This is the case for most of the commercial samples applied in the experimental section of this thesis.

3

EXPERIMENTS

In order to design an efficient adsorption process, one must first understand the properties of the adsorbent itself. In the previous sections, certain required and desirable properties for a suitable adsorbent have been discussed. A short outlook on possible future improvements to the desiccants is given in Chapter 6.
In the case of a porous material, many of the parameters outlined in Section 2.3.4 are not easily comparable because they not only depend on the chemical composition of the substrate, but also on its microscopic structure. Some can be measured with relative ease, for example the bulk density, but others require more sophisticated techniques. This section provides an overview of the investigated materials, the experiments conducted and the instruments used. The definition of desirable properties for an adsorbent leads to a number of measurable quantities, which are then used to describe the behavior of the materials. The necessary theoretical background is given in Chapter 2. According to the reasoning outlined there, this thesis shall focus mainly on the application of silica gels. In the following, the analytical methods and corresponding devices used within this project are introduced.
Material characteristics can roughly be divided into two main categories, namely *microscopic* and *macroscopic* properties. The former refers to attributes that are measured in closed systems, with small amounts of material, the latter to the application of the material as a packed bed in the actual drying process. From the requirements given by the conceptual process design outlined in Chapter 2, a series of experiments was conducted to verify and assess the potential of the proposed desiccants. The experiments are designed to cover all the characteristic quantities of the desiccant and the dehumidification process. A very coarse distinction can be made between experiments conducted in *closed systems*, and others that were run in an *open system*. To make measurements comparable and explicit, the properties of the adsorptive are usually given as their values at standard temperature and pressure conditions, abbreviated and indexed as *STP*. Several different reference conditions exist that are colloquially referred to as *standard*, a result of historical scientific development. They are all equally applicable, but of course values that are given in one system can't be directly compared to those referenced to another one. This is especially important when obtaining automatically generated results from different machines, as it is the case in this thesis. For all following sections, the term *standard conditions* and the corresponding index *STP* refer to the values given in Table 6.

Table 6: Standard conditions used within this thesis, as defined e.g. in ISO 10780.

Temperature		Pressure			
°C	°F	mbar	mmHg	psi	inHg
0	32	1013.25	760.00	14.6959	29.921

3.1 SAMPLES

From the definition of the requirements towards a suitable desiccant, a wide selection of silica gels, along with a few other materials, was acquired. So far, the term *materials from the silica gel group* has been used - in this section, a more detailed breakdown of the properties of and the differences between the investigated samples is given.
The majority of the samples came from chemical companies from all over the world, a few have been synthesized within the TUM CREATE project. Commercially available silica gels come in a certain variety in terms of shape and are often tailored to customer needs through additives.
Most products are beaded silica gels, with pellet diameters reaching from as low as a few micron to about 6 mm. Others come in an irregularly shaped, granular form. As mentioned in Section 2.5, silica gels can either be in pure form, or modified with humidity indicators. These are chemical compounds that are able to change their color according to the amount of water adsorbed by the silica gel. Commonly used indicators include cobalt(II) chloride ($CoCl_2$), which changes from a dark blue when dry to a pink color when moist (Fig. 27). This indicator, however, is becoming less common due to its toxicity: in 2008, cobalt dichloride was added to the *candidate list of substances of very high concern* by the European Chemicals Agency (ECHA). It is replaced mostly by phenolphthalein, which changes color from a light orange to colorless, or methyl violet which changes from orange to a dark green (Fig. 26). There are more indicators on the market, like ammonium iron(III) sulfate [110], but none of the silica gels investigated in this work use any of those.

Another type of desiccant can be considered as hybrid materials (see Section 2.5), these are made from salts that are embedded into the silica gel matrix. Among the samples investigated, only one was a hybrid material. *Artsorb* uses lithium chloride (LiCl) embedded in a silica gel matrix. Table 7 gives an overview of all samples that were investigated, both commercially available ones and synthesized ones are listed. All of them underwent closed system measurements, but some were only available in very small quantities so it was not possible to conduct open-system experiments.

Due to the design of the open system test stand, a pellet diameter larger than 2 mm was required for the obtained samples (see Section 3.4 for details). Since the pellets are not perfect spheres, and other silica gels are not round in the first place, they were sorted through a sieving process. Only particles that could pass a 5 mm sieve, but were retained by a 3 mm sieve, were used in the open system. For the closed system analysis, smaller pellets were also used, if available. For the design of the packed bed reactor, an estimate on the adsorption capacity per unit mass had to be at hand. Although the vapor adsorption experiments were already planned, no results were available yet. Values from literature and manufacturers data sheets varied within a rather large margin, so the obvious choice was to simply conduct an own, coarse assessment: a material sample was placed in a petri dish, and exposed to atmospheric conditions (both outdoors and indoors). Ambient conditions and exposure time were recorded, and the samples repeatedly weighed using the *Sartorius* precision balance. The specific water uptake is recorded at two distinct points, at indicator change and full saturation, in Table 8. For the design of the packed bed, the bulk density of the sample material is needed. It was measured for several samples after sieving to the desired particle diameter fraction. It was not considered necessary to analyze each and every one of them, since some of them came with a manufacturers reference, and others are very similar in their composition. Overall, it can

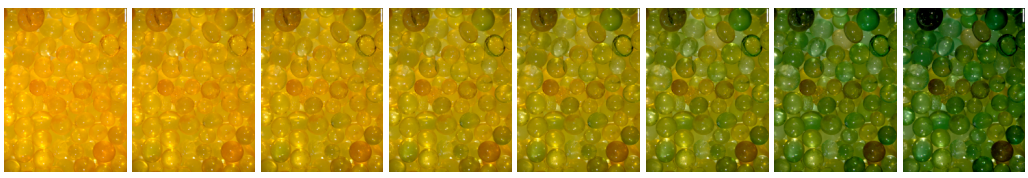

Figure 26: Indicating silica gel *HD-O* at different water loadings, from 0 % to 100 %.

Table 7: Overview of the materials used in this work. *Indicator* refers to the color change: orange-white (O/W) orange-green (O/G) and blue/pink (B/P).

ID	Product name	Manufacturer	Indicator	Remarks
SB-R	Sorbead R	BASF	no	also known as *Sorbead N*
SB-WS	Sorbead WS	BASF	no	resistant against liquid water
SB-C	Sorbead Chameleon	BASF	O/W	also known as *Sorbead Orange*
HD-O	HumiDri AO	Streampeak	O/G	
HD-W	HumiDri AW	Streampeak	no	
QP-B	Q-PAC Blue	Q-PAC	B/P	
DT-B	DelSORB beaded	Delta Adsorbents	no	
DT-G	DelSORB granular	Delta Adsorbents	no	
SA-O	Silica gel Orange	Sigma-Aldrich	O/W	
SA-T2	Type II	Sigma-Aldrich	no	
FL-36	Fluka 3-6	Fluka	no	
HK-O	HumiKill Orange	HumiKill	O/G	
HK-W	HumiKill White	HumiKill	no	
PROS	Prosorb	Prosorb	no	
ARTS	Artsorb	Fuji Silysia	no	impregnated with LiCl
TROP	TROPAgel	Tropack	no	bentonite clay
GN-1	Generic-1	unknown	no	generic packaging material
GK-O	Silicagel Orange	Gatt-Koller	O/W	
TC-1	1-SiO_2-2-4	TUM CREATE	no	*SBA-15*
TC-2	2-SiO_2-1-4	TUM CREATE	no	*SBA-15*
TC-3	3-SiO_2-1-1	TUM CREATE	no	*SBA-15*
TC-4	4-SiO_2-2-4	TUM CREATE	no	*SBA-15*
TC-5	5-SiO_2-1-3	TUM CREATE	no	*SBA-15*
TC-6	6-SiO_2-2-1	TUM CREATE	no	*SBA-15*
TC-7	7-SiO_2-2-2	TUM CREATE	no	*SBA-15*
TC-8	8-SiO_2-2-3	TUM CREATE	no	*SBA-15*
TC-8t	TC-8-treated	TUM CREATE	no	TC-8 after thermal treatment

Figure 27: Color transition of indicating silica gel *QP-B* at different water loadings, from 0 % to 100 %.

Table 8: Water uptake of some commercial samples. Dried at 130 °C, exposed for 48 hours at 31.1 °C , 75 % rh.

		at indicator change [g]			at saturation [g]		
Sample	m_{dry}	m_{ind}	m_{H_2O}	$\frac{m_{H_2O}}{m_{SG}}$	m_{sat}	m_{H_2O}	$\frac{m_{H_2O}}{m_{SG}}$
HD-O	14.4848	17.5760	3.0912	0.2134	19.4900	5.0052	0.3455
SA-O	15.4038	16.3791	0.9753	0.0633	21.0123	5.6085	0.3641
QP-B	14.6812	17.0595	2.3783	0.1620	18.9630	4.2818	0.2917
HK-O	14.0444	17.0156	2.9712	0.2116	19.1238	5.0794	0.3617
SB-C	14.6057	15.6259	1.0202	0.0698	20.0082	5.4025	0.3699

Table 9: Measured bulk densities of some samples.

Sample	Amount [ml]	Mass [g]	Density [kg/m³]
FL-36	500	370.6	741.2
SA-T2	500	369.5	739.0
SA-O	500	380.7	761.4
HD-O	500	405.9	811.8
HD-W	500	396.1	792.2

be stated that the differences in bulk density are two orders of magnitude lower than the required accuracy during packed bed design, and are therefor omitted.

3.2 SCANNING ELECTRON MICROSCOPY

To further substantiate the findings on the internal structure of the synthesized *SBA-15* silica gel that were to be obtained from N_2-adsorption, images were acquired using a scanning electron microscope (SEM). This procedure was performed on a material sample of *TC-6*. It is considered to be representative for all other TC-samples, since the synthesis process was identical. This could later be justified from the N_2-adsorption results, which also show only marginal differences between the batches. Image acquisition was done at the ZAE Bayern's facilities in Würzburg, Germany with a *Zeiss ULTRA Plus* Field Emission Scanning Electron Microscope (FESEM). The properties of this specific type of SEM are a huge advantage for the image acquisition in this case. Namely, it's ability to produce highly focused electron beams even at low acceleration potentials below 5 kV. The reason why this is particularly important for the sample to be measured is the poor electrical conductivity of silica gel. Even with some water adsorbed on the surface, the resistivity of silica gel is still in the order of magnitude of 10^{-13} Ωcm to 10^{-11} Ωcm [111]. In such non-conductive samples, electrical charges accumulate on the sample surface and cause electrostatic distortion of the acquired image. The often used method of sputter-coating the sample with a conductive material can not be applied here, since the expected pore network would easily be covered up. As mentioned earlier, a possible solution is the application of a low acceleration voltage - here, 2 kV. Together with the use of the in-lens detector, which works with low energy secondary electrons, this resulted in excellent images. Before the SEM analysis, the samples were pretreated as described in Section 3.3.1. Another set of images was taken on some of the commercial materials with a *FEI Quanta FEG Mk II* FESEM at the SMART-MIT Low Energy Electronic Systems (LEES) laboratory in Singapore.

3.3 CLOSED SYSTEM MEASUREMENTS

The aim of these characterization experiments is to enable predictions on the behavior of a certain material as a desiccant in the actual dehumidification process. This is necessary because the open system experiments conducted within this work require a sample amount of approximately 1.2 kg, which was only available for a few materials. The performance of the remaining samples must thus be predicted from their microscopic properties.

3.3.1 *Sample Preparation*

A suitable pre-treatment of the sample material is always required in order to obtain meaningful adsorption curves. The aim of this sample preparation is to achieve a reproducible adsorbent state, in which the following experiments are then performed. This is achieved by removing physisorbed species from the sample surface - a process commonly known as *degassing* or *outgassing*. Strictly speaking, the latter term refers only to spontaneous evolution, whereas the former denotes a stimulated removal of gas molecules from a substrate. Yet, they are commonly used synonymously even in scientific literature for the described process. A degassing procedure is carried out either under vacuum or with an inert carrier gas. In this thesis, the former approach is pursued. The principle is rather straight forward: the material sample, on which the adsorption measurement is to be performed, is exposed to a high vacuum and simultaneously heated to drive out gas and vapor molecules that may have been adsorbed during synthesis or simply from the ambient during storage. The pressure in the sample cell is measured, and when it remains constant below a defined threshold, the outgassing is considered complete. Ideally, the same sample cell is to be used for outgassing that is later used for the actual adsorption measurement. The reason is obvious - after outgassing, the transfer to the adsorption analysis should be as quick as possible and with as little exposure to the atmosphere as feasible. While this principle is simple, several challenges must be considered during the practical execution. Determination of outgassing parameters requires either a learning period or reference values from experience and literature. They are strongly dependent on the characteristics of the adsorbent: An elevated temperature accelerates the outgassing process, but structural and chemical changes (mechanical, sintering, reactions of surface groups) can be caused by overheating. On the other hand, some strongly bound species may only be removed at higher temperatures, even under strong vacuum. The application of the vacuum itself is also not without pitfalls, especially powdered samples can be carried away if pressure changes happen too quickly. Similarly, a sudden phase change of adsorbate can cause elutriation, or structural damage to the sample material by expansion. These possible effects must be accounted for by defining a suitable evacuation strategy and temperature profile. This profile consists of heating intervals, isothermal sections, and cooldowns. The time domain, i.e. heating rates and soaking times, needs to be selected according to the sample material's behavior. The adsorbent must be heated all the way through, and the adsorbed species need enough time to leave even bottleneck pores. A generous allowance in outgassing time, accompanied by conservative temperature levels is generally a good idea.
This is reflected in the outgassing profiles given in Tables 10 to 12. On the *Autosorb* device, the samples are first warmed up at a heating rate k_1 and held for a certain time h_1 at a temperature ϑ_1 -slightly above room temperature- under a slowly applied vacuum. They are then heated to the final temperature ϑ_2 at a rate k_2, and soaked for a certain duration h_2. They are then allowed to cool down under vacuum, and as soon as the sample temperature falls below 80 °C, the sample cell is automatically backfilled with nitrogen to ambient pressure. In the *Belsorp* outgassing system, a vacuum is first applied at room temperature, and when the pressure stabilizes, the heating profile is started. After completion, the sample cells are manually backfilled with N_2 to ambient pressure. Based on initial, very extensive outgassing routines, the duration and temperatures were subsequently adapted with increased understanding of the materials' behavior.

Table 10: Heating profiles used with the *Belsorp* device.

		P1	P2	P3	P4	P5	P6
ϑ	[°C]	85	85	85	85	90	55
k	[K/min]	1.03	1.38	3.10	0.52	0.56	0.27
h	[min]	120	60	45	720	720	720

Table 11: Heating profiles used for water vapor adsorption measurements on the *Autosorb* device.

		P1	P2	P3	P4	P5	P6	P7	P8	P9	P10
ϑ_1	[°C]	27	27	27	27	27	27	27	27	27	27
k_1	[K/min]	2	2	2	10	2	2	10	2	10	2
h_1	[min]	10	10	10	10	10	10	10	10	10	10
ϑ_2	[°C]	150	150	130	120	85	150	150	150	120	130
k_2	[K/min]	5	3	5	20	3	5	10	3	20	2.5
h_2	[min]	120	240	120	25	60	120	240	240	25	240

High outgassing temperatures of 130 °C or more were chosen to fully degas the adsorbents for N_2-adsorption and maximum-uptake-characterization. Low temperatures of 60 °C are used to gain insight into the adsorbents behavior at temperatures that will later be available in the dehumidification process. This is of course only of limited significance, since the open system does not operate under vacuum. This temperature profile is thus only used with a very small number of samples. The actual procedure was carried out with two different devices: the laboratory in Munich had a dedicated outgasser, which was a modified *Belprep-flow* device, that had been fitted with a vacuum system. In this setup, no degassing pressures lower than 1 Pa were reached. In Singapore, the *Autosorb iQ* instrument's integrated outgasser was used. It was connected to the device's vacuum system, consisting of a diaphragm pump and a turbomolecular pump. With this setup, degassing pressures down to 0.2 Pa were achieved. The instrument provided two extensions to the heating profile discussed above: a pressure-controlled heating function, which constantly measures the pressure of the evolved gas. Should the pressure exceed a pre-defined limit of 133 Pa, the heating rate is kept constant until the pressure falls back beneath the limit, and the profile continues. The outgassing procedure was considered complete when the pressure inside the sample cell remained constant. The device was set up to detect pressure increases of 6.7 Pa/min, but no increase was observable with any of the applied temperature profiles.
To accurately calculate specific quantities, an accurate measurement of the sample mass is necessary. For the experiments performed in Munich, a *Mettler Toledo* precision balance was used, in Singapore a *Sartorius Quintix224-1S* was employed. The procedure was the same in both locations: first, the cleaned and dried sample cell was weighed. Then, a suitable amount of sample was added, and weighed again. A third weighing was performed after the degassing procedure, where the sample cell was backfilled with pure nitrogen to keep weighing errors from buoyancy effects minimal.

3.3.2 *Nitrogen Adsorption*

Nitrogen adsorption is a common technique for surface characterization. The method follows the same volumetric measurement principle as described in Section 3.3.3 for vapor isotherms. These experiments provide the basis for the determination of material properties such as internal surface

Table 12: Heating profiles used for N_2 adsorption measurements on the *Autosorb* device.

		P1	P2	P3	P4	P5	P6	P7	P8
ϑ_1	[°C]	25	25	25	27	27	27	-	27
k_1	[K/min]	2	2	2	2	10	2	-	2
h_1	[min]	10	10	10	10	10	10	-	10
ϑ_2	[°C]	130	130	150	150	120	180	120	150
k_2	[K/min]	2.5	2.5	5	5	20	3	5	3
h_2	[min]	60	240	120	120	25	960	20	240

area, total pore volume and pore size distribution. This section gives a brief overview of the methods employed and their practical execution.
Nitrogen is commonly used as the adsorptive, on one hand because it is widely available at low cost, and on the other hand because of its physical properties: At 77 K, nitrogen is liquid and can thus double as a coolant bath. The properties of liquid nitrogen can be used to determine both the molecular cross section and the density of the adsorbate. Alternatives include, for example, Argon and Krypton, the latter having advantages specifically for low-surface adsorbents (s $\leq 1\,m^2/g$). A discussion on the advantages and disadvantages of the various adsorptives can be found in [45]. The wide usage of Nitrogen has led to a vast amount of published measurements on all kinds of materials. This allows for comparability of results, given that the measurements are performed and interpreted according to common procedures. These have been established in [49] - among others - and some methods have been standardized on national and international level (e.g. [112–115]). The measurements described in this section were conducted in accordance with these conventions. The device employed was a *Quantachrome Autosorb iQ Gas Sorption System, Serial No. 14715093001.* N5-grade Nitrogen (99.999 % purity), supplied by *Linde Gas*, was used as the adsorptive.

3.3.2.1 *N_2-Isotherms*

For simplicity purposes, the procedure is described for the measurement of the adsorption branch of the isotherm, but everything in this section is equally valid for the desorption branch. The instrument settings given are identical for both.
The samples were pretreated and outgassed as described in Section 3.3.1. Nitrogen isotherms were then recorded within the p/p_0 range from 0.025 to 0.995 . The reference pressure p_0 is measured in a dedicated glass cell, which is immersed in the LN_2 bath in close proximity to the sample cell. Due to the dosing algorithm of the instrument, the predefined p/p_0-values are rarely met exactly, instead the measurement point is recorded when it falls within a certain threshold. This is dependent on the configuration of the instrument, namely on the two parameters *tolerance* and *equilibration time*. The former is specified in tolerance classes from 0 to 9 , their meaning is explained in detail in the system's documentation [62]. During the analyses performed, the strictest tolerance class of 0 was chosen. This corresponds to the allowable variations listed in Table 13. The equilibration time can be set anywhere from 1 to 99 minutes, and was here set to 2 minutes. The meaning of this value is as follows: When, after opening the valve that connects the gas manifold to the sample cell (for an illustration, please see Section 3.3.3), the p/p_0-value falls within the limits set by the tolerance specifications, the equilibrium timer is started. If within the specified timeframe -in this case, 2 minutes- the cell pressure stays within a certain range, adsorption equilibrium is assumed and the value is recorded. The range in which the pressure is considered stable is determined by the instrument manufacturer's settings as less than 0.0008 atm, or 0.8106 mbar. If the pressure changes beyond this limit, it is assumed that the adsorbent is not yet saturated, and the adsorptive dosing

Table 13: The tolerance bands for the mesopore region, as used during the N_2-adsorption experiments [62]

Adsorption p/p_0			Desorption p/p_0	
$1{\cdot}10^{-5}$ to 0.01	0.01 to 0.025	0.025 to 1	0.1 to 0	1 to 0.1
$+2.5{\cdot}10^{-6}$ / $-8.3{\cdot}10^{-7}$	$+3{\cdot}10^{-5}$ / $-1{\cdot}10^{-5}$	$+3{\cdot}10^{-3}$ / $-1{\cdot}10^{-3}$	$+1{\cdot}10^{-5}$ / $-3{\cdot}10^{-5}$	$+1{\cdot}10^{-3}$ / $-3{\cdot}10^{-3}$

procedure continues. The same is of course true if the p/p_0-value falls outside the tolerance band during this time.

After reaching equilibrium conditions, the measured value is recorded as adsorbed volume at standard conditions, as denoted by the index *STP*. Since it is later needed for the BET analysis, the adsorbed mass is calculated by using the density of the adsorbate in the bulk liquid state, which is ρ_l = 0.808 kg/m³ at the respective conditions (p = 1013.25 mbar, T = 77 K). According to Dubinin [116], this approach is justified up to exactly this point, which constitutes the boiling point of LN_2 at standard pressure.

The number of measurement points that were recorded for each isotherm branch varies between 12 and 36. This is due to the fact that when the first samples were measured, their adsorption behavior was unknown. Thus, the dosing algorithm was set to use only very small amounts of Nitrogen per dose, in order not to "overshoot" the desired measurement point. It therefor took a long time to measure each sample. For subsequent experiments however, since the samples were expected to have similar characteristics, the dosing procedure was adjusted. This lead to a reduced measurement time per point, allowing to record a larger number during the same overall runtime.

3.3.2.2 *BET Surface Area*

The specific surface area is calculated from the BET model, which is derived from the BET theory, as introduced in Section 2.4.4. From this theoretical model, the monolayer volume of an adsorbed gas can be obtained. With this quantity known, the specific surface area of the adsorbent is then calculated at the point where exactly one monolayer is adsorbed to the surface. In a first step, the adsorbed weight of nitrogen is acquired from the isotherm measurements and then plotted according to the BET equation as

$$\frac{1}{W_{ads}\left[\left(\frac{p_0}{p}\right)-1\right]} = \frac{1}{W_{mono}\, c_{BET}} + \frac{c_{BET}-1}{W_{mono}\, c_{BET}}\left(\frac{p_0}{p}\right) \tag{3.3.1}$$

with W_{ads} being the adsorbed weight, W_{mono} the theoretical weight of a complete monolayer, and c_{BET} the BET constant as defined in Eq. (2.4.16). From Eq. (3.3.1), a linear plot is fitted through the measured data using least squares regression. This linear plot can be written in terms of slope

$$s = \frac{c_{BET}-1}{W_{mono}\, c_{BET}} \tag{3.3.2}$$

and the intercept

$$i = \frac{1}{W_{mono}\, c_{BET}}. \tag{3.3.3}$$

The weight of a completed monolayer can then be expressed by rearranging Eq. (3.3.1) and substituting Eq. (3.3.2) and Eq. (3.3.3) as:

$$W_{mono} = \frac{1}{s+i}. \tag{3.3.4}$$

The total BET surface area of the sample is then calculated from

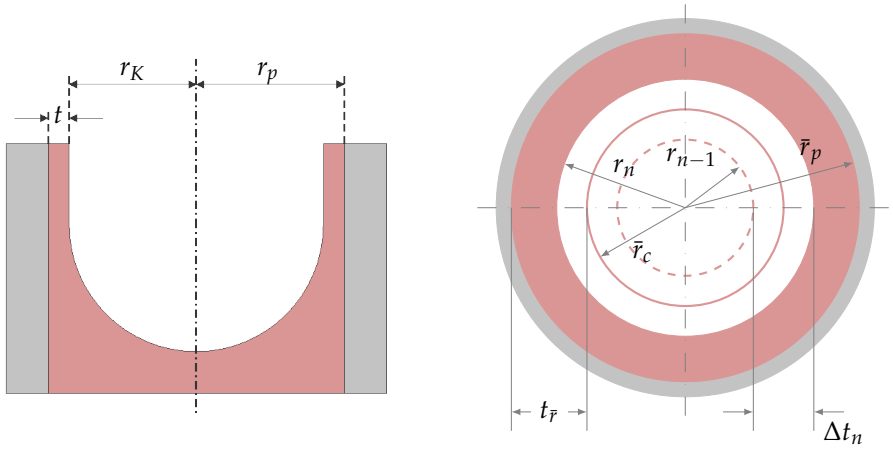

(a) filled pore dimensions

(b) changes during the desorption step

Figure 28: Pore radius r_p, Kelvin radius r_K and statistical layer thickness t in a pore undergoing capillary condensation. During a desorption step, the relative pressure is lowered from $(p/p_0)_{n-1}$ to $(p/p_0)_n$. The adsorbed layer thickness reduces by Δt_n. Illustrated are the Kelvin radii before (r_{n-1}) and after (r_n) desorption and the average Kelvin radius $\bar{r}_c$. $t_{\bar{r}}$ denotes the corresponding average thickness of the adsorbed layer. $\bar{r}_p$ is the average pore radius of all pores emptied of capillary condensate during this desorption step.

$$S_{BET} = \frac{W_{mono}\, N_A\, \sigma_{ads}}{V_m} \tag{3.3.5}$$

by using the cross-sectional area of the adsorbed gas molecule σ_{ads}, the Avogadro constant N_A and the molar volume of an ideal gas V_m.
Finally, we obtain the specific surface area as the total surface area divided by the sample mass:

$$s_{BET} = \frac{S_{BET}}{m_s} \tag{3.3.6}$$

3.3.2.3 *Pore Size Distribution*

For all samples that exhibited isotherms promising enough, according to the criteria defined in Section 2.4.4, pore size analysis was conducted. In Section 2.4.4, several methods for the assessment of pore size distribution have been mentioned. Which of these is applicable, can, to some extent, be predicted from the characteristics of the isotherm obtained. Type IV, H2 types are usually suitable isotherms for BJH analysis. The BJH method is a so-called "classical" method, due to being based on the Kelvin equation. Within this thesis, the BJH model was used where applicable. This section gives a short overview of the BJH algorithm and the underlying assumptions.
The idea behind this method is to correlate pore radii r_{p_n} with given relative pressures $(p/p_0)_n$ via the Kelvin equation. The amount of adsorptive that is desorbed during n individual desorption steps (ΔV_{pn}) is then plotted against the corresponding pore radius to obtain the pore size distribution. However, the Kelvin equation does not yield the pore radius r_p directly, but the Kelvin radius r_K. The difference between these two values is the thickness of the adsorbed layer, as illustrated in Fig. 28a.

This thickness is assumed to be the statistical thickness t of the multilayer at a given relative pressure p/p_0 . It can be calculated through the method introduced by Shull [117], using the nowadays widely accepted value of 3.54 Å for the monolayer thickness. This value was calculated by Lippens et al. [118] and is valid for nitrogen as an adsorptive, assuming a hexagonally close-packed

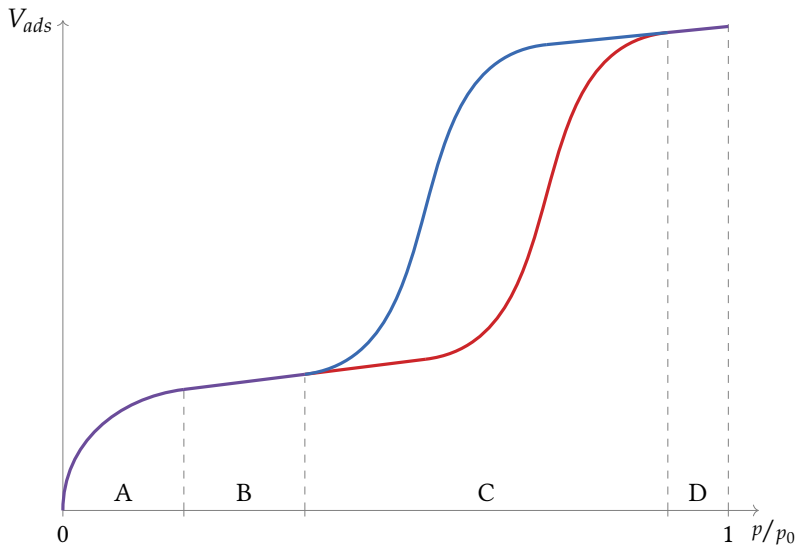

Figure 29: An idealized isotherm of Type IV. The adsorption branch is shown in red, the desorption branch in blue. The following characteristic regions can be identified:
A: Micropore filling occurs, and a first layer is formed. Adsorption behavior is governed by adsorbent-adsorptive interaction.
B: Multilayer formation occurs as described by the BET model. Adsorption behavior is governed by adsorptive-adsorbate interaction
C: Capillary condensation sets in during adsorption, during desorption vapor pressure depression leads to the formation of a hysteresis loop.
D: The pores are filled, only marginal amounts are adsorbed as $p/p_0 \rightarrow 1$.

structure with an occupied area of 16.27 Å^2 per molecule in the adsorbed multilayer. This yields the statistical thickness in Å:

$$t = 3.54 \left(\frac{V_{ads}}{V_{mono}} \right) \tag{3.3.7}$$

Several more convenient methods have been derived to calculate the statistical multilayer thickness t. The ones most widely used are the Halsey equation [119], the Carbon Black STSA method [120] and the equation published by de Boer et al. [121]. The latter one is an experimental fit to the Harkins-Jura equation [122] and is used throughout this thesis. Using the thermodynamic properties of nitrogen, it can be written in the following form:

$$t = \sqrt{\frac{13.99}{0.034 + \frac{p}{p_0}}} \tag{3.3.8}$$

With the above values, it also yields the statistical thickness in Å. Using Eq. (3.3.8) and the Kelvin equation (Eq. (2.4.33)), the actual measurement process can then be executed as follows: The initial status when applying this method is a completely filed pore system. This is usually the case when p/p_0 approaches unity and is indicated by a plateau on the upper end of the isotherm (section D in Fig. 29).

To quantify the pore volume, the BJH algoritm uses a simplified model of cylindrical, open ended pores. From this initial state $(p/p_0)_1$, the relative pressure is lowered to $(p/p_0)_2$.

At this point, evaporation from the largest pores occurs, as illustrated in Fig. 30. During this step, a certain volume of asdsorbate ΔV_1 is desorbed from the largest pores. This volume consists of the

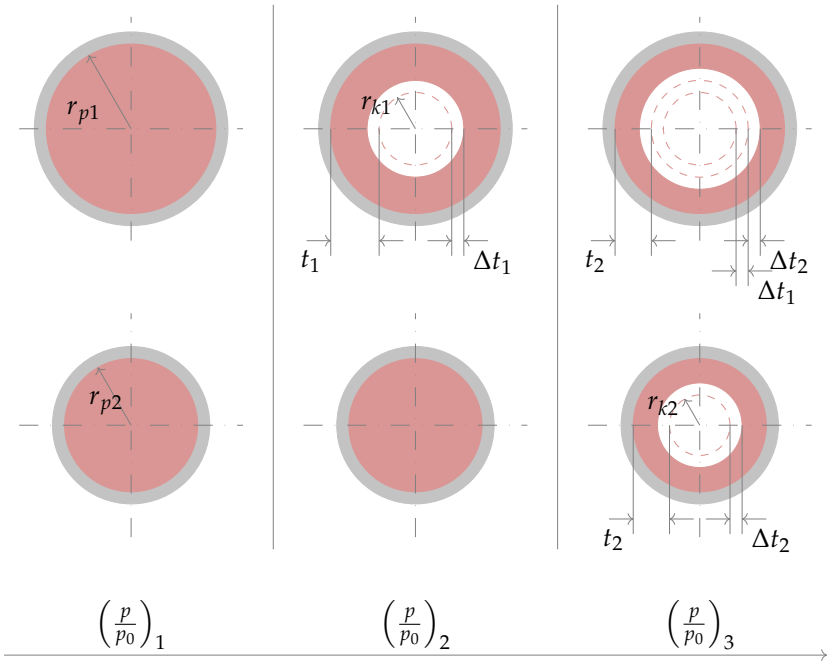

Figure 30: Steps in BJH pore size analysis.

capillary condensate released, but also from a thinning of the adsorbed multilayer Δt_1. According to Fig. 30, the volume of the largest pore V_{p_1} can be expressed using the desorbed volume ΔV_1:

$$V_{p_1} = \left(\frac{r_{p_1}}{r_{K1} + \Delta t_1}\right)^2 \Delta V_1 \tag{3.3.9}$$

The next step, however, is slightly more complicated than the first: When the relative pressure is lowered further to $(p/p_0)_3$, the amount ΔV_2 is desorbed. The second largest pore is now emptied from its capillary condensate and the adsorbed multilayer thickness is reduced just like in the first step. But in addition, a second reduction in thickness of the adsorbed multilayer by Δt_2 occurs also in the largest pore. The volume of the second largest pore V_{p_2} must thus be expressed as:

$$V_{p_2} = \left(\frac{r_{p_2}}{r_{K2} + \Delta t_2}\right)^2 \left(\Delta V_2 - V_{\Delta t_2}\right) \tag{3.3.10}$$

To simplify the computation of $V_{\Delta t_2}$, the authors suggested an expression that uses the average exposed area $A\,c_1$ of the first pore, from which desorption occurs:

$$V_{\Delta t_2} = \Delta t_2\, A\, c_1 \tag{3.3.11}$$

This equation can be generalized for all desorption steps from the first to the n-th step $(p/p_0)_n$.

$$V_{\Delta t_n} = \Delta t_n \sum_{i=1}^{n-1} A\, c_i \tag{3.3.12}$$

In order to obtain an expression for the pore volume, Eq. (3.3.12) is substituted into the generalized form of Eq. (3.3.10)

$$V_{p_n} = \left(\frac{r_{p_n}}{r_{Kn} + \Delta t_n}\right)^2 \Delta V_n - \left(\frac{r_{p_n}}{r_{Kn} + \Delta t_n}\right)^2 \Delta t_n \sum_{i=1}^{n-1} A\, c_i \tag{3.3.13}$$

The problem with using the exposed surface $A\,c$ is that it varies with every desorption step. It is therefor more convenient to make use of a constant quantity - the pore surface area A_p. This area can be easily found by using the pore volume obtained in each previous step:

$$A_p = \frac{2\,V_p}{r_p} \tag{3.3.14}$$

$A\,c$ can then be calculated from A_p by assuming average values $\bar{r}_p$, $\bar{r}_c$ and $t_{\bar{r}}$ during each desorption step. These quantities are illustrated and described in Fig. 28b.

We can then find the average exposed surface area $A\,c_{n-1}$ for any desorption step where the relative pressure is lowered from $(p/p_0)_{n-1}$ to $(p/p_0)_n$ with the following relation:

$$A\,c = A_p\,\frac{\bar{r}_c}{\bar{r}_p} \tag{3.3.15}$$

Also, we can see from Fig. 28b that the average Kelvin radius $\bar{r}_c$ can be expressed as the difference between the average pore size $\bar{r}_p$ and the average thickness of the adsorbed layer, i.e. $\bar{r}_c = \bar{r}_p - t_{\bar{r}}$. With this relation, the parameter c is then defined as follows

$$c = \frac{\bar{r}_p - t_{\bar{r}}}{\bar{r}_p} \tag{3.3.16}$$

and substituted into Eq. (3.3.12) to obtain the final expression for the pore volume:

$$V_{p_n} = \left(\frac{r_{p_n}}{r_{Kn} + \Delta t_n}\right)^2 \Delta V_n - \left(\frac{r_{p_n}}{r_{Kn} + \Delta t_n}\right)^2 \Delta t_n \sum_{i=1}^{n-1} c_i\,A_p \tag{3.3.17}$$

In the original publication, the authors suggested treating c as a constant. With the development of modern computers, it is now possible and common to calculate values for c during each individual step.

3.3.3 *Water Vapor Adsorption*

It has been discussed in Section 2.4.4 and Section 2.5, that the uptake capacity for adsorptives is not a constant value in many adsorbents. It is instead a function of temperature and the relative pressure of the adsorptive. This is also true for silica gels, especially in the case of the structured, mesoporous materials. The aim of the vapor adsorption experiments is to determine the moisture uptake capabilities for different adsorbents under varied conditions, represented in the form of adsorption isotherms. From these, the enthalpy of adsorption is calculated. Experiments were conducted on sites in both Singapore and Germany. Most of the structured silica gels were analyzed in the facilities of the *Bavarian Center for Applied Energy Research (ZAE)*, the commercial silica gels were analyzed at TUM CREATE's laboratory in Singapore. Two different devices were utilized, the one in Germany being a *BELSORP-aqua3*, the one in Singapore being a *Quantachrome Autosorb iQ-MP* with vapor option. The latter is the same instrument that was used for the nitrogen adsorption experiments. Since it includes the optional vapor analysis kit, it allows for easy conversion to H_2O-adsorption measurements.

The conversion involves only a few simple steps. First, a heater for the gas manifold needs to be turned on, to avoid condensation in the pipes and, for the same reason, the gas ballast valve for the first stage vacuum pump needs to be opened. Second, the pressure reference cell is removed, since the reference pressure p_0 is calculated instead of measured, as explained later in this section. Then, the adsorptive is introduced by installing a glass vial containing pure water, taken from a *Merck Milli-Q* system. The final step is changing the thermostatic vessel. While during the N_2-adsorption experiments the sample cells are immersed in a dewar with liquid nitrogen, during the H_2O-adsorption measurements a different solution is required: Instead of the LN_2-dewar, a double-walled,

(a) The modified sidewall seen from the outside (clear part). Tubes lead to the *Julabo* thermostat. The door can now be fully closed.

(b) The interior with thin, flexible tubes connected to the Dewar. This allows unrestricted up- and downward motion without obstruction.

Figure 32: Installation of the modified sidewall with hose connectors built for the Autosorb iQ instrument. Clear blue parts are original, transparent parts are custom built.

recirculating dewar with a water bath is used to create stable conditions for the measurements. Between the walls of the vessel, water is circulated by a *Julabo FP50-MA* recirculating thermostat. A thermocouple was added to the water bath for constant monitoring of the temperature using a *Graphtec GL-220* data logger.

After finishing the conversion and conducting initial calibration tests, it was found that the temperature stability of the water bath could be significantly improved by some modifications to the factory-proposed setup: The manual suggests to simply leave the door to the compartment with the dewar and the sample open, in order to run the tubes to the thermostat. However, with the equipment available in the TUM CREATE workshops, it was a simple task to build a replacement side wall for the instrument that allowed for the installation of proper tube connections and allowed the instrument door to remain closed during the analysis procedure. The modifications are depicted in Fig. 32. Also visible is the different tubing on the outside and the inside - while the external tubing focuses on a low pressure drop and rigidness, the internal tubing needs to be soft and flexible to allow easy up- and downward motion of the dewar support platform.

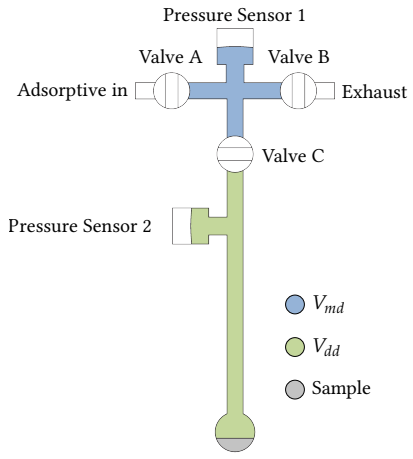

Figure 31: Illustration of the dosing procedure with dead volume (V_{dd}) and manifold volume (V_{md}).

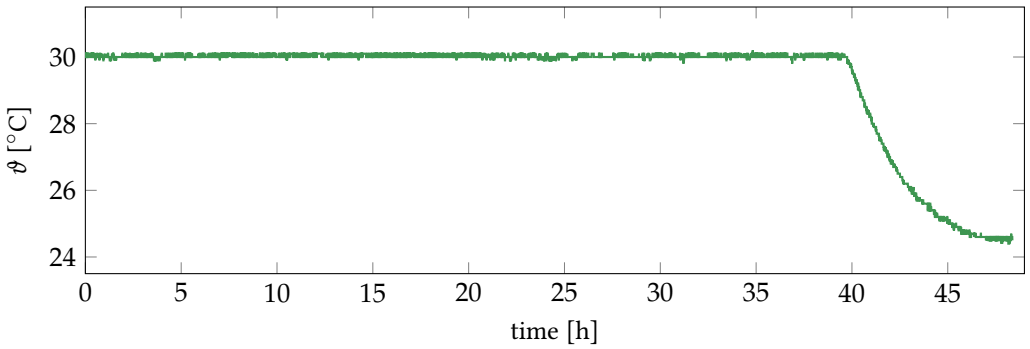

Figure 33: Logged water bath temperature during analysis run of a *TC-8 treated* sample. The setpoint was 30 °C. After the analysis, the thermostat is switched off and the bath gradually returns to room temperature.

The temperature of the water bath was recorded over several hours both during calibration and also during measurements, and found to be reliably stable, both under idle and experimental conditions. A time series from the calibration procedure is shown in Fig. 33.

The *BELSORP* device in Germany had no such issues, since it was designed specifically for vapor adsorption measurements and incorporates design features such as a sealed sample chamber and a thermostatic dewar. The only external device needed is a recirculating thermostat, here a *Julabo F25-ME* was used. Both devices employ the same operating principle: the constant volumetric gas adsorption method. This method, together with the gravimetric method, is the most extensively used measurement principle for gas adsorption measurements. The setup is sketched Fig. 31, and the principle is as follows: Before each measurement, both instruments automatically determine the dead volume (V_{dd}) using helium. *Dead volume* refers to the space inside the sample cell that is not taken up by the sample, as shown in Fig. 31. Since the dead volume is different for each cell as well as for different amounts of sample material, it is necessary for it to be re-measured before a new analysis is started. Helium is used under the assumption that adsorption to the cell walls and to the sample can be neglected, which is usually valid for mesoporous materials. To determine the V_{dd}, the system is first evacuated and then helium is introduced into the instrument's gas manifold through valve A. The manifold volume (V_{md}) is calibrated. At pressure sensor 1, the initial pressure is measured as $p_{1i}(1)$. Valve C is then opened and closed again a few seconds later. By then, helium gas has diffused from V_{md} to V_{dd}, and the resulting pressures $p_{1e}(1)$ and $p_{2e}(1)$ are measured at pressure sensor 1 and pressure sensor 2, respectively. Since helium can be treated as an ideal gas at measurement conditions [50, p. 244], the dead volume can now be calculated from the following equation:

$$V_{dd}(1) = \frac{(p_{1i}(1) - p_{1e}(1))\, V_{md}}{p_{2e}(1)} \tag{3.3.18}$$

Afterward, more helium is introduced into the manifold and the procedure is repeated as described above. The number of repetitions depends on the instrument parameters, as specified by the manufacturer. In general, after n repetitions the dead volume can be calculated as follows:

$$V_{dd}(n) = \frac{(p_{1i}(n) - p_{1e}(n))\, V_{md} + p_{2e}(n-1)\, V_{dd}(n-1)}{p_{2e}(n)} \tag{3.3.19}$$

The value used for V_{dd} is then determined from a best-fit model through n points.
While helium is being treated as an ideal gas during the dead volume measurement, for adsorbent gases and vapors the measured dead volume needs to be corrected for non-ideality. The deviation from ideal behavior is often expressed through a non-ideality factor α. They can be derived from

equations of state, for example from the van-der-Waals equation as published by Emmett and Brunauer in [123]. The corrected dead volume V'_{dd} is:

$$V'_{dd} = V_{dd}\,(1 + \alpha p) \tag{3.3.20}$$

The actual gas or vapor adsorption measurements follow the same principle. Instead of helium, the adsorptive is now introduced into V_{md}. As before, the initial pressure is measured as $p_{1i}(n)$. After opening valve C, adsorptive gas comes in contact with the sample and is subsequently adsorbed. This causes a drop in system pressure until the adsorption equilibrium is reached after some time. The equilibrium pressures are then read as $p_{1e}(n)$ and $p_{2e}(n)$.
To quantify the amount of gas/vapor adsorbed on the sample, the change in gas volume is calculated from the non-ideal gas law and divided by the sample mass m_s. It is expressed as volume under standard conditions (T_{STP} = 273.15 K, p_{STP} = 101.325 kPa). Two equations are needed, one for the volume change in the manifold and one for the volume change inside the dead volume, they will be referred to as V_1 and V_2, respectively:

$$V_1(n) = \frac{(p_{1i}(n) - p_{1e}(n))\,V_{md}\,T_{STP}}{p_{STP}\,m_s\,T} \tag{3.3.21}$$

$$V_2(n) = \frac{(p_{2e}(n-1) - p_{2e}(n))\,V'_{dd}\,T_{STP}}{p_{STP}\,m_s\,T} \tag{3.3.22}$$

The change during the n-th adsorption point measurement is the sum of the individual volume changes

$$\Delta V = V_1 + V_2 \tag{3.3.23}$$

and the total adsorbed volume at point n can hence be expressed by

$$V(n) = V(n-1) + \Delta V. \tag{3.3.24}$$

The desorption isotherm is measured accordingly: Instead of introducing adsorbate through valve A, the manifold is now evacuated through valve B. Subsequently, valve C is opened and gas starts to desorb from the sample surface until an equilibrium is reached. The pressures are measured as described for the adsorption process. This is again repeated n times, the residual adsorbed volume is calculated in the same way, using the exact same equation as during the adsorption measurement. Since it is customary to express the adsorption isotherm in terms of adsorbed amount against relative equilibrium pressure p/p_s [49], it is required to either measure or calculate the saturation pressure p_s for the adsorptive at a given temperature. For water vapor, several methods exist to calculate the saturation pressure. It could, however, not be determined which method is used by the respective analysis software of the individual instrument's manufacturers - therefor, these are replaced by values calculated with the same formula. In this work, the equation developed by Wagner and Pruß [32], as recommended by the *International Association for the Properties of Water and Steam (IAPWS)* is applied:

$$p_s = p_c \exp\left(\frac{T_c}{T}\left(a_1\,\nu + a_2\,\nu^{1.5} + a_3\,\nu^3 + a_4\,\nu^{3.5} + a_5\,\nu^4 + a_6\,\nu^{7.5}\right)\right) \tag{3.3.25}$$

with the coefficients a_i given in Table 14a and the following identity:

$$\nu = 1 - \frac{T}{T_c}. \tag{3.3.26}$$

T_c and p_c denote critical temperature and critical pressure, respectively. Their values are given in Table 14b. Throughout this thesis, the saturation pressure p_s is used synonymously with the

Table 14: Values used in Eq. (3.3.25) for the calculation of water vapor saturation pressure at a given temperature and critical temperature, pressure and density of water with uncertainties as given in [124].

(a) Wagner-Pruß coefficients

Coefficient	Value
a_1	-7.85951783
a_2	1.84408259
a_3	-11.7866497
a_4	22.6807411
a_5	-15.9618719
a_6	1.80122502

(b) Critical point of water

Symbol	Value (ϵ = 0.1)	Unit
T_c	647.096 $\pm\epsilon$	K
p_c	22.064 $\pm$ 0.27ϵ $\pm$ 0.005	MPa
ρ_c	322 $\pm$ 3	kg/m^3

equilibrium vapor pressure p_0, as described in Section 2.1.4.
Finally, the instrument parameters for tolerance and equilibration time were set. The tolerance values were identical to the N_2-adsorption measurements, their meaning is the same as described in Section 3.3.2.3. The equilibration time was set to 600 s.

3.3.4 *Thermal Analysis and Mass Spectrometry*

To better understand the characteristics of the different adsorption materials, especially the ones synthesized in-house, they were investigated through thermal analysis measurements. The results allow to further confirm or dismiss similarities in the materials' characteristics. Keeping in mind the chemical composition of the silica gel, it is evident that the heating temperature can not be set arbitrarily high. A temperature of 450 °C is deemed a good compromise in accordance with literature results on the topic [84]. Owing to the synthesis procedure, namely the template removal by solvent extraction, there is a possibility of residual templating agent having remained within the silica gel. From the properties of the block-copolymers described in Section 2.5, they can be expected to decompose at these temperatures. The experiments were performed on a *Mettler-Toledo TGA/DSC 1 STARe* combination device, which was coupled and synchronized to a *Pfeiffer Vacuum ThermoStar GSD 320 T2* mass spectrometer. With this setup, three types of measurements could be performed simultaneously:

- thermogravimetric analysis (TGA)
- differential scanning calorimetry (DSC)
- mass spectrometry (MS)

The measurements were conducted in open, 100 µl aluminum crucibles. The analysis chamber was vented with synthetic air at a flow rate of 50 ml/min, which acts as both atmosphere and carrier gas. Before each run, a *blank curve* was recorded using an empty crucible. This is necessary to account for instrumental or environmental influences - mainly buoyancy effects, where the mass of the empty crucible seemingly increases during the heating process. The blank curve is then used as the baseline and deducted from the actual sample measurement data. For an accurate weight measurement, the mass of the empty crucibles had to be determined with a high precision of 10^{-5} g. They were weighed with a *Mettler-Toledo XS* analytical balance. For each material, a small amount was analyzed with a specified heating profile. The heating profiles are given in Table 15. For the thermal analysis, only profiles *P1* to *P3* were applied, *P4* was used to create a heat-treated batch of a *SBA-15* sample - more details can be found in Section 3.1. These profiles are actually not much

Table 15: Heating profiles for TGA analysis. The sample is first held at temperature ϑ_1 for a certain time h_1. It is then ramped up at a rate k to ϑ_2, where the sample is held for another interval h_2.

		P1	P2	P3	P4
ϑ_1	[°C]	25	25	25	25
h_1	[min]	15	30	30	30
k	[K/min]	5	5	5	5
ϑ_2	[°C]	450	450	450	255
h_2	[min]	30	30	10	10

different from each other, they are merely evolutions of the initial profile - after it was found that the analysis did not take much time, the initial holding period h_1 was extended from 15 minutes to 30 minutes. Similarly, after discovering that the second holding period h_2 did not yield any further insights, it was shortened from 30 minutes to 10 minutes.

During the analysis, heat flow and sample weight are continuously measured within the device. If any gaseous products are generated, they are carried to the mass spectrometer by the purging gas stream. Since the devices are synchronized with each other, reaction products showing up in the mass spectrum can be accurately assigned to thermal events recorded in TGA. This method is often referred to as *evolved gas analysis*. Since this analysis is not the main scope of this project, but has more of a supportive character, it shall be only briefly described here - for further reading, great introductions can be found, for example, in [125].
The mass spectrometer is run in *multiple ion detection* (MID) mode. Instead of recording a full mass spectrum, where the ion current is plotted as a function of the mass-to-charge ($^{m}/_{z}$) ratio, the mass spectrometer will detect specific ions over the analysis time. Which ones to select depends on the expected ions. Possible evolved compounds during the experiments conducted here are water, either desorbing from the surface or water of crystallization at higher temperatures and combustion products. The following *m/z* values are selected, with the corresponding compound for an ion charge of $z = +1$ given in parentheses: 1 (H), 2 (H_2), 12 (C), 17 (OH), 18 (H_2O) and 44 (CO_2). It must be noted that a signal will be obtained for every compound of the same respective mass-to-charge ratio. Also, multiple-charged ions will cause a detector signal according to their charge. These are not considered here, neither are different isotopes. To establish certainty on the nature of the respective compound, further analysis of the evolved gases would be required. In the case at hand, the method is deemed accurate, since the composition of the investigated materials is well documented. Also, no quantitative analysis is necessary.

Knowledge of the specific heat capacity is important within this project for the consideration of the cool-down process of the dried adsorbent, and, at a possible later stage, for a proper packed bed design. In this case, only the former is considered. The desorption process is performed by passing a stream of warm air through the packed bed, thus heating up the adsorbent and removing the adsorbate. Afterward, the adsorbent will still remain warm due to the heat stored within the silica gel bed. The amount of heat remaining in the packed bed can be quantified if the specific heat for the bulk material is known. This is why the specific heat capacity was calculated from DSC data for the bulk material only. The specific heat capacity of the loaded adsorbent can vary greatly from the value of the dry adsorbent [126, 127].
The basic principle of obtaining the specific heat from differential scanning calorimetry (DSC) data is to heat up a known amount of sample under a controlled atmosphere. Heating is performed at a constant rate to a specified temperature while recording the heat flow required to reach this equilibrium. The heat flow is then divided by the heating rate to obtain the specific heat capacity.

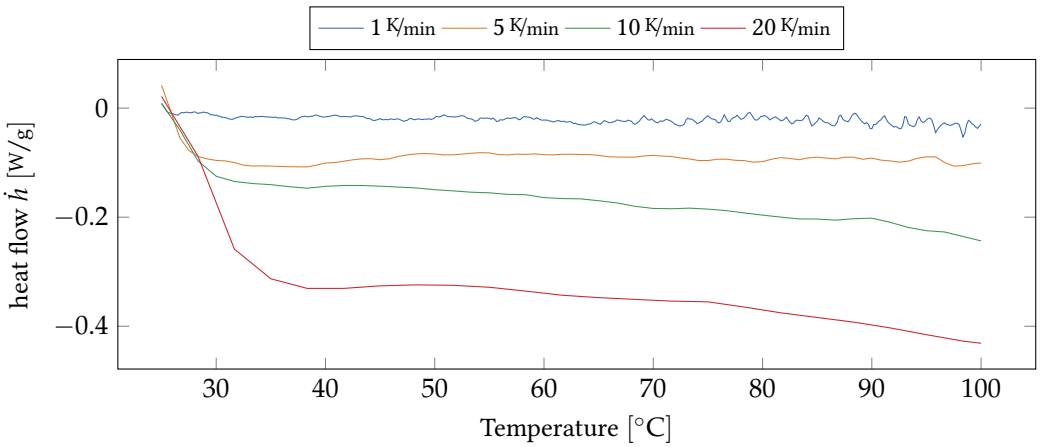

Figure 34: Comparison of several different heating rates to assess the stability of the heat flow $\dot{h}$. Taken on *SBA-15* sample.

$$c_p = \frac{\dot{h}}{k_{DSC}} \tag{3.3.27}$$

$\dot{h}$ is the specific heat flow per unit of sample mass, measured in W/g, whereas k_{DSC} refers to the applied heating rate in K/s.

The measurements were taken with the same *Mettler-Toledo TGA/DSC 1 STARe* device that was also used in TGA and MS analysis. Appropriate analysis parameters were identified through a prestudy. This consisted of repeated DSC experiments with varying heating rates k_{DSC} in a range between 1 K/min and 20 K/min. The most appropriate rate for the silica gel samples was identified as 5 K/min: smaller rates tend to yield large errors due to poor signal-to-noise ratios at very small heat flows. Larger rates lead to a temperature gradient within the sample, which cause a typical slope in heat flow measurement data. This means that for a material with a small thermal conductivity, thermal equilibrium between the surface and the core of the sample has not yet been reached. At a rate of 5 K/min, a sufficiently stable heat flow was obtained, indicative of equilibrium conditions having been reached. The above mentioned effects are visualized in a comparative plot of four different heating rates in Fig. 34. Although the later selected 5 K/min plot still shows some noise, a fitted regression line is sufficiently constant to assume thermal equilibrium. Most of the samples showed a peak in heat flow during the beginning of the measurement process. This is due to the endothermic desorption process of superficial moisture being desorbed, an assumption that was verified through mass spectrometry. The part in question is therefore omitted in the evaluation process, as only the specific heat capacity of the bulk material is considered.

3.4 OPEN SYSTEM TEST STAND

The previous experiments have all been conducted under a controlled atmosphere in a closed system. They employed only very small amounts of desiccant and were focused on its microscopic properties. While the results give a good indication on the expected adsorption capacity per unit mass, the operation in a packed bed process can not directly be deduced from these experiments alone. Major differences include for example equilibration: under the controlled conditions of a closed system, full equilibrium is always ascertained at every partial pressure point. Conditions are uniform and steady. In an open system with a rather fast flowing fluid phase, this is rarely going to be the case: turbulent flow conditions inside the packed bed, non-uniform exposure of the desiccant due to the

flow conditions inside the reactor, temperature variations due to the released enthalpy of adsorption may all affect the mass transfer. The experiments described in this section consider this behavior of the desiccant in a packed bed reactor, and attempt to quantify the difference to an idealized system under defined conditions. The test bench presented in this section has been designed for this purpose. The design scenario is the expected operating condition in an electric vehicle in Singapore. The dimensions of the components are modeled after the preliminary considerations outlined in Section 2.2. They are built to scale according to the requirements that have been found in Chapter 2, and their design bears in mind the actual restrictions in a vehicle - mainly due to weight and space limitations. This is why some components, namely the packed bed reactors and the airflow switching valves, are not standard parts but specifically designed and built for this project. They do naturally not match the optimization standard of mass-produced automotive parts in terms of weight and size, but they give a fairly good indication about these parameters. The operating principle is exactly the same as in the proposed, actual usage scenario: The air is passed to the adsorber chambers, which can be filled with different types of silica gel. In one chamber, adsorption takes place, while the other can be regenerated Fig. 40. The air is then cooled back to ambient conditions through the air cooler. Multiple sensors are installed along the air path and connected to a data logging device. This set of sensors records temperature, humidity and pressure at all significant locations. The following paragraphs describe the individual components and operation of the experimental setup, which was built in TUM CREATE's RP7 Lab. Laboratory conditions were almost constant, the temperature was set at 22.5 °C and stable to ± 0.3 K. Ambient air pressure varies only marginally with atmospheric conditions, this is in good correlation with the general situation in Singapore (see Section 1.2).
The system consists of the following components, which are highlighted in Fig. 36:

1. Atmosphere Generation Chamber
2. Packed Bed Reactors
3. Switching Valves
4. Air Cooler
5. Blower
6. Hose System
7. Data Acquisition and Controls
8. Sensors

3.4.1 *Atmosphere Generation Chamber*

This is the first stage of the experimental setup. Its purpose is to generate an airflow of defined conditions for different operating scenarios. The air flow rate is adjusted through the blower controls, the chamber provides the requested temperature and humidity levels. During the adsorption cycle, these are set to mimic those that can be expected on the road in Singapore. For the desorption cycle, the conditions provided should be such that are realistically available in an electric vehicle. Measurements with TUM CREATE's own electric vehicle, *EVA*, serve as a reference, as discussed in Section 2.2. From these considerations, the teststand setpoints are chosen for the adsorption and desorption measurements. During adsorption, the aim is an intake air temperature of 30 °C with a water content x of 25 g/kg. The regeneration temperature is set at 60 °C with no fixed water content. To provide these defined ambient environmental conditions within the laboratory, a *Memmert UF30* laboratory oven was modified accordingly. The entire setup is shown in Fig. 35, with the numbers corresponding to the following description.

Fresh air enters the oven from the bottom (2) and is heated in the preheating chamber (3). It reaches the desired temperature in the oven chamber, with the temperature adjusted through the integrated thermostat. To control the humidity, a set of two ultrasonic vaporizers (7) had been installed inside the oven. Each of those is submerged into a 500 ml laboratory beaker (6) containing deionized water from the in-house supply. The rate of evaporation can be independently regulated through a two-channel, adjustable power supply unit in a range from 19 V to 24 V. Since no technical data was available on the ultrasonic vaporizers, their characteristics had to be found experimentally. The vaporization rate was adjusted as needed in order to obtain the desired water content in the air leaving the chamber. This setup allows to simulate the conditions for a wide spectrum of air flow rates, that would correspond to vehicular air change rates within the range that has been found the most interesting (Section 2.2). A fan (1) inside the oven chamber ensures proper mixing of the entire volume, before the humid air is channeled via the opened air flap (4) through the ovens air outlet (5). From there it reaches the blower's air intake through an insulated hose. The connection was made via a customized adapter piece, mounted to the oven's rear wall.

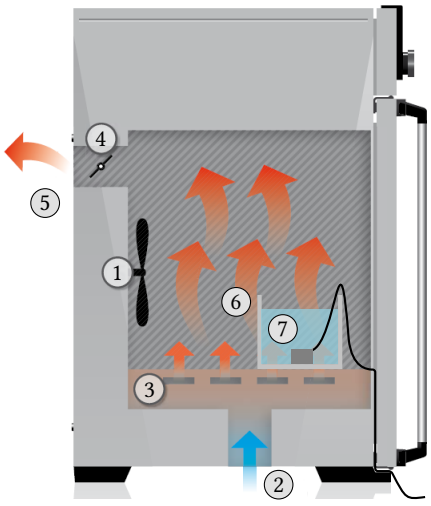

Figure 35: Schematic of the *Memmert UF30*, set up as the climate chamber. Drawing based on [128].

3.4.2 *Packed Bed Reactors*

The actual adsorption system consists of two packed bed reactors that are loaded with desiccant samples. The design stage was not straightforward, since some of the most crucial parameters are mutually dependent on one another - for example, the total mass of adsorbent loaded to the bed and the pressure drop. If the adsorbent mass is to be increased while the cross section of the vessel remains unchanged, there are only two ways of achieving this: either the bed becomes longer, or the bulk density of the desiccant increases. Both factors cause a rise in pressure drop, as is evident from their appearance in the Ergun equation (Eq. (2.6.1)). Of course the adsorbent mass directly affects the drying performance, which is the main aspect of the device. In order to keep the overall mass small, the desiccant mass should also be as small as possible. On the other hand, it needs to be large enough to allow for reasonably long operating times before regeneration is necessary. Determining the required amount of desiccant is therefor the first step of the design phase:
From the previous analysis of the vehicle's air changes per hour and its geometry, the necessary dehumidification performance can be estimated. The required drying capacity is calculated for the different air change rates and the ambient conditions usually found in Singapore. The values for the adsorption capabilities of silica gel are, at his stage, taken from literature, manufacturer data sheets, and own, preliminary measurements (see Table 8). They provided a reasonably accurate estimate at this stage, until proper vapor adsorption curves had been recorded. In a completely ideal case, the dehumidifier would reduce the intake humidity to the target value. For the state change discussed in Chapter 2, this would mean a reduction by 15.8 g/kg - from x_1 = 21.6 g/kg to x_2 = 5.8 g/kg. It must already be accepted that this can not be reached with silica gel, due to the adsorption characteristics described in Section 2.5 - at low relative humidity, the specific adsorption capacity is drastically reduced. In a completely adiabatic process as sketched in Fig. 9a, x_2 = 5.8 g/kg would correspond to a relative humidity of just 3.3 %. In order to actually achieve this value over an extended period of time, the length of the packed bed and the amount of desiccant would have to be increased to an extent where the entire design becomes unreasonably large. Therefor, these boundary conditions

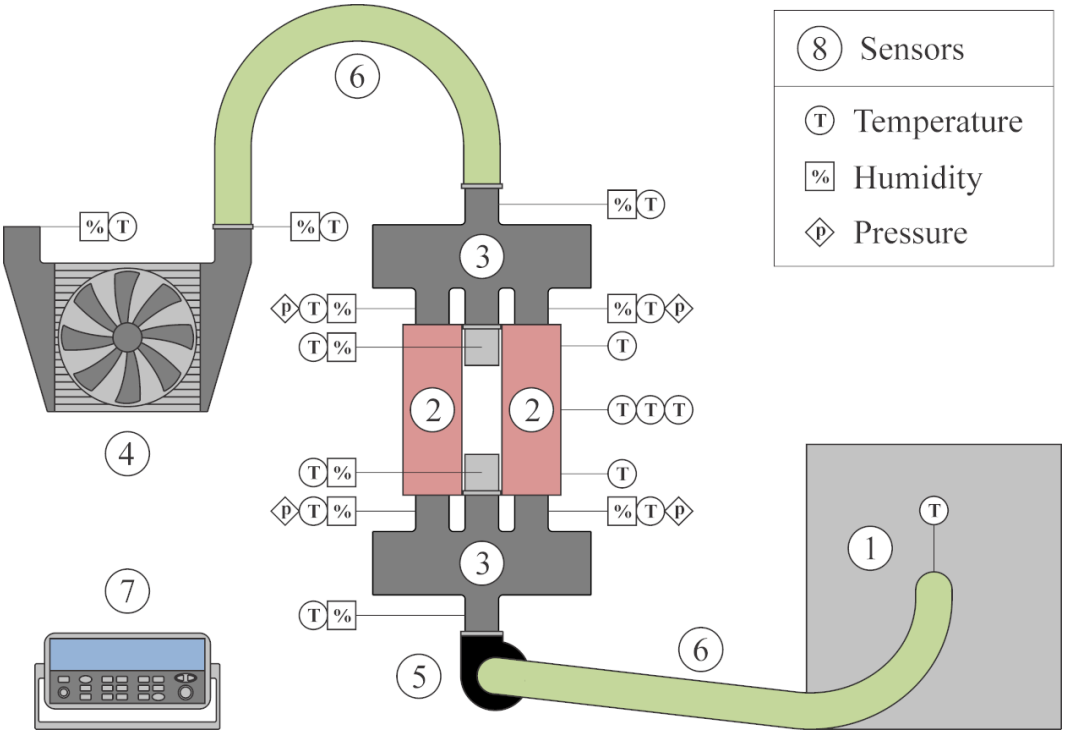

Figure 36: Schematic of the open system test stand. Numbers are corresponding to the list below.

are used as design guidelines with a best-case scenario in mind, the actual performance is later evaluated and design changes for further development are suggested in later chapters. In order to find a starting point for the design, the silica gel's humidity-dependent specific adsorption capacity is ignored for the moment, and it is assumed that the entire moisture reduction can be achieved in the packed bed with a very optimistic adsorption capacity of 0.3 g_{H_2O}/g_{SG}. At 10 ACH, using *EVA*'s volume of 3.82 m^3, and an air density of ρ_{air} = 1.157 kg/m^3, a mass flow of

$$\dot{m} = \frac{10\,h^{-1}\,3.82\,m^3}{1.157\,kg/m^3} = 0.012\,kg/s$$

is obtained. We thereby arrive at a required dehumidification capacity of 0.194 g_{H_2O}/s, or 698 g_{H_2O}/h. Assuming an adsorption capacity of 0.3 g_{H_2O}/g_{SG} and an operating time of 30 minutes, the required desiccant volume would amount to 1.163 kg. With a bulk density of 0.8 g/cm^3, this amount corresponds to a packed bed volume of 1454 cm^3. A corresponding estimate can be done from the desorption perspective. Since the aim is to regenerate the desiccant exclusively with waste heat, the desired drying capacity must match the available energy that is available to reactivate the desiccant. The available waste heat can then be calculated from Eq. (2.2.1), with the input values taken from the simulations discussed earlier (Table 2b). The effective reference consumption P_{ref} at 10 ACH is then obtained from the total energy consumption ($W_{ttl,ref}$) and the duration of the Singapore taxi driving cycle (STDC):

$$P_{ref} = \frac{W_{ttl,ref}\,3.6}{t_{drivecycle}} P_{ref} = \frac{1189\,Wh\,3.6}{1310\,s} = 3267\,W. \tag{3.4.1}$$

In the considered electric vehicle, the combined efficiency of power train and transmission is η_{pwr} = 0.89, a value that is similar to many contemporary electric vehicles. The energy that is lost as heat is thus $P_{PT} = 0.11 \cdot 3267\,W = 359.4\,W$.

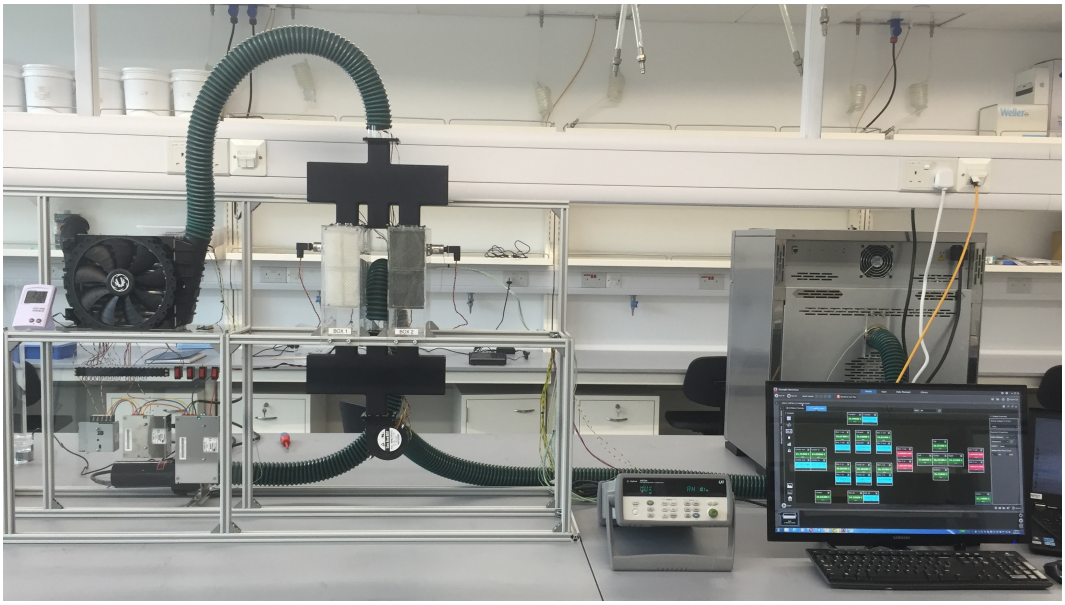

Figure 37: The actual open system test stand

The contribution from air conditioning, $P_{A/C}$, is calculated from the values for solar irradiation, heat flow through the vehicle body and passenger heat emission. For the considered scenario, these amount to P_{solar} = 146 W, P_{body} = 56 W, and P_{pass} = 132 W, respectively. The remaining load caused by the air change can be found from the change in specific enthalpy of the fresh air Δh_{rest}, and the air mass flow of $\dot{m}_{air}$ = 0.012 kg/s. The specific enthalpy change is found according to the methods introduced in Chapter 2 to be 19 kJ/kg. It corresponds to the state change from Z_{VI} to Z_{IV} in Fig. 9a - the part of the A/C process that has to be accomplished by the refrigeration cycle. For the latter, a COP of 2.5 is assumed. This leads to a total waste heat flow of

$$\dot{Q}_{waste} = P_{PT} + \left(P_{solar} + P_{body} + P_{pass} + \Delta h_{rest}\, \dot{m}_{air}\right) \left(1 + \frac{1}{2.5}\right) = 1146.2\,\text{W}. \tag{3.4.2}$$

In order to make sense of this amount in terms of regeneration capacity, one of the quantities measured during the vapor adsorption experiments comes into play: the enthalpy of adsorption. According to Section 2.4.4, it is identical to the energy required to remove the adsorbate from the adsorbent. With this, the required amount of energy to regenerate the desiccant bed can be calculated to be

$$H_{regen} = m_{ads}\, q_{ads} \tag{3.4.3}$$

and the corresponding regeneration time is

$$t_{regen} = \frac{H_{regen}}{\dot{Q}_{waste}} \tag{3.4.4}$$

For the scope of this preliminary design calculation, an average enthalpy of adsorption of 3.2 kJ/g is assumed (own measured values can be found in Table 24). The water adsorbed during 30 minutes of operation amounts to 349 g, and hence the required regeneration energy is 1117 kJ, with a regeneration time of less than 17 minutes. It is important to note that this is only a coarse estimate. Under realistic conditions, it will be difficult to transfer the waste heat to the packed bed: Elaborate duct work is required, heat losses will occur and even the fraction that arrives in

the packed bed will not be available in its entirety for the regeneration process due to the heat capacity of the adsorbent. Also, this calculation doesn't take into account the quality of the waste heat, namely the temperature at which it is available. These shortcomings must be considered, but they still allow for a general feasibility investigation.

Besides the drying performance, the pressure drop is another key parameter affecting the overall system efficiency. While one of the aims of the system design was overall compactness, the pressure drop was considered more crucial in the laboratory setting. The reasoning is simply that a wider range of experiments can be conducted with a single set of blowers. For a given blower type, the pressure drop determines the achievable air flow rate. With the blower characteristics known, the necessary electric power can be obtained.
There is a lot of optimization potential through proper modeling of fluid dynamics, heat- and mass transfer in the reactor. The sheer extent of this topic could, however, justify an entire research project on its own, and therefor, a simpler approach had to be chosen: With the mass flow rates obtained for the considered air change rates, a series of iterative calculations was conducted using the Ergun equation (Eq. (2.6.1)). For the fluid component, the density of air was assumed, as before, to be $\rho_{air} = 1.157\,\mathrm{kg/m^3}$, and the respective viscosity $\eta = 1.81 \cdot 10^{-5}\,\mathrm{Pa \cdot s}$. When it comes to the packed bed parameters, special attention needs to be given to an accurate estimation of the porosity ε. The sensitivity towards any variation of this parameter is very large. To illustrate the impact, Table 16 lists the pressure drop of a hypothetical, simple cubic packing of spherical particles (ε= 0.477) for comparison. To obtain a more accurate estimate, the relation

$$\varepsilon = 1 - \frac{\rho_{bulk}}{\rho_{solid}} \tag{3.4.5}$$

can be used [129]. This approximation is applicable if the fluid density is much smaller than the particle density, which is a justified assumption here. The density of a porous silica gel particle is $1.13\,\mathrm{g/cm^3}$, this is not to be confused with the *true density* of the solid material, which is $2.2\,\mathrm{g/cm^3}$ [130, 131]. This yields a porosity of ε= 0.36, which is well in line with literature values for randomly packed spherical particles (ε= 0.359 to 0.375) [132]. Another optional parameter is the pellet size and its geometry. The latter part is not considered here; all samples will be assumed to consist of spherical pellets. It is obvious that the smaller the pellet diameter, the larger the superficial contact area, and thus the adsorption performance, but conversely, the pressure drop increases. The practical approach to the packed bed design was therefor determined firstly by the most commonly available pellet size: Most samples obtained from commercial manufacturers came in a range from 2 mm to 6 mm, sometimes with a wide distribution over the batch. Hence, prior to filling the reactors, the desiccant pellets were sorted through sieves with mesh openings from 3 mm to 5 mm. Pressure drop calculations were conducted for both the worst-case scenario and the best case scenarios, i.e. a uniform pellet size of 3 mm and 5 mm, respectively. The remaining parameters are the bed thickness, or bed length l, and the flow velocity v. At a given desiccant loading, the flow velocity is determined by the ratio between the required airflow and the packed bed cross section. At a given amount of adsorbent, this determines the bed length or vice versa. As previously mentioned, if the bed length is chosen too long, the pressure drop will become large, if chosen too short, the adsorption capacity will suffer because of an early breakthrough. To avoid such problems, a preliminary experiment was conducted. Consisting of a sample column of *QP-B* at a bed length of 50 mm, it showed suitable drying behavior under several operating conditions. This was then used as a starting point for varying the cross section of the packed bed and repeatedly calculating the corresponding pressure drop for different boundary conditions (particle diameter d_{pt}, porosity ε). Results are compiled in Table 16. The maximum allowable pressure drop was set at 5 mbar, which corresponds to an airflow of $69\,\mathrm{m^3/h}$ (see Fig. 41a). The additional pressure drop caused by piping and auxiliary devices, like valves and air cooler, is not yet considered. As no manufacturer data was available on the subject, another 5 mbar was reserved for this part of the teststand. A total pressure drop of 10 mbar allows to maintain the airflow required to simulate 10 ACH with the selected blower. The resulting packed

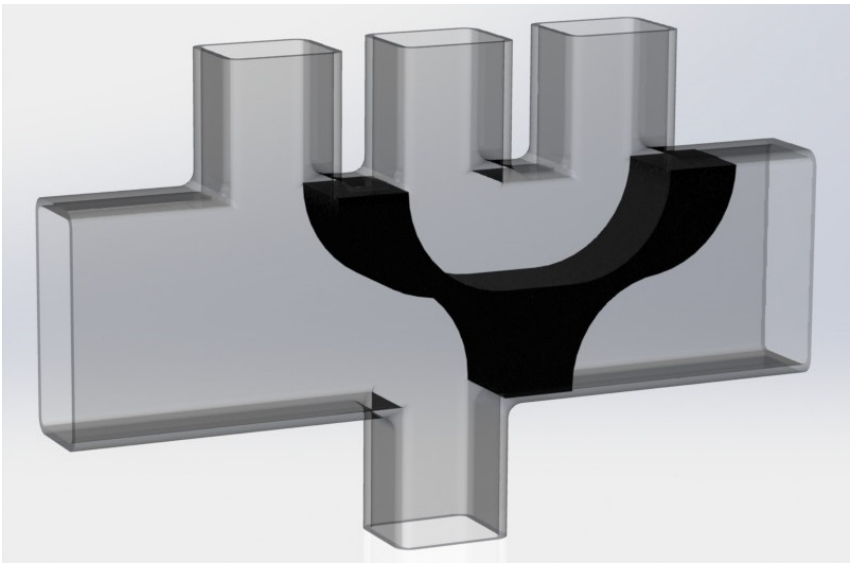

Figure 38: The valve body and housing.

bed dimensions are a length l of 53.8 mm and a cross-sectional area of 25725 mm^2, which yields a flow velocity of v = 0.825 $^m/_s$.
Finally, the geometric layout was chosen among several possible setups; the V-shaped packed bed is a trade-off between a compact, simple design and considerations from fluid dynamics - namely the pressure drop discussed above. As it is strongly dependent on the packed bed length, this dimension needed to be kept rather short. Instead, the other dimensions were enlarged, while still preserving the overall compact dimensions that give this design an edge over the continuous process. The "outer" volume, meaning the space under the V-shaped packed bed, allows for an even distribution of the humid air flow, but the base plate causes an additional pressure drop as well as the "inner" volume, which is smaller than the outer one and thus also not optimal in terms of flow obstruction. Overall, the system constitutes a good starting point, but leaves a considerable potential for optimization. Fig. 39 shows the final dimensions of the packed bed reactors. From the measurements at hand, the volume of the desiccant compartment can be calculated at 1433 cm^3.
The reactor vessels were custom made using clear acrylic with a thickness of 3 mm. Parts were designed using the *SolidWorks* CAD platform and manufactured using a *Epilog Legend 36EXT* laser cutter system. They were joined and sealed with *Acrifix 1R 0192* reaction adhesive. Expanded stainless steel with a mesh width of 2 mm was used as adsorbent support, from top and bottom. To introduce the actual packed bed, the reactors were filled through two openings from the top. The desiccant was loaded through a funnel all the way to the top, then the openings were sealed with laser-cut nitrile butadiene rubber (NBR) gaskets and the lids screwed shut with five stainless steel M3-screws each. They were carefully shaken throughout the filling process to allow for settling of the desiccant pellets. The loadings employed for the individual experiments are shown in Table 27. The loaded masses calculated with the bulk densities from Table 9, are within an error band of -1.3 % to +2.8 %, with a median of +0.53 %. It can be concluded that the packed bed reactors were sufficiently shaken and the bulk densities are consistent with a randomly packed bed.

3.4.3 *Switching Valves*

The main design considerations for the switching valves was a solution that is as lightweight and small as possible. As mentioned earlier, the experimental setup was also considered a proof-of-concept to demonstrate the feasibility of a dehumidification system compact enough to be installed

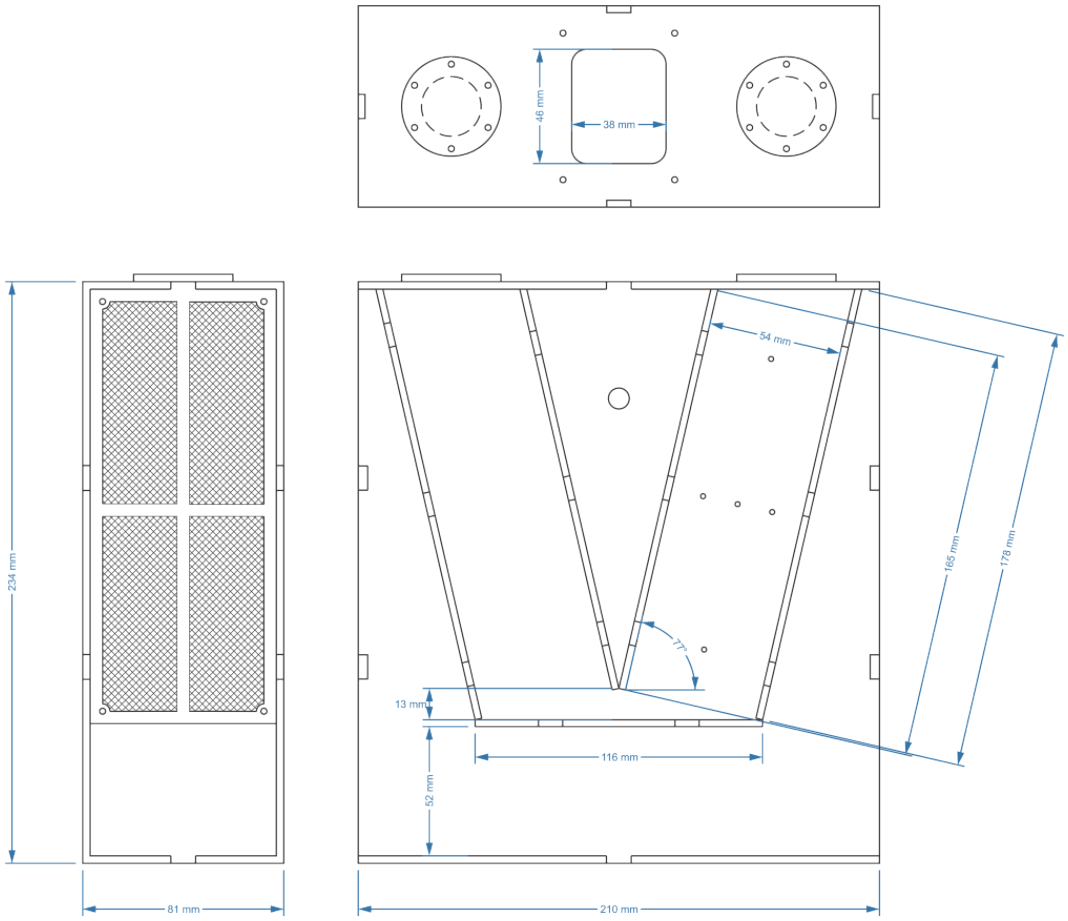

Figure 39: Measurements of adsorber *Box 2* (packed bed temperature measurement sites are visible).

Table 16: Pressure drop for different air change rates, porosity values ε and pellet diameters d_{pt}.

ACH	Air flow [m^3/h]	Porosity ε [-]	d_{pt} [mm]	Δp [mbar]
10	38.2	0.36	3	1.44
		0.36	5	0.72
		0.477	3	0.47
		0.477	5	0.24
20	76.4	0.36	3	4.57
		0.36	5	2.46
		0.477	3	1.53
		0.477	5	0.84
30	114.6	0.36	3	9.39
		0.36	5	5.21
		0.477	3	3.19
		0.477	5	1.79

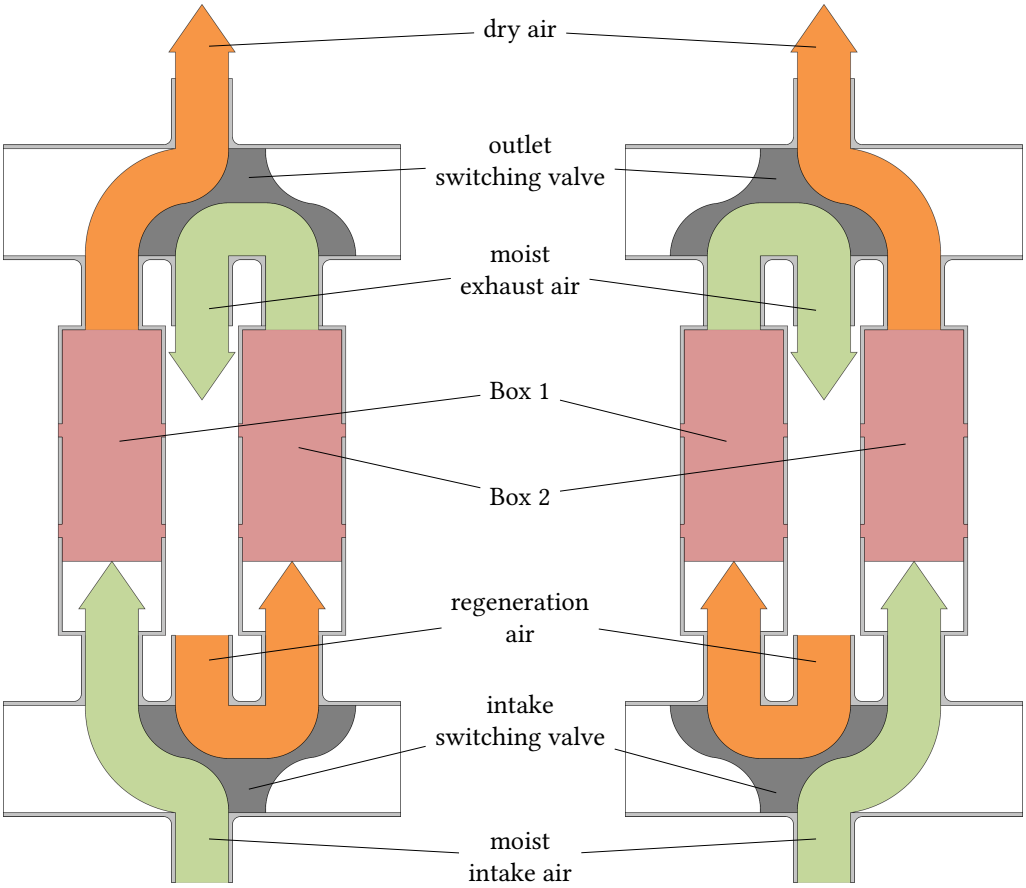

(a) Position 1: left packed bed in adsorption mode, right packed bed in desorption mode.

(b) Position 2: left packed bed in desorption mode, right packed bed in adsorption mode.

Figure 40: The two operation modes of the alternating batch process. Green denotes cool, humid air. Hot, dry air is drawn orange.

in a vehicle. In this case however, this objective was compromised by the available manufacturing methods.

The valves have also been designed with the *SolidWorks* CAD platform, and were manufactured through rapid prototyping. Valve body as well as housing were 3D-printed from polyamide at *Shapeways, Inc.*. In order to keep the complexity low, the valve plugs were manufactured as solid bodies, and the wall thickness of the housing was chosen rather large - in future designs, this is a big opportunity for further weight savings. Also, the tolerances during this manufacturing process are rather high, and the parts were hence finished in the TUM CREATE workshop by hand. Here, they were also assembled into their final form which is sketched in Fig. 38 and can be seen in Fig. 37. Switching capability was added through the installation of two stainless steel rods, which are shifted manually between their end positions. An automated solution, which would switch the valves through remotely controlled servos, was designed but ultimately omitted due to unnecessary complexity. The experiments were always performed under supervision, so automation was not required in this case. In a future application, this feature can however be added without any conceptual changes.

The valves provide the means to channel the airflow in alternating directions through the two packed beds. Fig. 40 illustrates the principle: While ambient air is channeled through one packed bed to be dried, hot air can be passed through the other packed bed to regenerate the desiccant.

These processes can happen simultaneously, but it is also possible to run just one experiment in either adsorption reactor.

3.4.4 *Air Cooler*

After the adsorption process, the air flow is heated up due to the released enthalpy of adsorption. To cool the airflow back down to near-ambient temperature, an aluminum air cooler is employed. An approximation for the amount of heat to be removed by the air cooler can be made from the reference process outlined in Section 2.1.4: it corresponds to the state change from the outlet of the adsorption process to the inlet of the evaporator, represented by Z_V and Z_{VI}, respectively, in Fig. 9a. The specific enthalpy difference is Δh_{V-VI} = -28.5 kJ/kg. At the given mass flow of $\dot{m}$ = 0.012 kg/s, the required cooling performance $\dot{Q}_{cooler}$ amounts to

$$\dot{Q}_{cooler} = \dot{m}\,\Delta h_{V-VI} = -342\,\mathrm{W} \tag{3.4.6}$$

For this experiment, a commercially available automotive charge air cooler was used. Several models were compared according to their weight-volume ratio, this specific cooler was chosen because of the low weight of 1920 g and the 50 mm hose fittings. Since no design data was provided by the manufacturer, it's suitability was roughly assessed from its application parameters as a charge air cooler for high-performance engines. The cooler was equipped with a 230 mm fan to improve cooling performance.

3.4.5 *Blower*

The fans, or blowers, are the component that provide the necessary air flow. In the experimental setup described here, the blower is used to transfer air from the atmosphere generation chamber through the adsorption reactors. It was chosen according to the required air flow rate, together with the predicted pressure drop, as discussed earlier in this section. From a range of commercially available radial fans, the *SanAce B97 (9BMB24P2K01)* was selected, and its fittings modified to fit the setup. The characteristics of this blower are given in [133]. The relationship between pressure drop and air flow for this blower is plotted in Fig. 41. Power is supplied at 24 V by a *TDK Lambda LS100-24* power supply unit. To adjust the airflow rate, this model provides the possibility to be controlled through a pulse width modulation (PWM) signal, which was realized through a *Pololu Mini Maestro* PWM controller [134].

3.4.6 *Air Ducts*

Connections between the individual components were made using acrylic flanges with flat rubber seals, all of which were custom built. The gaskets were cut from 1 mm NBR using the *Epilog* laser cutting system. For the air ducts, *IPL Volcano TPRA* thermoplastic rubber hoses with an inner diameter of 51 mm were utilized. They were selected for their high operating temperature of up to 125 °C as well as having a steel spiral reinforcement. This enables for the duct to maintain a stable cross section over the entire spectrum of operating conditions.
For air flow measurements, a portable *CEM DT-8880* hot wire anemometer was used. This device consists of a hand-held probe, which is connected to a control unit. The air velocity was determined at both the cooler outlet and the exhaust port. Details on these measurements are discussed in Chapter 4.
At this point, the laboratory setup contains all the necessary parts that would be needed for implementation into an electric vehicle. The following parts are sensors and data acquisition equipment necessary for the experiments performed, that would not be required under real-life

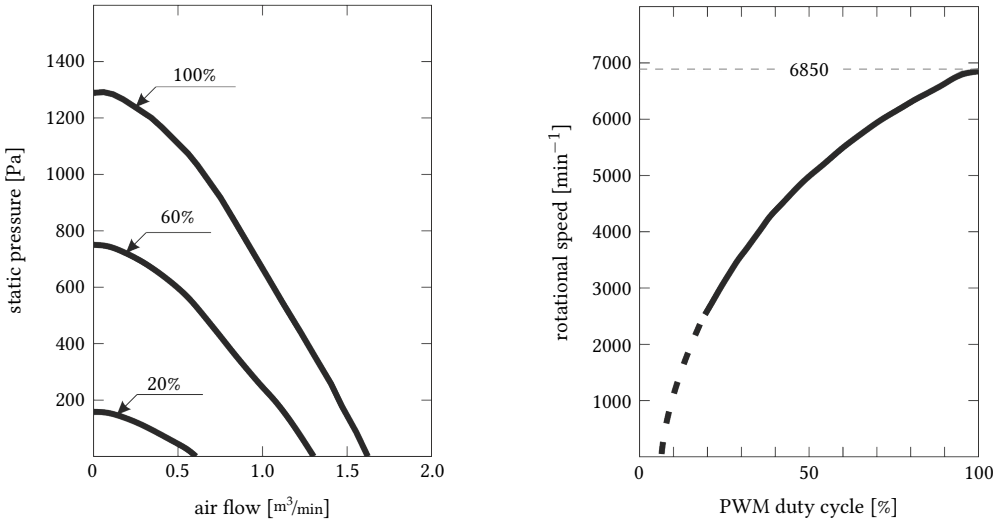

(a) Pressure drop for three PWM duty cycles.

(b) Power output over PWM cycles

Figure 41: Characteristics of the *SanAce B97 (9BMB24P2K01)* blower. On the left hand side the achievable pressure drop at a given air flow, on the right, the output power is plotted against the PWM signal.

conditions. For later reference, Table 17 lists the masses of the individual components of the laboratory setup.

3.4.7 *Sensors*

Several measurement points in the experimental setup were identified to be relevant to characterize the adsorption and desorption processes. On all these locations, sensors were placed to determine the thermodynamic properties of the process air, as well as the pressure drop across the adsorption system and the temperature distribution within the packed bed. An overview of the installed sensor setup is given in Fig. 36 and explained in Table 18. The installed sensor system consists of thermocouples, pressure transducers and relative humidity sensors. These are the basic properties that need to be measured, from which all other necessary thermodynamic parameters can be calculated. The theoretical background to these operations is given in Section 2.1.4. All sensors

Table 17: Mass of core components of the open system test stand.

Device	Amount	m [g]
adsorbent containers	2	650
valve body	2	167
valve housing	2	335
air ducts	1	250
blower	1	190
air cooler	1	1920
air cooler fan	1	399
desiccant packed bed	2	1100 (app.)
total		7263

Table 18: The sensor sites with the corresponding names and the IDs of the humidity sensors, as given in Table 19

No.	Site description	Site name	ID	Sensor type
1	Outlet adsorber *Box 1*	box 1_{out}	96	Humidity & Temperature
2	Exhaust pipe	exhaust	90	Humidity & Temperature
3	Outlet adsorber *Box 2*	box 2_{out}	86	Humidity & Temperature
4	Transfer line to cooler	transfer	94	Humidity & Temperature
5	Inlet adsorber *Box 1*	box 1_{in}	89	Humidity & Temperature
6	Ambient air inlet	fresh air	95	Humidity & Temperature
7	Inlet adsorber *Box 2*	box 2_{in}	85	Humidity & Temperature
8	From atmosphere chamber	hot air	83	Humidity & Temperature
9	Inlet air cooler	$cooler_{in}$	91	Humidity & Temperature
10	Outlet air cooler	$cooler_{out}$	93	Humidity & Temperature
11	Outlet adsorber *Box 1*	box 1_{out}	n/a	Pressure
12	Inlet adsorber *Box 1*	box 1_{in}	n/a	Pressure
13	Outlet adsorber *Box 2*	box 2_{out}	n/a	Pressure
14	Inlet adsorber *Box 2*	box 2_{in}	n/a	Pressure
15	Packed bed - left side	left	n/a	Temperature
16	Packed bed - center low	c_{low}	n/a	Temperature
17	Packed bed - center mid	c_{mid}	n/a	Temperature
18	Packed bed - center top	c_{top}	n/a	Temperature
19	Packed bed - right side	right	n/a	Temperature

have been calibrated and connected to the data acquisition system as described in the following subsections for each sensor type.

THERMOCOUPLES For the temperature measurements, a total of seventeen thermocouples were installed. The utilized model was the NiCr-Ni (K-Type) manufactured by *Labfacility*. In this version, the base metal wires have a length of 3 m and are are protected with a glassfibre insulation. The accuracy was according to IEC 584 Class 2, which means a tolerance of $\pm$ 2.5 °C or $\pm$ 0.0075 ϑ - whichever is higher. While the K-type thermocouple is defined between -270 °C and 1300 °C, the operating range for this tolerance class is defined only between -40 °C and 1200 °C. It is further limited by the constraints of the insulation, which is only suitable for temperatures between -50 °C and 350 °C. The expected temperatures measured during experiments are well within the limitations of the thermocouples; they are conducted between the laboratory's room temperature up to 150 °C. The thermocouples were placed into the air flow according to Fig. 36, and inside the packed bed. They were inserted through drilled holes until the center of the air duct or packed bed, respectively. Epoxy resin and cyanoacrylate glue were used to keep the sensors in place and seal the bores.

PRESSURE TRANSDUCERS To measure the pressure drop over the packed bed and the cooler, four pressure transducers *Honeywell PX2CN2XX250PSCH* were used. This is a sealed gauge sensor with a measurement range from 14.7 psi_a to 250 psi_a. The manufacturer specifies an accuracy of $\pm$ 0.25 % of the full scale span for operating temperatures between -40 °C and 125 °C. The sensor requires a supply voltage of 12 V, which was provided by a *TDK Lambda LS50-12* power supply

Table 19: Calibration data for *Honeywell HIH-4010-004* humidity sensors used in the experimental setup.

				U_{out} [V]		Offset	Slope
Serial no.	Wafer no.	MRP	ID	0 % rh	75.3 % rh	[mV]	[mV/% rh]
36113300079	03143C11	9167403	83	0.838375	3.167739	838.375	30.934453
36113300081	03143C11	9167403	85	0.840594	3.167441	840.594	30.901019
36113300082	03143C11	9167403	86	0.837676	3.163055	837.676	30.881528
36113300085	03143C11	9167403	89	0.837654	3.160011	837.654	30.841387
36113300086	03143C11	9167403	90	0.838842	3.167167	838.842	30.920652
36113300087	03143C11	9167403	91	0.835819	3.179022	835.819	31.118239
36113300089	03143C11	9167403	93	0.835060	3.167020	835.060	30.968919
36113300090	03143C11	9167403	94	0.836749	3.169735	836.749	30.982547
36113300091	03143C11	9167403	95	0.837848	3.170833	837.848	30.982537
36113300092	03143C11	9167403	96	0.834745	3.169678	834.745	31.008417

unit. 250 Ω resistors were used to convert the sensor output signal from a current between 4 mA and 20 mA to a voltage between 1 V and 5 V. To obtain absolute pressure readings, the offset was adjusted for the internal gauge of 14.7 psi. These values were converted by the data acquisition (DAQ) system to *mbar* by using a conversion factor of 68.9476 $^{\text{mbar}}/_{\text{psi}}$. In order to calibrate the baseline, an *Ahlborn FHAD 46-41* sensor was used to provide the reference pressure. The pressure transducers were all placed next to this sensor and a measurement was run for 7 minutes. While the accuracy was well within the given error band, the baseline around which the measured values were scattered showed a significant, but stable offset. From this measurement series, both average and median were calculated, which differed by less than 0.11 %. The average was chosen as the baseline and the offset then adjusted to the value measured with the calibrated *Ahlborn FHAD 46-41* sensor.

HUMIDITY SENSORS A total of ten *Honeywell HIH-4010-004* humidity sensors were installed according to the diagram in Fig. 36. The supply voltage of 5 V was provided by a *Cosel PBA10F-5* power supply unit. As with the thermocouples, the humidity sensors were fixed using cyanoacrylate glue and the bores were sealed with epoxy resin. The sensors were provided with a calibration certificate issued by the manufacturer. With these calibration values, the output is converted from a voltage signal to a relative humidity value (% rh) according to the following relation:

$$rh\ [\%] = \frac{U_{out} - offset}{slope} \tag{3.4.7}$$

The values for *slope* and *offset* are unique to each sensor, they are documented in Table 19.

3.4.8 *Data Acquisition and Controls*

To collect and record the measurement data from the sensors, an *Agilent LXI 34972A* DAQ system has been selected. This system can be equipped with up to three measurement modules, on which the actual measurement channels are located. For this application, two *34901A 20-Channel Armature Multiplexer* modules were selected. One was used for the measurement of humidities and pressures, the other used for thermocouples. The data logger can be set up directly for all letter-designated types of thermocouples. It includes an internal reference junction temperature, which was used in

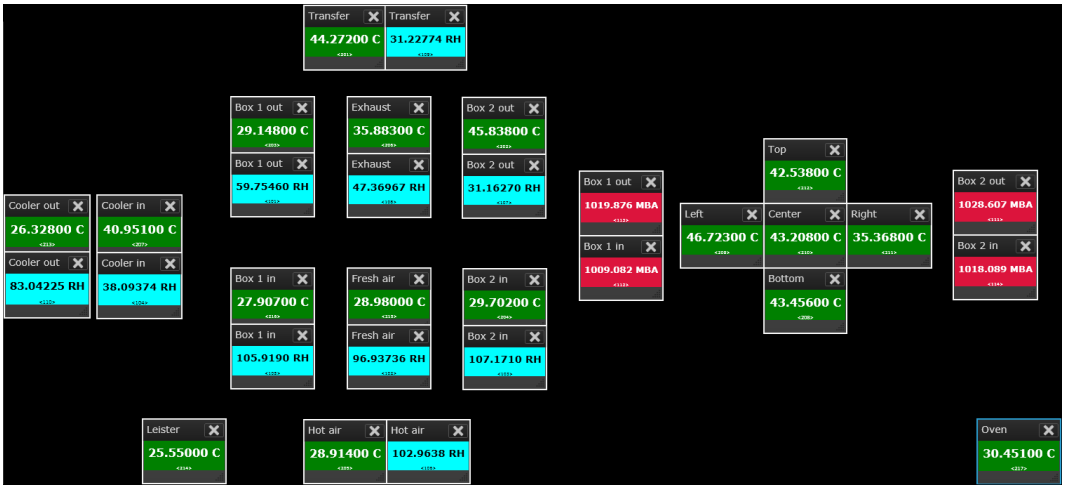

Figure 42: The *BenchVue* software configured for use with the open system test stand.

this setup. The manufacturer provides a dedicated software named *BenchVue* to visually monitor the entire measurement system. This software provides a convenient, color-coded visualization for the sensor readings. The position of the sensors on screen matches their physical position in the setup. Humidity readings are shown in blue, temperature readings in green, and pressure readings in red (Fig. 42). The software was configured corresponding to the layout specified in Fig. 36, with two further temperature sensors placed in the *Memmert* oven and at an ambient reference site, respectively.

4

RESULTS

Within this chapter, the results obtained from the previously described experiments are presented as plots and in tabulated form, together with corresponding discussions. Circumstances that led to deviations from the ideal experimental conditions are pointed out and examined in detail. The results are ordered in the same way as the experiments themselves were introduced in the previous chapter, meaning that the scanning electron microscopy images are presented first, followed by the closed system measurements and concluded by the open system experiments.

4.1 SCANNING ELECTRON MICROSCOPY

A selection of images taken with scanning electron microscopy is presented here, both a *SBA-15*-type structured gel and commercially available silica gels were investigated. Although a non-conductive material, extraordinarily good pictures could be obtained for the *SBA-15*-type structured gel. They reveal deeper insight into the structure, especially at higher magnification - different levels are shown in Fig. 43. A pore system can be observed that is consistent with both the expectations from the synthesis process, as well as the N_2-adsorption measurements. At lower resolutions, the surface can be identified as an agglomerate of smaller structures with wide cavities between them. A closer look reveals two main structural units, a well-defined, rod-shaped type and a bulk part. On further investigation, the rod-type subunit often shows broken edges that expose the internal pore system - this part can be recognized very well in Fig. 43d. In this image, the pores with a diameter of approximately 5 nm can be identified. The pore size and wall thickness are visible and their dimensions as expected, although the blur of the image must be taken into account - meaning that that there is an unknown error margin in the readings. In this case however, they also coincide very well with the nitrogen adsorption measurements and can be considered indicative of the actual structure. The measurement was performed with *TC-6*.

From the commercial materials, a glassy type (*QP-B*), a specialized, water-resistant type (*SB-WS*) and a bentonite clay sample (*TROP*) were investigated. No deeper insight into the porous structure was possible here. The commercial materials revealed a dense, compact structure with no visible pore system. Increasing magnification or otherwise adjusted settings yielded no benefit. A summary of the three selected materials at magnifications between 10^4 to $2{\cdot}10^4$ is shown in Fig. 44. Herein, the surface of a *SBA-15*-type sample and the commercial silica gels can be compared: The glassy surface of the *QP-B* sample is smooth, with the exception of a few scratches and depositions. The surface of both *SB-WS* and *TROP* are rough by comparison, but with no access to deeper regions of the sample. Also, even at larger magnifications and with different instrument settings, no image of the pore network could be obtained. Most likely this is due to the combination of several unfavorable factors: low conductivity in combination with the high density of the material. However, these findings can be used to explain the materials' mechanical properties discussed in Section 3.1 - the compact, coherent microscopic structure of the commercial samples leads to larger mechanical stability than the loose network of the *SBA-15*-type silica gel - which is a quite brittle material and is known to have a rather low density and low crush strength [135].

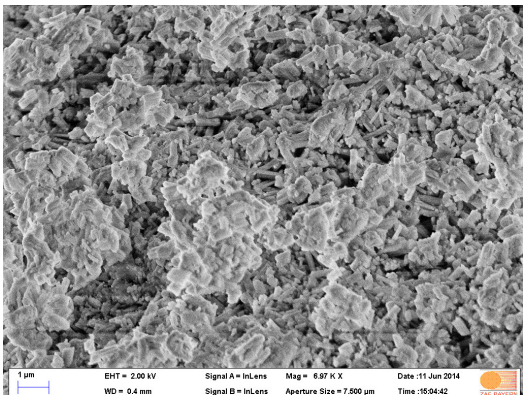

(a) This resolution shows the structure of the *SBA-15*-type Silica Gel as an agglomerate of smaller structures.

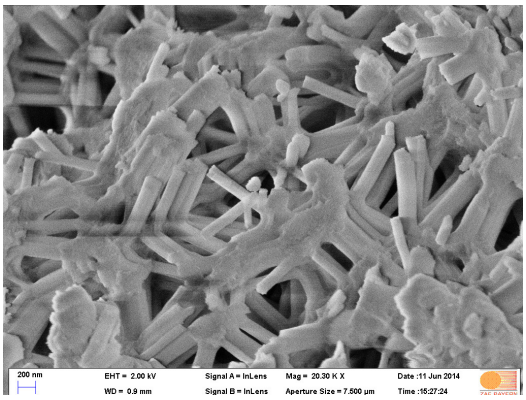

(b) Further magnification reveals rod-shaped structures and larger, coherent parts.

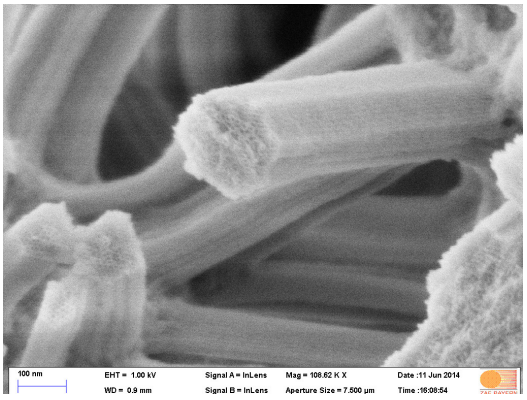

(c) The breaking edges of the rods and the bulk structure expose the expected porous structure.

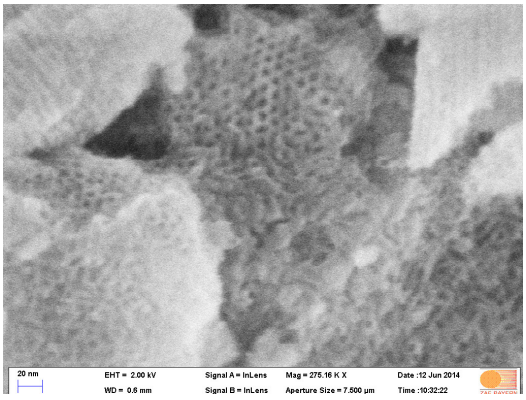

(d) Magnification of a selected section: a hexagonal order of the pore system can be identified, with equal pore diameter at the expected size of app. 5 nm.

Figure 43: SEM images of the *SBA-15*-type Silica Gel in different resolutions, from smaller to larger.

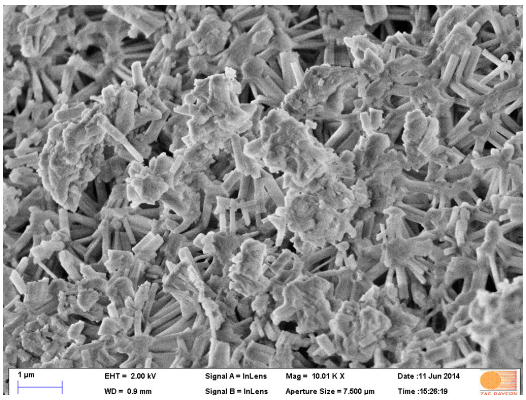

(a) The surface structure of *TC-6* as seen at a magnification of 10^4

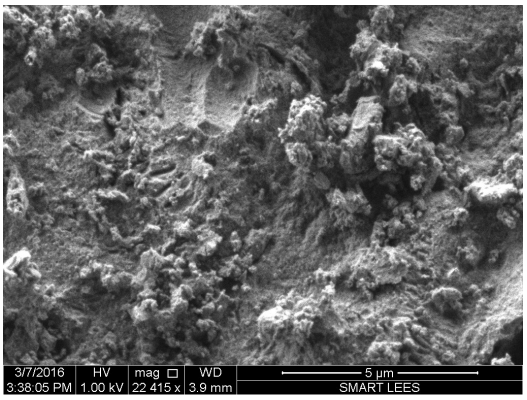

(b) The surface structure of *SB-WS* as seen at a magnification of $1.1 \cdot 10^4$

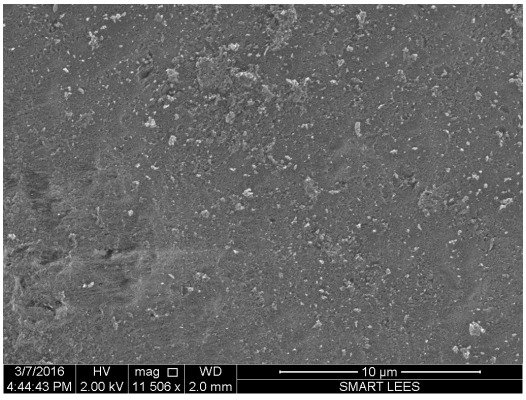

(c) The surface structure of *QP-B* as seen at a magnification of $2 \cdot 10^4$

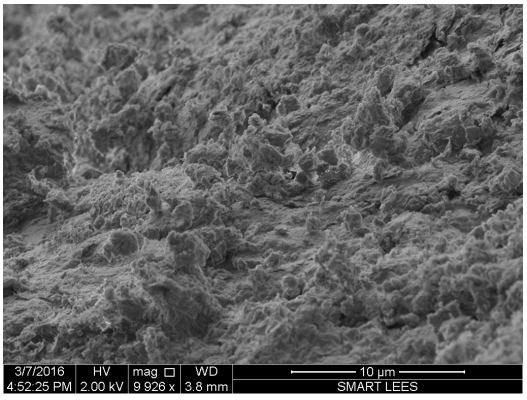

(d) The surface structure of *TROP* as seen at a magnification of 10^4

Figure 44: Comparison of the *SBA-15*-type sample *TC-6* with the commercially available *SB-WS*, *QP-B* and *TROP* materials at magnifications between 10^4 to $2 \cdot 10^4$.

4.2 CLOSED SYSTEM MEASUREMENTS

Measurements taken in a closed system refer to all measurements where the adsorbent had not been exposed to the environment, but instead been subjected to a controlled atmosphere. These measurements offer an insight into the microscopic properties of the adsorbents. As they are common methods for adsorbent characterization, they allow for the comparison of adsorbent properties with literature values. They are also generally easier to reproduce than open system measurements, as the latter are conducted in experimental setups which are tailored to a specific problem or application. This means that experimental parameters, i.e. temperature, pressure, adsorber design, etc. will vary greatly and might affect the comparability of results. The closed system methods employed in this project were nitrogen gas adsorption, water vapor adsorption, thermogravimetric analysis and differential scanning calorimetry, as described in Chapter 3.

4.2.1 *Nitrogen Adsorption*

The results of the nitrogen adsorption measurements are presented in the form of isotherms, specific surface area and pore size distribution data. The following samples were pre-treated as described in Section 3.3.1, applied heating profiles are documented within Table 21.

4.2.1.1 *N_2-Isotherms*

For all these samples, N_2-adsorption measurements were performed using the procedures described in Section 3.3.2.3. For the sake of readability, most plots are found in Appendix A.1. As an example, Fig. 45 shows two distinct N_2-isotherm plots - their characteristics are described in the following. Fig. 46 illustrates results obtained for sample material *SA-T2* during BET surface area measurement and pore size distribution analysis according to the BJH method.

When analyzing the recorded N_2-adsorption isotherms, a small learning curve can be identified. As the *Autosorb* device was brand new, no reference settings or prior experience existed. However, comparable devices were used before, and together with the manual and online discussions with other researchers, a reasonable starting setup was identified. Still, to get a sense of measurement duration and required equilibration times, the fist measurements were run on the pessimistic side. This means a lower number of defined p/p_0-points, and rather long equilibration time presets. During the course of this thesis, more and more confidence in the method and the specific machine was gained and thus the quality of the results also improved. This is noticeable by shorter measurement times at the same accuracy, a higher resolution due to more points obtained, especially in the hysteresis region where sudden changes occur.
The resulting isotherms are characterized according to the IUPAC classification outlined in Section 2.4.4. Classification results are given within Table 21 and the corresponding isotherm plots can be found in Appendix A.1. Four groups can be identified:

- Type I isotherms without hysteresis
- Type I isotherms with hysteresis
- Type II isotherms with H3 hysteresis
- Type IV isotherms with H1 hysteresis

The occurrence of *Type I*-isotherms is typical for microporous adsorbents, whereas the presence of a hysteresis loop is usually associated with mesoporous structures. Few of the commercial materials exhibit textbook *Type I*-isotherms, instead, the majority seems to be in line with a *mixed-type* behavior. This is expressed by a *Type I*-adsorption branch, while showing some hysteresis in the desorption branch. This loop does not fit into the IUPAC classification scheme. A likely

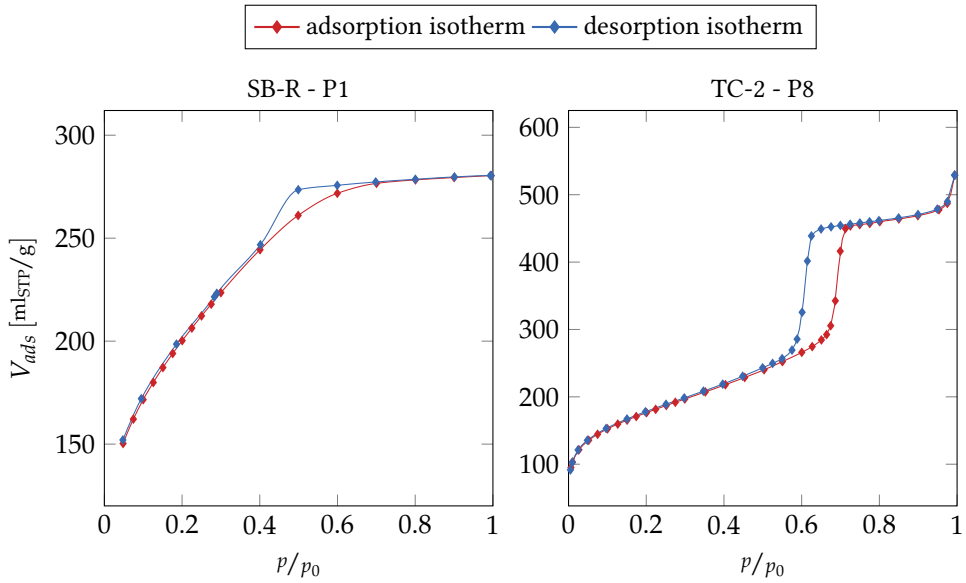

Figure 45: Examples of N_2-isotherms for a commercial material (left) and a *SBA-15*-type silica gel (right).

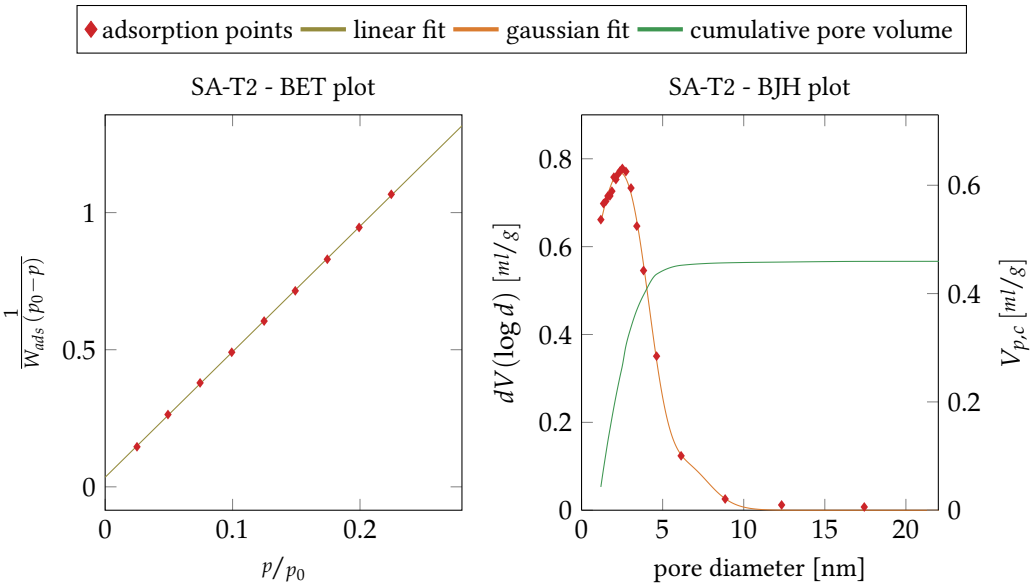

Figure 46: Example of BET plot (left) and BJH pore size distribution with cumulative pore volume $V_{p,c}$ (right) for the same sample (*SA-T2*).

explanation is that the adsorption behavior is governed by the microporous structure, but a small fraction of mesopores contributes a certain amount of capillary condensation that can be observed as a small hysteresis loop (e.g. *QP-B* and *SA-T2* in Fig. 74, *SB-C*, *SB-R* and *SB-WS* in Fig. 76). This could later be confirmed by BJH pore size analysis: while the mean value of the pore size distribution can be found within the micropore region, the distribution extends well into the mesoporous regime. The behavior of the *SBA-15*-type silica gels however is entirely as expected: all of them exhibit *Type IV*-isotherms with a prominent *Type H1* hysteresis loop (see Fig. 75). This is typical of mesoporous materials and has been observed many times [69, 136, 137] for *SBA-15*-type structures. One feature of the observed isotherms deviates form the textbook *Type IV*-isotherm, namely the additional "knee" at high relative pressures of $p/p_0 > 0.9$. This is caused by surface condensation after the completion of capillary condensation [138, 139]. Regardless of the specific isotherm and hysteresis classification, the hysteresis loop's lower closing point is observed in a region of $0.4 < p/p_0 < 0.45$. This is also an expected phenomenon, as the location of this point is determined by the adsorptive rather than the adsorbent. For N_2 at 77 K, it is to be anticipated at approximately $p/p_0 = 0.42$ [49], which is in good agreement with the findings presented here. *TC-5*, *TC-3*, and *TC-8* in Fig. 75 deviate from the ideal behavior. For the latter two, the loop closure is not well defined. Possible reasons include insufficient outgassing and unsuitable equilibration time settings - here, both can be ruled out, as the same settings did not lead to the same errors in the other *SBA*-15 materials. Instead, this behavior is caused by the amount of sample material being too small: for the two measurements in question, only 26 mg of material were used. Small impurities, like water vapor from ambient air that may be introduced between outgassing and actual measurement, cause a larger error than they would with more sample material. For all other *SBA*-15 samples, at least 70 mg were used. The *TC-5* isotherm, despite the unfamiliar shape, is considered to be correctly recorded. *TC-5* was the first *SBA*-15 sample within this project on which N_2-adsorption analysis was performed, and too few values were measured in the regions of interest, i.e. the hysteresis loop and the "knee" region. The apparent loop in this latter part is a phenomenon without any physical meaning: it is caused by the mathematical interpolation model having too few points. These shortcomings were fixed for the following measurements. The isotherm data is subsequently used to perform BET surface area analysis and BJH pore size distribution calculations.

4.2.1.2 *BET Surface Area*

From the isotherm data, the surface area was calculated according to the BET method described in Section 3.3.2.3. For BET analysis, a range from $p/p_0 = 0.05$ to $p/p_0 = 0.3$ is frequently cited in literature. However, this is not universally applicable and yields erroneous results in (partly) microporous adsorbents. Silica gels are known to deviate from linearity already well below $p/p_0 = 0.2$ [140][141]. To account for this behavior, the following formal procedure, as introduced in [142] and standardized in ISO 9277, was used - it specifies two criteria which indicate that one is working within a valid relative pressure range: First, the BET-constant c_{BET} must be positive. Second, the term $V_{ads}\ (p_0 - p)$ is required to continuously increase with p/p_0. The point where this is no longer the case determines the upper limit of the BET method's applicability. This approach is illustrated in Fig. 47. Also, p/p_0-increments were chosen in a way that at least six measurement points were available for the BET plot, i.e. more measurements were taken in the range between $p/p_0 = 0.01$ to $p/p_0 = 0.2$ than at higher relative pressures. After determining the range of applicability, the BET plot is fitted through these points by linear regression using the least-squares-method. The BET surface area is then calculated according to Eq. (3.3.6), and tabulated in Table 20.

The internal surface areas range from 562.46 m^2/g to 774.06 m^2/g in the commercial silica gels, and from 551.09 m^2/g to 773.92 m^2/g in the *SBA-15*-type structured materials. For the commercial gels, the values are within the range that is expected from literature [45, 47, 53] and manufacturer's data sheets. Most of the commercial silica gels actually fall into a much narrower range of 678.18 m^2/g to 774.06 m^2/g, with the exception of *QP-B* (562.46 m^2/g), *GN-1* (581.90 m^2/g) and *ARTS* (278.88 m^2/g). Only

Table 20: BET surface areas, BET constants and corresponding p/p_0 range, measured with N_2 at 77 K. The BET-plot parameters slope (s) and intercept (i) as well as the coefficient of determination R^2 are included.

	p/p_0 limits						
Sample	lower	upper	s	i	R^2	c_{BET}	s_{BET} [m^2/g]
SB-C	0.049	0.224	4.7067	0.0336	0.99986	141.02	734.69
SB-R	0.048	0.225	4.8216	0.0357	0.99989	136.20	716.99
SB-WS	0.025	0.224	5.0967	0.0385	0.99990	133.36	678.18
HD-O	0.048	0.235	4.9066	0.0246	0.99972	200.81	706.25
HD-W	0.048	0.212	4.8380	0.0250	0.99983	194.14	716.13
QP-B	0.048	0.272	6.1301	0.0617	0.99983	100.42	562.46
DT-B	0.049	0.224	4.5912	0.0205	0.99969	225.00	755.18
DT-G	0.048	0.190	4.6576	0.0161	0.99976	290.84	745.16
SA-O	0.025	0.224	4.6745	0.0321	0.99990	146.60	739.94
SA-T2	0.025	0.225	4.5773	0.0349	0.99991	132.33	755.10
FL-36	0.025	0.235	4.4778	0.0213	0.99975	211.26	774.06
GN-1	0.025	0.229	5.9542	0.0308	0.99989	194.38	581.90
GK-O	0.025	0.223	4.7672	0.0368	0.99992	130.39	724.93
PROS	0.025	0.249	4.6351	0.0405	0.99991	115.47	744.86
ARTS	0.025	0.280	12.4106	0.0773	0.99984	161.48	278.88
TROP	0.025	0.177	29.2021	0.0683	0.99985	428.74	118.98
TC-2	0.027	0.224	5.5024	0.0339	0.99990	163.18	629.05
TC-3	0.026	0.225	5.0280	0.0281	0.99989	180.14	688.80
TC-5	0.025	0.227	5.4452	0.0287	0.99982	190.92	636.22
TC-7	0.025	0.224	6.2744	0.0452	0.99992	139.83	551.09
TC-8	0.026	0.225	4.7375	0.0305	0.99992	156.54	730.42
TC-8t	0.026	0.200	4.4839	0.0161	0.99978	279.46	773.92

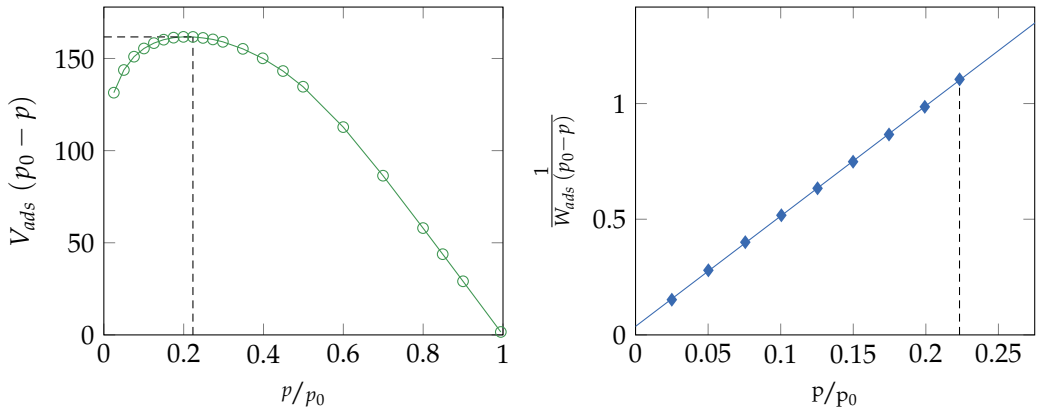

Figure 47: Illustration of the method used to determine the range of applicability of the BET plot. The maximum of the $V_{ads}\ (p_0 - p)$-plot (left) determines the last point that should be used for the BET plot, here located at p/p_0 = 0.2232.

QP-B and *GN-1* show surface areas lower than 600 m^2/g at otherwise similar characteristics. This can be explained by the rather low porous volume combined with comparably high average pore diameters of approximately 2.3 nm and 2.5 nm. This reasoning can partially be applied to *ARTS*, too, which exhibits a very large average pore diameter well within the mesopore region. However, here the influence of the LiCl must also be considered: the salt crystals block parts of the pores and do not contribute to the surface area.
For the structured gels, the difference in surface area is consistent with the variations in pore volume (see Table 21). As the synthesis parameters were identical for all samples, the most likely reason for the variations is insufficient template removal. Inhomogeneous sample composition is another possibility, especially for low sample amounts. But the fact that surface area variations were observed in experiments with large amounts of sample mass as well as in experiments with low sample mass makes an issue with template removal more likely - especially since this theory could be backed up with the results from thermal analysis: *TC-8t*, the thermally treated version of *TC-8*, exhibits the largest surface area of all structured silica gels.
A surface area could be calculated for *TROP* (the bentonite clay sample), which is smaller than that of the silica gels. This is in line with the anticipated characteristic, as *TROP* does not exhibit a pronounced porous structure. Its numerical value, however, cannot be considered accurate, for the same reasons given in the following section.

4.2.1.3 *Pore Size Distribution*

For the calculation of pore size distributions, the BJH method described in Section 3.3.2.3 was applied. Since little was known about the internal structure of the commercial materials, the desorption branch was initially used for all samples. However, it became evident that in many of the commercial samples, the approach led to unsatisfactory results - namely non-uniform distribution curves. When this behavior was observed, the problems could be completely mitigated by using the adsorption branch instead. Together with the observation that this behavior occurred in samples that later showed pore size maxima on the verge of, or within, the micropore region, this phenomenon can with a high level of confidence be attributed to the causes discussed in Section 2.4.4 (percolation effects due to bottleneck- and interconnected pores). Table 21 lists pore size maxima determined with the BJH method. Given are the maximum measured value and the diameter calculated from a fitted Gaussian distribution, along with the classification according to IUPAC, the isotherm branch that was used for BJH analysis and the outgassing profile applied during pretreatment. The respective isotherm branch which was selected for BJH analysis is also highlighted in the result plots.
It is noteworthy that many analysis software suites provide an option to ignore p/p_0-values below 0.35 (or similar, depending on the respective manufacturer) during BJH analysis. This supposedly coincides with the beginning of capillary condensation, which forms the foundation of the BJH method. However, as already pointed out in the previous section, inspection of the N_2-isotherms reveals that capillary condensation occurs at even lower relative pressures - consequently, no points were omitted here. The pore size maxima are given as both the maximum observed value, and as the maximum of a fitted Gaussian distribution curve. Corresponding plots are found in Appendix A.2, these also show the cumulative pore volume $V_{p,c}$. The pore size analysis from the adsorption branch yielded results that are in good agreement with literature values for the unstructured silica gels [45, 47, 53]. The fitted distribution curves are broad, reaching from the micropore region well into the mesoporous regime, representing the unordered pore network. Especially *SB-WS* exhibits an extraordinarily wide range of pore sizes. For all *SBA-15*-type samples, calculation from the desorption branch yielded sharp peaks at just above 5 nm, a value which is expected from the synthesis method, and already hinted by the SEM images. This ordered, mesoporous system is the dominant structure, but the interconnecting micropores (described in Section 2.5) can also be clearly identified: the cumulative pore volume shows a steep rise in the micropore region, followed by a flatter section in the beginning of the mesoporous area, before it rises sharply again at the average

Table 21: Pore size maxima according to the BJH method Section 3.3.2.3. $V_{p,c}$ = cumulative pore volume, OGP = Outgassing Profile, according to Table 12.

		Isotherm			Max. pore diameter [nm]		
Sample	OGP	Type	Hysteresis	Branch	Measured	Gaussian	$V_{p,c}$ [ml/g]
SB-C	1	I	-	Ads	2.38	2.25	0.37699
SB-R	1	I	-	Ads	2.25	2.25	0.37757
SB-R	2	I	-	Ads	2.52	2.33	0.37533
SB-WS	1	I	-	Ads	2.38	2.31	0.46378
SB-WS	6	I	-	Ads	2.52	2.30	0.44754
QP-B	1	I	-	Ads	3.08	3.33	0.31446
QP-B	2	I	-	Ads	2.23	2.27	0.31717
HD-O	1	I	-	Ads	2.30	2.03	0.33446
HD-W	2	I	-	Ads	1.92	1.92	0.30837
DT-B	1	I	-	Ads	1.87	1.75	0.33020
DT-G	3	I	-	Ads	1.51	1.57	0.26549
SA-O	3	I	-	Ads	2.25	2.35	0.42782
SA-T2	4	I	-	Ads	2.52	2.37	0.46108
FL-36	4	I	-	Ads	1.77	1.87	0.39843
GN-1	4	I	-	Ads	2.55	2.48	0.32632
GK-O	4	I	-	Ads	2.37	2.52	0.44301
TROP	4	II	H3	Ads	1.19	0.34	0.15047
PROS	5	I	-	Ads	3.05	2.98	0.51553
ARTS	7	IV	H1	Ads	9.58	10.00	0.69215
TC-2	8	IV	H1	Des	5.33	5.33	0.89388
TC-3	8	IV	H1	Des	5.51	5.46	0.99670
TC-5	4	IV	H1	Des	4.63	5.25	0.82363
TC-7	8	IV	H1	Des	5.06	5.22	0.82807
TC-8	8	IV	H1	Des	5.51	5.44	0.96332
TC-8t	8	IV	H1	Des	5.51	5.49	0.99663

pore diameter. In general, $V_{p,c}$ is much larger in the structured materials than in the commercial silica gels. In the heat-treated sample *TC-8t*, the cumulative pore volume is slightly increased, but not beyond typical values for untreated materials, e.g. *TC-3*. The pore diameter remains identical. In *ARTS*, a part of the pore volume is taken up by salt crystals and this value is therefor not representative of the pure silica gel. The pore size distribution curve can be affected if the salt preferably blocks pores of a certain diameter. Here, in accordance with literature [143], the pore size is plausible: for hybrid adsorbents, silica gels with a pore diameter of 10-13 nm are commonly used. In the case of *TROP*, the measured pore size distribution must be met with caution - although a numerical value can be calculated, it is likely not representative of the pore diameter. The BJH method fails in montmorillonite-type materials due to the metastability of the adsorbed multilayer, caused by non-rigid clay structure and a low degree of pore curvature [144].
As for the comparison of cumulative pore volume with the macroscopic, bulk density (Table 27), there is a good agreement for many of the samples, with two outliers: *PROS* would be expected to show a very low density, due to its high $V_{p,c}$, and correspondingly, *DT-G* should have a high density. In the case of *PROS*, the walls between the pores exhibit less micropores than it is the case in other samples, causing a denser solid fraction of the silica gel. The large void volume is instead attributable to a large share of wider pores, evident from the tail of the pore size distribution curve. *DT-G*, while having a small average pore diameter and a small cumulative pore volume, shows a low bulk density. In this case, the macroscopic structure is responsible for the behavior, as *DT-G* comes in granulated form and does not form the same close-packing as the spherical particles of the other sample materials.

4.2.2 *Water Vapor Adsorption*

4.2.2.1 *H_2O-Isotherm and Adsorption Capacity*

According to the principles described in Chapter 3, water vapor adsorption measurements were performed for most samples. Due to time constraints with the measurement devices, not all samples could be run, therefor, a pre-selection had to be conducted: Samples that have obviously similar characteristics, as revealed by N_2-adsorption analysis, were placed later in the queue. Samples, where enough material was available to conduct both closed- and open-system-measurements, were preferred. A temperature of 30 °C was chosen, in order to closely resemble the environmental conditions that are encountered during the desiccant's intended application. For some, isotherms were recorded also at 20 °C to allow for calculation of isosteric enthalpies of adsorption. Since, again, this was not possible to be performed on all samples, a representative selection was chosen. For the samples synthesized at TUM CREATE, all types of measurement were conducted. It was furthermore ascertained that at least one commercial sample comes from one of the following groups: narrow-pore gel without indicator, narrow-pore gel with indicator, silica gels with additives and a bentonite clay for comparison. The results are presented in form of isotherm plots (Fig. 49 to Fig. 52). The adsorption capacity is given at different p/p_0-values, in gravimetric units. The latter are calculated according to Eq. (4.2.1) as $^{mg_{H2O}}/_{g_{adsorbent}}$ from the molar volume (V_m) at *STP* conditions and the molar mass of water (M_{H_2O}):

$$m_{ads} = \frac{V_{ads}\, M_{H_2O}}{1000\, V_m}. \tag{4.2.1}$$

H_2O-adsorption measurements are likely the ones most directly application-related among the closed system measurements: The characterization of its water uptake behavior is crucial when determining the suitability of a certain material as a desiccant in the dehumidification process. H_2O-isotherms were thus the first closed system measurements that were conducted. Thanks to extensive experience and knowledge from the ZAE Bayern's staff, high-quality results could be obtained from the first measurement on the *Belsorp* device. The most important factors to be

mentioned are pre-treatment techniques for samples and empirical values for equilibration times and the position of measurement points. At this stage, only *SBA-15*-type silica gels were analyzed. These shall be discussed first.

The adsorption-desorption plots for both temperatures, 20 °C (Fig. 49) and 30 °C (Figs. 48 and 50), are almost as expected from the textbook for mesoporous materials - *Type IV* isotherms with prominent hysteresis of *H1*-type. However, the closing point after the hysteresis loop is in many cases not as well-defined as it should be: instead, the desorption branch is often located above the adsorption isotherm. This is the case for all isotherms measured on the *Belsorp* device at 20 °C (Fig. 49), although to a lesser extent than in some isotherms obtained at 30 °C (*TC-1 P2, TC-2 P4, TC-3 P4, TC-4 P3* and *TC-5 P2* in Fig. 48 as well as *TC-6 P4, TC-7 P2* and *TC-8 P3* in Fig. 50).

This behavior is often associated with two key sources of error: incomplete outgassing during sample preparation or insufficient equilibration times. In the case at hand, the explanation is most likely a different one, since the outgassing procedure was monitored with pressure gauges and was properly completed every time. Instead, it is worth taking into account the subsequent measurements that were conducted on the same samples - here *TC-5 P2, TC-5 P1* (both Fig. 48) and *TC-5 P3* (Fig. 50): the quality of the isotherm drastically improves, with no changes to the equilibration settings. It is therefor plausible to assume that irreversible reactions between the silica gel and the water occurred, either involving surface groups or irreversible micropore filling. This is further supported by a noticeable change in the adsorption branch of the hysteresis loop; in the second experiment with the same sample, the lower "knee" shifts from $p/p_0 = 0.8$ to ca. $p/p_0 = 0.73$, leading to a narrower hysteresis loop. That was the case for all samples that underwent more than one adsorption-desorption cycle. This could be an indication for pore size reduction due to swelling, but it seems unlikely since the total adsorption capacity was not reduced. After the second adsorption-desorption cycle, no further significant changes in the position of the hysteresis loop could be noticed, but the maximum adsorbed amount at the target relative pressure $p/p_0 = 0.95$ was by 11 % lower. Again, it's doubtful that this is caused by a reduction in pore size, as the effect can also be observed in low p/p_0-regions, beyond the point where capillary condensation plays a role. Other samples showed this behavior even during the second adsorption-desorption cycle, namely the two *TC-4 P3* and *TC-8 P3* experiments in Fig. 50. This makes sample contamination as an explanation unlikely, but points instead to problems with outgassing profile *P3* - supported by the observation that neither *TC-1 P2* and *TC-1 P1* nor *TC-7 P2* and *TC-7 P1* exhibit similar issues. The reason for this phenomenon being less pronounced in the 20 °C-isotherms is simply that they were measured after the ones at 30 °C.

The overall adsorption behavior is compiled in Table 22 and Table 23, to provide a direct comparison with commercial silica gels that are discussed in the following. These findings allow for an optimistic outlook regarding the application of *SBA-15*-type silica gels in an adsorption-based drying process: their ordered pore network and high adsorption capacity, together with similar regeneration characteristics make them a good candidate for further development. Their low density would, however, require a larger design volume of the adsorption reactors to achieve the same absolute adsorption capacity. The mechanical stability of the brittle material may also require it to be aggregated into pellets - a procedure that has been shown to decrease adsorption capacity, due to blocked adsorption sites as a result of necessary binder addition [135].

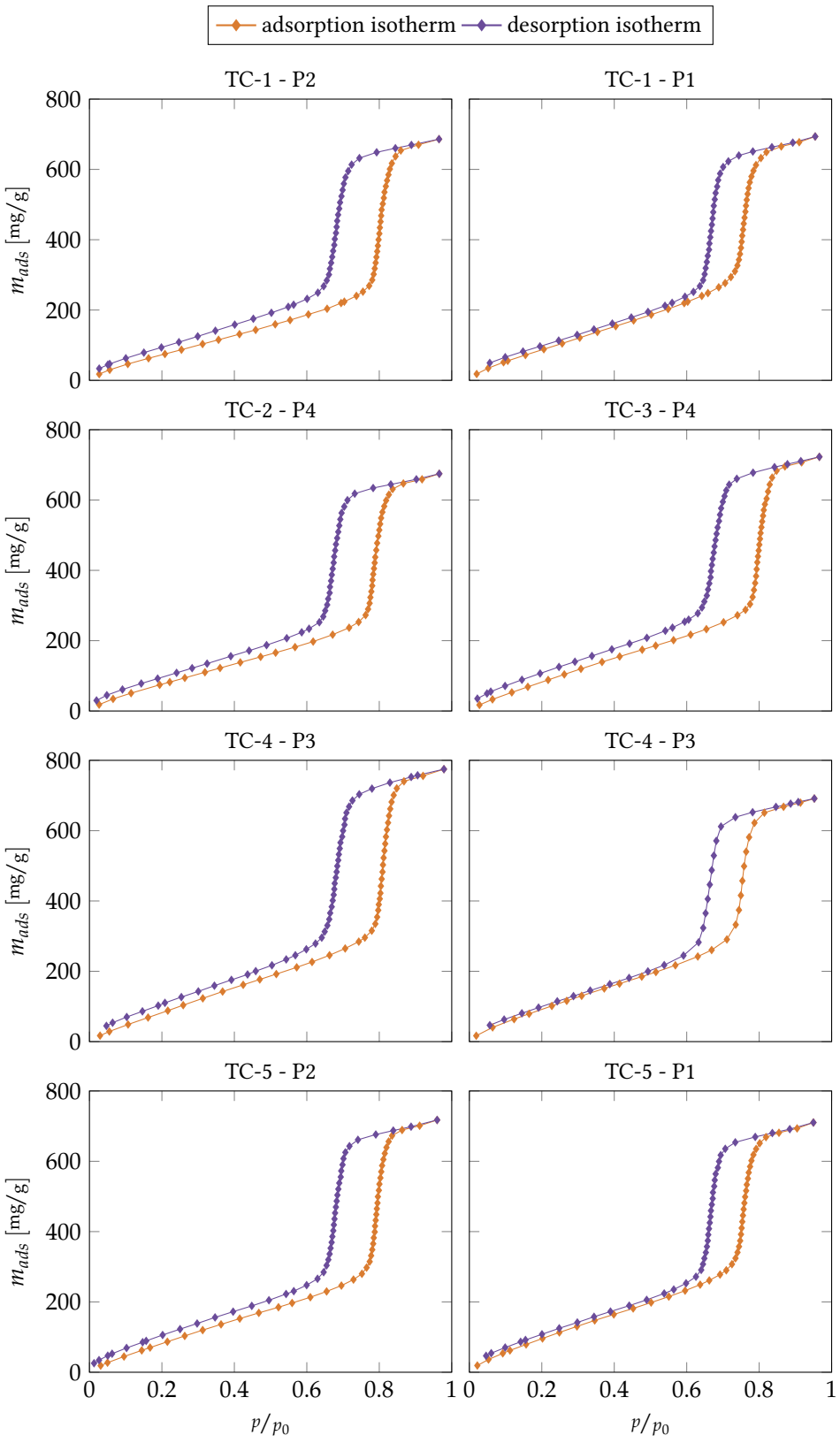

Figure 48: Compilation of H_2O-isotherms measured on the *Belsorp* device at 30 °C.

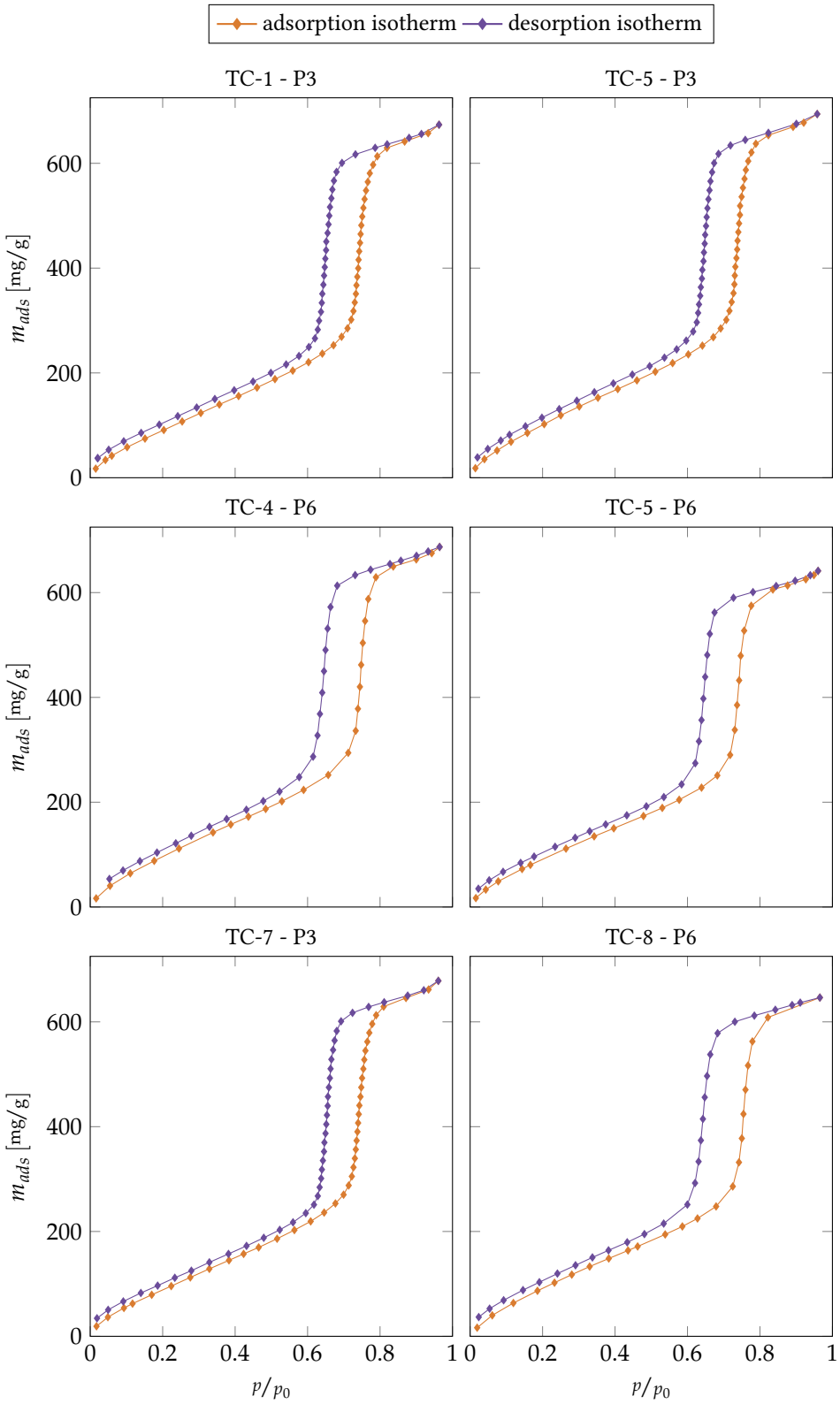

Figure 49: Compilation of H_2O-isotherms measured on the *Belsorp* device at 20 °C.

Commercially available silica gels were characterized with the *Autosorb* device in Singapore. During the first experiment, it turned out that the instrument settings were not directly transferable: especially the equilibration times used on the *Belsorp* required some adjustments to cater to the more microporous nature of the commercial gels. After some measurements, as with the N_2-isotherms, the quality could be improved. For the sake of completeness, also the earliest one (*SB-C P1* in Fig. 53) is presented - here, the effects of insufficient equilibration times can be observed: the open isotherm, where the desorption branch does not join the adsorption branch again, as well as uneven, jittery isotherms. The former was easily fixed with longer equilibration times, the latter remained a problem with the *Autosorb* device. Another issue that had never been encountered with the *Belsorp* device can be seen in all 20 °C-isotherms from Fig. 51: known as isotherm crossing, the desorption isotherm intersects with the adsorption branch in the low p/p_0-region. This is often a sign of leakage or contamination in the instrument, but in this case, it was not. The system was cleaned and evacuated overnight and passed all leak tests - additionally, the problem never appeared during experiments at 30 °C, although the experimental setup was identical. The probable cause is instead considered to be either a propagating error or a possible miscalibration of the sample cell (when in vapor adsorption mode, the device uses a shorter sample holder). The latter can only be mitigated with an updated calibration file from the instrument manufacturer.
Besides these issues, the overall shape of the isotherms at both 20 °C and 30 °C is again as expected: the commercial silica gels show *Type IV* isotherms with hysteresis of *H2*-type. This is typical for (at least partly) microporous adsorbents, and coherent with the findings from the BJH analysis (see Section 4.2.1.3). The maximum specific uptake capacity of the commercial gels is much lower than that of the structured *SBA-15* type, the same behavior that was already found in the N_2-isotherms. This is again caused by their different pore systems, the well-defined cylindrical pores of the mesoporous *SBA-15*-type samples take up a much larger amount of adsorptive during the capillary condensation phase than the unordered silica gels with smaller pore diameters. In the lower p/p_0-segment, before the onset of the hysteresis loop, the adsorption capacity of the two groups is similar - in many cases, the unordered silica gels even outperform the structured *SBA-15*-type. The decisive factor here is the larger specific surface area, as indicated by BET analysis (see Table 20), which provides more adsorption sites. For better comparability, the numerical values for major relative pressures are compiled in Table 22 and Table 23 - the qualitative behavior is identical at 20 °C and 30 °C.

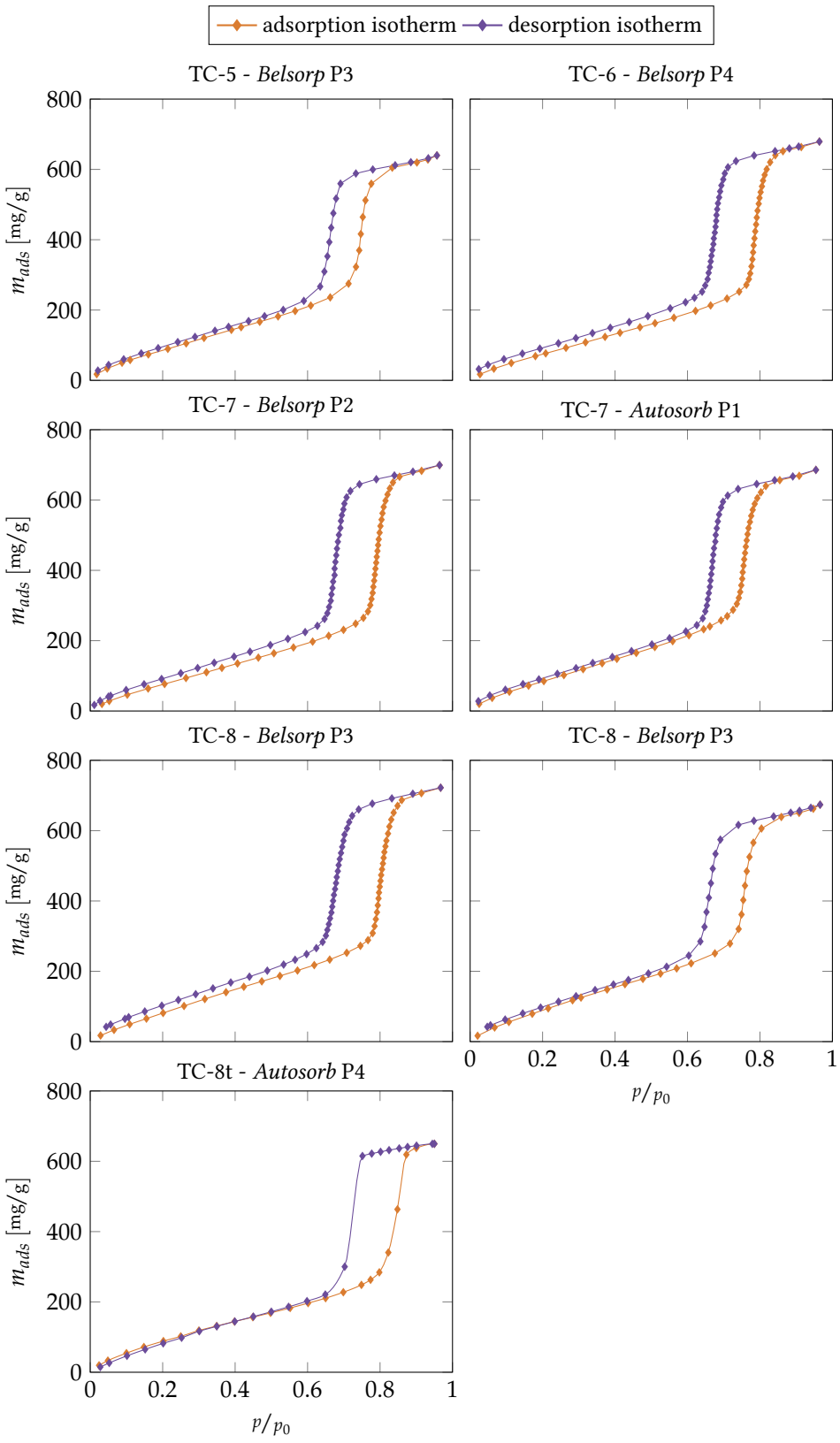

Figure 50: Compilation of H_2O-isotherms measured on different devices at 30 °C.

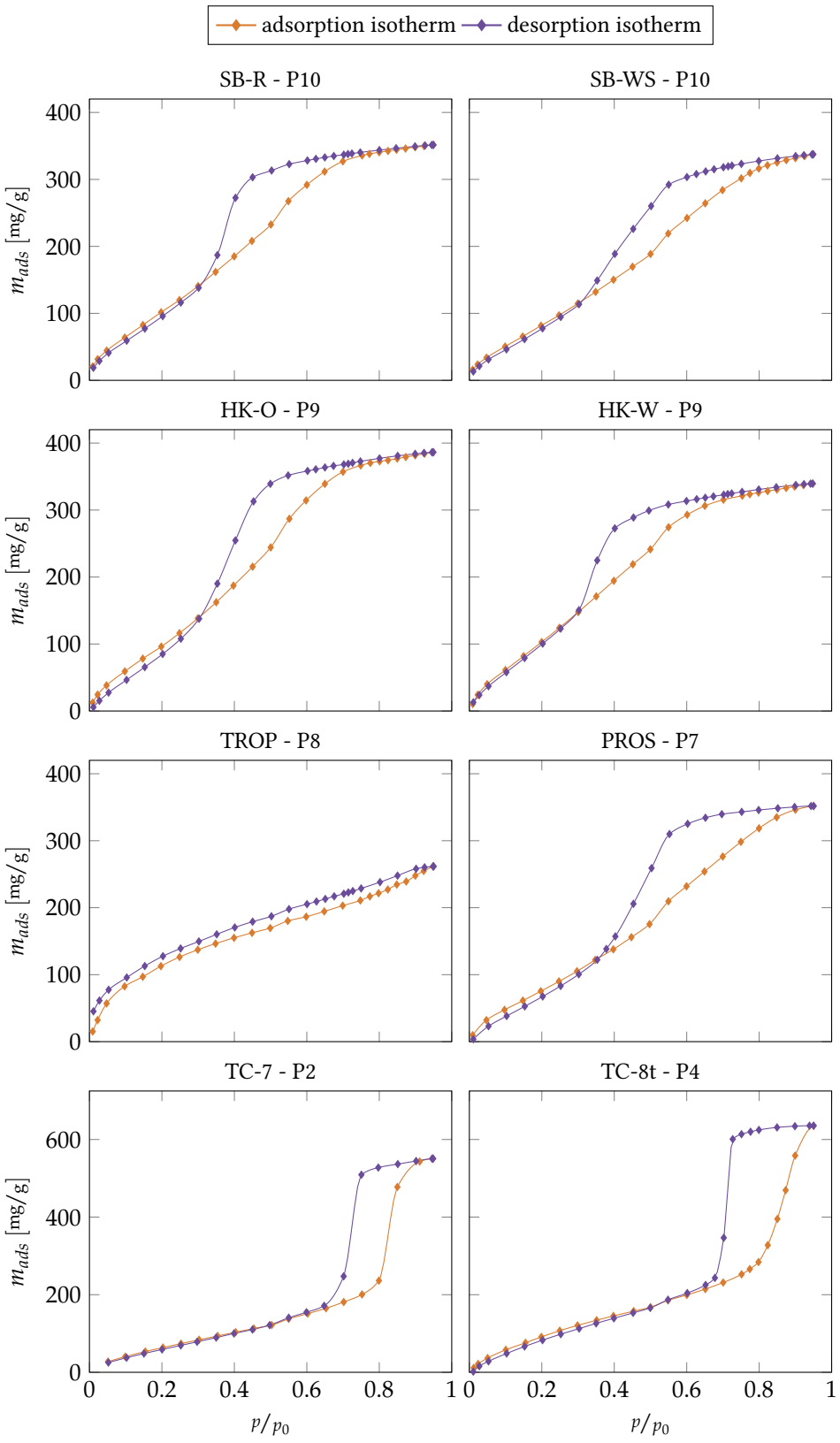

Figure 51: Compilation of H_2O-isotherms measured on the *Autosorb* device at 20 °C.

For the commercial silica gels, the loop closure is shifted to much smaller p/p_0-values compared to *SBA-15*: For *SB-R*, *HK-O* and *HK-W* in Fig. 53 as well as *PROS* and *QP-B* in Fig. 52 the loop closure happens approximately at $0.25 \leq p/p_0 \leq 0.35$. In the *SBA-15*-type silica gels, the loop closure point is located at $0.6 \leq p/p_0 \leq 0.65$ - although this point could not be identified clearly for all samples, due to the above discussed errors. In the case of *SB-WS* (in Fig. 53), no closure point could be identified. This is attributed to insufficient outgassing, the employed profile *P9* has a short holding time. This worked well for *HK-O* and *HK-W* (Fig. 53), but not for *SB-WS*. Although the outgassing procedure was deemed complete as no pressure rise could be detected within the given time frame, the procedure was obviously not finished. In contrast, the isotherm recorded at 20 °C exhibits proper loop closure at $p/p_0 = 0.35$. Here, the sample was pre-treated much longer with outgassing profile *P10*. This suggests that the pore system is much more complex than that of the other silica gels, which will need to be considered for the application in a desiccant dehumidification process. Special cases are, as expected, the materials that belong to other species: these are *TROP*, the bentonite clay shown as *TROP P8* in Figs. 51 and 52, and *ARTS*, the LiCl-impregnated material (Fig. 52). Their characteristics are different from the materials discussed so far. The clay exhibits low maximum adsorption capacity, but at smaller p/p_0-values it exceeds that of most silica gels. Contrary to the shape of the N_2-isotherms, the H_2O-isotherm exhibits only small hysteresis, but a non-closing loop. This is a common observation in montmorillonite clays [145], and is caused by the irreversible intercalation of water molecules and associated changes in the clay's structure [144]. The hybrid material *ARTS* (Fig. 52) shows the influence of both the salt (LiCl) and the silica gel adsorption. Its uptake capacity exceeds those of other unstructured silica gels by a factor of 1.4 to 1.7. The adsorption branch can be divided in three parts: first, up to $p/p_0 = 0.43$ the water uptake is governed by physical adsorption and the formation of salt hydrates ($LiCl \cdot H_2O$) [143, 146]. Afterward, a small plateau occurs until $p/p_0 = 0.5$ followed by a sharp increase in water uptake caused by the deliquescence of the salt.

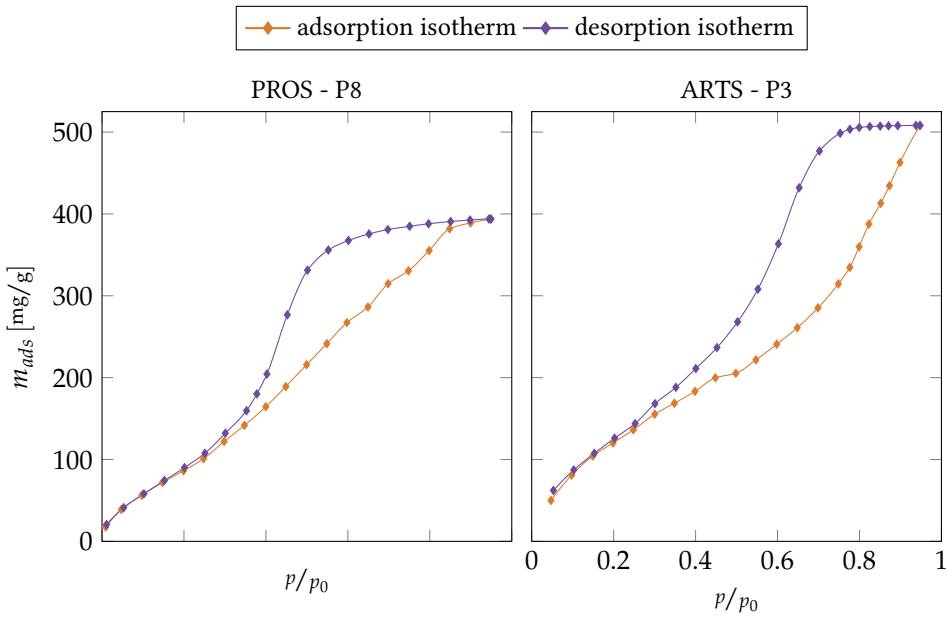

Figure 52: Compilation of H_2O-isotherms measured on the *Autosorb* device at 30 °C.

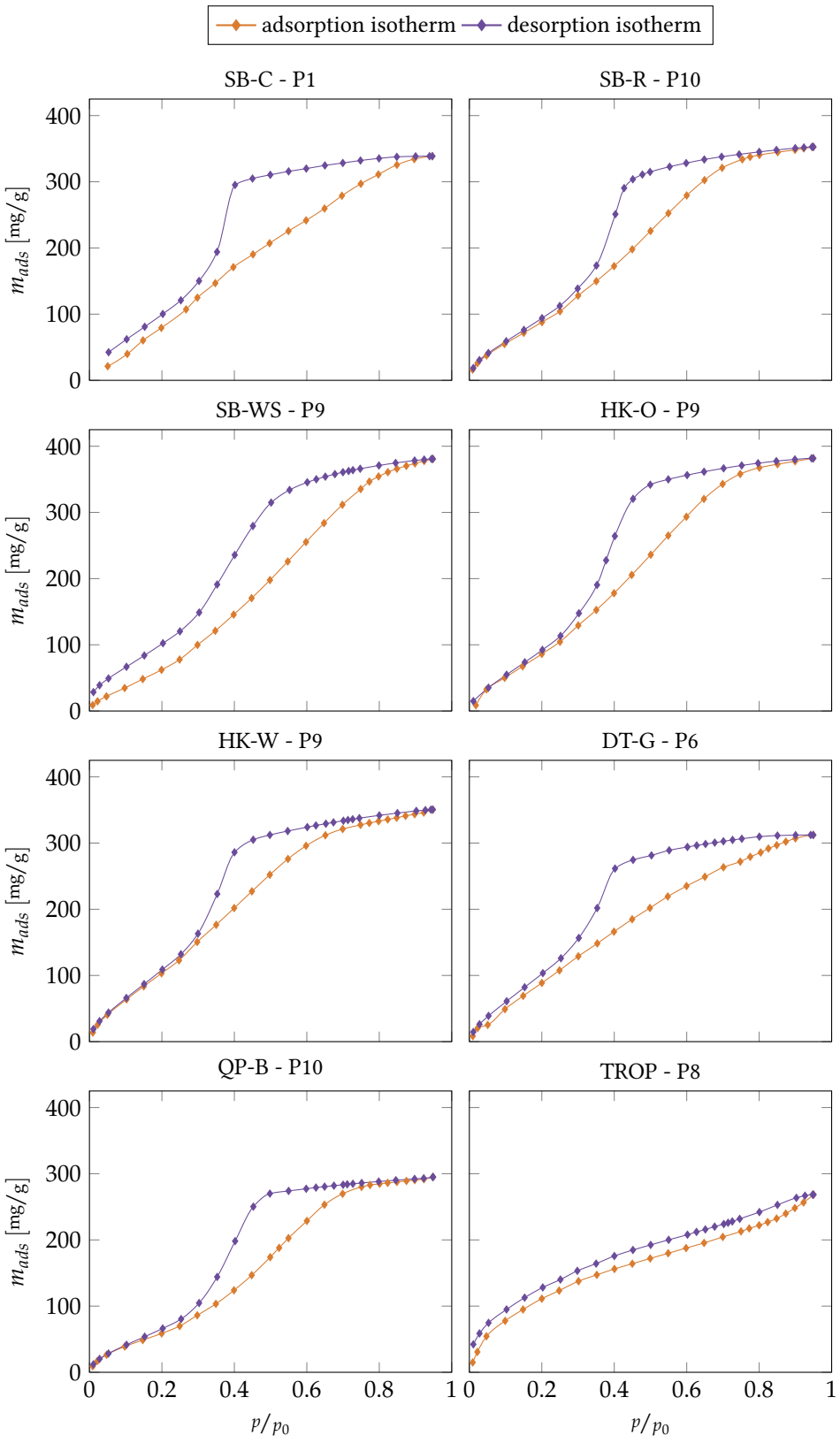

Figure 53: Compilation of H_2O-isotherms measured on the *Autosorb* device at 30 °C.

4.2.2.2 *Enthalpy of Adsorption*

As mentioned already in Section 2.4.3, the enthalpy of adsorption is of great interest to quantify the amount of energy that is needed to regenerate the adsorbent. All modern adsorption analysis instruments usually provide a software option to automatically calculate the enthalpy of adsorption [62, 147]. However, since the measurements were done on different instruments and the underlying algorithms were unknown, it was decided to do the calculations separately - especially since the theory has already been outlined and the method is not too extensive. In this section, the enthalpy of adsorption is calculated from Eq. (2.4.32). To apply this method, two isotherms at different temperatures T_1 and T_2 need to be available. Within this section, we will assume that $T_1 > T_2$. The theoretical principle is illustrated in Fig. 54. Isosteres are represented as horizontal lines here. The isosteric enthalpy of adsorption q_{st} is calculated using the intersections between isosteres and the two isotherms.

It is noteworthy that, in this case, it is required to use the absolute pressure data from both isotherms ($p_{1,i}$ and $p_{2,i}$) at a given adsorbed volume, instead of the otherwise mainly used relative pressure p_i/p_0. In the latter case, the calculated enthalpy of adsorption would be too low - by exactly the absolute value of the enthalpy of vaporization of the adsorptive Δh_{vap}. Another issue with this method can be seen from Fig. 54 - for low adsorbed amounts, the pressure differences are very small - this leads to a high susceptibility towards errors in this region. Also, some practical issues needed to be accounted for: First, the isotherm measurement points are recorded at given relative pressures - it is not feasible to preset a desired adsorbed volume. Each of those relative pressures naturally corresponds to different adsorbed volumes when recorded at different temperature. This means, that the adsorbed volumes do not match, and at least on one isotherm, the corresponding value has to be found from approximation. To account for this behavior, a small algorithm was designed that uses linear interpolation between two points of the T_1 isotherm and then finds the corresponding, interpolated value on the T_2 isotherm. The approach is illustrated in Fig. 55a. Second, while it is not strictly necessary to interpolate on both isotherms, it was found that this approach avoids an issue where computation errors occurred in case the first value of the T_1 isotherm was smaller than the first value of the T_2 isotherm: Since they are very close to each other numerically, averaging between the first and second measurement point led to successful computation.

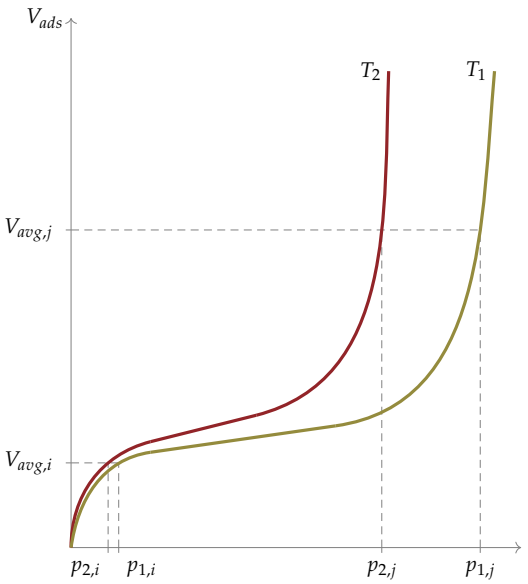

Figure 54: Two isotherms T_1 and T_2, plotted with V_{ads} as a function of absolute pressure p.

Enthalpies of H_2O-adsorption were calculated for all samples where two isotherms were available. Since the measurement times for one complete isotherm was quite long, this was not possible for all samples. A pre-selection was therefor done to cover those materials that exhibit different properties. At least one sample from each group was selected. The first temperature value was chosen according to the real-life operating conditions of the dehumidification process at T_1 = 30°C. For the second value, T_2 = 20°C was chosen with the application in mind, but also in accordance with literature [45], where a temperature difference of 10 K is recommended. Mean and average values are given in Table 24, and in Figs. 56 and 57 the enthalpy of adsorption is plotted as a function of adsorbed volume. Plotted along with the calculated isosteric enthalpy of adsorption is the standard enthalpy of condensation of the adsorptive (H_2O) at 30 °C, which, as hinted above, the q_{st}-plot asymptotically

Table 22: Selected values from the adsorption isotherm data at 30 °C presented in Section 4.2.2.1 (linear interpolation where necessary).

		p/p_0									
Sample	OGP	0.1	0.2	0.3	0.35	0.4	0.5	0.6	0.7	0.8	0.9
Autosorb - m_{ads} [mg/g]											
SB-C	P1	39.9	81.5	127.8	152.0	173.4	209.2	243.2	280.8	312.2	334.8
SB-R	P10	57.2	90.5	129.4	150.0	176.7	227.3	283.1	322.4	341.1	348.5
SB-WS	P9	36.4	64.8	101.9	122.5	150.2	199.9	260.3	313.1	356.4	374.3
QP-B	P10	40.3	60.5	88.0	104.0	127.7	175.9	232.1	270.4	285.1	290.5
DT-G	P6	51.7	92.0	130.1	147.6	169.6	203.6	237.3	263.7	286.5	307.4
HK-O	P9	51.9	88.2	129.0	155.6	180.2	239.9	294.6	344.9	368.5	377.5
HK-W	P9	64.6	106.9	153.6	176.8	206.0	254.3	298.8	321.6	333.8	343.8
PROS	P8	58.6	89.0	124.2	143.1	168.4	217.7	271.0	316.4	359.8	389.3
ARTS	P3	83.0	121.3	155.9	171.1	184.3	206.0	242.4	287.1	363.3	466.3
TROP	P8	79.8	113.6	138.1	147.1	157.4	172.7	189.1	205.0	223.5	249.5
TC-7	P3	39.8	60.4	82.1	91.4	103.2	126.0	151.7	184.4	248.3	539.8
TC-8t	P4	57.6	88.6	120.1	132.2	146.5	169.7	197.4	230.7	287.6	638.9
Belsorp - m_{ads} [mg/g]											
TC-1	P2	44.5	72.7	99.9	113.7	127.5	155.6	186.1	222.3	415.4	667.2
TC-5	P2	46.3	81.5	115.6	131.9	147.9	178.4	210.1	248.8	530.3	698.2
TC-7	P2	45.5	75.3	104.1	118.7	133.2	162.1	192.9	231.2	516.9	679.0
TC-1	P1	53.5	86.7	119.7	136.5	152.7	186.1	222.5	272.6	625.3	674.8
TC-5	P1	57.0	95.4	131.3	148.7	164.8	197.7	233.9	283.5	648.9	692.4
TC-7	P1	51.7	83.9	115.2	131.1	146.7	178.7	213.9	263.0	617.7	666.9
TC-4	P3	46.2	82.1	118.4	136.2	153.3	186.8	221.3	262.3	397.9	749.6
TC-8	P3	46.0	81.0	115.4	132.2	148.4	179.5	211.5	249.3	446.4	701.4
TC-2	P4	45.8	76.1	104.8	119.2	133.5	161.8	191.9	229.5	514.3	654.7
TC-3	P4	46.5	82.2	117.0	133.9	150.2	181.4	213.5	251.7	468.9	702.8
TC-6	P4	44.8	74.4	102.8	117.3	131.5	159.7	190.4	228.7	525.2	660.2
TC-4	P3	54.7	91.6	126.8	143.7	160.1	192.9	229.7	282.8	635.8	676.0
TC-5	P3	54.4	85.4	116.3	131.6	146.5	176.3	209.5	264.9	578.3	619.3
TC-8	P3	53.1	89.1	123.2	139.2	154.9	185.6	219.0	267.2	598.5	648.6

Table 23: Selected values from the adsorption isotherm data at 20 °C presented in Section 4.2.2.1 (linear interpolation where necessary).

		p/p_0									
Sample	OGP	0.1	0.2	0.3	0.35	0.4	0.5	0.6	0.7	0.8	0.9
Autosorb - m_{ads} [mg/g]											
SB-R	P10	66.3	105.5	142.3	163.1	188.9	233.8	295.1	327.6	341.1	348.2
SB-WS	P10	52.1	84.9	116.1	132.9	153.8	190.0	245.2	285.2	318.0	331.9
HK-O	P9	61.7	100.0	140.2	162.8	192.6	246.0	319.2	357.7	373.2	381.8
HK-W	P9	63.1	106.7	148.9	171.2	198.5	242.9	294.6	315.4	326.7	335.3
PROS	P7	49.5	78.7	107.3	123.3	141.6	178.7	235.8	278.1	321.6	346.6
TROP	P8	85.0	116.0	138.1	146.9	156.4	170.4	187.9	203.7	223.5	248.7
Belsorp - m_{ads} [mg/g]											
TC-1	P3	57.6	90.1	121.9	137.7	153.0	184.9	219.5	275.1	618.0	649.4
TC-5	P3	63.1	100.6	135.5	151.7	166.9	198.6	234.5	293.8	642.6	671.8
TC-7	P3	56.4	88.5	119.7	135.0	150.1	181.0	216.1	271.0	621.2	652.9
TC-4	P6	59.8	96.1	129.6	145.7	161.1	192.2	228.0	284.8	634.1	663.3
TC-5	P6	57.0	91.0	122.1	137.0	151.2	180.1	213.2	270.6	587.4	619.1
TC-8	P6	55.7	91.4	123.7	138.9	153.4	182.8	214.8	265.2	584.9	629.0

approaches at higher adsorbed volume. This behavior is expected from the theory of multilayer formation, as described in Section 2.4.4. As mentioned in Section 2.4.3, an ideal desiccant would adsorb large amounts of water, while requiring little energy for regeneration. For the silica gels under investigation, the enthalpy of adsorption is expected to exhibit the following behavior: At low relative pressures and low adsorbent coverage ($m_{ads} \leq 100\,\mathrm{mg/g}$), a high enthalpy of adsorption is observed, which quickly decreases during the formation of higher layers and ultimately capillary condensation. With increasing adsorbed mass m_{ads}, the enthalpy of adsorption approaches the enthalpy of vaporization of pure water - a behavior that is explained by the previously described adsorption models.

Most of the results presented in Fig. 56 (*SB-R*, *HK-O* and *TC-7*) and Fig. 57 (*TC-1*, *TC-4*, *TC-5*, *TC-7* and *TC-8*) are consistent with this expected behavior. The "knee" occurring at high coverage corresponds to the transition from capillary condensation to surface adsorption, here, the enthalpy of adsorption should correspond to the enthalpy of vaporization over a free water surface. Deviations are the result of error propagation from measurement inaccuracies.

For the commercial silica gels, also the numerical values for calculated averages (see Table 24) correspond with those found in literature. For unstructured silica gels the reported enthalpy of adsorption ranges between 2.43 kJ/g to 2.8 kJ/g [126, 148, 149]. However, average values are of very limited significance - the high enthalpy values in the low coverage region distort the calculated result drastically. There may be some merit to using arithmetic means if materials of identical characteristics are compared, but even then, the boundaries between which $q_{st,avg}$ is evaluated would be required to match exactly. Even small variations of the lower limit already lead to large differences, as evident from the *SBA-15* plots and the corresponding averages in Table 24. The samples *SB-WS* and *PROS* both produced erroneous results. Although the enthalpy of adsorption is within the anticipated order of magnitude, *SB-WS* shows very high q_{st}-values at low coverage, quickly dropping to values below that for pure water. *PROS* constantly exhibits values lower

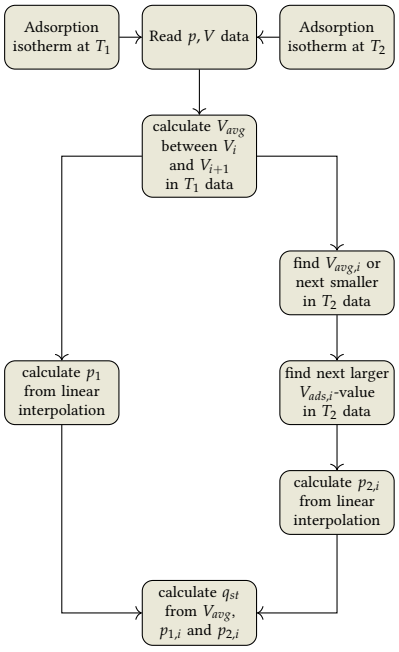

(a) Flowchart to calculate the isosteric enthalpy of adsorption from two isotherms.

		V_{ads}		q_{st} [kJ/g]		
Sample	Dev.	min	max	max	min	avg
TC-7	AS	39	676	3.052	2.491	2.577
TC-8t	AS	33	801	2.944	2.283	2.523
SB-R	AS	26	437	4.541	2.388	2.919
SB-WS	AS	23	472	6.337	1.909	2.710
HK-O	AS	26	472	4.818	2.665	2.923
HK-W	AS	24	433	1.838	2.286	2.232
PROS	AS	35	487	0.942	1.895	1.743
TROP	AS	28	327	2.584	2.373	2.497
TC-1	BS	30	803	4.388	2.295	3.037
TC-4	BS	36	820	3.067	2.250	2.539
TC-5	BS	29	847	5.051	2.080	2.990
TC-7	BS	30	839	4.342	2.131	2.867
TC-8	BS	35	729	2.776	2.405	2.478

(b) Minimum, maximum and average values of the isosteric enthalpy of adsorption, measured on *Autosorb* (AS) and *Belsorp* (BS) devices.

Figure 55 & Table 24: Calculation method and results therefrom of the isosteric enthalpy of adsorption.

than the enthalpy of vaporization of pure water. An explanation can be found in the rather poor quality of the corresponding isotherm measurement, which has been discussed in the respective Section 4.2.2.1. The applied method for the calculation of q_{st} is inherently susceptible to small errors in the measurement of a certain adsorbed amount. These lead to large errors in the calculation of the isosteric enthalpy of adsorption according to Eq. (2.4.32). This is due to the small pressure difference between the two isotherms, especially at low adsorbent coverage, illustrated in Fig. 54. *TROP* exhibits a rather stable q_{st} over the entire adsorption range, pointing to the lack of high-energy adsorption sites. The absence of capillary condensation has already been discussed in the context of adsorption isotherms. Although this behavior seems reasonable, the results need further evaluation if *TROP* was to be considered for the dehumidification process: the Clausius-Clapeyron-method used to calculate the isosteric enthalpy of adsorption is strictly valid for reversible processes only, and some of the structural changes in the montmorillonite are irreversible.

4.2.3 *Thermal Analysis and Mass Spectrometry*

4.2.3.1 *Thermogravimetric Analysis and Mass Spectrometry*

The samples underwent TGA measurements using the temperature profile given in table Table 15. Before each batch, an empty crucible was measured to obtain a *blank curve*, a baseline value which is then deducted from the actual signal to account for the crucible itself. The same method was applied for the mass spectrum, where the blank baseline signals were subtracted to eliminate, for example, impurities of the carrier gas or background noise.
Evolved gas was passed through the mass spectrometer, and due to the devices being synchronized, the time stamps of the measurements are consistent. The ion currents can therefore be plotted directly below the TGA diagram, which allows to conveniently match thermogravimetric events and their reaction products, should they occur. The TGA-plots show relative mass of the sample

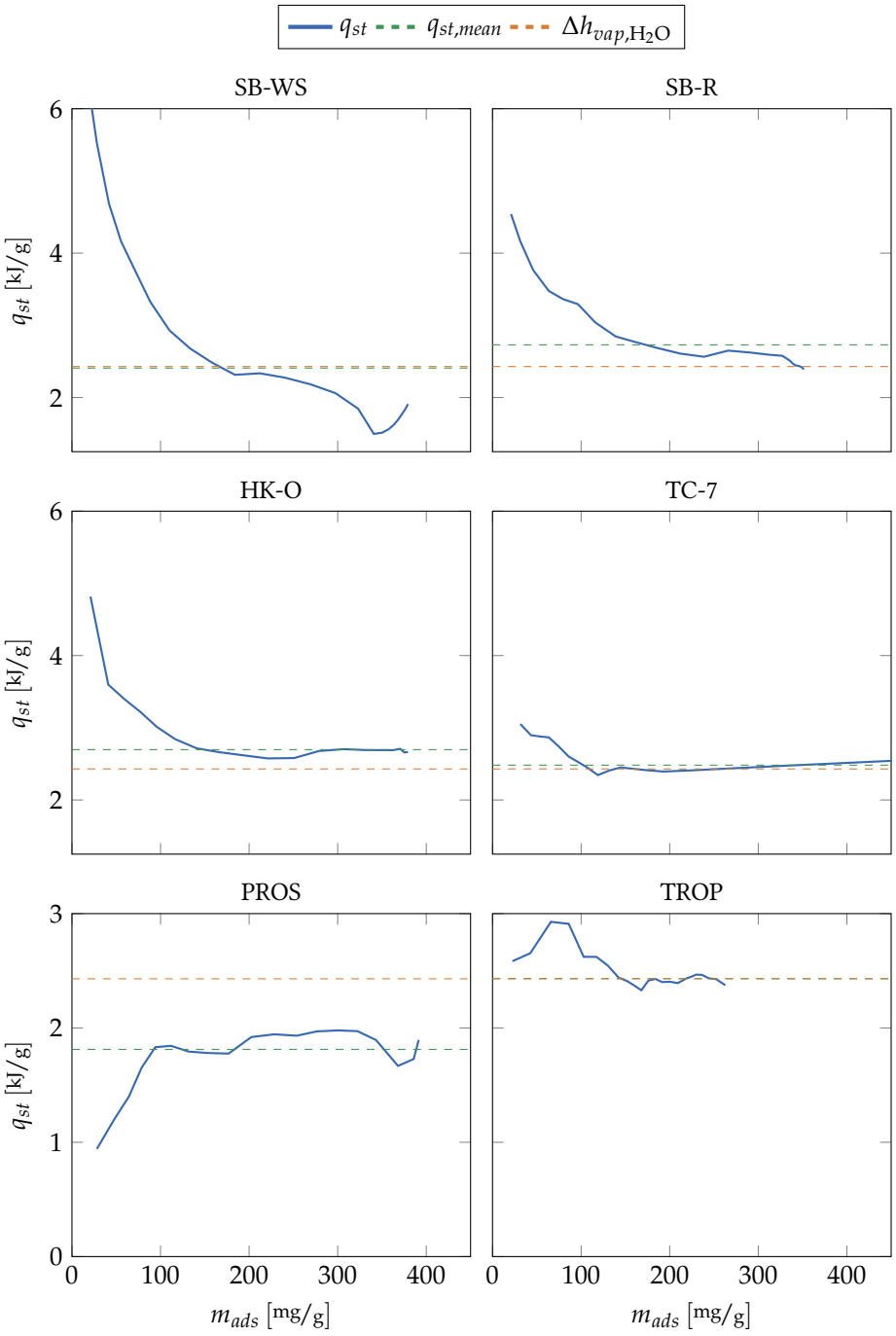

Figure 56: Isosteric enthalpy of adsorption as a function of adsorbed water m_{ads}. The enthalpy of condensation for pure water at 30 °C (2.43 kJ/g) is plotted in orange for reference.

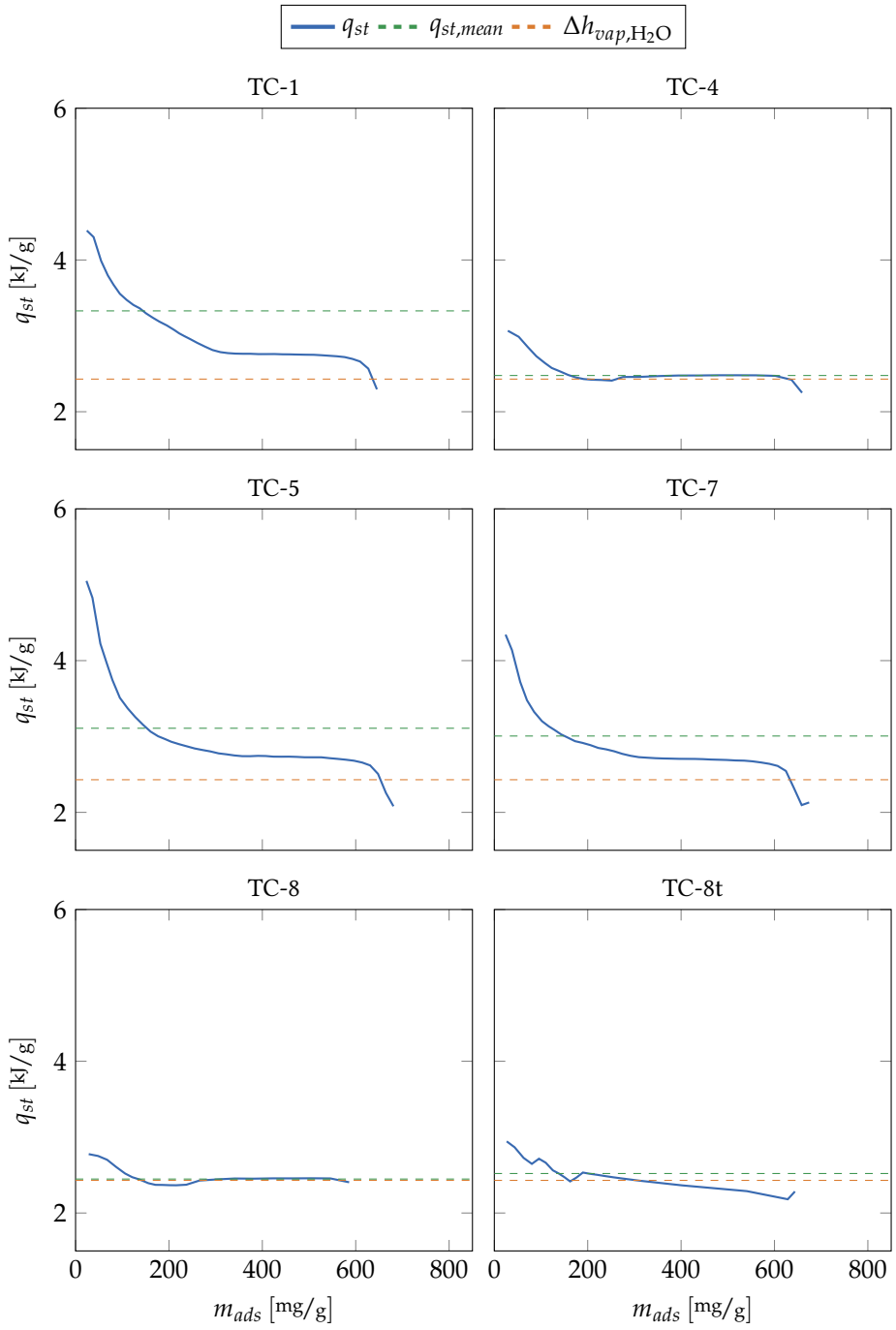

Figure 57: Isosteric enthalpy of adsorption as a function of adsorbed water m_{ads}. The enthalpy of condensation for pure water at 30 °C (2.43 kJ/g) is plotted in orange for reference.

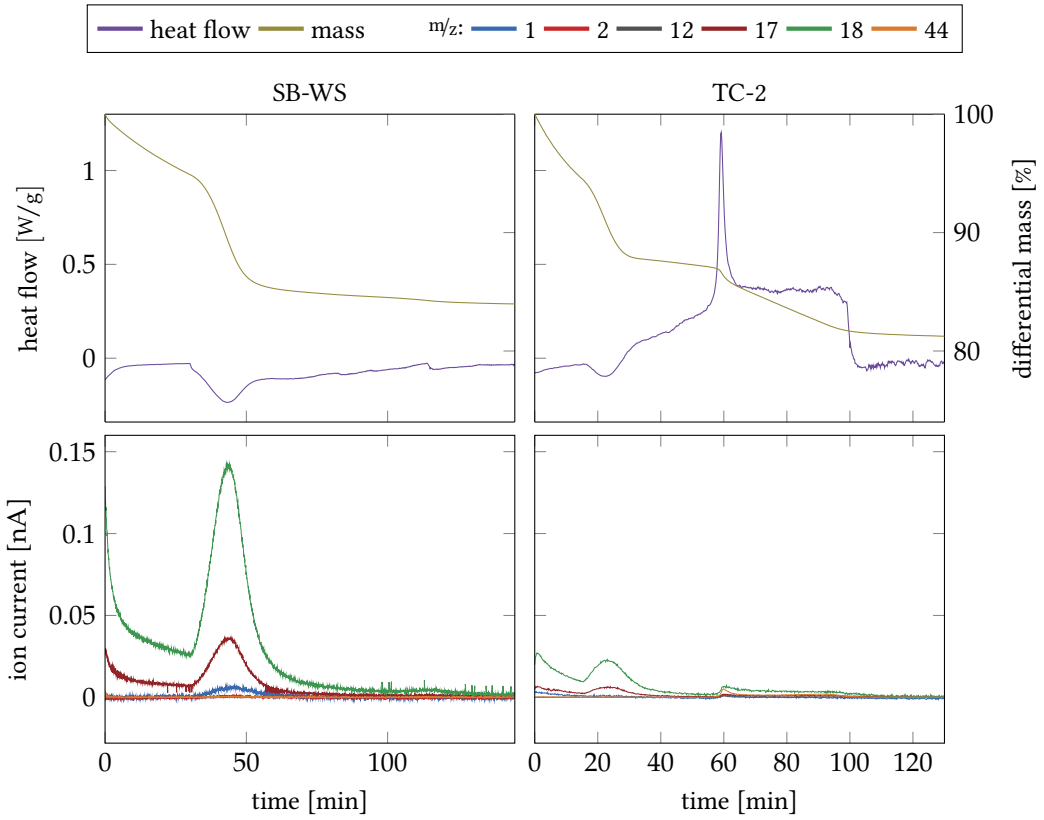

Figure 58: Examples of thermal analysis results for a commercial silica gel (*SB-WS*) and an *SBA-15* sample (*TC-2*).

and the heat flow. In the latter, endothermal (negative) peaks point to desorption of water, exothermal (positive) peaks to combustion phenomena. This is supported by the appearance of possible combustion products in the mass spectrometry plots. Fig. 58 shows two examples of measurement results for a commercial silica gel (*SB-WS*) and an *SBA-15* sample (*TC-2*). The full set of result plots is found in Appendix A.4. The TGA/MS measurements constitute an important part of the overall characterization process: Since not all samples could be investigated during N_2- and H_2O-adsorption measurements due to the long analysis time, a pre-selection had to be conducted. In general, the TGA method can be applied to sort different adsorbents according to their maximum adsorption capacity, by simply keeping them in the same, humid atmosphere for an extended period of time, and then measuring the desorbed weight. This, of course, is only applicable to reversible physisorption processes, and is not an accurate characterization procedure, as the end of the adsorption process is not measured. However, if the compared materials are similar enough, this method allows for a quick sorting into a priority series for subsequent, more time-consuming measurements. Besides this very practical purpose, important insights into the thermal behavior during heating can be gained from thermal analysis. The most important ones being appropriate regeneration temperatures and the onset of adsorbent degradation.

For the commercial silica gels (Figs. 83 to 85), the remaining mass is between 76 % to 84 %, with most of the change occurring between the initial conditions at 25 °C and 170 °C (after ca. 60 minutes). This is caused by the desorption of water, as indicated by the corresponding endothermal peak in the heat flow plot and supported by the appearance of ion current peaks for both m/z ratios of 17 and 18 (pointing to OH and H_2O, respectively). This step is followed by a less steep decrease, resulting from the decomposition of silanol groups at temperatures above 200 °C (after 65 minutes) [150].

For four samples (*SB-C* in Fig. 83, *SA-T2* and *TROP* in Fig. 84, and *DT-B* in Fig. 85), a rise in heat flow is observed after the first desorption step, which points to an exothermal process. However, no reaction products are observed with the present mass spectrometer settings. The relative mass change does not differ from the other samples, the rise in heat flow must therefor be caused by other reasons. Phase changes or oxidation reactions with the carrier gas are possible, although unlikely, as the chemical composition of the silica gel samples is very similar. The phenomenon is also not confined to a specific group, it is observed in both indicating and non-indicating materials. The latter considerations do not include *TROP*, since the exact structure is not known. Overall, the origin of the exothermal heat flow must be considered inconclusive for all the samples in question. During the analysis of *QP-B* (Fig. 83), an unknown error caused a lost data connection to the mass spectrometer, therefor, no ion current data exists after 59.6 minutes.
Figs. 86 and 87 show the batches of *SBA-15*, which are virtually identical in their behavior, as is expected due to their identical synthesis parameters. Up to temperatures of ca. 200 °C, occurring here at 50 minutes due to the different heating profile, the behavior is the same as in the previously discussed commercial samples. The main difference is that the ion current signal is about an order of magnitude lower, since the samples were already dry. Of significant interest is the heat flow peak that occurred at around 240 °C and was accompanied by peaks in the MS spectrum that could match CO_2 and H_2O - pointing to a combustion reaction of an organic compound. This likely originates from residual templating agent that was used during the synthesis of the *SBA-15*-type materials, as has been observed before [151]. This decomposition reaction goes on until the analysis is stopped at 450 °C (after 100 minutes), where it abruptly ends. During this interval, smaller amounts of reactants are generated and the sample mass diminishes further. In some analyses, even for the same sample, a shift can be observed in the maximum heat flow peak - both for desorption and decomposition reactions. These shifted peaks can be explained by a difference in sample mass: in larger samples, they appear to come later due to delayed heat-up.
Although it was not at the core of this project, a thermally treated *SBA-15* sample (*TC-8t*) was prepared. The goal was to obtain a sample with the residual templating agent completely removed. In order to limit damage to the structure, the temperature was raised to just beyond the observed peak of the combustion phenomenon. It was carried along throughout all following analyses to further investigate the behavior. Any deviations in its properties would have been detected. However, the observed alterations during both N_2- and water vapor adsorption experiments were minor; they are discussed in the respective sections.

4.2.3.2 *Specific Heat Capacity*

The specific heat capacities have been calculated for several sample materials according to the method described in Section 3.3.4. One batch consisted of up to six samples. Considered are the measurements at 30 °C and 60 °C, the average in this interval is also calculated. The values for c_p are compiled in Table 25.
Since the specific heat capacity in this case has been calculated from heat flow data, the different water content causes a large difference in the measured values. The observed c_p is smaller for the *SBA-15*-type samples, as they had much less water adsorbed onto them. For the commercial gels however, the measurements are quite in line with the findings from [126]. Overall, these results constitute a decent indication, but the variations between them are too high - if an adsorption dehumidification system were to be designed based on one of the investigated materials, the measurements should be repeated in order to obtain higher precision and accuracy. Especially the large differences in the measured values among the *SBA-15*-type samples indicate that the applied method needs further refinement. Possible mitigations include adjustments to the form and size of the samples, as well as adaptations to the heating profile and pre-treatment procedure.

Table 25: Specific heat capacity (c_p) at 30 °C and 60 °C, obtained from DSC analysis.

	Specific heat capacity $[\mathrm{kJ/kg\,K}]$		
Sample	$c_{p,30°C}$	$c_{p,60°C}$	$c_{p,avg}$
TC-2	0.2967	1.2056	0.7511
TC-3	0.2965	1.0926	0.6946
TC-4	0.3304	1.3582	0.8443
TC-5	0.0893	0.4316	0.2604
TC-6	0.2557	1.0365	0.6461
TC-7	0.1502	0.5842	0.3672
TC-8	0.3023	1.3344	0.8183
TC-5	0.1918	0.8247	0.5082
SB-C	0.5887	1.6141	1.1014
SB-R	0.7303	1.9549	1.3428
SB-WS	0.5989	1.6586	1.1288
HD-O	0.9403	2.7672	1.8538
QP-B	0.6415	1.4715	1.0565
DT-B	0.5870	1.7306	1.1588
SA-O	0.7436	2.1283	1.4359
SA-T2	0.5887	1.4330	1.0108
FL-36	0.7724	2.2324	1.5024
GN-1	0.9702	2.9041	1.9372
TROP	0.4704	1.1045	0.7875

4.3 OPEN SYSTEM MEASUREMENTS

The open system measurements were performed with the setup described in Section 3.4. The term *open* refers to the fact that the system is in direct contact with the ambient atmosphere. While the overall aim was to understand all facets of the performance of a desiccant in a cyclically operated, open system, the individual aspects will be addressed in separate paragraphs for the sake of clarity: After a few general remarks and an introduction into the data acquisition procedure, the different topics consist of adsorption performance, desorption performance, the system's cooldown behavior, pressure drop and the performance of auxiliary components.
From a practical standpoint, it can be said that the functionality of the open system test stand was rather difficult to control, as many settings had to be simultaneously monitored and adjusted manually. The *Memmert* oven, together with the ultrasonic evaporators, provided a sufficient atmosphere generation. However, the water content of the intake air was difficult to maintain at a precise level, especially at high preset humidity and low air flow rates. While the input temperature is perfectly stable, the input humidity was regularly subject to low-frequency fluctuations, with a prominent ramp-up first, before a somewhat stable plateau is reached. Although the oven chamber was equipped with a fan, this issue is probably caused by insufficient mixing within the chamber. In future setups, this could quite easily be met by using a larger chamber. Another shortcoming of the present setup was the necessity to open the atmosphere generation chamber's door to refill the water reservoirs - sometimes while the experiments were running. These events can be seen (e.g. in Figs. 61, 100 and 128) as downward spikes in the input humidity signal, representing the drop in humidity caused by the ingress of dry, ambient air from the laboratory environment. The spike is usually preceded by a decline in inlet humidity, resulting from one (or both) jars running low on water. This issue, again, can be overcome with a larger chamber and more (or larger) evaporation units.

4.3.1 *Measurements and Data Acquisition*

The measured values in the open system test stand were recorded as described in Sections 3.4.7 and 3.4.8. Although all signal channels were permanently logged, the ones not relevant for either adsorption or desorption measurements were omitted in the respective plots to improve readability. To evaluate the measurements, a *MATLAB* program was written that performs all operations from signal treatment to thermodynamic calculations. The results presented in this section are all generated by this program, which is documented in Appendix B.

During initial operation trials after assembly, a erroneous signal was found in one humidity sensor's output, namely sensor no.1, ID 96 at the outlet of adsorber *Box 1*. Under idle condition of the test stand, the humidity values of all sensors are expected to be identical and to correspond to the humidity of the laboratory's atmosphere. However, the sensor in question produced spikes in the positive voltage direction. These outliers were random in appearance, but consistent in their magnitude. The erroneous readings were up to 40 times higher than the baseline value, which itself was coherent with the expected value. The latter was determined by comparing the measurement to a calibrated *Ahlborn FHAD 46-41* humidity sensor. It was thus determined that the error could be corrected through signal treatment. Therefor, a mathematical filter is applied to correct the measurement signal during data evaluation. The function of this filter is as follows:
In a first step, a suitable baseline is identified that represents the measurement generated by "'true"' readings, i.e. values that are not outliers. As mentioned before, this is relatively easy because outliers are only present in one direction. After manual examination of the readings, it was found that a signal spike occurs at an average frequency of one in three measurements. This behavior makes a moving median filter a suitable choice for a reference. The challenge in median filtering is the choice of the filter order, meaning the number of data points over which the median is calculated. If it is chosen too low, outliers are not reliably identified, but if it is chosen too high, the filter becomes less

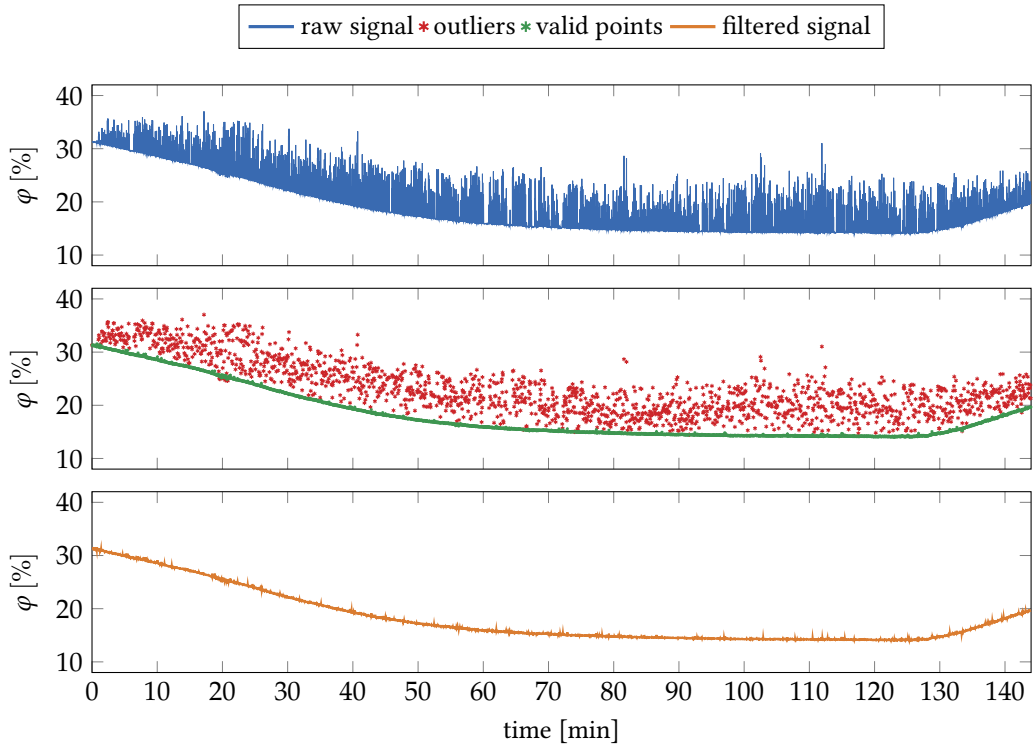

Figure 59: The signal filtering procedure on sensor H1. Outliers are identified and replaced by linear interpolation.

sensitive. This can go as far as that the filter smooths out signal variations that actually represent valid measurements. A good indicator towards a suitable filter order is the percentage of data points that have been removed during filtering: if it remains roughly constant when increasing the filter order, an increase in the filter order yields no further benefit. From this analysis, a moving median over 30 consecutive data points was deemed suitable. With a measurement resolution of 1.57 s, this means a time interval of 47.1 s. With the characteristics of the adsorption process, and taking into account the sensor response time of 5 s, this filter provides good accuracy at sufficient sensitivity. In the second step, the definition of an outlier is established. The sensor manufacturer's datasheet [152] states a repeatability of 0.5 % rh. This means, that at constant conditions, the measured value should be within $\pm$ 0.5 % rh when compared to the previous reading. It is not to be confused with the accuracy of the sensor, which is defined as the deviation of the measured value from the true value. The sensor accuracy is specified at $\pm$ 3.5 % rh. The repeatability is thus used to define an abnormal signal spike: if a measurement deviates more than 0.5 % rh from the median filter, it is marked as an outlier. In a third step, the outliers are removed from the data set. It is noteworthy that the median filter only serves as a reference - the evaluated signal consists of the original data points. Where an outlier was removed, it is replaced by linear interpolation between the preceding and following point to keep the dimension of the data set constant. In a final step, the corrected readings were compared to the calibrated *Ahlborn FHAD 46-41* and found to be well within the accuracy band of $\pm$ 3.5 % rh as specified by the manufacturer.
It was later discovered that during the course of experiments, the error diminished. After a few weeks, the sensor did not produce the outliers anymore. Instead, it returned to its specified operating parameters. This behavior is likely attributable to a contamination on the sensor. It had probably been introduced during assembly of the test stand, and was later removed during regular maintenance. Since the signal filtering process in no way affects a correct signal, it was left in place.

4.3.2 *Adsorption and Desorption Measurements*

The open system test stand was set up according to the description in Chapter 3. Measurement results are presented and discussed here. Before the adsorption reactors were loaded, some of the sample materials were sieve-sorted to obtain a defined particle size distribution - this procedure is described in Section 3.1. Others came pre-sorted by the manufacturer, with a given particle size distribution that could be directly used. The packed beds were weighed in fully dried condition with a *Kern PCB 6000-1* laboratory balance. Subsequently, all samples of which enough material was available underwent the same testing procedure, often several times under slightly modified conditions. Most significant changes were, for example, modified regeneration temperatures or different air flow rates. Table 27 gives an overview of the samples and the amount used. In this context, *SB-WS* stands out: even though the same volume was loaded as for other samples, it's total weight is significantly lower due to its lower density. This is consistent with the manufacturer's data sheet [153], which also lists a density that is 12.5 % lower than for the other *Sorbead*-type desiccants. Air flow rates were measured initially for a variety of samples in both adsorption reactors, using a hot wire anemometer. The readings were rather unstable at first, and the hand-held device had to be fixated in a defined position in order to obtain reproducible measurements. The locations chosen were the exhaust port and the outlet of the air cooler. The values were virtually identical for all samples investigated here, which is not surprising: due to the sieve sorting of the sample material, the same pellet diameters are selected, although probably with slightly different distributions. This leads to the same pressure drop over the packed bed, and consequently, with the other conditions constant, to an equal air flow rate. In some cases, adsorption experiments were run with reduced blower speeds. Due to unavailability of the anemometer that was used to measure the initial air flow, the air flow rates for these measurements had to be calculated using the blower characteristics diagram in Fig. 41b, and the affinity laws for fans. The latter can be found in various ways, for example through dimensional analysis using Buckingham's π-theorem [154], or derived from fundamental fluid mechanics [155]. At constant impeller diameter, the following relations for volume flow $\dot{V}_i$, attainable pressure drop Δp_i and fan power P_i are valid if the initial rotational speed n_1 is changed to a different speed n_2:

$$\frac{n_1}{n_2} = \frac{\dot{V}_1}{\dot{V}_2} = \left(\frac{\Delta p_1}{\Delta p_2}\right)^{\frac{1}{2}} = \left(\frac{P_1}{P_2}\right)^{\frac{1}{3}}, \tag{4.3.1}$$

From Fig. 41b, the non-linear correlation between fan speed and PWM signal level can be obtained: a reduction of the PWM signal to 50 % results in a reduction in fan speed to 71 % of the original value, setting the PWM signal to 25 % reduces the fan speed to 47 %. For the approximate calculation of the blower's power consumption, the simplifying assumption of a constant blower efficiency is made. In reality this is not the case, and thus the calculated pumping power of the fan P_i will slightly differ from the electrical power consumption at different fan speeds. The resulting values for the different operating scenarios are tabulated in Table 26. Desorption experiments were always carried out with full blower speed.
To compare the drying performance of the different configurations, the adsorbed mass of water was calculated from the water content reduction Δx_{out-in}. As this value represents the difference in water content per unit mass of *dry* air, the dry air mass flow must be calculated first, using the density of dry air. The latter can be found with the ideal gas law, with the total pressure p, water vapor pressure p_w, and absolute temperature T at a given measurement site:

$$\rho_{air} = \frac{M_{air}\ (p - p_w)}{RT}, \tag{4.3.2}$$

Multiplied with the measured volumetric air flow, this yields the momentary adsorption rate

$$\dot{m}_{ads} = \dot{V}\, \rho_{air}\, \Delta x_{out-in}, \tag{4.3.3}$$

Table 26: Measured and *calculated* fan parameters for different PWM signal settings and valve positions (ads = adsorption mode, des = desorption mode).

PWM [%]	n_{fan} [rpm]	P_{fan} [W]	Mode	$\dot{V}$ $\left[\mathrm{m^3/min}\right]$
100	6850	38.9	ads	0.45
			des	0.98
50	4900	*14.2*	ads	*0.32*
25	3200	*4.0*	ads	*0.21*

Table 27: Dry mass of the samples used in the open system test stand experiments.

Sample	Box	m_{dry}[g]
SB-R	1	1063.8
SB-WS	2	944.0
SB-C	2	1107.8
QP-B	2	1201.2
SA-O	1	1076.6
SA-T2	1	1068.5
HD-W	2	1137.0
PROS	1	1042.8
DT-B	2	1119.7
DT-G	1	1044.3
HK-O	2	1140.1

which is then integrated to obtain the adsorbed mass m_{ads} within a given time interval:

$$m_{ads} = \int_{t_0}^{t_i} \dot{m}_{ads}\, dt. \tag{4.3.4}$$

The integration is carried out numerically using the *MATLAB* software tool. Upper limits t_i for integration are the entire experiment duration t_e, and two characteristic time intervals, t_1 = 60 minutes and t_2 = 30 minutes, which allow a comparison between the individual samples and experimental conditions. The results are tabulated in Tables 28 to 31 and presented in form of the recorded plots. As a convention, *adsorbed* amounts carry a negative sign, since mass is removed from the air flow; *desorbed* amounts are added to the air flow and thus counted positive.

The form of the result plots is as follows: The first graph on the upper left shows the water content x of intake and outlet air. The adjacent plot visualizes the amount of water that is adsorbed or desorbed per minute ($\dot{m}_{ads}$ and $\dot{m}_{des}$, respectively).
The middle plots show the temperatures ϑ_i for inlet, outlet and a few additional measurement points of interest. During adsorption, these are the temperatures at the begin of the transfer line to the air cooler, at the cooler inlet and at the cooler outlet. This allows an assessment of the cooler's performance and the temperature drop between adsorber outlet and cooler inlet. During desorption, the cooler is not in use - instead, the temperature of the exhaust air is measured. As the temperature drop in the valve is negligible due to the short path length, this value should be identical to the temperature measured at the outlet of the packed bed. Alongside the individual temperatures, the difference between inlet and outlet ($\Delta\vartheta_{out-in}$) is shown.

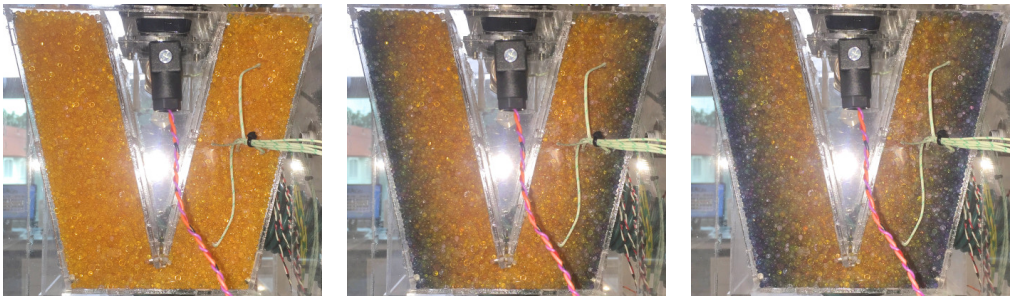

(a) Start of experiment, dry (b) After 16 minutes (c) After 25 minutes

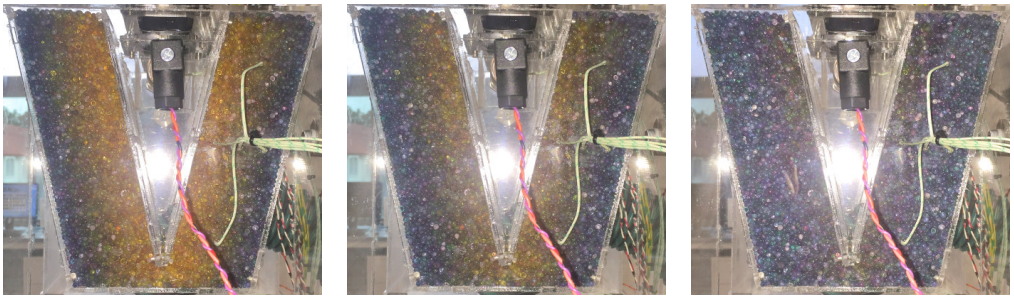

(d) After 29 minutes (e) After 42 minutes (f) After 54 minutes

Figure 60: Progression of indicator color change in *HK-O* during the adsorption process shown in Fig. 65.

The last row shows the pressures measured at both sides of the packed bed. The quality of these pressure measurements must be considered rather poor, as is discussed in the following section in detail. Adsorber *Box 2* was equipped with additional temperature sensors at several positions within the packed bed. Accordingly, the measurement results include an extra plot, compared to those from adsorber *Box 1*. The sensors are labeled *left*, *right* and *center* according to their position in the packed bed when looking at the vessel from the front (as seen, for example, in Fig. 60). The *center* position is further divided in an upper *(top)*, middle *(mid)*, and lower *(low)* measurement site. This set of thermocouples allows to follow the adsorption reaction zone as it propagates through the packed bed. Indicating silica gels also provide a visual hint on the progress of the adsorbent's saturation, however, this can't be considered an accurate measure and is shown in Figs. 60a to 60f for illustration purposes only. The results are grouped according to the respective packed bed reactor they were measured in (*Box 1* and *Box 2*).

Table 28 & Table 29: Adsorbed and desorbed mass of water during the experiments in adsorber *Box 1*.

	Fan	Time	Air flow	Adsorbed mass [g_{H_2O}]			
Sample	[%]	[min]	[m^3/min]	Total	60 min	30 min	Plot
FL-36	100	95	0.45	-51.6	-43.8	-31.6	Fig. 89
SB-R	100	96	0.45	-172.0	-125.4	-68.4	Fig. 91
SB-R	50	65	0.32	-178.3	-169.2	-91.0	Fig. 93
SA-O	100	92	0.45	-303.1	-226.4	-120.0	Fig. 61
SA-O	50	76	0.504	-329.3	-257.2	-119.7	Fig. 62
SA-T2	50	71	0.32	-220.7	-187.6	-88.3	Fig. 96
SA-T2	25	49	0.21	-133.3	n/a	-81.0	Fig. 63
SA-T2	50	69	0.32	-251.7	-224.7	-114.5	Fig. 64
PROS	100	100	0.45	-310.7	-192.6	-96.3	Fig. 100
PROS	50	65	0.32	-236.3	-218.0	-94.8	Fig. 102
DT-G	100	70	0.45	-167.6	-139.3	-50.0	Fig. 103
DT-G	25	120	0.21	-225.2	-122.1	-59.8	Fig. 105

	Time	Air flow	Desorbed mass [g_{H_2O}]			
Sample	[min]	[m^3/min]	Total	60 min	30 min	Plot
FL-36	101	0.98	370.2	315.0	174.9	Fig. 90
SB-R	149	0.98	90.2	152.8	116.3	Fig. 92
SB-R	65	0.98	120.9	121.1	83.9	Fig. 94
SA-O	77	0.885	186.5	180.0	105.8	Fig. 66
SA-O	55	0.98	15.9	n/a	15.8	Fig. 99
SA-T2	76	0.98	67.2	74.7	48.5	Fig. 95
SA-T2	79	0.98	143.2	146.2	83.3	Fig. 97
SA-T2	93	0.98	96.5	110.8	53.4	Fig. 98
PROS	65	0.98	371.7	368.5	187.9	Fig. 101
DT-G	62	0.98	156.9	156.7	96.8	Fig. 104

Table 30 & Table 31: Adsorbed and desorbed mass of water during the experiments in adsorber *Box 2*.

	Fan	Time	Air flow	Adsorbed mass [g_{H_2O}]			
Sample	[%]	[min]	[m^3/min]	Total	60 min	30 min	Plot
SB-WS	100	94	0.45	-99.5	-75.3	-52.6	Fig. 107
SB-WS	50	88	0.32	-149.0	-111.7	-58.2	Fig. 109
QP-B	50	90	0.32	-101.8	-75.0	-41.3	Fig. 112
QP-B	25	144	0.21	-145.3	-77.4	-43.1	Fig. 113
HD-W	100	101	0.45	-285.4	-182.2	-103.2	Fig. 114
HD-W	25	128	0.21	-133.2	-85.0	-48.2	Fig. 117
HD-W	100	80	0.45	-267.6	-187.6	-84.7	Fig. 118
SB-C	100	173	0.45	-550.1	-235.5	-120.0	Fig. 119
SB-C	50	124	0.32	-311.4	-168.4	-87.4	Fig. 121
SB-C	25	160	0.21	-316.9	-130.4	-68.3	Fig. 123
DT-B	100	68	0.45	-217.5	-206.3	-113.1	Fig. 124
DT-B	25	127	0.21	-219.9	-103.1	-48.9	Fig. 126
DT-B	100	91	0.45	-259.5	-174.9	-79.7	Fig. 128
HK-O	100	71	0.45	-352.2	-310.2	-158.3	Fig. 65
HK-O	50	106	0.32	-252.9	-165.4	-96.1	Fig. 130
HK-O	25	203	0.21	-299.6	-104.3	-46.5	Fig. 132
HK-O	100	55	0.45	-147.3	n/a	-92.4	Fig. 134
HK-O	100	89	0.45	-334.7	-244.8	-134.4	Fig. 135

	Time	Air flow	Desorbed mass [g_{H_2O}]			
Sample	[min]	[m^3/min]	Total	60 min	30 min	Plot
SB-WS	64	0.98	51.7	49.7	32.7	Fig. 106
SB-WS	58	0.98	225.4	n/a	160.0	Fig. 108
QP-B	68	0.98	261.5	250.1	154.8	Fig. 110
QP-B	57	0.98	81.2	n/a	47.5	Fig. 111
HD-W	54	0.98	186.0	n/a	141.5	Fig. 115
HD-W	118	0.98	153.4	114.1	54.8	Fig. 116
SB-C	124	0.98	449.2	289.3	142.3	Fig. 120
SB-C	114	0.98	312.5	230.9	123.2	Fig. 122
DT-B	89	0.98	237.3	215.2	121.8	Fig. 125
DT-B	87	0.98	166.7	144.1	64.3	Fig. 127
HK-O	83	0.98	180.4	168.7	76.1	Fig. 129
HK-O	102	0.98	302.3	276.3	141.8	Fig. 67
HK-O	80	0.98	281.6	263.4	135.8	Fig. 131
HK-O	77	0.98	314.5	300.6	215.5	Fig. 133
HK-O	62	0.45	157.9	157.1	119.9	Fig. 68

4.3.2.1 *Adsorption Performance*

The findings on the microscopic level in a closed system are largely consistent with the behavior of the materials in the open system test stand. For seven of the presented samples, enough material was available to conduct all tests. Macroscopic uptake can, for example, be compared by means of the 60 minute value at 50 % fan power from Tables 28 and 30 with the values in Table 22. Of course the different density of the bulk material must be taken into account here (see Table 27 for reference). The maximum uptake values measured during closed system vapor adsorption are not reached in the open process, but the relative performance of the materials is consistent with their relative uptake capacity at high relative pressures of $p/p_0 > 0.85$.
Results from the open system experiments are visualized in five (adsorber *Box 1*) or six (adsorber *Box 2*) grouped plots. Their layout is as follows: In the first row, the x- and ϑ-sections of the result plots can be regarded as *break-through curves* of the adsorption reactor. The break-through curve is an established concept as a measure of the conditions at the end of the adsorption stage. In gas treatment, this curve represents the state of the gas at the outlet of the adsorber, it can be plotted for example for humidity, temperature or concentration of other species. For the case of air drying, water content and temperature are the parameters of highest interest.
As the considered processes are assumed to be adiabatic, the adsorption characteristics for a packed bed are not represented by the adsorption isotherms. The adsorption- and desorption paths can instead be understood as a curve of adiabatic equilibria within the isotherm space - for an in-depth explanation of the underlying theory, the work of Hauer [82] and the book by Ruthven [47] are recommended. In a packed bed of silica gel performing an adiabatic dehumidification process, the largest dehumidification performance is observed at the very beginning of the reaction, with the desiccant fully dried. Due to the high enthalpy of adsorption in the formation of low layers, this is where the largest temperature increase happens. The adsorption path follows a high-temperature isotherm. As the enthalpy of adsorption decreases, the temperature rise also decreases, and the adsorption path intersects with lower-temperature isotherms, until the adsorbent is fully saturated. At this point, the outlet conditions become identical to the inlet conditions. This behavior can be observed in all experiments conducted: the dehumidification process always starts with a sharp decrease in humidity, before assuming a nearly constant phase of dehumidification performance. Towards saturation, the $\dot{m}_{ads}$-plot approaches zero, as the inlet and outlet conditions converge. A corresponding pattern is reflected in the ϑ- and $\Delta\vartheta_{out-in}$-plots, where initially a sharp increase happens as a large amount of heat is released - this is due to the high enthalpy of adsorption at low coverages (see Section 4.2.2.2). As the adsorption reaction progresses, less heat is released per adsorbed unit mass, and the temperature of the dried air flow decreases again. In most experiments, the temperature profile was used as an indicator for decreasing adsorption performance.
From the integration of $\dot{m}_{ads}$, the adsorbed mass of water is obtained. To make results comparable between the individual experiments, the adsorption capacity for a duration of 30 minutes and 60 minutes is considered. If not explicitly stated otherwise, all adsorbed amounts within this section refer to the value after 60 minutes. Generally, a lower air flow leads to lower dew points (i.e. lower outlet water content) for a longer period of time, but the mass adsorbed over a given time frame decreases by approximately the same factor that the air flow is lowered. Within the conducted experiments, this behavior can only be assessed in those experiments that exhibit comparable conditions regarding the progression of intake water content over time - ideally, this should have been the case for all experiments, but due to the difficulties outlined in the introduction to Section 4.3.2.5, was not generally the case. For the adsorption experiments conducted in adsorber *Box 1*, Table 28 lists the results and reveals unexpected behavior in some of them. First and foremost, it can be stated that the silica gels investigated in this series of experiments are anticipated to show a similar behavior: they have similar microscopic properties and were sieve-sorted for the same pellet diameter. Large differences can therefor point to variations in the experimental conditions. In the following, the individual experiments shall be discussed and said variations explained further.

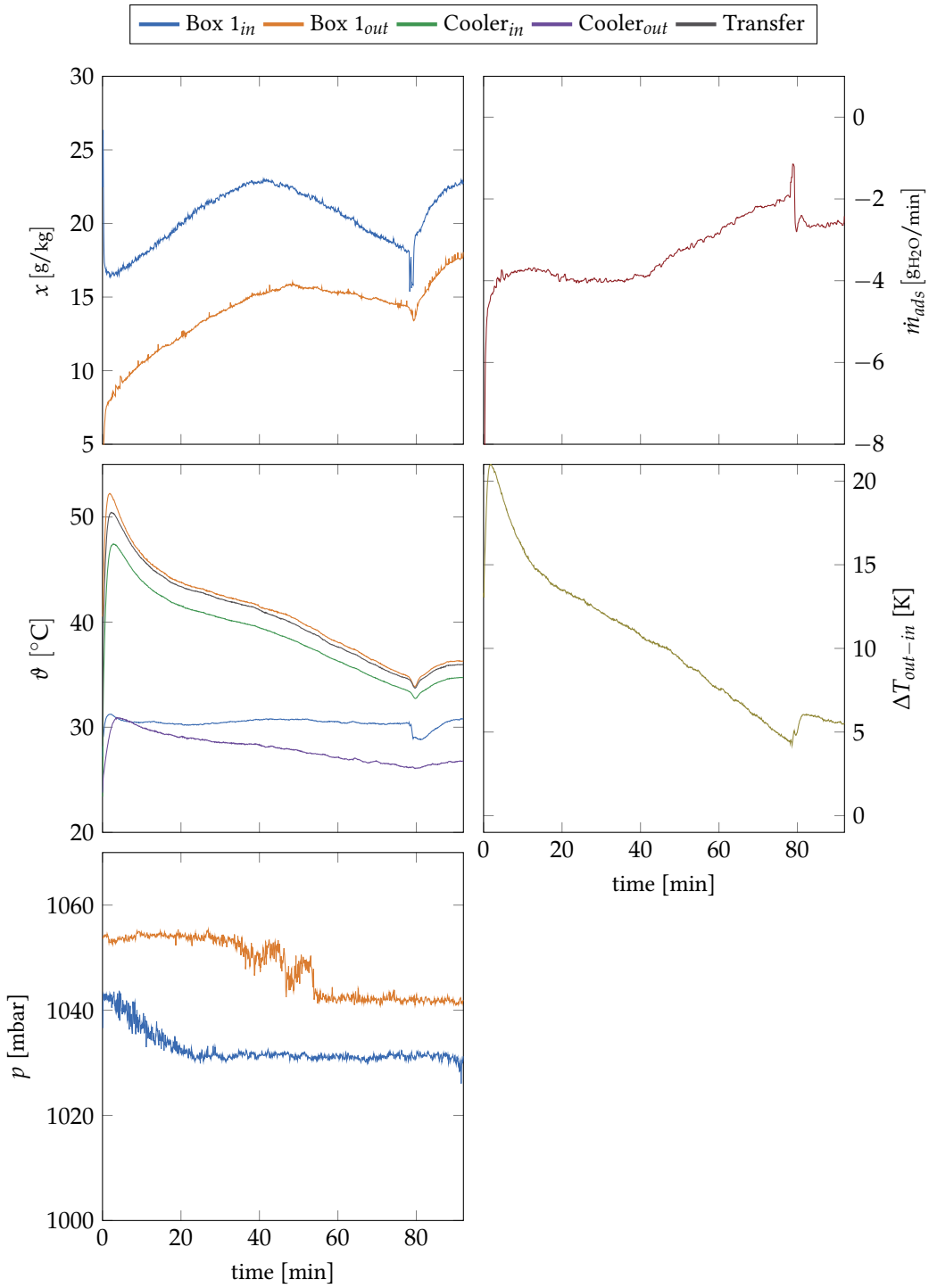

Figure 61: *Box 1* in adsorption mode at 100 % fan power. Loaded sample: *SA-O*

In the interest of coherence and readability, only the most relevant plots are directly included in this section, the remainder can be found in Appendix A.5.
FL-36 (Fig. 89), the very first experiment with the test stand, must be regarded as flawed. A malfunction occurred in the ultrasonic evaporator system, which led to very dry inlet air, producing an erroneous result for the adsorption capacity. During the fault analysis, leaks were discovered and gaskets had to be replaced. The assembly was rebuilt and the ultrasonic evaporators rewired, unfortunately too much of the sample material was lost in the process. The adsorption experiment could thus not be repeated.
The second set of experiments was conducted with *SB-R*, which shows a counter-intuitive behavior: the adsorbed amount with 50 % fan PWM setting is larger than at 100 % - the expected result would be a difference by about the same factor the mass flows differ from each other (as outlined in Section 4.3.2.5, $\dot{m}_{50\,\%}/\dot{m}_{100\,\%} = 0.71$). An explanation can be found when investigating Fig. 91 more closely. Even though most of the initial problems with the test stand had been fixed, two issues remained: The temperature of the intake air was unstable at first, and the humidity levels in the intake air were still too low. The first issue was resolved through adjustments to the *Memmert* oven's air flap position and heating settings. The second issue was mitigated by the addition of a second ultrasonic evaporator and a revised control strategy. After these adjustments, adsorber *Box 1* produced satisfactory results, as seen in Fig. 93. The water content x_{in} of the intake air could still not be held at a stable level, but remains within an adequate range to obtain a meaningful result. Within the first 20 minutes, the air drying performance is strongest with $\dot{m}_{ads}$ reaching a minimum at -3.2 g/min, subsequently decreasing to -2 g/min. This decrease coincides with the outlet temperature approaching the inlet temperature, $\Delta\vartheta_{out-in}$ dropping from an initial maximum of 15 K to 7 K towards the end of the experiment.
The same qualitative behavior is observed in the experiments with *SA-O*, in Fig. 61 a stable dehumidification performance of -4 g/min was present until 40 minutes in, with a subsequent decrease to -2 g/min. This experiment involved the previously mentioned refilling of the evaporator jars. However, the influence of this measure is minimal here: a small spike is observed in both the $\dot{m}_{ads}$ and $\Delta\vartheta_{out-in}$ plots, but they quickly approach the values from before the refilling. This indicates that the maximum saturation at the given conditions had already been reached. A noteworthy aspect is the extraordinarily high outlet temperature at the start of the experiment of 53 °C. This is attributable to the fact that this batch had been dried at 100 °C before being loaded into the adsorber box. After desorption of this desiccant at 60 °C, as was the predominantly used set-point during the open system experiments, the experiment is repeated with the fan PWM setting reduced to 50 %. The effect can be seen in Fig. 62 as a lower outlet temperature of just 40 °C, due to the lower enthalpy of adsorption that is released in a desiccant that is not fully dried.
This confirms two insights that could already been gained from Section 4.2.2.1: fully drying the desiccant provides little benefit over partial drying, as the vast amount is adsorbed during the capillary condensation phase at higher adsorbent coverage. The other effect can easily be overlooked due to the scaling of the plots, but is obvious on closer examination of the x-plots: in Fig. 61, the outlet water content is significantly lower over the first several minutes, than in Fig. 62. This behavior reflects, again, the strong adsorptive forces of the lower layers, which lead to the high enthalpy of adsorption release, and therefor ultimately to a lower achievable remaining water content. In the ϑ-plot for this experiment, one of the shortcomings of the manually actuated setup is visible: The temperatures of both the transfer line and the cooler inlet show a large difference, while both are much lower than the adsorber outlet temperature. This is caused by the outlet side valve being accidentally left in desorption mode for the first 37 minutes, meaning that the outlet air was not channeled through the air cooler, but through the exhaust pipe instead. After switching to the correct position, the temperature sensor on the transfer line assumes the same temperature as *Box 1 outlet* almost instantaneously. The sensor at the air cooler inlet follows the same pattern at a slightly lower level, this is discussed in the following paragraphs of this section. The resulting error regarding the air flow rate was corrected during the calculations for the total desorbed amount.

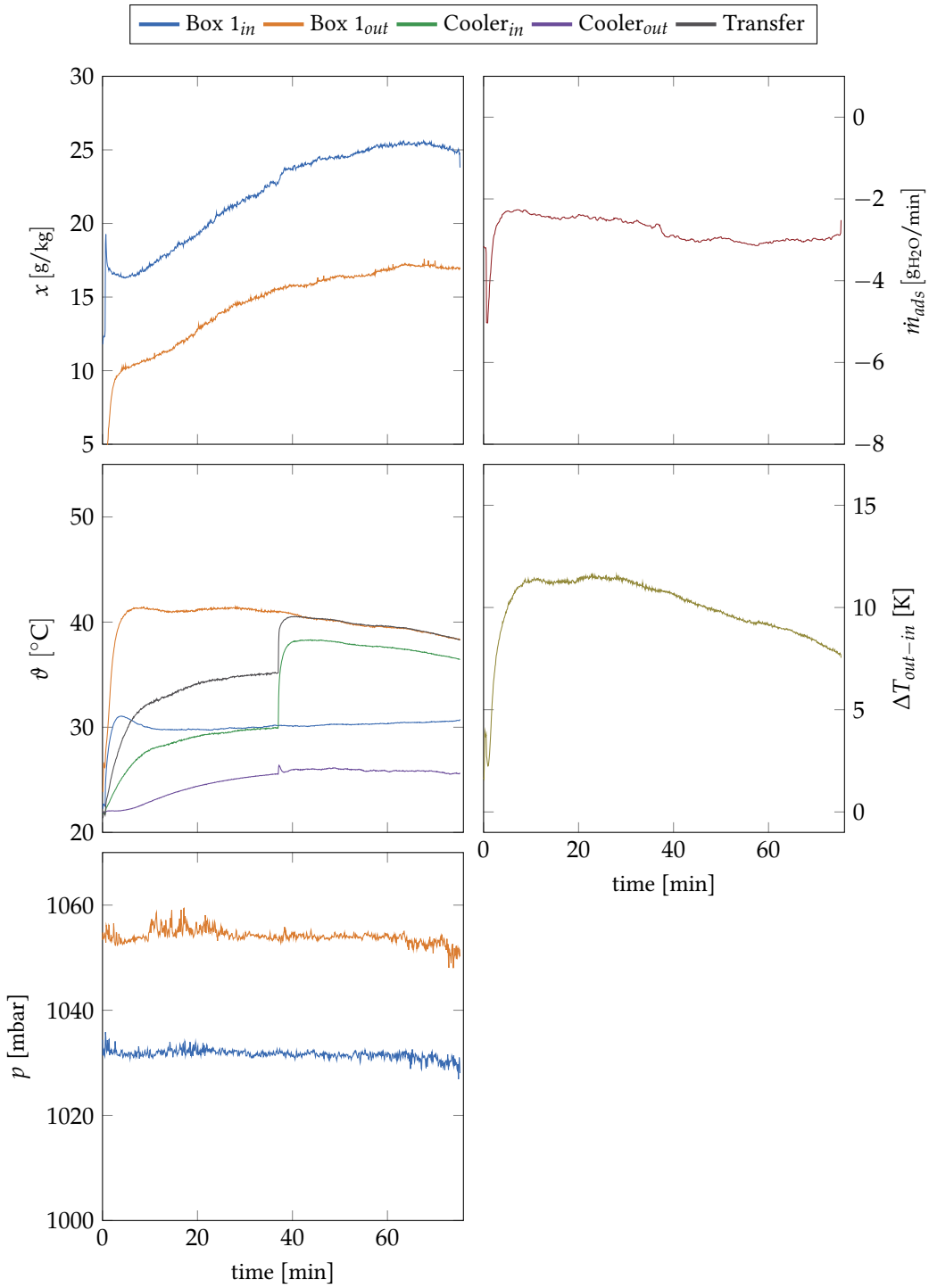

Figure 62: *Box 1* in adsorption mode at 50 % fan power. Loaded sample: *SA-O*

Together with the overall higher intake humidity in the second experiment with just 50 % fan PWM setting, this explains the odd effect of more water being adsorbed over the same time frame. Three adsorption measurements were conducted with *SA-T2* samples, two at 50 % and one at 25 % fan PWM setting. The first one (Fig. 96) is characterized by a slow increase in intake air humidity, but an overall stable measurement. The outlet humidity is consistently lowered by an amount between -7 g/kg to -9 g/kg, with the maximum difference reached at the 37 minute mark, where also, consequently, the drying performance is highest with -3.5 g/min. This is caused by the slow increase in intake humidity, and therefor a longer period until saturation behavior begins. This point can also be recognized in the $\Delta\vartheta_{out-in}$-plot. After a ramp-up phase, caused in part by an increased intake temperature, the outlet temperature is consistently raised by about 13 K above the intake temperature until the 30 minute mark. The difference then starts to decline, indicating a decrease in the released enthalpy of adsorption and thus the reaction coming to an end. The following experiment at 25 % fan PWM setting (Fig. 63) is one of the most successful runs, the intake humidity quickly reaches a value of 20 g/kg and increases steadily, overshooting the set target value of 25 g/kg slightly, which could then be held with reasonable accuracy. The drying performance as a function of intake humidity can be monitored very well in the $\dot{m}_{ads}$-plot, and the temperature increase in the $\Delta\vartheta_{out-in}$-plot. The latter is stable at 15 K over a duration of 20 minutes, before declining again. The reason for reaching a higher absolute value than in the experiments conducted at 50 % fan PWM setting lies in the slower decrease of the enthalpy of adsorption. The second experiment conducted at 50 % fan PWM setting (Fig. 64) also shows a very stable inlet water content x_{in} of approximately 25 g/kg. The $\Delta\vartheta_{out-in}$-plot on the other hand must be assessed extra carefully in this case, as it can be potentially misleading: although the decline begins immediately after briefly reaching a temperature spread of 15 K, the outlet temperature remains stable at 45 °C until minute 22. The perceived decline is therefor not caused by a slowing reaction producing less heat, but instead by an unstable behavior of the inlet temperature, which exhibits a faulty, continuous increase. The achieved decrease of the water content Δx_{out-in} in both of these experiments exhibits remarkable values of -10 g/kg to -12 g/kg, consistently held over almost 60 minutes. When it comes to the total adsorbed amount, these two samples are in good agreement with the theoretical values; the first measurement at 50 % fan PWM setting suffers from the same problem as other experiments before - due to the slow increase in intake water content, the adsorbed amount is lower over the same timeframe of 60 minutes.

In the first experiment with *PROS* (Fig. 100), it is evident that insufficient drying led to unsatisfactory performance. The exhaust water content is high and the outlet temperature rise is very low. The reason is most likely a leak in the storage container, where the sieved sample was stored in activated condition. After regeneration, the following experiment (Fig. 102) led to the expected behavior, resulting in -191.5 g_{H_2O} of water adsorption at 50 % fan PWM setting - much higher than the -169.2 g_{H_2O} observed at 100 %.

DT-G is the only silica gel sample in this experiments which did not have a spherical shape. It underwent the same sieving procedure, and the bulk density is identical to the beaded samples (and hence the macroscopic porosity ε would be the same). The pressure drop should still differ due to the deviation from the spherical shape of the particles, which has not been taken into account in the previous calculations. The measured airflow was however identical to the values measured for the beaded packed beds, which can be interpreted as the deviation due to the changed pressure drop in the packed bed being outside the accuracy limits of the flow meter. The pressure sensors that were installed in the test stand did, as mentioned earlier, not deliver any meaningful values. The adsorption measurements show several noteworthy aspects. First of all, the adsorbed masses at 100 % and 25 % fan PWM setting do not match the ratio that would be expected from the air flow rates. The reason can again be found in the corresponding plots (Fig. 103 and Fig. 105). During the experiment with the fan PWM level set to 100 %, the intake side humidity sensor experienced a power loss, which took approximately 6 minutes to fix - this is when the signal returns. The power loss also affected the atmosphere generation chamber and led to unstable intake temperature and

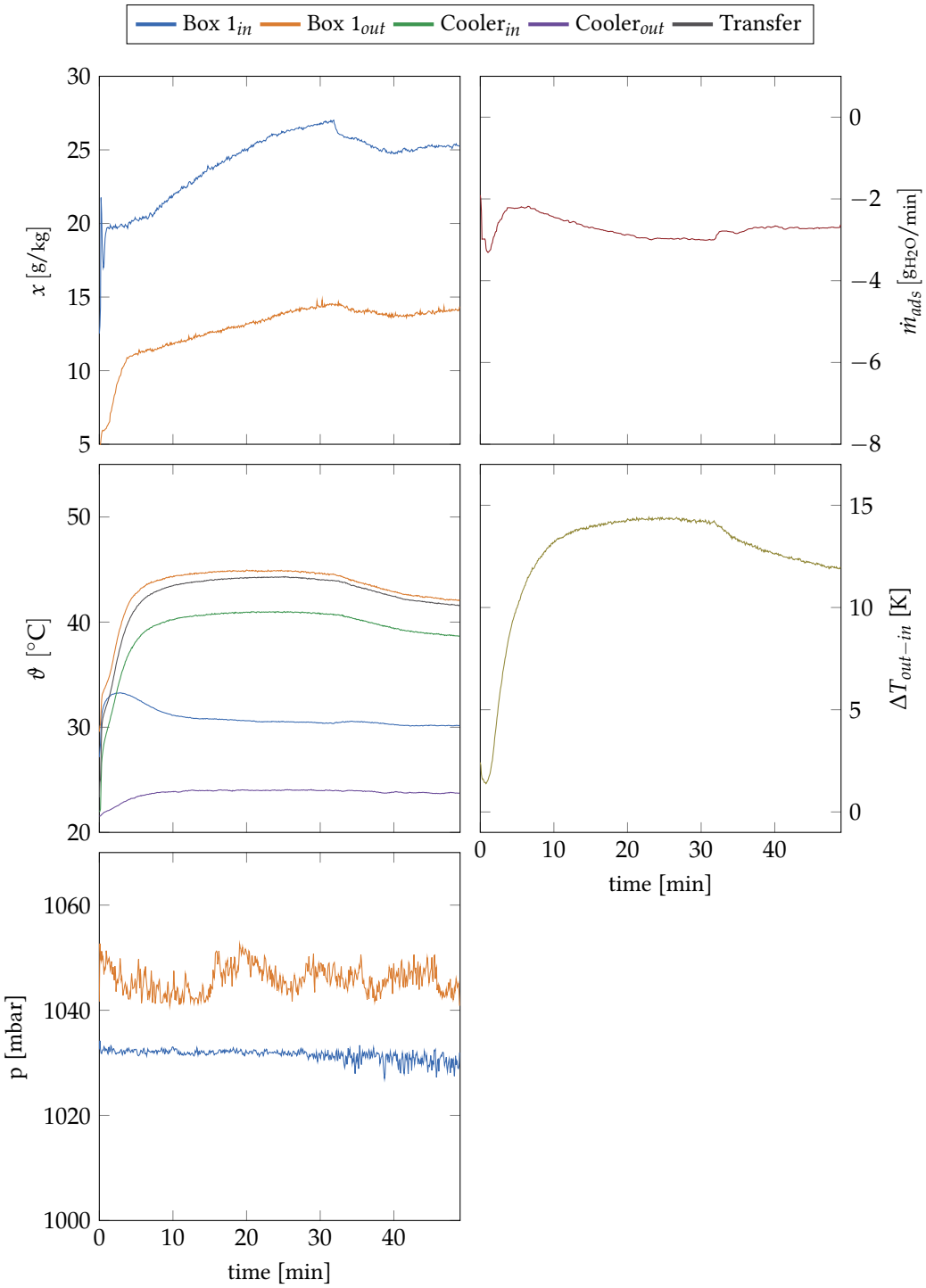

Figure 63: *Box 1* in adsorption mode at 25 % fan power. Loaded sample: *SA-T2*

low intake humidity. As described in Section 3.1, lower ambient humidity causes a lower specific water uptake. The sample itself came straight from the container in activated condition, which, as before, is reflected in a high initial reaction temperature. The measurements taken at 25 % fan PWM setting are governed by large variations in intake humidity towards higher levels, thus increasing the specific adsorption capacity. Over a course of 30 minutes these -partly erroneous- conditions lead to the odd result that the adsorbed amount at 25 % is actually higher than at 100 % fan PWM setting. Although the behavior inverts after 60 minutes, both measurements must be regarded as flawed to an extent where they should be repeated.

During the discussion so far, distinct, recurring phenomena have been identified and explained using the experiments conducted in adsorber *Box 1* as examples. When comparing two measurements, these factors must be carefully accounted for. Most importantly, slow ramp-up rates of the intake air's water content can cause a difference in water adsorption over a defined duration. On the other hand, different pretreatment doesn't show a significant influence on the overall adsorption capacity, but very much so on the temperature rise during the initial stage of the adsorption reaction. Silica gels activated at higher temperatures exhibit peak temperatures that are up to 10 K higher than for silica gels activated at 60 °C. Also noteworthy is the dependence of dehumidification performance ($\dot{m}_{ads}$-plot) of the intake air water content - the higher the water content, the more water vapor is adsorbed. The achievable outlet water content varies between 10 g/kg during the first minutes of the reaction, and can be considered stable at 15 g/kg for all experiments that were not subject to any errors.

The same patterns can be found in adsorber *Box 2*, and therefor, will not be elaborated in detail again - only if unique effects are present, a deeper look is taken. In general, the experimentation time in adsorber *Box 2* was longer than for adsorber *Box 1*. Another distinction can be made with regard to the additional measurement sites that were not present in *Box 1*, namely, the temperature sensors that illustrate the temperature gradient over the packed bed. These are depicted in the bottom-right plot, their designation is explained in Section 3.4. During the adsorption experiments, the progression of the adsorption reaction can be observed at several positions in the packed bed: In principle, all plots track the behavior of the outlet temperature profile, especially the signal from the end of the packed bed (*left*) is more or less identical. The inlet side (*right*) which is in contact with the cooler, moist inlet air, is much lower in its absolute value, but exhibits the characteristics of the adsorption reaction: initially, a sharp increase shows the early stage where the enthalpy of adsorption is large, and then gradually flattens out, until it is almost identical to the inlet air temperature. This point marks the end of the reaction in this part of the packed bed. The other signals follow the same behavior, but are delayed in accordance with the reaction zone moving through the packed bed. Ultimately, all temperature signals would assume the inlet airs temperature when the packed bed is fully saturated and cooled down. The latter effect is discussed in a later paragraph within this section.

Both *SB-WS* and *QP-B* (Figs. 107, 109, 112 and 113) show a less favorable drying behavior than other desiccants, which perform more or less similar (after accounting for the experimental deviations). The 60 minute adsorption performance is very low, and only in the case of Fig. 107 can it be explained by a low intake water content - as has been the case in earlier experiments. In Figs. 109, 112 and 113, a conspicuous observation is that both materials exhibit a low spread between intake- and outlet humidity over the entire course of the experiment. With the data at hand, no definitive explanation can be found - although the H_2O-isotherms also show a lower uptake capacity of *QP-B* compared to other commercial silica gels, this difference should not amount to the uptake discrepancy observed here - especially since the bulk density of *QP-B* is rather high, and the sample mass in the adsorption reactor was 27 % higher than that of *SB-WS*. For the latter, the observed performance is in sharp contrast with its closed-system adsorption capacity at $p/p_0 > 0.9$, which is among the highest for the unstructured silica gels (see Table 22). Therefor, the open system uptake capacity should even be higher than average, especially after accounting for the lower bulk density. One possible

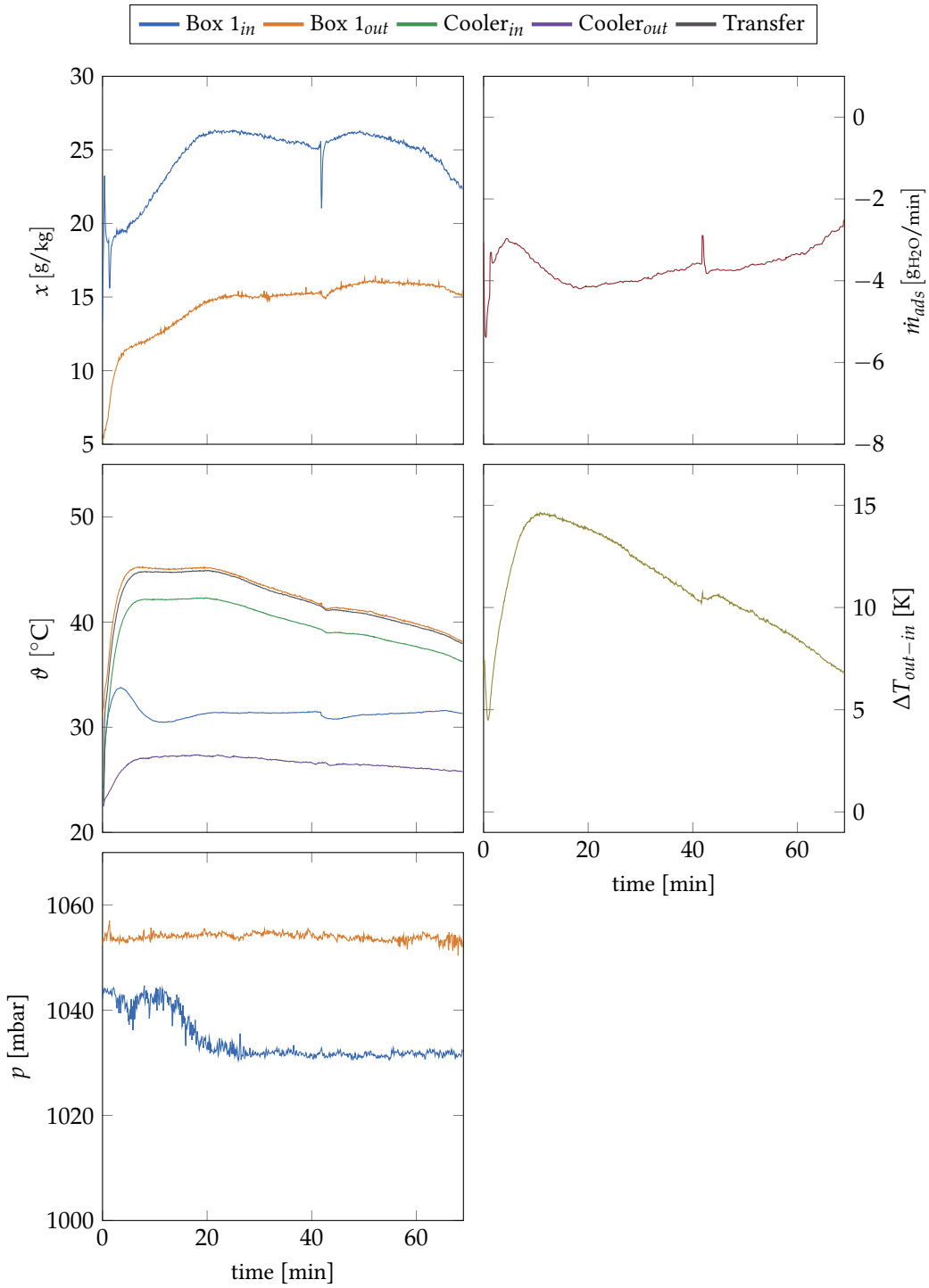

Figure 64: *Box 1* in adsorption mode at 50 % fan power. Loaded sample: *SA-T2*

explanation is contamination from dust, this is however not likely since both materials were stored and handled exactly the same as the others. Another reason could be that these desiccants require higher regeneration temperatures at the given conditions. As already briefly described in Section 4.2.2.1, the cause for this is not entirely clear, but from the observed microscopic data, kinetic limitations arising from a complex pore system fit as an explanation: the 30 °C-isotherm shows lower adsorption capacity than e.g. *SB-R* at relative pressures of $p/p_0 < 0.8$, but then surpasses other materials by a considerable margin. The latter effect is likely caused by capillary condensation effects, *SB-WS* has a wide pore size distribution and a large pore volume. Together with the need for longer outgassing times, this behavior indicates that the equilibration time is much longer for this material than for the others, which is consistent with limited mobility to and from adsorption sites. The same considerations also hold for *QP-B*, but due to a much narrower pore size distribution and a low internal surface area, this material shows lower adsorption capacity throughout the entire relative pressure range. Not even its higher bulk density allows to compensate this in the open system - here, the discussed kinetic limitations lead to *QP-B* showing the least advantageous drying behavior. It stands to reason that the regeneration conditions in the open system are insufficient to reactivate *SB-WS* and *QP-B* in adequate time.

HD-W (Figs. 114, 117 and 118) exhibits a similar adsorption capacity as samples in adsorber *Box 1* experiments, with the same issues regarding an apparently higher uptake capacity at lower fan power than expected. As before, this can be explained by the overall higher water content in the intake humidity over the course of the experiment.

SB-C (Figs. 119, 121 and 123) shows exactly the expected behavior, the adsorbed amounts correspond very well with the different fan power stages. The first experiment (Fig. 119) stands out in terms of stability of the intake humidity: although several downward peaks can be observed, caused by refilling of the reservoirs, the overall consistency is better than in all other experiments. This results in a very high value for the 60 minute adsorption performance. This sample came fully dried directly from the container, which is reflected in the high initial adsorption temperature that can be seen in Fig. 119.

Also for *DT-B* (Figs. 124, 126 and 128), the results are consistent with the expected behavior. Noteworthy herein is the third adsorption experiment, shown in Fig. 128, which yields only a slightly lower adsorbed amount after 60 minutes, although the sample had been regenerated under more humid conditions (see next paragraph). The lower uptake can be explained by initially lower water content in the intake air, as compared to the first experiment (Fig. 124).

The first experiment with *HK-O* (Fig. 65) overshot the water content set point and thereby caused a high adsorbed amount after 60 minutes. The following measurements at lower fan powers, shown in Figs. 130 and 132, are in line with the expected behavior. Even the experiment with 25 % fan PWM setting (Fig. 132) yields a result as expected, although the previous regeneration was done in more humid conditions. Finally, two experiments were conducted with higher regeneration temperatures, with a set point of 90 °C. The results are shown in Figs. 134 and 135. Although the more complete drying of the desiccant is, again, reflected in higher initial temperature peaks during adsorption, the overall performance in terms of 30 minute- and 60 minute adsorption capacity, is not improved.

It must be acknowledged that the results quoted in Table 28 and Table 30 have limited significance without this accompanying assessment of the respective experimental conditions. Only when taking into account the variations in these conditions can individual results be selected that allow for direct comparison. With this in mind, the performance of the investigated samples does not show differences that can be definitely pointed out with the results at hand. Just two samples, *SB-WS* and *QP-B* showed a more unfavorable behavior than the other samples under the investigated conditions. For the others, it can be concluded that even with an unstable humidity control, the system response is stable: the air flow's water content is always lowered by approximately the same amount, the outlet water content tracking the inlet water content with a difference of 7-10 g/kg in well-performing experiments with 100 % fan PWM setting, and up to 12 g/kg in well-performing experiments with 50 % and 25 % fan PWM setting. In many experiments however, Δx_{out-in} is considerably smaller.

Regardless of this phenomenon the value remains fairly consistent within the respective experiment, larger variations could all be explained by external factors. Lastly, it must be acknowledged that the inherent properties of silica gel as a desiccant, as introduced in Section 3.1, prohibit low dew points. Under the experimental conditions, and even at large Δx_{out-in}-values, a limit of $x_{out} = 10\,\text{g/kg}$ in the outlet water content seems to be hard to surpass.

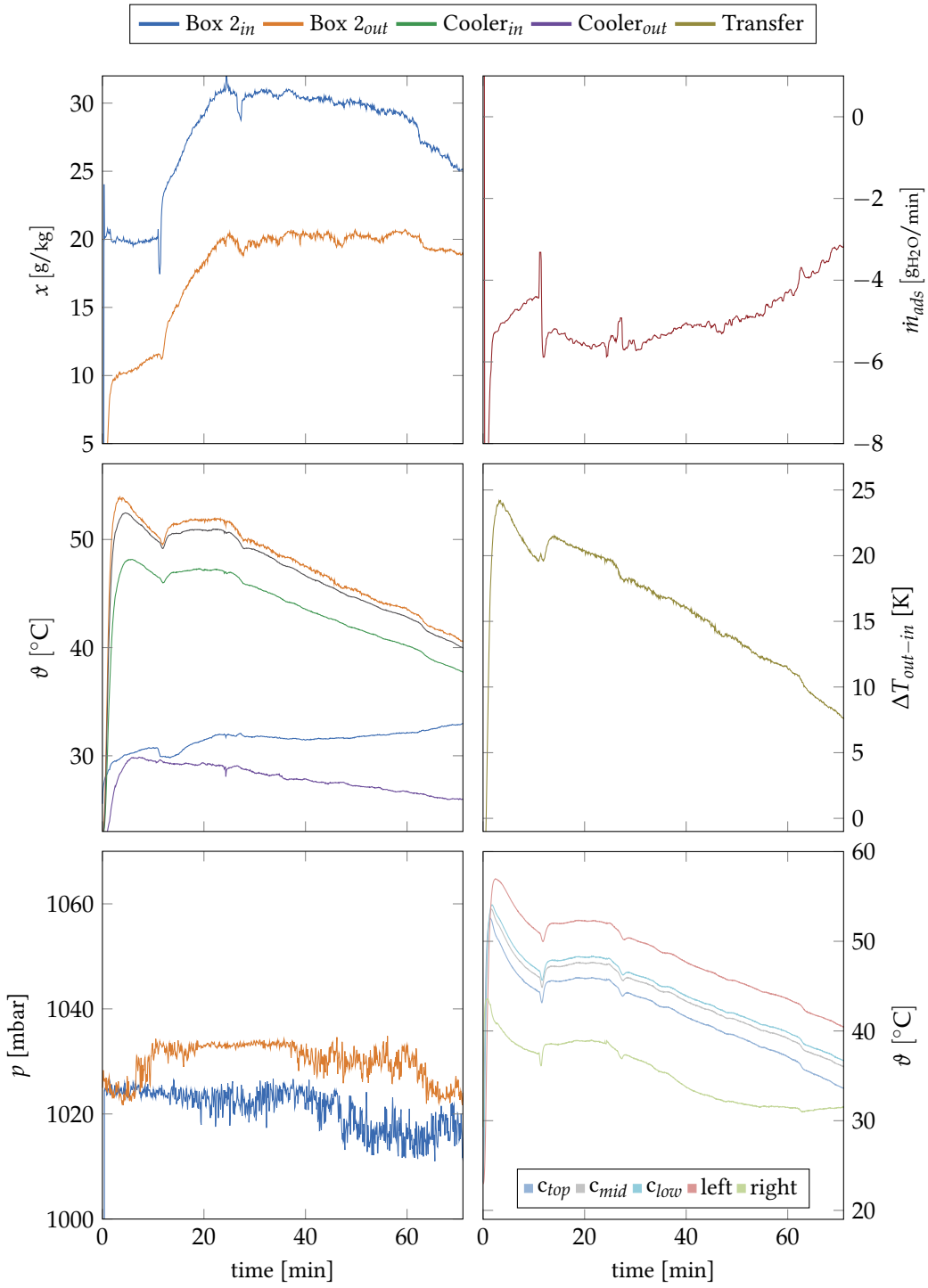

Figure 65: *Box 2* in adsorption mode at 100 % fan power. Loaded sample: *HK-O*

4.3.2.2 *Desorption Performance*

For the desorption part of the experiments, the ultrasonic evaporators were switched off and the temperature was increased to a set point of 60 °C. As mentioned in Section 4.3.2.5, the valve located on the adsorber outlet was switched to exhaust mode during desorption. This means that the airflow is not directed through the transfer line and the cooler, but instead directly discharged to the ambient. Because of the short flow path length and the low thermal conductivity of the valve material, the temperature drop here is negligible at lower temperatures. The plots at the exhaust pipe and the packed bed outlet are almost always completely overlapping. At higher temperatures, small deviations occur. All experiments conducted show a very stable temperature profile of the inlet temperature. The difference in inlet- and outlet water content could be tracked very well, and the desorption reaction was considered complete when the difference, represented by $\dot{m}_{\mathrm{ads}}$, became zero. In case the experiment was allowed to continue to run, a dehumidification effect is observed even at 60 °C: the outlet humidity plot crosses the inlet humidity plot, indicating a lower outlet- than inlet humidity. In adsorber *Box 1*, this can be observed in Fig. 95, Fig. 99 and Fig. 97, in adsorber *Box 2* it was the case in Fig. 115.
During the experiments conducted with *HK-O* in adsorber *Box 2*, some desorption measurements were performed with elevated water content in the intake air (Figs. 127 and 131). No measurable adverse effect on the adsorption performance could be determined, but the regeneration time was significantly increased.
Table 29 and Table 30 list the desorbed amounts. They are often above the expected values - which would be the same as what had been adsorbed during the previous experiment. The reason for this anomaly is that the experiments were not performed right after one another. Over night, or over weekends, the desiccant continued to adsorb some moisture from the ambient.
The temperature gradient over the packed bed, thus the progression of the regeneration zone and the resulting equilibrium conditions can be followed with the additional sensors in adsorber *Box 2* (bottom-right plot). The intake side (*right*) is the first to be in direct contact with the hot, dry regeneration air, and thus, the desorption reaction occurs here first. The center part (c_{low}, c_{mid}, c_{top}) follows with a delay of several minutes, and the outlet side (*left*) comes last. Ultimately, the gradient disappears as the bed has assumed a uniform temperature close to that of the regeneration air. A particularity in these plots is the crossing of the outlet side signal over the center part, which occurs at the very beginning of the adsorption reaction. This is due to the fact that the center part is enclosed from two sides by the packed bed with the ongoing endothermic desorption reaction, whereas the outlet side is close to the warmer outlet air flow. While the desorption experiments were, in general, much easier to control and yielded excellent results, some minor issues still occurred: Fig. 90 shows a spike on the intake humidity sensor. The cause is unclear, no errors were found and it remained an isolated event.
During the experiments with *SA-O*, some noticeable effects could be observed: In Fig. 66, the outlet side valve had been in the wrong position for the first 13.7 minutes. The air was channeled through the air cooler instead of going directly through the exhaust pipe, causing a lower air flow. The calculations for the total desorbed amount have been adjusted accordingly. Fig. 99 shows a typical example of an already quite dry adsorbent. No adsorption experiment had been performed after the previous drying procedure shown in Fig. 66, consequently, only the amount of water had to be desorbed that entered the vessel from the ambient.
The desorption of the *PROS* sample, Fig. 101, is characterized by several experimental inaccuracies. First, a higher initial humidity, as a result of residual moisture in the system. Although, to a much lesser extent, this can be observed in most desorption experiments, it is especially prominent in this case. It is most likely caused by spillage of water from the ultrasonic evaporators. The second faulty part is an erroneous set point of the regeneration temperature, which is at 70 °C instead of the desired 60 °C. A slight hysteresis between adsorber outlet and exhaust pipe can be observed, this occurred in some experiments and is probably due to thermal losses in the valve system, which

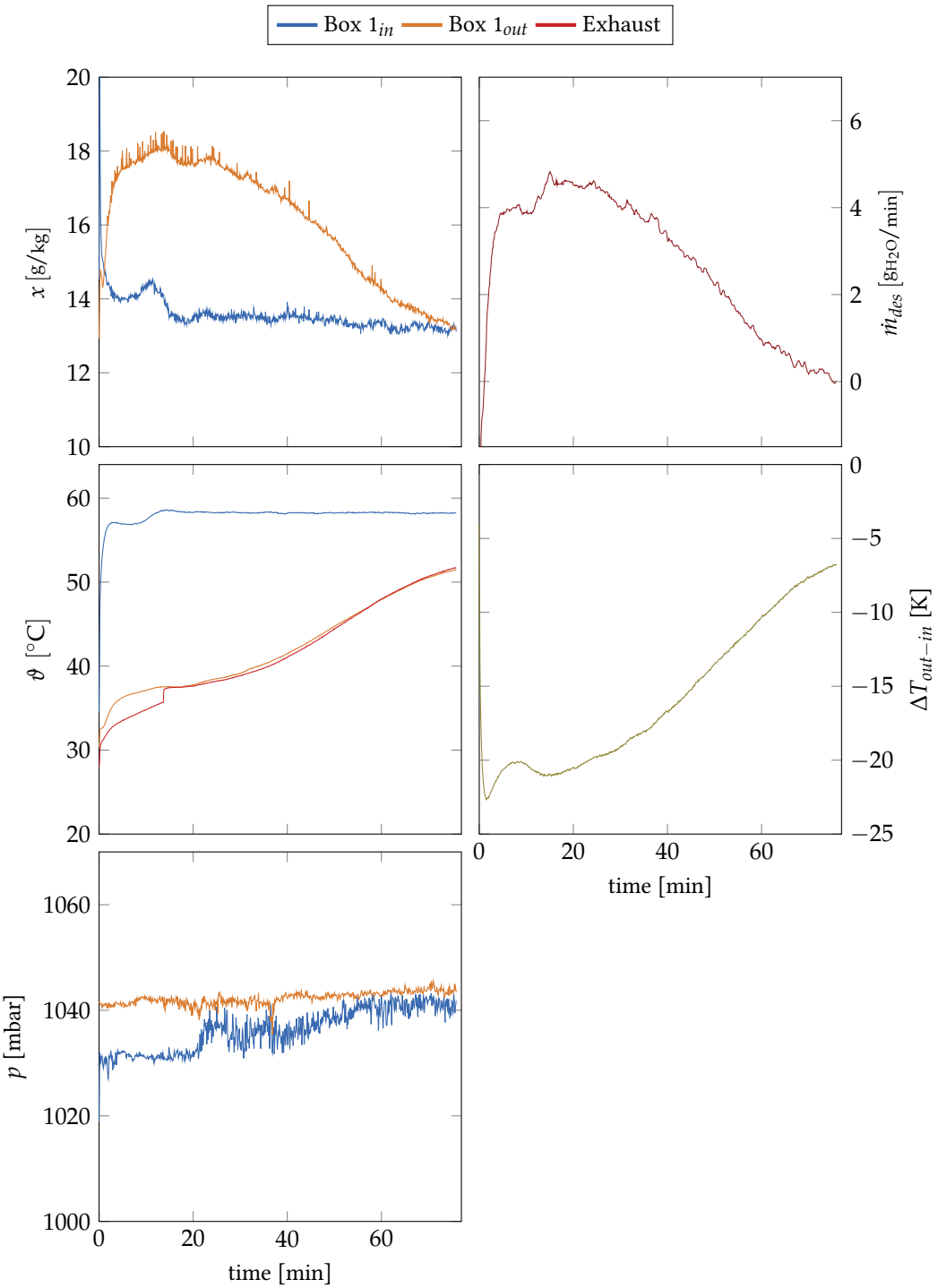

Figure 66: *Box 1* in desorption mode. Loaded sample: *SA-O*

are aggravated at higher temperatures.
The first desorption experiment with *DT-G* (Fig. 104) shows no flaws: after 60 minutes the desiccant is dried, as is evident from the $\dot{m}_{\text{ads}}$-plot reaching zero and from the outlet temperature steadily rising towards the inlet temperature.
Another example of an initially almost dry desiccant sample can be seen in Fig. 106, the first desorption experiment with *SB-WS*. In contrast to the previous experiments, the $\dot{m}_{\text{ads}}$-plot remains slightly positive, even though the graphs for inlet- and outlet water content (x_{in}, x_{out}) are very close already after 30 minutes. Together with the properties found in the H_2O-vapor adsorption experiments discussed in Section 4.2.2.1, this can be interpreted as evidence that the applied regeneration temperature is too low for this desiccant. This conjecture is supported by the behavior observed in Fig. 108, where the same effect occurs and the desorption process takes longer than for other desiccants.
The same effect is present in the experiments with *QP-B*. Both Fig. 110 and Fig. 111 show non-closing plots for water content x, and, consequently, the $\dot{m}_{\text{ads}}$-plot remains positive. It stands out that the total desorbed amount over a given time frame is not so much different from the other samples, which did not suffer any reduced adsorption capacity issues. The reason can again be found in the sequence in which adsorption and desorption happened: the drying experiments were performed directly before the adsorption experiments, but the next desorption experiment followed sometimes many hours later. It is reasonable to assume that this is when additional water was adsorbed from the atmosphere, which then shows up during the next desorption. Due to the earlier discussed slow kinetics of both *SB-WS* and *QP-B*, the difference is much larger than in other commercial silica gels.
During the desorption of the *HD-W* sample (Fig. 115), the oven failed just short of the 30 minute-mark. Although the desorption was very efficient to that point, as characterized by a large spread in both the $\Delta\vartheta_{out-in}$ and the $\dot{m}_{\text{ads}}$-plots, it must be considered incomplete and was thus repeated before the next adsorption experiment. This is shown in Fig. 116, here the residual humidity is desorbed. Although the spread between inlet and outlet water content $\dot{m}_{\text{ads}}$ is not as large as before, the integrated value shows that moisture was present in the desiccant bed - the effectively desorbed value is only 15 % smaller than during the preceding experiment. As with the samples before, also *HD-W* is not fully dried during the desorption experiments, characterized by $\dot{m}_{\text{ads}}$ remaining slightly positive.
Also *SB-C* suffers from this shortcoming, even with an extraordinarily long desorption time, as in Fig. 120. The duration is owing to the previous adsorption experiment (Fig. 119) with a similar extent and a very large total adsorbed amount. The fact that the desorbed amount is lower than what was adsorbed before can partly be attributed to the incomplete desorption procedure, but also to co-desorption while adsorber *Box 1* was regenerated: due to the valves not being entirely leak-tight, a small amount of hot air is continuously channeled to the respective other adsorber, while one is being regenerated. When the desorption is carried out directly after the the end of the adsorption experiments, this error is minimized - as is evident from the experiments depicted in Fig. 121 and Fig. 122, where the adsorption of -311.4 g_{H_2O} is followed by the desorption of 312.5 g_{H_2O}, although the latter also exhibits the issue of $\dot{m}_{\text{ads}}$ never reaching zero.
DT-B does not have this problem: although the desorption process takes about 30 % longer than what was observed in the experiments with adsorber *Box 1*, $\dot{m}_{\text{ads}}$ becomes zero eventually in both Fig. 125 and Fig. 127. The latter is a desorption experiment under humid conditions, as can be seen from the higher inlet water content value x_{in}. It also exhibits a spike in all plots, which is caused by a failure in the atmosphere generation chamber control, causing the *Memmert* oven to switch off. This leads to the temperature drop which is seen in the inlet temperature curve due to the lack of heating, and the humidity spike due to the buildup of moist air while the fan was not running.
Similarly, *HK-O* also does not exhibit any issues reaching a $\dot{m}_{\text{ads}}$-value of zero, although Fig. 129 shows a slight instability at the end, where the temperature control became unstable. The $\dot{m}_{\text{ads}}$-plot returns to a slightly positive value with elevated temperatures, as would be expected: desorption

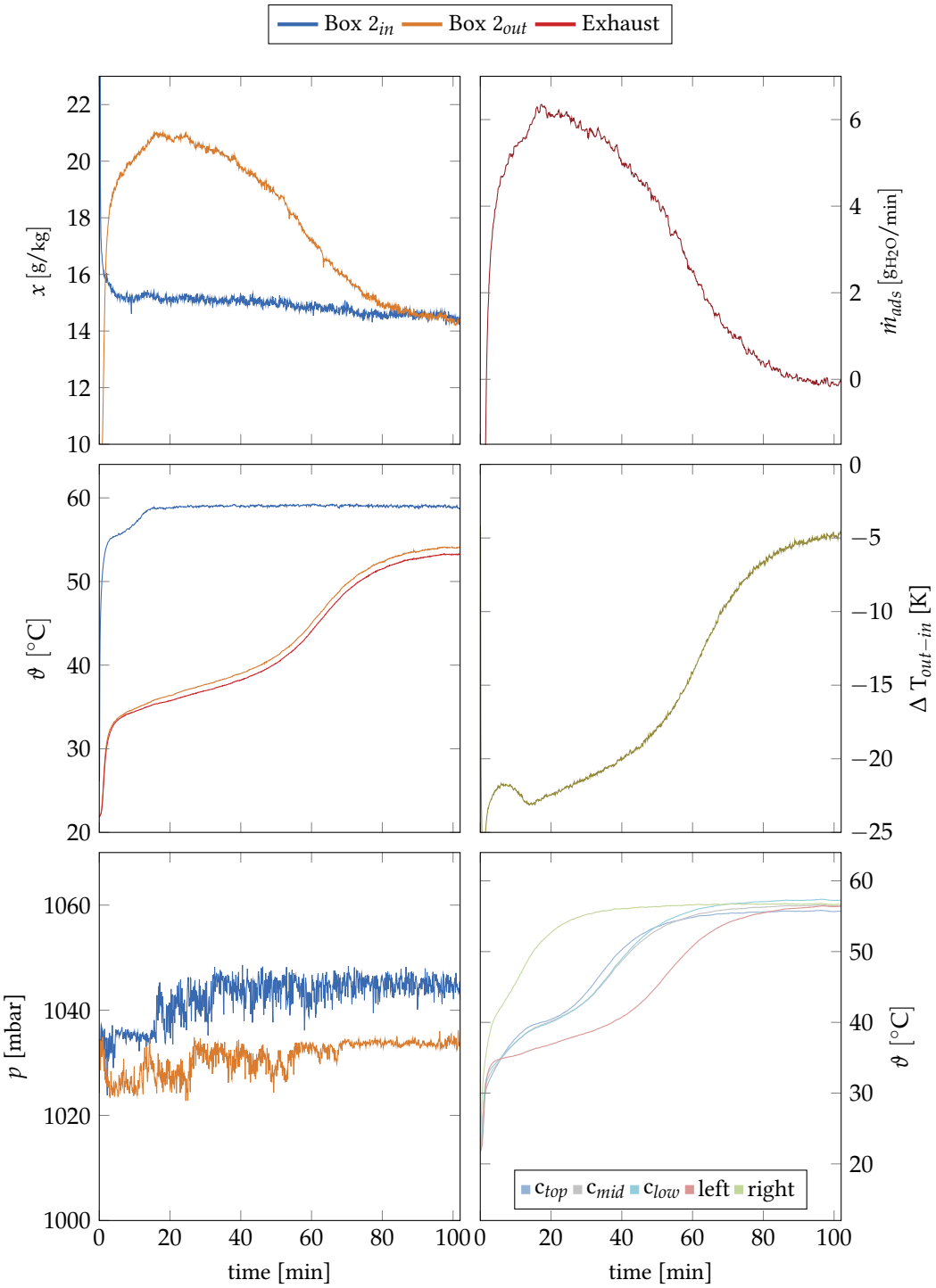

Figure 67: *Box 2* in desorption mode. Loaded sample: *HK-O*

at higher temperatures leads to more thorough desiccant drying, as has been shown earlier in elevated-temperature desorption experiments, which were also conducted with *HK-O*. Fig. 67 does not show any peculiarities. The experiment shown in Fig. 131 was conducted with more humid inlet air, again reflected in a higher inlet air water content x_{in}. The fact that the desorption process takes about the same time is attributable to the smaller desorbed amount. In contrast, the next desorption (Fig. 133) was conducted with an elevated inlet temperature at a setpoint of 90 °C, which was only reached stably after 20 minutes. The drying performance within both the 60 minute- and 30 minute-interval is increased, desorbing about 10 % more as compared to the previous experiment in Fig. 67. The desorption presented in Fig. 68 can be considered a "'bonus"' experiment, it was conducted under both elevated temperature, increased intake water content and the air flow was channeled through the air cooler instead of the exhaust pipe. The latter is the reason that the exhaust temperature is significantly lower than the outlet temperature. Due to the lower air flow, the period where the outlet water content is highest is prolonged, even with elevated temperature. The overall desorption performance seems to be only mildly affected at best, since the sample dries to approximately the same level as in the previous experiment.
Overall, it can be concluded that the desorption procedure can be sufficiently conducted at temperatures of 60 °C, although higher temperatures increase the drying performance slightly. This must, however, be paid for with a longer cooldown time, and if no active cooling measures are available, this phenomenon might even overcompensate the benefits that could be gained from higher-temperature regeneration. The time required to reach a sufficiently dry desiccant ranges from 40 minutes to over 120 minutes, depending on the amount of water to be desorbed. For the average amounts that can be expected to be adsorbed during an operating time of 60 minutes, an approximately identical, corresponding desorption time can be expected. As within the adsorption experiments, no significant difference was apparent between most of the samples. For the issues encountered, satisfactory explanations could be found.

4.3.2.3 *Cooldown*

The cooldown curves of the packed bed in adsorber *Box 2* have been recorded with the thermocouples placed within the packed bed. The starting temperature corresponds to the final temperature after regeneration of the packed bed, in most cases, 60 °C, but for two measurements, the desorption temperature had been set to 90 °C (Figs. 68 and 133). It seems reasonable to assume that convective heat transfer dominates the cooldown process - firstly because of the large surface area of the silica gel packed bed exposed to the airflow, as compared to the surface area of the silica gel pellets which is in contact with the acrylic walls. Secondly, the temperature profile shows that the section located on the intake side cools down fastest, which would also be expected. However, the upper and the lower section of the packed bed center exhibit the second-fastest cooling rate, sometimes even intersecting the plot of the outlet side, where the packed bed is also exposed directly to the ambient air. The middle section of the packed bed center consistently shows the slowest cooling rate. This discrepancy can likely be attributed to the different proximity to the outer walls, where conduction and radiative heat transfer to the environment have larger contributions. This leads to the conclusion that, while other mechanisms of heat transfer are also observable, convection seems to play the dominant role. The cooldown process of the packed bed could thus greatly be enhanced by moving small amounts of air through the packed bed, especially since the total amount of heat stored in the packed bed is relatively small: to cool down a dry *HK-O* silica gel bed from 58 °C to 28 °C, the amount of heat to be removed is

$$Q_{cool} = c_p \, m_{HK-O} \, \Delta\vartheta = 33.5\,\mathrm{kJ}. \tag{4.3.5}$$

Herein, the mass of the *HK-O* packed bed from Table 27 was used (m_{HK-O} = 1.14 kg), and a c_p-value of 980 J/kgK from [156]. As mentioned earlier, it is obvious that the cooldown procedure takes longer if the packed bed has been regenerated at higher temperatures.

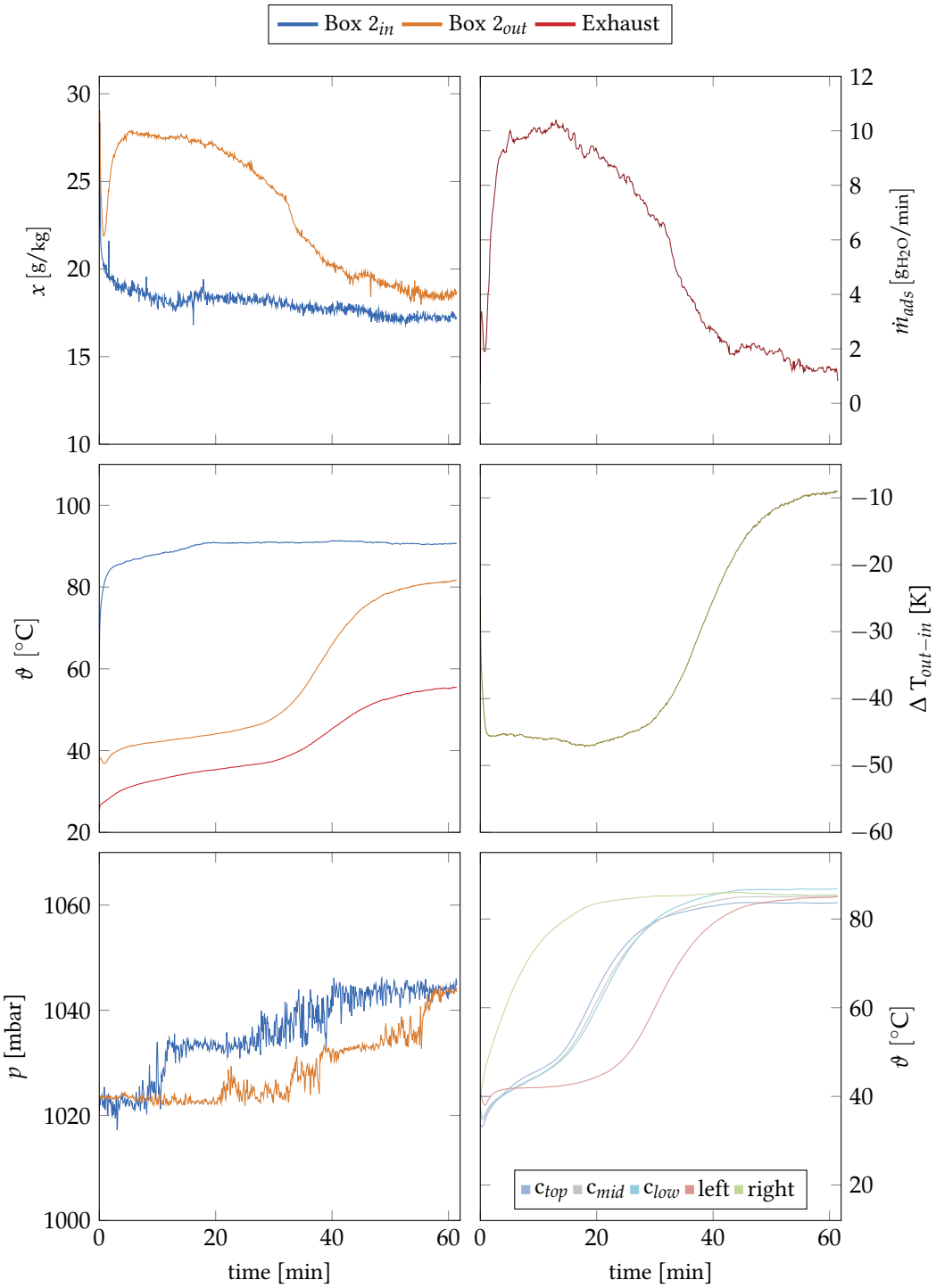

Figure 68: *Box 2* in desorption mode, with increased regeneration temperature. Loaded sample: *HK-O*

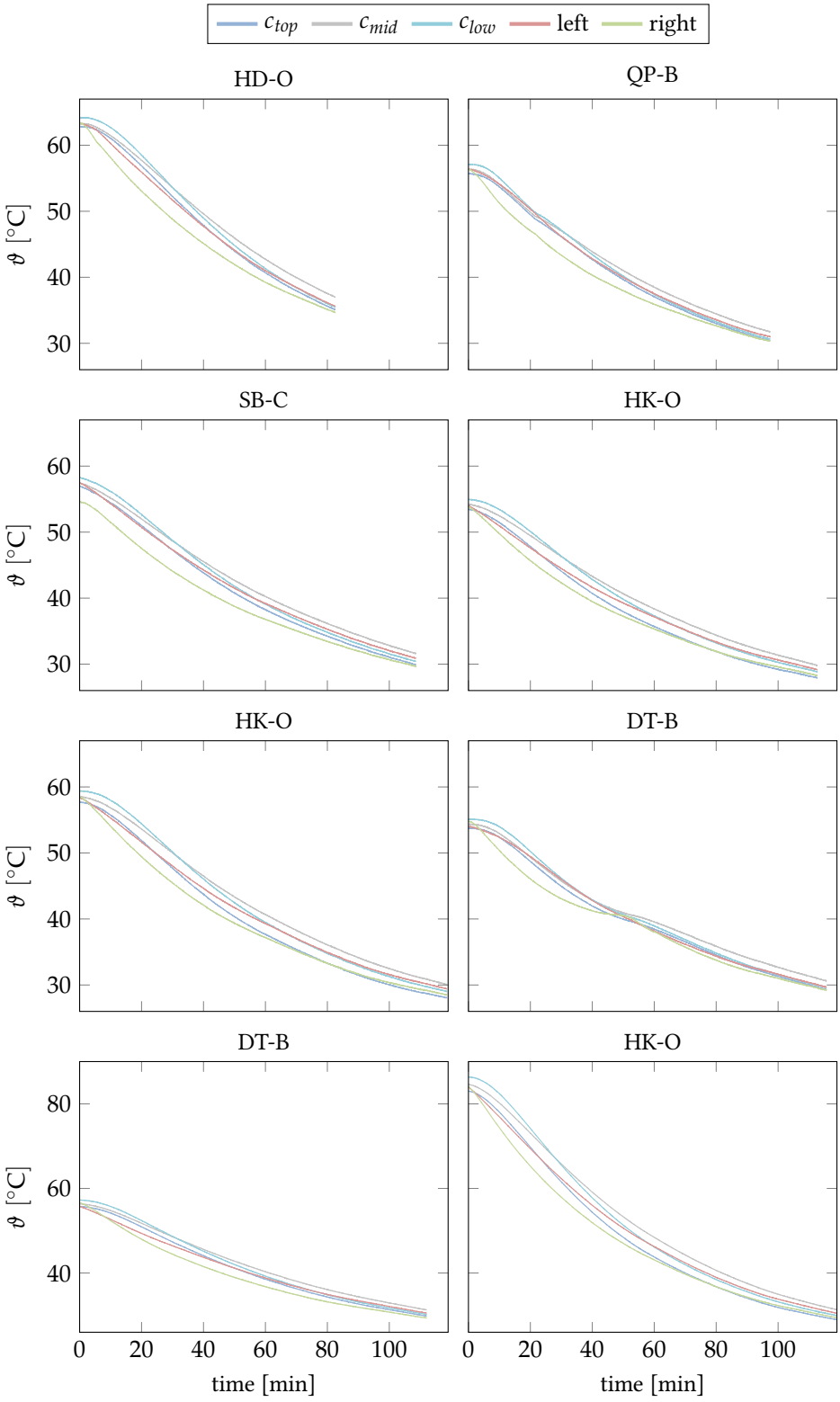

Figure 69: Cooldown of the packed bed to ambient temperature.

4.3.2.4 *Pressure Drop*

According to the blower's characteristics (Fig. 41), the pressure drop corresponding to the measured air flow of 0.98 m^3/min would be 6.7 mbar. The predicted pressure drop in the packed bed, pessimistically calculated for an average particle diameter of 3 mm, would amount to just 2.9 mbar (Eq. (2.6.1)). The remaining 3.8 mbar must thus be caused by the intake section, the outlet section and the valve. This is a reasonable assumption given the sharp edges and generally non-aerodynamically favorable design of the inlet and outlet ports. In adsorption mode, the air flow is further reduced to 0.45 m^3/min, which is attributable to the pressure loss caused by the transfer line and the air cooler. The pressure sensors, which were installed in the adsorption reactors directly before and after the packed bed, unfortunately proved to be of no use. While the signals are quantitatively in the expected range, their qualitative behavior is opposite to what should have been observed: instead of the intake side pressure being higher than the outlet pressure, the sensors behave vice versa. This phenomenon occurred with both sensor pairs, in both reactor vessels. Since the signals at atmospheric conditions were inconspicuous, the behavior can be most likely explained with insufficient sensitivity at small pressure changes. In future experiments, this could be mitigated by using sensors with a narrow measurement range and high sensitivity, and possibly by the addition of one or more backup sensors.

4.3.2.5 *Auxiliary Devices*

A brief paragraph shall be dedicated to the results relating to the air cooler and the air ducts. The latter mainly have an impact on the pressure drop of the overall system, which is evident from the air flow measurements. Another aspect are the thermal losses. In the main connection line between the atmosphere generation chamber and the supply air fan, these were addressed through design measures (i.e. the connection was kept as short as feasible) and through thermal insulation. No specific measures were taken to insulate the transfer line between the outlet valve and the cooler inlet, which is referred to as *Transfer* in the adsorption plots. A constant temperature difference of 3-4 K between in- and outlet of this hose can be observed in the ϑ-plots.
The performance of the subsequent air cooler is remarkable, at the observed conditions it reliably cools down the air flow to just above ambient temperature, but by not more than 18-20 K. The laboratory temperature was set at 22.5 °C and stable to $\pm$ 0.3 K. The initial temperature peak and inlet fluctuations are to a large extent buffered by the cooler's thermal mass, so the outlet temperature signal is in most cases a smooth curve.

5

DISCUSSION

This chapter is dedicated to a thorough discussion of the previously presented results, tying everything together into the framework of the proposed dehumidification process. The feasibility of the latter is evaluated with the help of the results at hand. Their significance and mutual relationship is assessed and sources of error are highlighted.

With the results presented so far, a complete process can be designed following the approach introduced in Section 2.2: experimentally obtained process parameters from the dehumidification unit are applied to the boundary conditions defined by a reference vehicle's air conditioning process in specified environmental conditions. The vehicle's energy consumption is then evaluated and the potential advantage of the dehumidification system is assessed.

The air conditioning process shall be discussed according to the method introduced in Section 2.1.4: the overall process is plotted and analyzed in a Mollier chart, and the efficiency is calculated. The following diagram in Fig. 70a is based on a scenario representing the best performing experiments (Figs. 63, 64 and 96) with *SA-T2* silica gel. Therein, reductions in water content Δx_{out-in} corresponding to an average dehumidification performance of up to -3.6 g/min could be achieved. These parameters remain fairly constant, even when the intake humidity gradually ramps up over experimentation time. This behavior is visible in the water content diagrams, where a nearly constant spread between the intake- and the outlet plot is maintained.

The initial thermodynamic state for the dehumidification process Z_I is thus placed at a value that occurs under real-life operating conditions, but is also present in the experiments.

The following process points are then found from the results of the adsorption measurements. In a first step, the achieved temperature difference between in- and outlet air is assessed. After an initial peak, the intake temperature stabilizes. The outlet temperature follows the characteristics described in Section 4.3.2, starting with a peak, then maintaining a fairly constant value at constant adsorption conditions and decreasing as adsorption performance reduces. This leads to a distinct shape of the $\Delta\vartheta_{out-in}$-plots: after the initial peak, a plateau of varying length follows, which is then followed by linear decline. From the considered experiments, only Fig. 63 exhibits a distinct plateau. The outlet temperature in this region is considered for the placement of point Z_{II} in the diagram, as it represents a larger thermal load than the following, lower temperatures. If there is no distinct plateau, the initial peak temperature should be used for the same reason. Therefor, Z_{II} is chosen corresponding to the achievable reduction of Δx_{out-in} = -10 g/kg. At this point, it is immediately visible that the process does not behave like an adiabatic packed bed, since Z_I and Z_{II} are not located on a line of the same enthalpy. This is caused by both the heat required to warm up the desiccant bed, and also due to the previously discussed heat losses to the ambient. During the adsorption process, which is represented by this state change from points Z_I to Z_{II}, the intake air's enthalpy is reduced by 11 kJ/kg. The third point, Z_{III}, corresponds to the state at the outlet of the air cooler. The water content x_{III} remains identical to x_{II}, but the temperature is decreased. The assumption for the chosen value can be justified by the results of the experiments: although the temperature gradient in the lab was larger, the performance of the air cooler is sufficient to provide the required cooling power even at a lower temperature gradient and reduce the air temperature to approximately 3 K above ambient temperature. The respective change brings the total reduction of

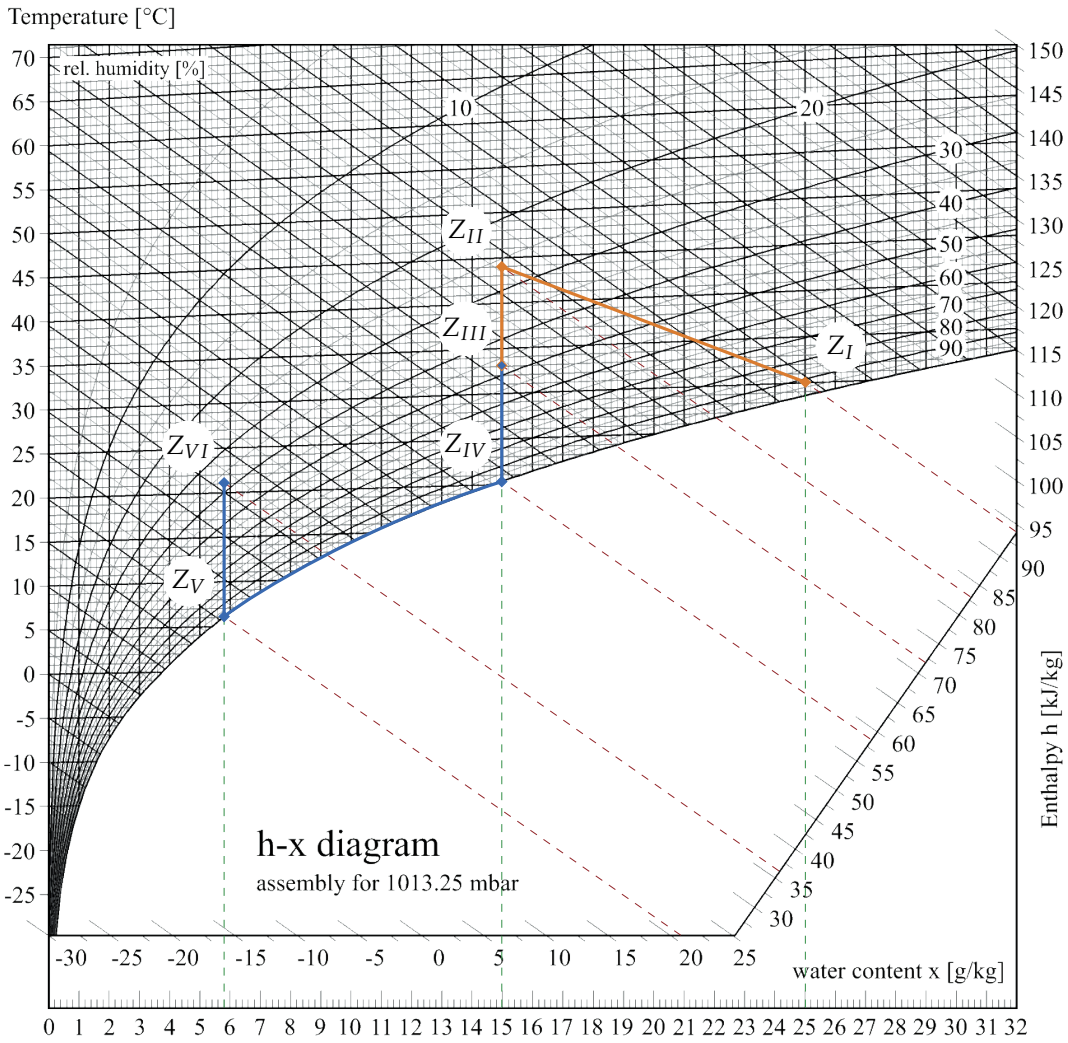

(a) Possible dehumidification process with *SA-T2* silica gel - scenario 1.

State Z_i	ϑ_i [°C]	x_i [g/kg]	h_i [kJ/kg]	φ_i [%]
Z_I	30.0	25.0	94.0	92
Z_{II}	44.0	15.0	83.0	26
Z_{III}	33.0	15.0	72.0	47
Z_{IV}	20.3	15.0	58.5	100
Z_V	6.0	5.8	20.5	100
Z_{VI}	21.0	5.8	36.0	38

(b) Thermodynamic states of air as depicted in Fig. 70a, specific enthalpy values rounded to 0.5 kJ/kg.

Figure 70 & Table 32: Possible dehumidification process - scenario 1.

the intake air's specific enthalpy to Δh_{I-III} = -22 kJ/kg.

From this point forward, the regular, refrigeration-based A/C-system needs to take over to complete the remaining process steps (in Figs. 70a and 71a, this part is shown in blue). This includes further cooling to the dew point Z_{IV}, and the moisture removal through condensation until state Z_V is reached. The total change in specific enthalpy is then Δh_{III-V} = -51.5 kJ/kg. Parameters for the individual state points are tabulated in Table 32.

A comparison of this process plot with the idealized sketch from Fig. 9a identifies the main differences as follows: First, the adsorption process is not adiabatic, and second, the desired reduction in water content can not be reached at the given air flow rates. The former does not constitute a negative influence on the overall process, whereas the latter leads to reduced efficiency in comparison with the desired process. After the initial peak, caused by the strong adsorption forces at low adsorbent coverage, a lower barrier is observed at approximately x_{out} = 10 g/kg that is rarely reached during any of the experiments. This leads to an increase in the part of the air conditioning process that has to be performed by the refrigeration cycle. The reason for this limitation lies in the inherent property of silica gels to exhibit a strong dependency between the *relative* humidity of the intake air and the adsorption capacity (see Section 2.5). At Z_{II}, the relative humidity is already reduced to just 25 %. Here, other desiccants like molecular sieves would be able to provide a much better result, but at the previously discussed disadvantages - most notably, the much higher regeneration temperature. The observed reduction in water content x leads to a deviation in total moisture adsorption capacity, as compared to the requirements outlined in Section 3.4: there, a reduction of Δx_{out-in} = -15.8 g/kg is assumed, whereas the achievable reductions with the present setup, as discussed, are only between Δx_{out-in} = -10 g/kg to -12 g/kg.

The questions that remain are if the process is still suitable at this enthalpy reduction potential, and if mitigation measures or design improvements could help to increase its efficiency. A method for assessing the process' efficiency has been introduced in Eq. (2.2.5). This method shall now be applied to the operating scenario from Section 2.2 to illustrate the potential and limitations of this specific process. Instead of the generic vehicle, TUM CREATE's electric taxi *EVA* is used along with values found from the experiments with the desiccant *SA-T2*.

First, it must be noted that the experimental air flow rates are fairly low, with the different fan PWM settings corresponding to just 7 ACH, 5 ACH and 3.3 ACH in TUM CREATE's vehicle *EVA*. As per Eq. (4.3.1), the power consumption of the fan is reduced accordingly. For this analysis, it is assumed that regeneration consumes the same amount of power - in an actual application however, the regeneration air flow can possibly be supplied by the existing radiator fans.

The necessary amount of water to be removed from the air flow can be deduced from the assumptions of Section 3.4. Here, an adsorbed amount of 349 g of water per 30 minutes was postulated for an air change rate of 10 ACH. For the measured volume flows corresponding to 5 ACH and 3.3 ACH, this would be reduced to 174.5 g and to 116.3 g, respectively. The fact that these values could not be achieved by any of the conducted experiments (Tables 28 and 30), can be entirely explained by the lower-than-expected reduction in water content Δx_{out-in}.

For the proposed process assessment as outlined in Section 2.2, the following other necessary input parameters need to be gathered: With a desiccant mass of 1068.5 g per adsorption reactor (Table 27), the total mass of the dehumidifier adds up to m_{dh} = 7200 g. *EVA*'s curb weight is m_{car} = 1500 kg, which is lower than the earlier assumed 1780 kg - however, the latter included two passengers. The difference is negligible since it doesn't significantly affect the overall result. In general, if the vehicle weight is assumed higher than it actually is, this would cause an underestimation of efficiency rather than an overestimation. Calculated from the affinity laws, the reduced power consumption of one fan amounts to 14.2 W. Other required values, namely sensitivity ξ and COP, shall remain the same as in Section 2.2. Care must be taken when using the energy consumption values of the reference scenario (see Table 2a) - there, the assumption for the cabin volume was set to 5 m^3, whereas the actual cabin volume that is used in the design at hand, is already more precisely known to be only

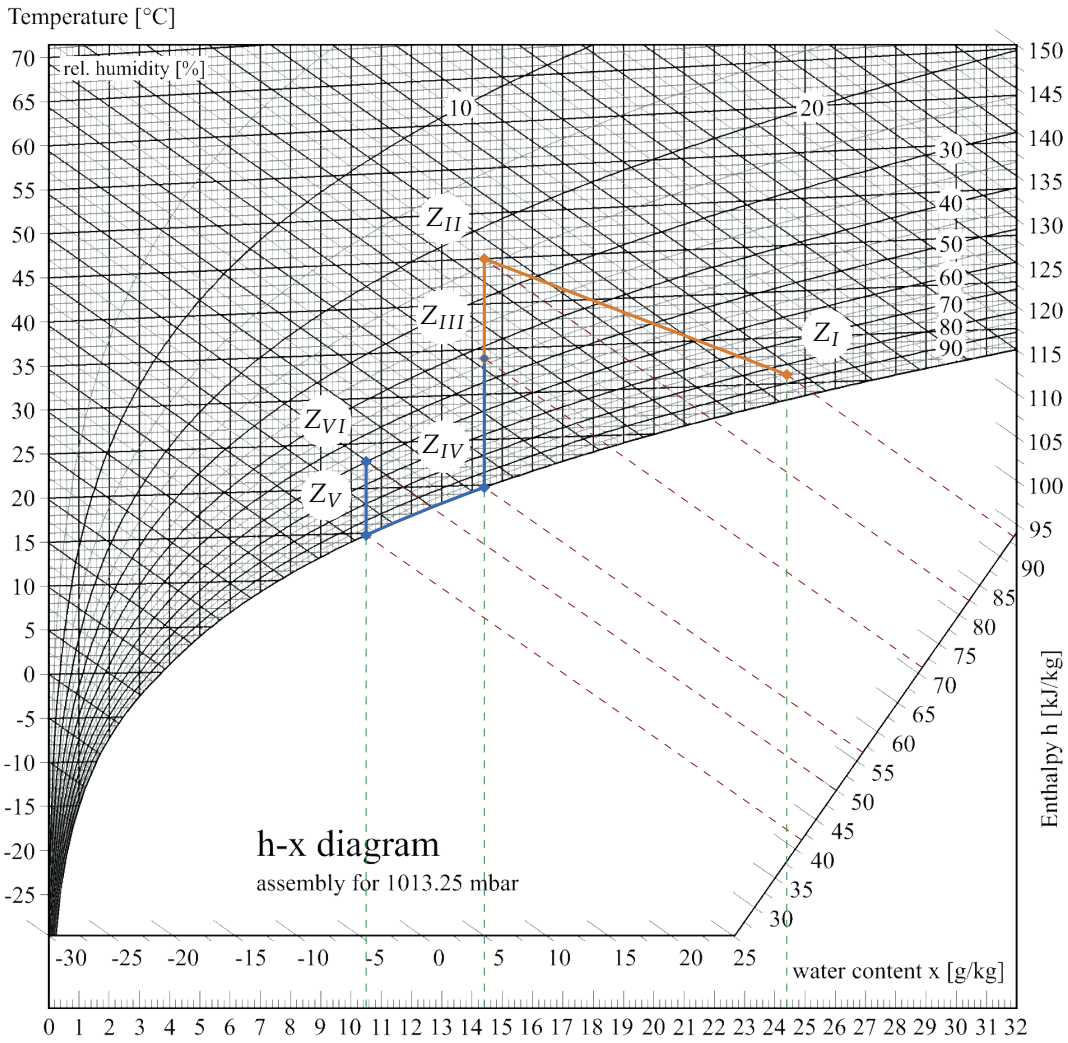

(a) Possible dehumidification process with *SA-T2* silica gel - scenario 2 (as per [7]).

State Z_i	ϑ_i [°C]	x_i [g/kg]	h_i [kJ/kg]	φ_i [%]
Z_I	31.0	24.4	93.5	85
Z_{II}	45.0	14.4	82.5	23.9
Z_{III}	34.0	14.4	71.0	43.1
Z_{IV}	19.7	14.4	56.5	100
Z_V	14.8	10.5	41.5	100
Z_{VI}	23.0	10.5	50	60

(b) Thermodynamic states of air as depicted in Fig. 71a, specific enthalpy values rounded to 0.5 kJ/kg.

Figure 71 & Table 33: Possible dehumidification process - scenario 2.

$3.82\,\mathrm{m}^3$. The reference consumption is therefor recalculated with this smaller volume and for every assessed air change rate. Otherwise, conditions remain unchanged, as no significant alterations were made to neither the window- and body area nor to *EVA*'s power train. After this adjustment, the reference consumption is calculated according to Eq. (3.4.1), and amounts to $P_{ref,5}$ = 3.048 kW for 5 ACH.
Lastly, the initial assumptions made by Agua regarding the ambient conditions during the pre-studies (as per Table 2a) differ slightly from the ones outlined above. In spite of the divergence in both temperature and relative humidity, the specific enthalpy of the two states differs by only $0.4\,\mathrm{kJ/kg}$. This is neglected herein, as it does not alter the result significantly. With a year-round operating time of 12 months, as is common in Singapore, the postulated Eq. (2.2.5) yields

$$\eta_{dh,5} = \frac{5\,ACH \;\; 3.82\,\mathrm{m}^3 \;\; 1.157\,\mathrm{kg/m}^3 \;\; 22\,\mathrm{kJ/kg}}{\left(\frac{12}{12} \;\; \frac{7.2\,\mathrm{kg}}{1500\,\mathrm{kg}} \;\; 0.36 \;\; 3048\,\mathrm{W} + 28.4\,\mathrm{W}\right) 3.6 \;\; \cdot \;\; 2.5} = 1.605 \tag{5.0.1}$$

This means that savings provided by this dehumidification setup outweigh the additional energy consumption by a factor of approximately 1.6. Because of the low air change rate, the effect on the vehicle's range is less pronounced - with the calculation method from Section 2.2, the A/C-system's power consumption is decreased by 9 %. The vehicle's available range increases by 1.4 %. To achieve air change rates of 15 ACH, as proposed in earlier chapters, the dehumidification system's performance needs to be increased. With the given process, this could be achieved in two ways: Firstly, the amount of desiccant can be expanded, and secondly, a desiccant that exhibits better drying performance can be applied. Both measures can of course be taken simultaneously.
Further analysis of the influence of the individual parameters in Eq. (5.0.1) provides insight into how to address the scale-up procedure. Fig. 72 shows the sensitivity towards the key factors: P_{ref} and COP are not part of the dehumidifier design, but are included to illustrate the significance of their accurate measurement, in order to obtain a meaningful result for η_{dh}.
Among the parameters that are dictated by the dehumidifier design, as expected, the dehumidifier's mass m_{dh} contributes the least amount - a 1 %-increase leads to a decrease in $\eta_{dh,5}$ by just 0.16 %. This is the result of the already low sensitivity of the investigated electric vehicle towards added mass. Adding more desiccant can therefore be considered a viable option. The addition of desiccant must, however, be conducted in a way so that the second-most important factor is increased by only the bare minimum: the additional power consumption P_{dh}, where an increase by one percent leads to a decrease in $\eta_{dh,5}$ by 0.84 %. P_{dh} is mainly determined by the fan power required to provide the necessary air flow while overcoming the pressure drop caused by the system. More specifically, the overall pressure drop can be divided into a part that is caused by ducts and air cooler, and another part determined by the characteristics of the packed bed (see Section 2.6.2). The main focus should therefor be on minimizing the additional pressure drop while increasing the flow rate. For the packed bed, this means that desiccant should be added while simultaneously increasing the packed bed's cross section, thus keeping the length constant. In the case at hand, the length is deemed suitable - as demonstrated by the experiments, the packed bed exhibits a satisfactory ratio of drying performance to pressure drop - especially at low flow rates. It is very important to note that the required fan power can not simply be scaled with affinity laws, as they only apply to the same fan type. As mentioned in Section 2.2, a different fan needs to be selected to fit the scale-up scenario. For example, blowers suitable for 15 ACH at a consumption of around 84 W, including regeneration air flow, are readily available from all major manufacturers. Since the additional mass m_{dh} is less relevant than the additional electrical consumption P_{dh}, a larger air cooler can also be considered in order to decrease the overall pressure drop.
With these results, a refined prediction regarding the dehumidifier's effect on vehicle performance can be attempted in the range up to 15 ACH: Simple linear up-scaling of the device geometry and desiccant mass suggest an increase in m_{dh} of 588 g per additional ACH. Accordingly, linear interpolation of required fan power yields 5.6 W per additional ACH. Following the principle from

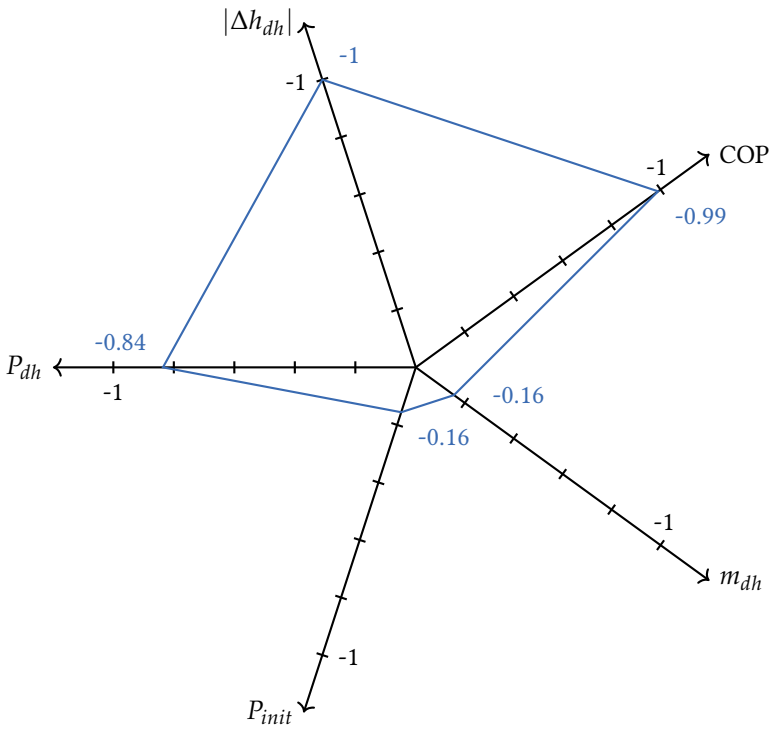

Figure 72: Sensitivity analysis of the influence of five parameters on η_{dh}

Section 2.2, the effect is visualized in the plots in Fig. 73 for a scenario with the same boundary conditions. A very important aspect of this plot to be considered is that the air change rates do not match with Fig. 12 due to the different interior volume. Furthermore, the plots are only applicable to the scenario sketched in Fig. 71a, since the numbers are based on the original assumptions by Agua [7]. Neither the result from Eq. (5.0.1) nor the plots in Fig. 73 quantitatively represent the more realistic setting from Fig. 70a. While the ambient conditions were comparable, the cabin conditions were chosen differently. These cause a lower load on the A/C system than the conditions in Fig. 70a, and consequently the consumption caused by the A/C is underestimated. This doesn't affect the absolute effect of the dehumidifier in terms of energy consumption reduction, but the effect on the percentage vehicle range will be different if the cabin temperature is set to lower values.
The second option to improve the performance of the dehumidification system, besides the addition of desiccant material, is the application of a desiccant that exhibits better drying performance at the same regeneration conditions. This can lead to a larger reduction in water content - thus further decreasing the enthalpy of the intake air, $|\Delta h_{dh}|$. This has the largest impact on $\eta_{dh,5}$, a change by 1 % in $|\Delta h_{dh}|$ directly causes a 1 % change in $\eta_{dh,5}$. As an example, the dashed plots in Fig. 73 illustrate the potential of the dehumidification system if the water content x could be decreased by Δx_{out-in} = -11 g/kg and Δx_{out-in} = -12 g/kg.
During the desorption experiments, it has been discovered that the proposed 30 minute operating cycles are not possible. The regeneration of the desiccant at the given conditions can not be completed in less than approximately 60 minutes, regardless of the loading of the desiccant. This is mainly caused by the time needed to heat up the desiccant. Also, it is likely aggravated by thermal losses to some extent, which could possibly be improved through a different design. However, the necessary design changes, like insulation, could affect the adsorption part of the process and the cool-down time negatively. Further improvement could be achieved by increasing the desorption air flow, but it is unlikely that this measure alone could decrease the necessary desorption time by 30 minutes. Another obvious solution, an auxiliary heater, would drastically reduce the efficiency of

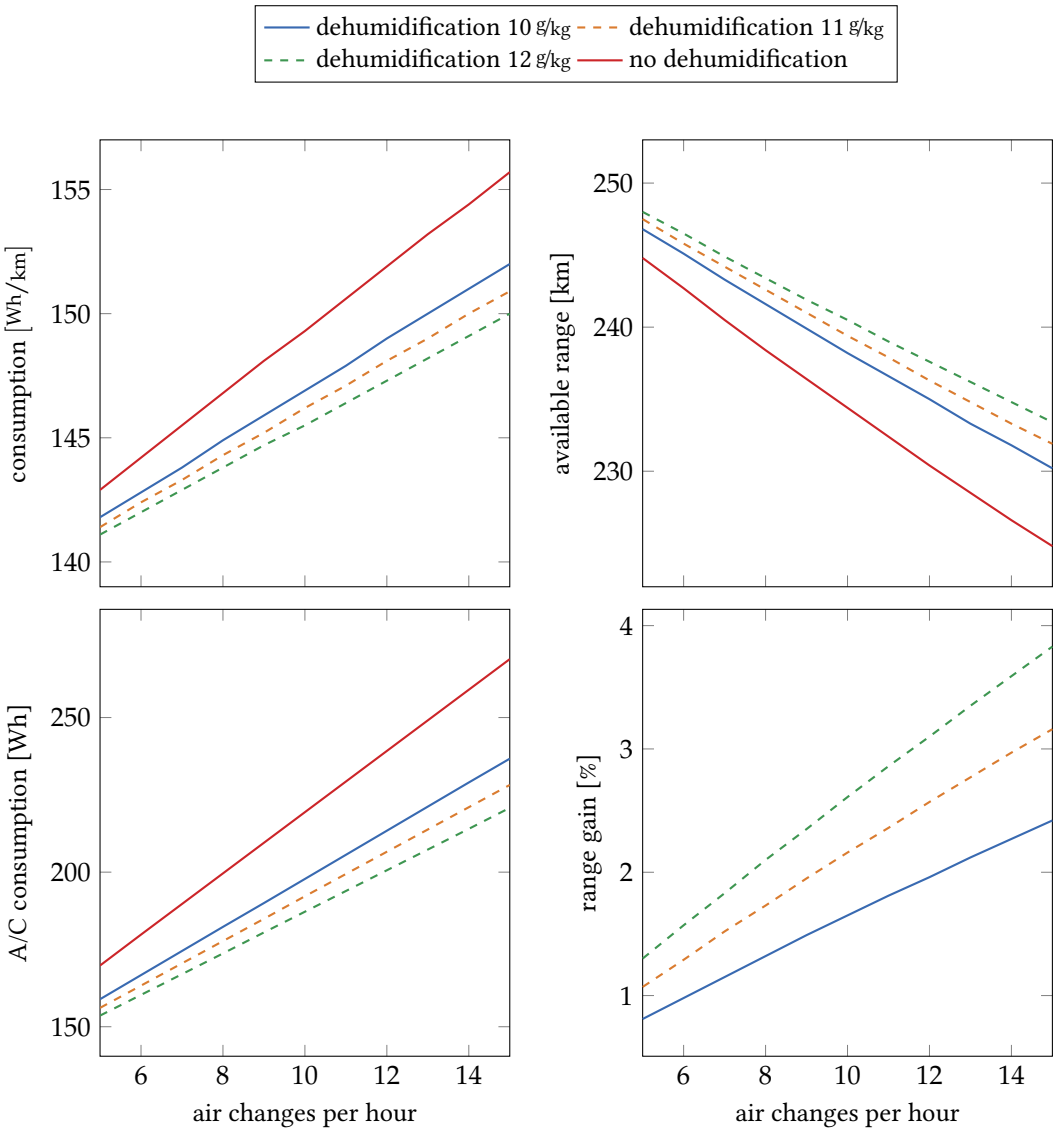

Figure 73: Effect of the outlined dehumidification process on range and consumption of *EVA* under the assumptions from Table 2a.

the dehumidification device and should thus only be considered if justified by the overall efficiency assessment.
As the dehumidification performance in the experimental setup is still maintained at a satisfactory level after 60 minutes, using operating cycles of the same duration seems the most favorable approach. The suggested improvements can of course be considered nevertheless.
This leads to the conclusion that the two most important factors to keep in mind when scaling up the device are: first, higher air change rates must be met by an increase in desiccant material, and can not simply be achieved by faster cycles. Second, when increasing the amount of desiccant, the pressure drop must be considered first and foremost, as an increased flow rate otherwise leads to an exponential increase in the dehumidifier fan's energy consumption.
Overall, these results show that satisfactory performance can be obtained even in this first iteration on lab scale. The conclusions drawn, along with necessary steps for further development, are the subject of the next chapter.

6

CONCLUSION

Summarizing the previous sections, it can be concluded that a desiccant-based dehumidification system constitutes a beneficial addition to an electric vehicle under certain boundary conditions. For the operating scenario that has been mainly investigated within the TUM CREATE program - electromobility in tropical megacities - the effect of active humidity reduction is presented based on simulations of the *EVA* prototype taxi. Literature studies on thermal comfort show that the presented, experimental system at hand is already capable of achieving comfortable air change rates in passenger cars. Here, the increase in air change rate at constant energy consumption, as well as the decrease in energy consumption at equal air change rate, outweigh the energy demand arising from weight increase and additional electricity consumption. One main takeaway is that the added weight, which is introduced by the dehumidification device, produces a much less severe adverse reaction than the additional energy consumption caused by the fans required to drive the process. Especially in scenarios where the device is used frequently, this aspect requires careful consideration. The added weight is more important when the question of installing the device at all is the more relevant one, for example in climate zones where the A/C is used only a few months per year. This is the main reason why, even for a purely experimental setup, the goal was to achieve an as-low-as-achievable system mass: with the laboratory system weighing in at just over 7.2 kg, this has been adequately realized. In Section 2.2, a simple method is suggested to quickly assess the usefulness of a dehumidification device in an electric vehicle under known boundary conditions.
From the possible approaches to drying the intake air, an adsorption-based solution is best suited for automotive application. Only solid-state desiccants that can undergo sorption processes which are fully reversible at low regeneration temperatures are suitable for electric vehicles.
The specific process design can be continuous, i.e. employing a desiccant wheel, or batch-type. In an experimental or prototype setup, the batch-type design has an edge, because many different material samples can be assessed with little effort. Manufacturing even a single desiccant wheel is a complicated and comparatively expensive procedure. However, once a suitable desiccant has been identified, the desiccant wheel might constitute a superior solution to the batch-type. Its truly continuous operation characteristics and the lack of a diverter valve system could constitute a real advantage for a mass-produced solution in the automotive industry. The prerequisite is of course, that the adsorption and regeneration characteristics that were found in the open system test stand can be replicated in a desiccant-coated wheel.
For the different material samples, the combination of N_2-adsorption measurements, thermal analysis and H_2O-isotherms yield enough information to qualitatively predict their behavior in the open system test stand. SEM imaging does not provide any further insights, but it was possible to verify the predicted structural properties of the *SBA-15* samples.
The open system test stand suffers from some shortcomings in maintaining constant experimentation parameters, which led to a tedious evaluation process of the individual experiments. This was especially prominent during the adsorption measurements. A setup with a more stable atmosphere generation chamber will clearly yield results that are directly comparable with one another, and facilitate the quantitative assessment of adsorption performance. Improving the pressure measurement with both better sensor placement and increased sensitivity will help to verify the pressure

drop over certain parts of the setup. Continuous air flow measurement would also prove very helpful. But even with the system's characteristics being less then ideal, the open system test stand yielded satisfactory results that substantiate the theoretically predicted process design. With many desiccant samples, good drying results show that significant energy savings are already achievable with this basic setup. A packed bed length of 50 mm to 60 mm seems like a good compromise between performance and pressure drop. Scale-up calculations illustrate that design modifications can drastically improve performance.

The open system results were obtained exclusively with commercial silica gel samples where enough material had been available. Other investigated desiccants are limited to the closed-system assessment. Some stand out far enough to justify further investigation in future projects: The *SBA-15*-type silica gels exhibit very large specific adsorption capacity - mainly attributable to their own low density. They also seem extremely well suited for high relative humidity - the high uptake capability make them a prime candidate in this segment. Unfortunately, their adsorption capacity at lower relative pressures, namely before the onset of capillary condensation at approximately 75 % relative humidity, is lower than that of unstructured silica gels. Their mechanical properties must also be investigated further. The best performance according to Table 22 could be expected from a hybrid material like *ARTS*, but the regeneration conditions and the long-term stability require further investigation.

Based on these results and the general evolution of electric vehicle technology, a few challenges and opportunities of the presented technology are identified in some closing remarks.

An argument can be made for the integration of an electric heater to fully dry the desiccant during charging breaks. While this is technically possible with little additional effort, it is a bit beside the point of using waste heat to drive the system. This approach would fundamentally change all considerations from the previous chapters - if the dehumidification device is only regarded as a range-extension system, a better and simpler method might be to increase the vehicle's battery size by the additional mass that the dehumidification system would introduce.

The proposed strategy of regenerating the desiccant with waste heat that is gathered in, and extracted from, the front thermal module, would require some variations from current designs and a different control strategy of the radiator blowers. Positioning the air cooler in a sufficiently cool air flow regime will help to maximize the system performance. The possibility of drying recirculated air in the adsorption system can also be considered. The overall practicability of the integration into a vehicle may depend on its type - while it might not be (economically) feasible in smaller cars, the case will be different in larger vehicles or even trucks.

For the regeneration part, emerging technologies can also help to improve the case: new legislation on refrigerants with a high GWP has recently pushed the development of alternative solutions, leading to a re-discovery of CO_2-based A/C systems. In the transcritical process, no traditional condenser is used, heat is instead rejected in a gas cooler which operates at higher temperatures than conventional, hydrofluorocarbon-based systems [157]. Although it is found in Section 4.3.2.5 that the effect of increased regeneration temperatures is minimal in a given desiccant, higher regeneration temperatures enable the use of a wider selection of adsorbents.

This leads to the final area in which room for improvement can be found: the adsorbent itself. Future desiccants may be accessible through the targeted synthesis of materials with specific properties. Introduced at the example of the *SBA-15*-type silica gels, variation of structural properties is already possible and common. Variation of surface groups could possibly be applied to other materials to tailor desired properties. Hybrid materials have been found to possess excellent characteristics, but they have yet to prove that those are sufficiently stable over extended usage periods.

All in all, it stands to reason that the proposed process deserves to remain under consideration for the application in electric vehicles, especially those operating in tropical climates. While many challenges are yet to be solved, the results at hand and the progress in all relevant fields are reason enough to be very optimistic about a real-world application in the near future.

BIBLIOGRAPHY

[1] Land Transport Authority of Singapore. Motor Vehicle Population by Type of Fuel Used. https://www.lta.gov.sg/content/dam/ltagov/who_we_are/statistics_and_publications/statistics/pdf/M09-Vehs_by_Fuel_Type.pdf, 2013. Accessed: 2013/10/16.

[2] Energy Market Authority of Singapore. Electric Vehicle Test-Bed. http://www.ema.gov.sg/ev, 2013. Accessed: 2013/10/16.

[3] Peel, M. C., Finlayson, B. L., and McMahon, T. A. Updated World Map of the Köppen-Geiger Climate Classification. *Hydrology and Earth System Sciences 11*, 5 (Oct. 2007), 1633–1644.

[4] Weber, R. Development of a Solar Roof Concept for the TUM CREATE Electric Taxi. Master's thesis, Technische Universität München, Lehrstuhl für Fahrzeugtechnik, Mar. 2013.

[5] Department of Economic and Social Affairs, Population Division. *World Urbanization Prospects: The 2011 Revision*, vol. ST/ESA/SER.A/322. United Nations, 2012, ch. The 30 Largest Urban Agglomerations Ranked by Population Size at Each Point in Time, 1950-2025, p. 318.

[6] ZSW Media Center - Data Service Renewable Energies. Electromobility Worldwide. https://www.zsw-bw.de/en/media-center/data-service.html#c6700, 2018. Accessed: 2019/11/19.

[7] Agua, F. M. M. Electric Vehicle Modeling and Simulation. Master's thesis, Technische Universität München - Lehrstuhl für Fahrzeugtechnik, 2012.

[8] Grossmann, H. *Pkw-Klimatisierung*. Springer Berlin Heidelberg, first ed., 2010. ISBN 9783642054952.

[9] Daly, S. *Automotive Air-Conditioning and Climate Control Systems*. Butterworth-Heinemann, first ed., July 2006. ISBN 9780750669559.

[10] Bhatti, M. S. Riding in Comfort: Part I - Evolution of Automotive Heating. *ASHRAE Journal 41*, 8 (Aug. 1999), 51–57.

[11] Bhatti, M. S. Riding in Comfort: Part II - Evolution of Automotive Air Conditioning. *ASHRAE Journal 41*, 9 (Sept. 1999), 44–50.

[12] Volkswagen AG. *Air Conditioner in the Motor Vehicle*. No. 208 in Self-Study Programme. Volkswagen AG, 1998.

[13] Hahne, E. *Technische Thermodynamik - Einführung und Anwendung*. Oldenbourg, München-Wien, 2004. ISBN 9783486576511.

[14] Park, Y. C., Kim, Y. C., and Min, M.-K. Performance Analysis on a Multi-Type Inverter Air Conditioner. *Energy Conversion and Management 42*, 13 (Sept. 2001), 1607–1621.

[15] Lemke, N., Mildenberger, J., and Graz, M. Unterstützung der Markteinführung von Pkw-Klimaanlagen mit dem Kältemittel CO2 (R744) - Prüfstandsmessungen und Praxistest. *Umweltbundesamt - Texte 64* (Oct. 2011), 59.

[16] Brown, J. S., Yana-Motta, S. F., and Domanski, P. A. Comparitive Analysis of an Automotive Air Conditioning Systems Operating with CO2 and R134a. *International Journal of Refrigeration 25*, 1 (Jan. 2002), 19–32.

[17] Deh, U. *Kfz-Klimaanlagen.* Vogel Fachbuchverlag, Würzburg, third ed., 2011. ISBN 9783834332127.

[18] Grundstein, A., Meentemeyer, V., and Dowd, J. Maximum Vehicle Cabin Temperatures under Different Meteorological Conditions. *International Journal of Biometeorology 53*, 3 (Feb. 2009), 255–261.

[19] Fanger, P. O. *Thermal Comfort. Analysis and Applications in Environmental Engineering.* Danish Technical Press., 1970.

[20] Fanger, P. O. Assessment of Man's Thermal Comfort in Practice. *Occupational and Environmental Medicine 30*, 4 (Oct. 1973), 313–324.

[21] van Hoof, J. Forty Years of Fanger's Model of Thermal Comfort: Comfort for All? *Indoor Air 18*, 3 (June 2008), 182–201.

[22] Alahmer, A., Mayyas, A., Mayyas, A. A., Omar, M. A., and Shan, D. Vehicular Thermal Comfort Models: A Comprehensive Review. *Applied Thermal Engineering 31*, 6-7 (May 2011), 995–1002.

[23] Frank, W. *Raumklima und thermische Behaglichkeit.* No. 104 in Berichte aus der Bauforschung. Verlag Ernst & Sohn, Berlin, 1975. ISBN 9783433007310.

[24] Temming, J. Fahrzeugklimatisierung und Verkehrssicherheit - Auswirkungen sommerlichen Klimas in Kfz auf die Leistungsfähigkeit der Fahrer. *FAT-Schriftenreihe 177* (2003).

[25] Lenzuni, P., Capone, P., Freda, D., and del Gaudio, M. Is Driving in a Hot Vehicle Safe? *International Journal of Hyperthermia 30*, 4 (June 2014), 250–257.

[26] Lee, K. Y. The East Asian Way-With Air Conditioning. *New Perspectives Quarterly 26*, 4 (Sept. 2009), 111–120.

[27] Kadle, P. S., and Bhatti, M. S. Dehumidifying Mechanism for Auto Air Conditioner with Improved Space Utilization and Thermal Efficiency. U.S. Patent 5,878,590, General Motors Corporation, Mar. 1999.

[28] Bhatti, M. S., Kadle, P. S., and Baker, J. A. Dehumidifying Mechanism for Auto Air Conditioner. U.S. Patent 5,509,275, General Motors Corporation, Apr. 1996.

[29] Northrup, Jr., L. L. Air Conditioning System with Regeneratable Desiccant Bed. U.S. Patent 4,180,985, Northrup, Incorporated, Jan. 1980.

[30] Kim, S., Kong, D., Lim, T., and Park, J. Reduced Power Demand with Hybrid Air Conditioning. *ATZ Worldwide 116*, 1 (Jan. 2014), 10–14.

[31] Baehr, H. D., and Kabelac, S. *Thermodynamik.* Springer Vieweg, BerlinHeidelberg, Apr. 2012. ISBN 9783642241604.

[32] Wagner, W., and Pruss, A. The IAPWS Formulation 1995 for the Thermodynamic Properties of Ordinary Water Substance for General and Scientific Use. *Journal of Physical and Chemical Reference Data 31*, 2 (2002), 387–535.

[33] Warnecke, G. *Meteorologie und Umwelt.* Springer Berlin Heidelberg, second ed., 1997. ISBN 9783540615934.

[34] Mollier, R. Das i, x-Diagramm für Dampfluftgemische. *Zeitschrift VDI 67* (1923).

[35] Ott, W., Klepeis, N., and Switzer, P. Air Change Rates of Motor Vehicles and In-Vehicle Pollutant Concentrations from Secondhand Smoke. *Journal of Exposure Science & Environmental Epidemiology 18*, 3 (July 2007), 312–325.

[36] Fletcher, B., and Saunders, C. J. Air Change Rates in Stationary and Moving Motor Vehicles. *Journal of Hazardous Materials 38*, 2 (Aug. 1994), 243–256.

[37] Grady, M. L., Jung, H., chul Kim, Y., Park, J. K., and Lee, B. C. Vehicle Cabin Air Quality with Fractional Air Recirculation. In *SAE Technical Paper Series* (Apr. 2013), SAE International.

[38] Jaakkola, J. J., Tuomaala, P., and Seppänen, O. Air Recirculation and Sick Building Syndrome: A Blinded Crossover Trial. *American Journal of Public Health 84*, 3 (Mar. 1994), 422–428.

[39] Zegenhagen, M. T., Ricart, C., Meyer, T., Kühn, R., and Ziegler, F. Experimental Investigation of a Liquid Desiccant System for Air Dehumidification Working with Ionic Liquids. *Energy Procedia 70* (May 2015), 544–551.

[40] Robens, E. Some Intriguing Items in the History of Adsorption. In *Characterization of Porous Solids III*. Elsevier, 1994, pp. 109–118.

[41] Scheele, C. W. *Chemische Abhandlung von der Luft und dem Feuer.* Magnus Swederus, Upsala und Leipzig, 1777.

[42] Kayser, H. Über die Verdichtung von Gasen an Oberflächen in ihrer Abhängigkeit von Druck und Temperatur. *Annalen der Physik 248*, 4 (1881), 526–537.

[43] Robens, E. Poröse Materialien - Kurze Vor- und Frühgeschichte. *Chemie Ingenieur Technik 82*, 6 (Apr. 2010), 763–768.

[44] Delhaes, P. *Science et Technique des Carbones : De l'Énergie aux Matériaux.* Lavoisier, Paris, 2012. ISBN 9782746245044.

[45] Rouquerol, J., Rouquerol, F., Llewellyn, P., Maurin, G., and Sing, K. S. W. *Adsorption by Powders and Porous Solids: Principles, Methodology and Applications.* Elsevier Science, second ed., 2013. ISBN 9780080970363.

[46] Dąbrowski, A. *Adsorption and Its Applications in Industry and Environmental Protection.* Elsevier Science, Amsterdam New York, 1999. ISBN 9780080557205.

[47] Ruthven, D. M. *Principles of Adsorption and Adsorption Processes.* Wiley-Interscience publication. Wiley, 1984. ISBN 9780471866060.

[48] Lennard-Jones, J. E. Processes of Adsorption and Diffusion on Solid Surfaces. *Transactions of the Faraday Society 28* (1932), 333.

[49] Sing, K. S. W. Reporting Physisorption Data for Gas/Solid Systems with Special Reference to the Determination of Surface Area and Porosity (Recommendations 1984). *Pure and Applied Chemistry 57*, 4 (Jan. 1985), 603–619.

[50] Lowell, S., Shields, J. E., Thomas, M. A., and Thommes, M. *Characterization of Porous Solids and Powders: Surface Area, Pore Size and Density.* Particle Technology Series. Springer Netherlands, 2006. ISBN 9781402023026.

[51] Nic, M., Jirat, J., Kosata, B., and Jenkins, A. *Compendium of Chemical Terminology - The "Gold Book".* IUPAC, second ed., 2006. ISBN 9780967855097.

[52] Bathen, D., and Breitbach, M. *Adsorptionstechnik*. VDI-Buch. Springer Berlin Heidelberg, Berlin, Heidelberg, 2013. ISBN 9783642182358.

[53] Do, D. D. *Adsorption Analysis: Equilibria and Kinetics*. Series on Chemical Engineering. World Scientific Publishing Co., Sept. 1998. ISBN 9781860941306.

[54] Brunauer, S., Emmett, P. H., and Teller, E. Adsorption of Gases in Multimolecular Layers. *Journal of the American Chemical Society 60*, 2 (Feb. 1938), 309–319.

[55] Langmuir, I. The Adsorption of Gases on Plane Surfaces of Glass, Mica and Platinum. *Journal of the American Chemical Society 40*, 9 (Sept. 1918), 1361–1403.

[56] Everett, D. H. Manual of Symbols and Terminology for Physicochemical Quantities and Units, Appendix II: Definitions, Terminology and Symbols in Colloid and Surface Chemistry. *Pure and Applied Chemistry 31*, 4 (Jan. 1972), 577–638.

[57] Sing, K. S. W., and Williams, R. T. Historical Aspects of Capillarity and Capillary Condensation. *Microporous and Mesoporous Materials 154* (May 2012), 16–18.

[58] Burgess, C. G. V., and Everett, D. H. The Lower Closure Point in Adsorption Hysteresis of the Capillary Condensation Type. *Journal of Colloid and Interface Science 33*, 4 (Aug. 1970), 611–614.

[59] Kadlec, O., and Dubinin, M. M. Comments on the Limits of Applicability of the Mechanism of Capillary Condensation. *Journal of Colloid and Interface Science 31*, 4 (Dec. 1969), 479–489.

[60] Harris, M. R. A Source of Error in Computation of Pore Size Data from Nitrogen Sorption Isotherms, 1965.

[61] BEL Japan, Inc. *BELSORP Precision Vapor Adsorption Measuring System - Belsorp-aqua3 Instruction Manual*. BEL Japan, Inc., 1-9-1, Haradanaka, Toyonaka, Osaka, Japan 561-0807, 2014.

[62] Quantachrome Instruments. *autosorb iQ and ASiQwin Gas Sorption System Operating Manual*, 05098-4.0 rev c ed. Quantachrome Instruments, 1900 Corporate Drive Boynton Beach, Florida, 33426 USA, 2009-2015.

[63] Haynes, J. M. Pore Size Analysis According to the Kelvin Equation. *Matériaux et Constructions 6*, 3 (May 1973), 209–213.

[64] Barrett, E. P., Joyner, L. G., and Halenda, P. P. The Determination of Pore Volume and Area Distributions in Porous Substances. I. Computations from Nitrogen Isotherms. *Journal of the American Chemical Society 73*, 1 (Jan. 1951), 373–380.

[65] Cranston, R. W., and Inkley, F. A. The Determination of Pore Structures from Nitrogen Adsorption Isotherms. In *Advances in Catalysis*. Elsevier, 1957, pp. 143–154.

[66] Dollimore, D., and Heal, G. R. An Improved Method for the Calculation of Pore Size Distribution from Adsorption Data. *Journal of Applied Chemistry 14*, 3 (Mar. 1964), 109–114.

[67] Broekhoff, J. C. P., and de Boer, J. H. Studies on Pore Systems in Catalysts IX. Calculation of Pore Distributions from the Adsorption Branch of Nitrogen Sorption Isotherms in the Case of Open Cylindrical Pores A. Fundamental Equations. *Journal of Catalysis 9*, 1 (Sept. 1967), 8–14.

[68] Broekhoff, J. C. P., and de Boer, J. H. Studies on Pore Systems in Catalysts X. Calculations of Pore Distributions from the Adsorption Branch of Nitrogen Sorption Isotherms in the Case of Open Cylindrical Pores B. Applications. *Journal of Catalysis 9*, 1 (Sept. 1967), 15–27.

[69] Ravikovitch, P. I., and Neimark, A. V. Characterization of Micro- and Mesoporosity in SBA-15 Materials from Adsorption Data by the NLDFT Method. *The Journal of Physical Chemistry B 105*, 29 (July 2001), 6817–6823.

[70] Ravikovitch, P. I., and Neimark, A. V. Density Functional Theory of Adsorption in Spherical Cavities and Pore Size Characterization of Templated Nanoporous Silicas with Cubic and Three-Dimensional Hexagonal Structures. *Langmuir 18*, 5 (Mar. 2002), 1550–1560.

[71] Choma, J., and Jaroniec, M. Applicability of Classical Methods of Pore Size Analysis for MCM-41 and SBA-15 Silicas. *Applied Surface Science 253*, 13 SPEC. ISS. (Apr. 2007), 5587–5590.

[72] Choma, J., Jaroniec, M., Burakiewicz-Mortka, W., and Kloske, M. Critical Appraisal of Classical Methods for Determination of Mesopore Size Distributions of MCM-41 Materials. *Applied Surface Science 196*, 1-4 (Aug. 2002), 216–223.

[73] Pedram, E. O., and Hines, A. L. Pure Vapor Adsorption of Water on Mobil Sorbead R Silica Gel. *Journal of Chemical & Engineering Data 28*, 1 (Jan. 1983), 11–14.

[74] Barton, S. S., Evans, M. J. B., Holland, J., and Koresh, J. E. Water and Cyclohexane Vapour Adsorption on Oxidized Porous Carbon. *Carbon 22*, 3 (1984), 265–272.

[75] Serbezov, A. Adsorption Equilibrium of Water Vapor on F-200 Activated Alumina. *Journal of Chemical & Engineering Data 48*, 2 (Mar. 2003), 421–425.

[76] Li, G., Xiao, P., Webley, P. A., Zhang, J., and Singh, R. Competition of CO2/H2O in Adsorption Based CO2 Capture. *Energy Procedia 1*, 1 (Feb. 2009), 1123–1130.

[77] Hu, Z., and Srinivasan, M. P. Preparation of High-Surface-Area Activated Carbons from Coconut Shell. *Microporous and Mesoporous Materials 27*, 1 (Jan. 1999), 11–18.

[78] BASF Catalysts. *F-220 Activated Alumina for Liquid and Gas Drying - Product Data Sheet*, bf-9212 rev. 12/09 ed. BASF SE, 67056 Ludwigshafen, Germany, Dec. 2009.

[79] Breck, D. W. *Zeolite Molecular Sieves: Structure, Chemistry, and Use.* Wiley, New York, 1973. ISBN 9780471099857.

[80] Puppe, L. Zeolithe - Eigenschaften und technische Anwendungen. *Chemie in unserer Zeit 20*, 4 (Aug. 1986), 117–127.

[81] Moore, E. A., and Smart, L. E. *Solid State Chemistry.* CRC Press, fourth ed., 2017. ISBN 9781439847909.

[82] Hauer, A. *Beurteilung fester Adsorbentien in offenen Sorptionssystemen für energetische Anwendungen.* PhD thesis, Technische Universität Berlin, Fakultät III - Prozesswissenschaften, 2002.

[83] Luna, F., Cecilia, J., Saboya, R., Barrera, D., Sapag, K., Rodríguez-Castellón, E., and Cavalcante, C. Natural and Modified Montmorillonite Clays As Catalysts for Synthesis of Biolubricants. *Materials 11*, 9 (Sept. 2018), 1764.

[84] Christy, A. A. Effect of Heat on the Adsorption Properties of Silica Gel. *International Journal of Engineering and Technology 4*, 4 (2012), 484–488.

[85] Mortimer, C. E., and Müller, U. *Chemie.* Georg Thieme Verlag KG, tenth ed., Oct. 2010. ISBN 9783134843101.

[86] Dengler, W., and Blenke, H. Untersuchung des Einflusses der Alterung technischer Adsorbentien auf das Adsorptionsgleichgewicht und die Sorptionsgeschwindigkeit. *Chemie Ingenieur Technik 46*, 6 (Mar. 1974), 244–245.

[87] Kresge, C. T., Leonowicz, M. E., Roth, W. J., Vartuli, J. C., and Beck, J. S. Ordered Mesoporous Molecular Sieves Synthesized by a Liquid-Crystal Template Mechanism. *Nature 359*, 6397 (Oct. 1992), 710–712.

[88] Björk, E. M. Synthesizing and Characterizing Mesoporous Silica SBA-15: A Hands-On Laboratory Experiment for Undergraduates Using Various Instrumental Techniques. *Journal of Chemical Education 94*, 1 (Dec. 2016), 91–94.

[89] Wanka, G., Hoffmann, H., and Ulbricht, W. Phase Diagrams and Aggregation Behavior of Poly(oxyethylene)-poly(oxypropylene)-poly(oxyethylene) Triblock Copolymers in Aqueous Solutions. *Macromolecules 27*, 15 (July 1994), 4145–4159.

[90] Hoffmann, F., Cornelius, M., Morell, J., and Fröba, M. Silica-Based Mesoporous Organic–Inorganic Hybrid Materials. *Angewandte Chemie International Edition 45*, 20 (May 2006), 3216–3251.

[91] Sattler, K., and Hoffmann, H. Ein neuartiger Glykolprecursor für Templatsynthesen und seine Wechselwirkung mit Tensid. *Chemie Ingenieur Technik 72*, 5 (May 2000), 487–491.

[92] de Ávila, S. G., Silva, L. C. C., and Matos, J. R. Optimisation of SBA-15 Properties Using Soxhlet Solvent Extraction for Template Removal. *Microporous and Mesoporous Materials 234* (Nov. 2016), 277–286.

[93] Hartmann, M., and Vinu, A. Mechanical Stability and Porosity Analysis of Large-Pore SBA-15 Mesoporous Molecular Sieves by Mercury Porosimetry and Organics Adsorption. *Langmuir 18*, 21 (Oct. 2002), 8010–8016.

[94] Chen, D., Wang, L., Ma, Y., and Yang, W. Super-Adsorbent Material Based on Functional Polymer Particles with a Multilevel Porous Structure. *NPG Asia Materials 8*, 8 (Aug. 2016), e301–e301.

[95] Henninger, S. K., Habib, H. A., and Janiak, C. MOFs as Adsorbents for Low Temperature Heating and Cooling Applications. *Journal of the American Chemical Society 131*, 8 (feb 2009), 2776–2777.

[96] Nóbrega, C. E. L., and Brum, N. C. L. *Desiccant-Assisted Cooling: Fundamentals and Applications*. Springer London, 2013. ISBN 9781447155645.

[97] Harriman, L. G. *The Dehumidification Handbook*. Munters Corporation, Amesbury, MA, second ed., 2002. ISBN 9780971788701.

[98] Angrisani, G., Minichiello, F., Roselli, C., and Sasso, M. Experimental Analysis on the Dehumidification and Thermal Performance of a Desiccant Wheel. *Applied Energy 92* (Apr. 2012), 563–572.

[99] Zhang, L. Z., and Niu, J. L. Performance Comparisons of Desiccant Wheels for Air Dehumidification and Enthalpy Recovery. *Applied Thermal Engineering 22*, 12 (Aug. 2002), 1347–1367.

[100] Dantherm Air Handling A/S. *Portable Adsorption Dehumidification*. Dantherm Air Handling A/S, Marienlystvej 65 DK-7800 Skive, Denmark, Jan. 2013.

[101] Geankoplis, C. J. *Transport Processes and Separation Process Principles: Includes Unit Operations*. Prentice Hall Professional technical reference. Prentice Hall Professional Technical Reference, Upper Saddle River, NJ, 2003. ISBN 9780131013674.

[102] Kruczek, B. Carman–Kozeny Equation. In *Encyclopedia of Membranes*. Springer Berlin Heidelberg, Berlin, Heidelberg, 2014, pp. 1–3.

[103] Brauer, H. Druckverlust in Füllkörpersäulen bei Einphasenströmung. *Chemie Ingenieur Technik 29*, 12 (Dec. 1957), 785–790.

[104] Brownell, L. E., Gami, D. C., Miller, R. A., and Nekarvis, W. F. Pressure Drop through Porous Media. *AIChE Journal 2*, 1 (Mar. 1956), 79–81.

[105] Jeschar, R. Druckverlust in Mehrkornschüttungen aus Kugeln. *Archiv für das Eisenhüttenwesen 35*, 2 (Feb. 1964), 91–108.

[106] Stichlmair, J., Bravo, J. L., and Fair, J. R. General Model for Prediction of Pressure Drop and Capacity of Countercurrent Gas/liquid Packed Columns. *Gas Separation & Purification 3*, 1 (Mar. 1989), 19–28.

[107] Ergun, S. Fluid Flow through Packed Columns. *Chemical Engineering Progress 48* (1952), 89–94.

[108] Reichelt, W. Zur Berechnung des Druckverlustes einphasig durchströmter Kugel-und Zylinderschüttungen. *Chemie Ingenieur Technik 44*, 18 (Sept. 1972), 1068–1071.

[109] Eisfeld, B., and Schnitzlein, K. The Influence of Confining Walls on the Pressure Drop in Packed Beds. *Chemical Engineering Science 56*, 14 (July 2001), 4321–4329.

[110] Merck Millipore. *Dry and Safe - Drying Agents from Merck Millipore*, W.283123 ed. Merck KGaA, 64271 Darmstadt, Germany, June 2013.

[111] Anderson, J. H., and Parks, G. A. Electrical Conductivity of Silica Gel in the Presence of Adsorbed Water. *The Journal of Physical Chemistry 72*, 10 (Oct. 1968), 3662–3668.

[112] DIN 66134. Determination of the Pore Size Distribution and the Specific Surface Area of Mesoporous Solids by Means of Nitrogen Sorption - Method of Barrett, Joyner and Halenda (BJH). Standard, Beuth Verlag GmbH, Saatwinkler Damm 42/43, 13627 Berlin, Feb. 1998.

[113] DIN 66139. Pore Size Analysis - Representation of Pore Size Distributions. Standard, Beuth Verlag GmbH, Saatwinkler Damm 42/43, 13627 Berlin, Mar. 2012.

[114] ISO 9277. Determination of the Specific Surface Area of Solids by Gas Adsorption - Bet Method. Standard, International Organization for Standardization, Geneva, CH, Sept. 2010.

[115] ISO 15901-2. Pore Size Distribution and Porosity of Solid Materials by Mercury Porosimetry and Gas Adsorption — Part 2: Analysis of Mesopores and Macropores by Gas Adsorption. Standard, International Organization for Standardization, Geneva, CH, Feb. 2006.

[116] Dubinin, M. M. Theory of the Physical Adsorption of Gases and Vapors and Adsorption Properties of Adsorbents of Various Natures and Porous Structures. *Bulletin of the Academy of Sciences of the USSR, Division of Chemical Science 9*, 7 (July 1960), 1072–1078.

[117] Shull, C. G. The Determination of Pore Size Distribution from Gas Adsorption Data. *Journal of the American Chemical Society 70*, 4 (Apr. 1948), 1405–1410.

[118] Lippens, B. C., Linsen, B. G., and de Boer, J. H. Studies on Pore Systems in Catalysts I. The Adsorption of Nitrogen; Apparatus and Calculation. *Journal of Catalysis 3*, 1 (Feb. 1964), 32–37.

[119] Halsey, G. Physical Adsorption on Non-Uniform Surfaces. *The Journal of Chemical Physics 16*, 10 (Oct. 1948), 931–937.

[120] Magee, R. W. Evaluation of the External Surface Area of Carbon Black by Nitrogen Adsorption. *Rubber Chemistry and Technology 68*, 4 (Sept. 1995), 590–600.

[121] de Boer, J. H., Lippens, B. C., Linsen, B. G., Broekhoff, J. C. P., van den Heuvel, A., and Osinga, T. J. The t-curve of Multimolecular N2-Adsorption. *Journal of Colloid and Interface Science 21*, 4 (Apr. 1966), 405–414.

[122] Harkins, W. D., and Jura, G. Surfaces of Solids. XIII. A Vapor Adsorption Method for the Determination of the Area of a Solid without the Assumption of a Molecular Area, and the Areas Occupied by Nitrogen and Other Molecules on the Surface of a Solid. *Journal of the American Chemical Society 66*, 8 (Aug. 1944), 1366–1373.

[123] Brunauer, S., and Emmett, P. H. The Use of Van Der Waals Adsorption Isotherms in Determining the Surface Area of Iron Synthetic Ammonia Catalysts. *Journal of the American Chemical Society 57*, 9 (Sept. 1935), 1754–1755.

[124] IAPWS (International Association for the Properties Water and Steam). Release on the Values of Temperature, Pressure and Density of Ordinary and Heavy Water Substances at their Respective Critical Points. http://www.iapws.org/release, 1992.

[125] Budzikiewicz, H., and Schäfer, M. *Massenspektrometrie*. Wiley-VCH GmbH, July 2012. ISBN 9783527329113.

[126] Chakraborty, A., Saha, B. B., Koyama, S., Ng, K. C., and Srinivasan, K. Adsorption Thermodynamics of Silica Gel-Water Systems†. *Journal of Chemical & Engineering Data 54*, 2 (Feb. 2009), 448–452.

[127] Chakraborty, A., Saha, B. B., Koyama, S., and Ng, K. C. Specific Heat Capacity of a Single Component Adsorbent-Adsorbate System. *Applied Physics Letters 90*, 17 (Apr. 2007), 171902.

[128] Memmert GmbH. *Memmert Universal Oven UN/UF - Operating Instructions*, d24022 ed. Memmert GmbH + Co. KG, Willi-Memmert-Straße 90-96 , D-91186 Büchenbach, Oct. 2014.

[129] Piesche. *Grundlagen der Mechanischen Verfahrenstechnik - Skriptum zur Vorlesung*. Universität Stuttgart, 2007.

[130] Brauer, H., and Varma, Y. B. G. *Air Pollution Control Equipment*. Springer Berlin Heidelberg, 1981.

[131] Pesaran, A. A., and Mills, A. F. Moisture Transport in Silica Gel Packed Beds—II. Experimental Study. *International Journal of Heat and Mass Transfer 30*, 6 (June 1987), 1051–1060.

[132] Dullien, F. A. L. *Porous Media - Fluid Transport and Pore Structure*. Academic Press, San Diego, second ed., 1992. ISBN 9780122236518.

[133] Sanyo Denki. *San Ace B97*. Sanyo Denki Co.,Ltd., 3-33-1 Minami-Otsuka, Toshima-ku, Tokyo, 170-8451, Japan, 2015.

[134] Pololu Corporation. *Pololu Maestro Servo Controller User's Guide*. Pololu Corporation, 920 Pilot Rd. Las Vegas, NV 89119 USA, 2014.

[135] de Magalhães, G. O., de Oliveira Notório Ribeiro, J., Vasconcelos, D. C. L., and Vasconcelos, W. L. Production of Pure Granules of SBA-15 Mesoporous Silica. *Materials Research 21*, 6 (Aug. 2018).

[136] Thommes, M., Köhn, R., and Fröba, M. Sorption and Pore Condensation Behavior of Pure Fluids in Mesoporous MCM-48 Silica, MCM-41 Silica, SBA-15 Silica and Controlled-pore Glass at Temperatures above and below the Bulk Triple Point. *Applied Surface Science 196*, 1-4 (Aug. 2002), 239–249.

[137] Thielemann, J. P., Girgsdies, F., Schlögl, R., and Hess, C. Pore Structure and Surface Area of Silica SBA-15: Influence of Washing and Scale-Up. *Beilstein Journal of Nanotechnology 2* (Feb. 2011), 110–118.

[138] Reichhardt, N. V., Nylander, T., Klösgen, B., Alfredsson, V., and Kocherbitov, V. Porosity and Surface Properites of SBA-15 with Grafted PNIPAAM: A Water Sorption Calorimetry Study. *Langmuir 27*, 22 (Nov. 2011), 13838–13846.

[139] Znamenskaya, Y., Björklund, S., Kocherbitov, V., and Alfredsson, V. Effect of Hydration and Dehydration on the Properties of SBA-15 Layer Studied by Humidity Scanning QCM-D. *Microporous and Mesoporous Materials 230* (Aug. 2016), 58–65.

[140] Everett, D. H., Parfitt, G. D., Sing, K. S. W., and Wilson, R. The SCI/IUPAC/NPL Project on Surface Area Standards. *Journal of Applied Chemistry and Biotechnology 24*, 4-5 (Apr. 1974), 199–219.

[141] Gregg, S. J., and Sing, K. S. W. *Adsorption, Surface Area and Porosity.* Academic Press, second ed., 1982. ISBN 9780123009562.

[142] Rouquerol, J., Llewellyn, P., and Rouquerol, F. Is the BET Equation Applicable to Microporous Adsorbents? In *Studies in Surface Science and Catalysis*, vol. 160. Elsevier, 2007, pp. 49–56.

[143] Gordeeva, L. G., and Aristov, Y. I. Composites 'Salt inside Porous Matrix' for Adsorption Heat Transformation: A Current State-of-the-Art and New Trends. *International Journal of Low-Carbon Technologies 7*, 4 (June 2012), 288–302.

[144] Sing, K. S. W., and Williams, R. T. Physisorption Hysteresis Loops and the Characterization of Nanoporous Materials. *Adsorption Science & Technology 22*, 10 (Dec. 2004), 773–782.

[145] Kraehenbuehl, F., Stoeckli, H. F., Brunner, F., Kahr, G., and Mueller-Vonmoos, M. Study of the Water-Bentonite System by Vapour Adsorption, Immersion Calorimetry and X-Ray Techniques: I. Micropore Volumes and Internal Surface Areas, Following Dubinin's Theory. *Clay Minerals 22*, 1 (Mar. 1987), 1–9.

[146] Aristov, Y. I., Tokarev, M. M., Cacciola, G., and Restuccia, G. Selective Water Sorbents for Multiple Applications, 1. CaCl2 Confined in Mesopores of Silica Gel: Sorption Properties. *Reaction Kinetics and Catalysis Letters 59*, 2 (Nov. 1996), 325–333.

[147] BEL Japan, Inc. *BELSORP Precision Vapor Adsorption Measuring System - Belsorp Analysis Software User's Manual.* BEL Japan, Inc., 1-9-1, Haradanaka, Toyonaka, Osaka, Japan 561-0807, 2013.

[148] Rezk, A. R. M. *Theoretical and Experimental Investigation of Silica Gel / Water Adsorption Refrigeration Systems.* PhD thesis, University of Birmingham, College of Engineering & Physical Sciences, 2012.

[149] Wang, X., Zimmermann, W., Ng, K. C., Chakraboty, A., and Keller, J. U. Investigation on the Isotherm of Silica Gel+Water Systems. *Journal of Thermal Analysis and Calorimetry 76*, 2 (2004), 659–669.

[150] Wang, D., Zhang, J., Yang, Q., Li, N., and Sumathy, K. Study of Adsorption Characteristics in Silica Gel–Water Adsorption Refrigeration. *Applied Energy 113* (Jan. 2014), 734–741.

[151] Kruk, M., Jaroniec, M., Ko, C. H., and Ryoo, R. Characterization of the Porous Structure of SBA-15. *Chemistry of Materials 12*, 7 (July 2000), 1961–1968.

[152] Honeywell International Inc. *Heavy Duty Pressure Transducers - PX2 Series*, 50069942 rev. g - en ed. Sensing and Control, 1985 Douglas Drive North Golden Valley, MN 55422, Mar. 2014.

[153] BASF Catalysts. *KC-Trockenperlen WS - Produktdatenblatt*, bf-9248 ger a4 rev. 08/11 ed. BASF SE, 67056 Ludwigshafen, Germany, Aug. 2011.

[154] Logan, E. *Handbook of Turbomachinery*. M. Dekker, New York, 2003. ISBN 9780824748470.

[155] McPherson, M. J. *Subsurface Ventilation and Environmental Engineering*. Springer Netherlands, 1993. ISBN 9789401115506.

[156] Jeong, J., Yamaguchi, S., Saito, K., and Kawai, S. Performance Analysis of Desiccant Dehumidification Systems Driven by Low-grade Heat Source. *International Journal of Refrigeration 34*, 4 (June 2011), 928–945.

[157] Lorentzen, G., and Pettersen, J. A New, Efficient and Environmentally Benign System for Car Air-Conditioning. *International Journal of Refrigeration 16*, 1 (Jan. 1993), 4–12.

[158] Rodes, C., Sheldon, L., Whitaker, D., Clayton, A., Fitzgerald, K., Flanagan, J., DiGenova, F., Hering, S., and Frazier, C. Measuring Concentrations of Selected Air Pollutants inside California Vehicles: Final Report. Tech. Rep. dot:15680, California Environmental Protection Agency, 1998.

[159] Offermann, F. J., Colfer, R., Radzinski, P., and Robertson, J. Exposure to Environmental Tobacco Smoke in an Automobile. In *Proceedings of the 9th International Conference on Indoor Air Quality and Climate* (2002), pp. 506–511.

[160] Knibbs, L. D., de Dear, R. J., and Atkinson, S. E. Field Study of Air Change and Flow Rate in Six Automobiles. *Indoor Air 19*, 4 (Aug. 2009), 303–313.

[161] Engelmann, R. J., Pendergrass, W. R., White, J. R., and Hall, M. E. The Effectiveness of Stationary Automobiles As Shelters in Accidental Releases of Toxic Materials. *Atmospheric Environment. Part A. General Topics 26*, 17 (Dec. 1992), 3119–3125.

[162] Park, J. H., Spengler, J. D., Yoon, D. W., Dumyahn, T., Lee, K., and Ozkaynak, H. Measurement of Air Exchange Rate of Stationary Vehicles and Estimation of In-vehicle Exposure. *Journal of Exposure Analysis and Environmental Epidemiology 8* (1998), 65–78.

LIST OF FIGURES

LIST OF TABLES

A

RESULT PLOTS

Due to the large amount of measurement data gathered, a plot is only included in the main section of this thesis when needed. For the purpose of completeness and for reference, the plots for all remaining measurements are comprehensively collected in this appendix. Presented are

- N_2-Isotherms
- BJH Plots
- BET Plots
- TGA-MS Plots
- Open System Plots

in the order corresponding to the outline of Chapter 4.

A.1 N_2-ISOTHERMS

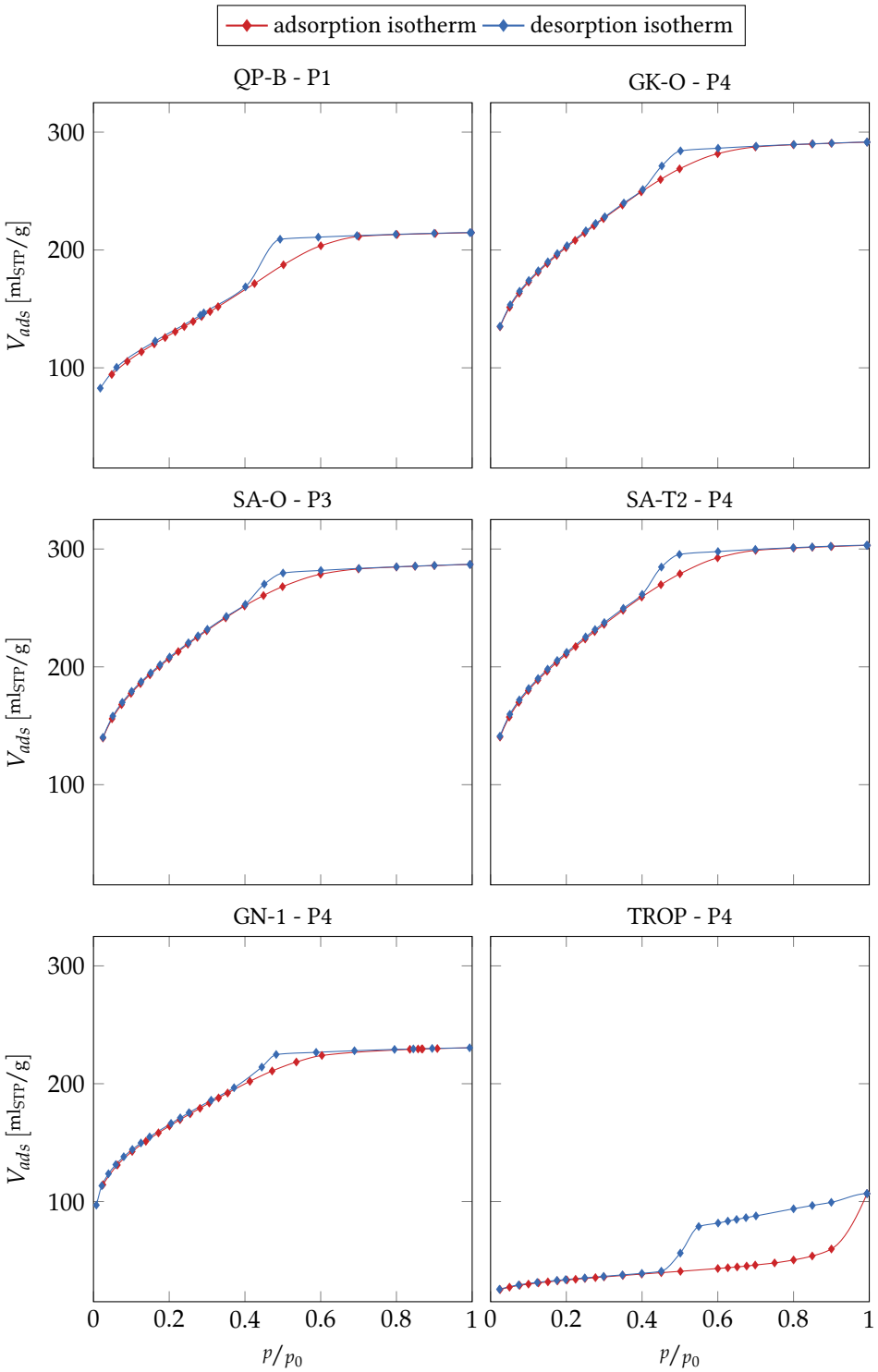

Figure 74: Compilation of N_2-isotherms for different materials.

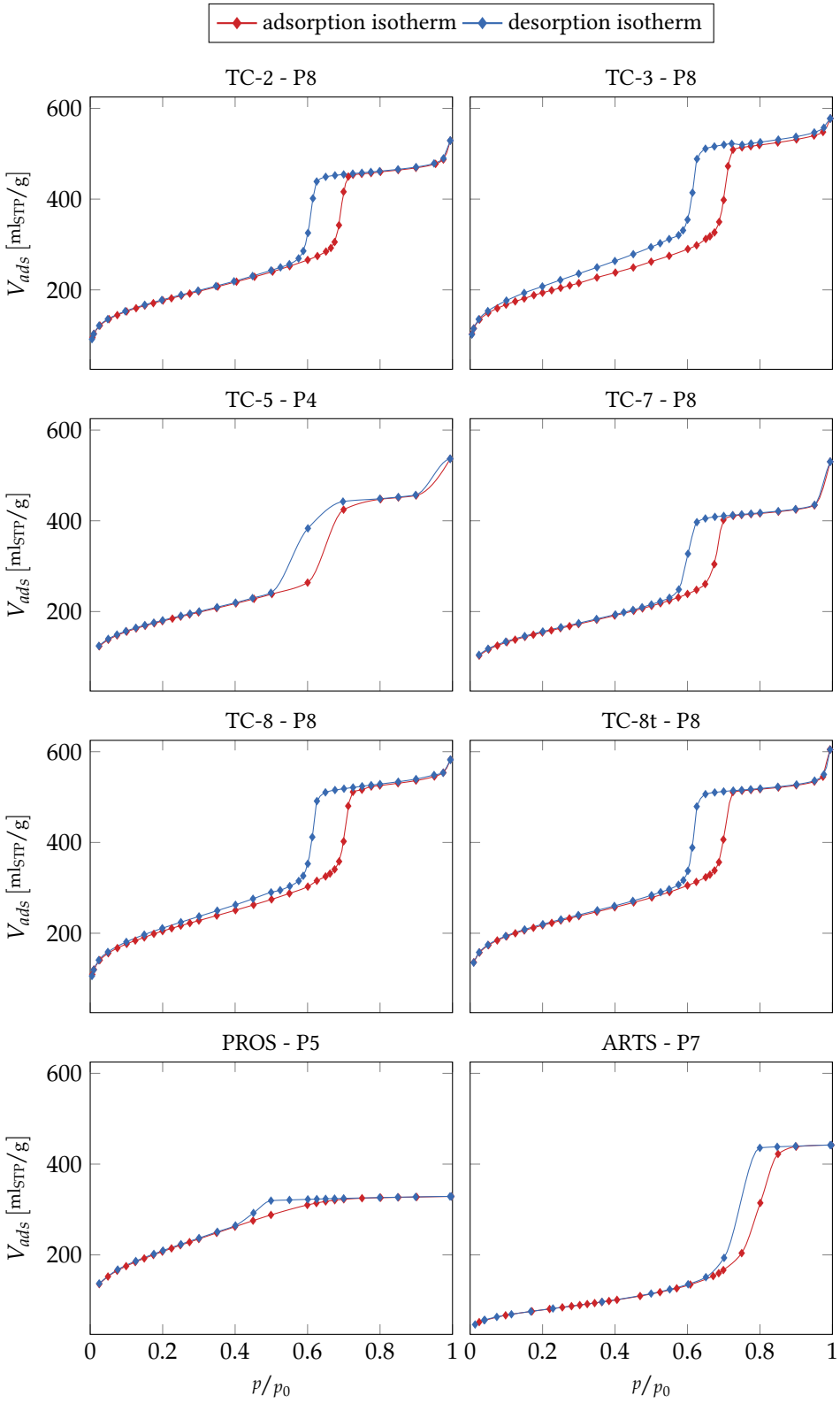

Figure 75: Compilation of N_2-isotherms for different materials.

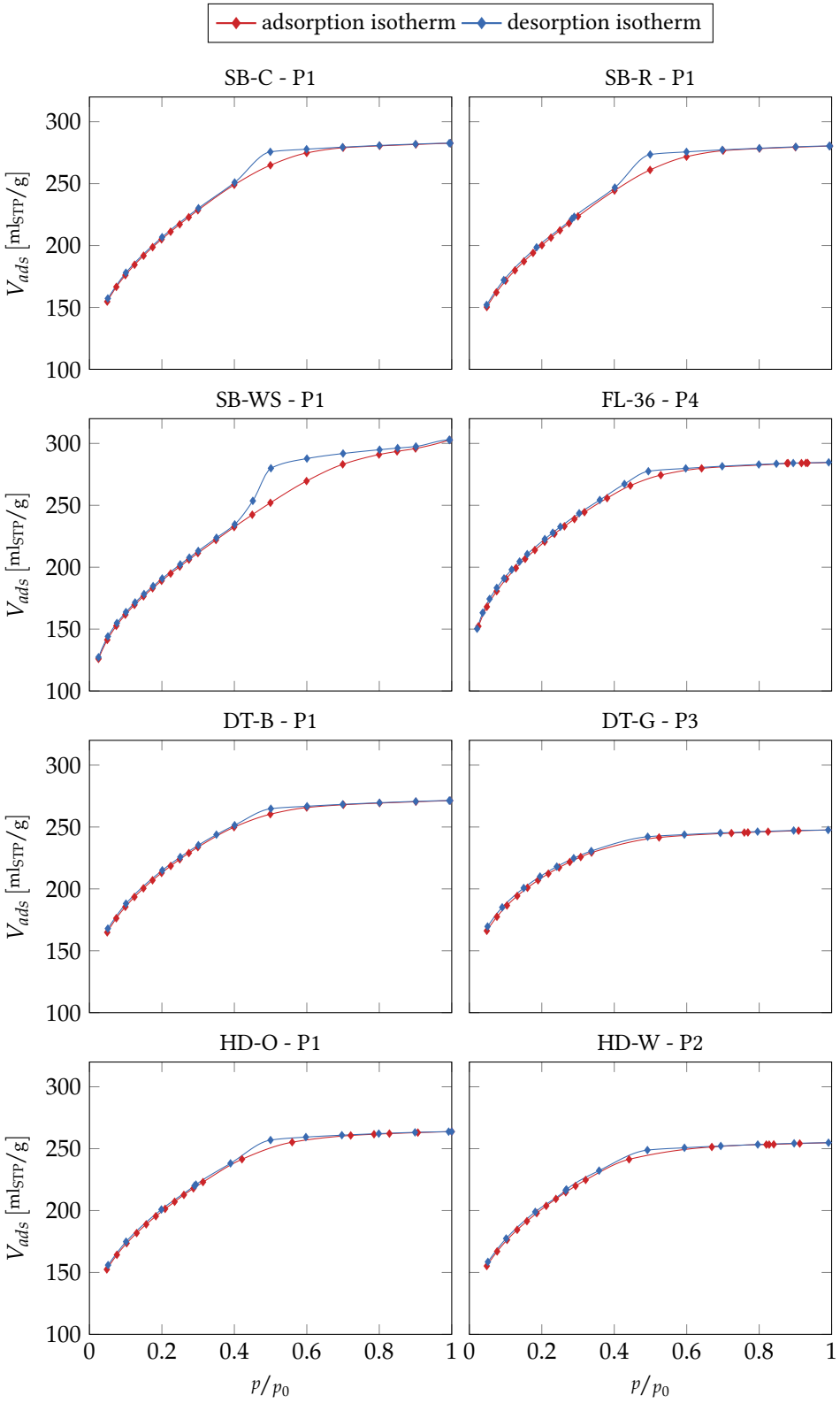

Figure 76: Compilation of N_2-isotherms for different materials.

A.2 BJH PLOTS

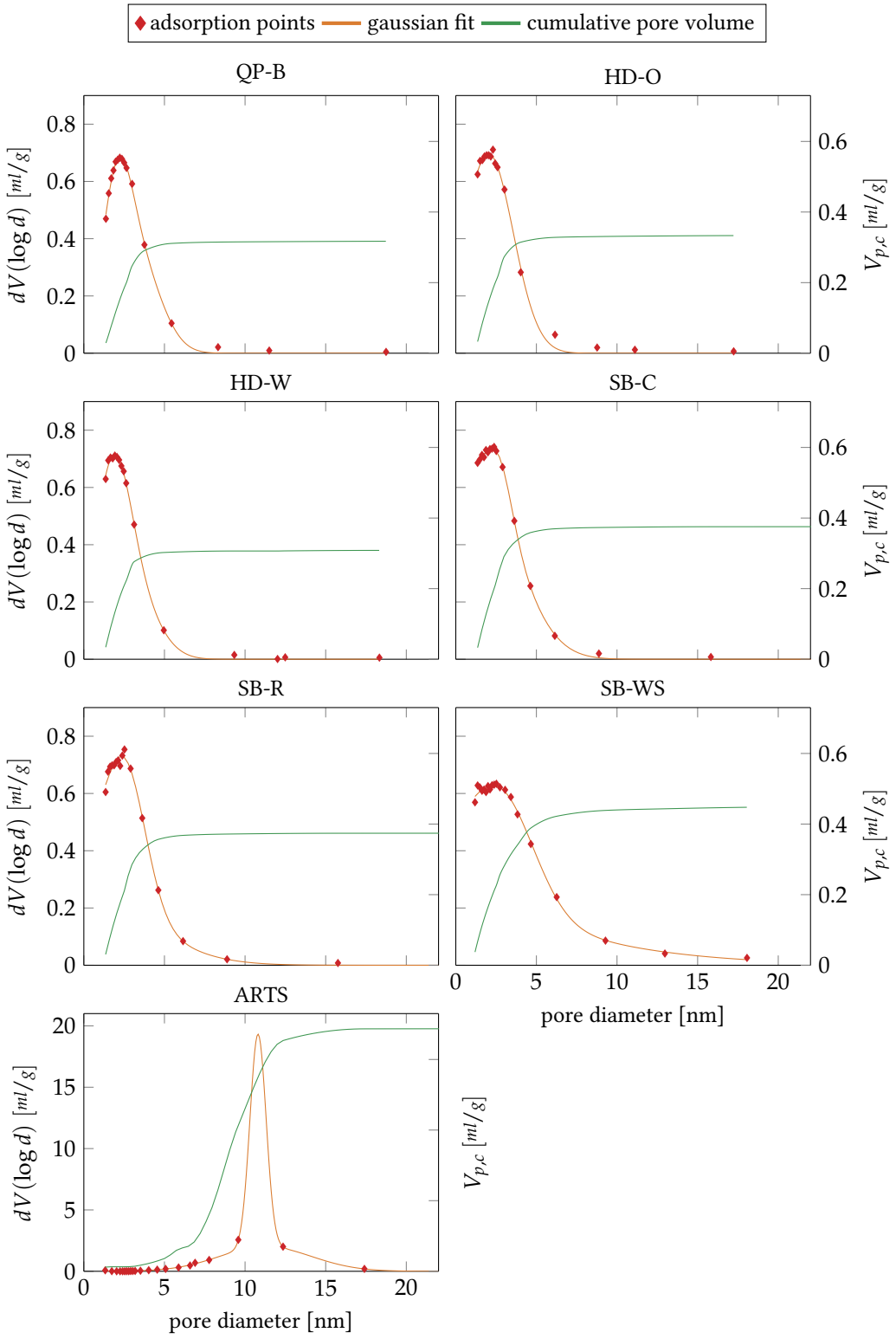

Figure 77: Pore size distribution (as $dV(\log d)$) and cumulative pore volume ($V_{p,c}$) from BJH analysis.

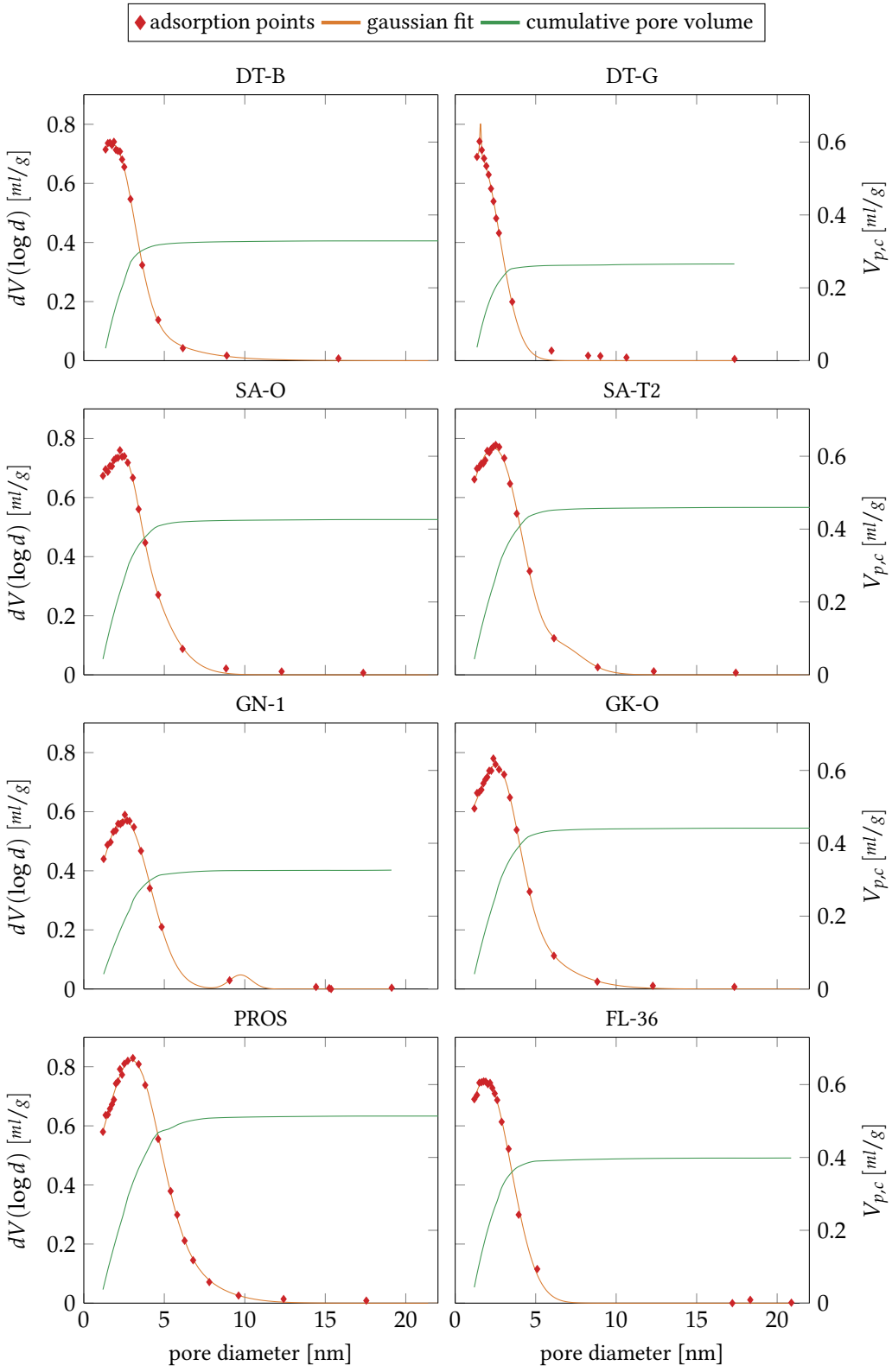

Figure 78: Pore size distribution (as $dV(\log d)$) and cumulative pore volume ($V_{p,c}$) from BJH analysis.

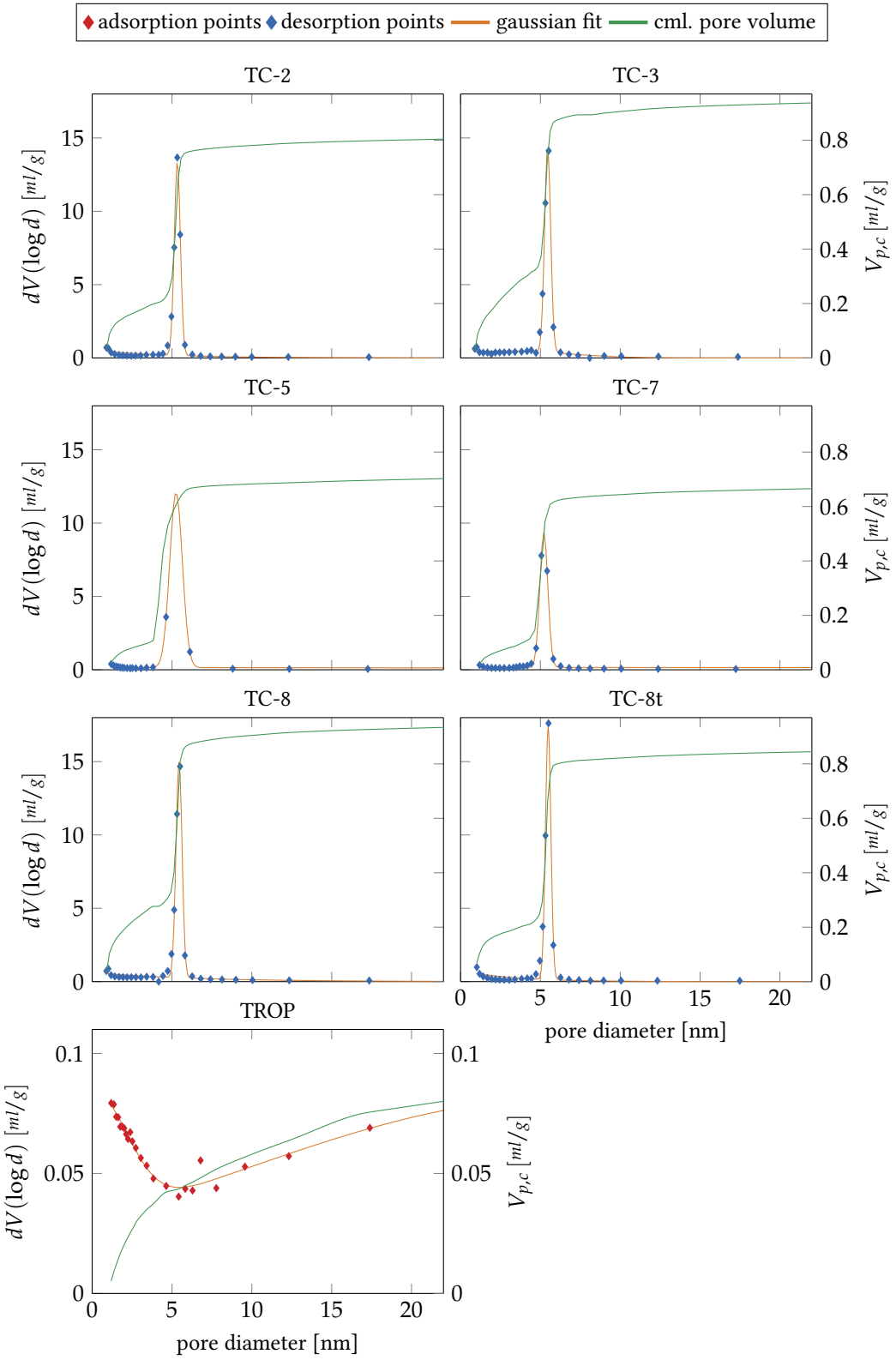

Figure 79: Pore size distribution (as $dV(\log d)$) and cumulative pore volume ($V_{p,c}$) from BJH analysis.

A.3 BET PLOTS

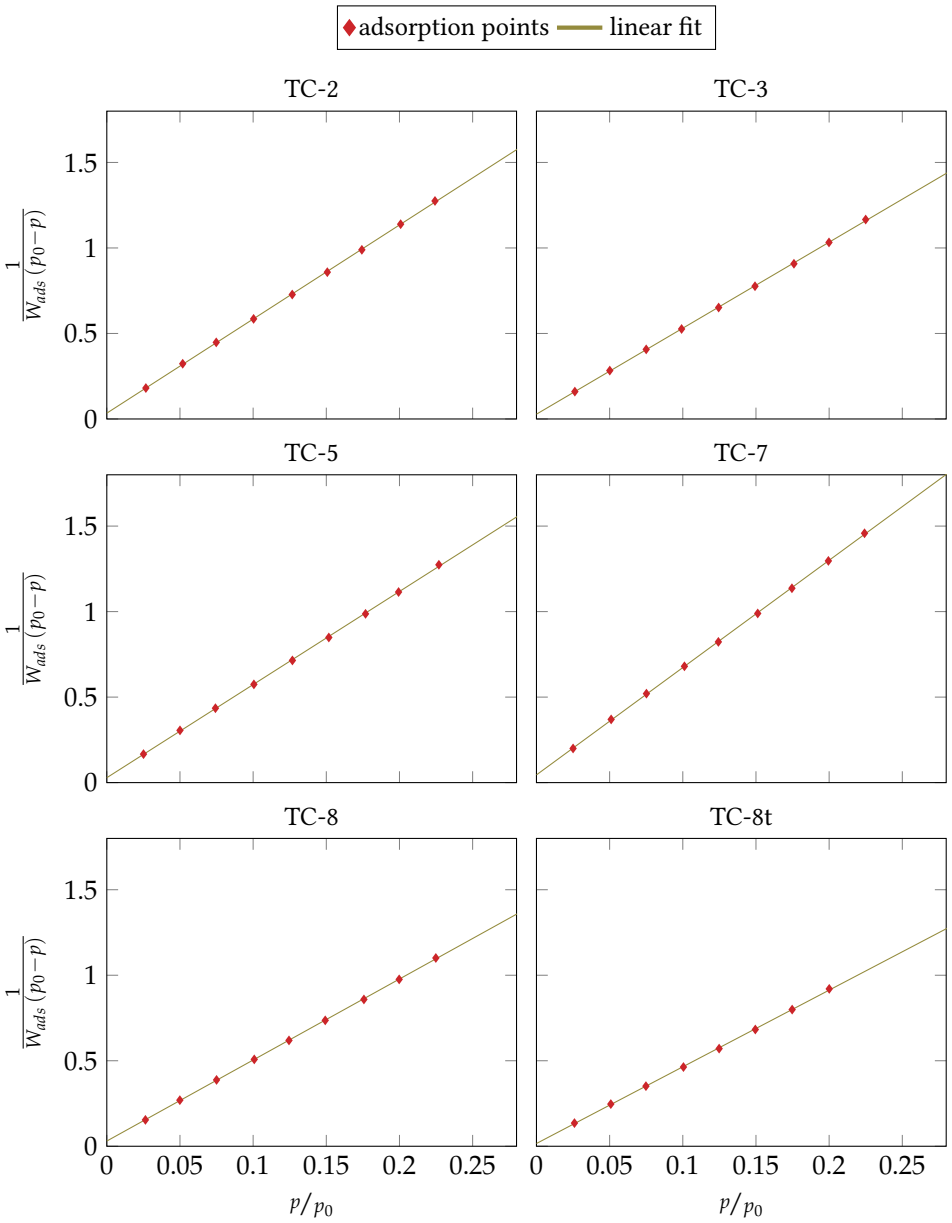

Figure 80: Compilation of the BET plots used for surface area calculation.

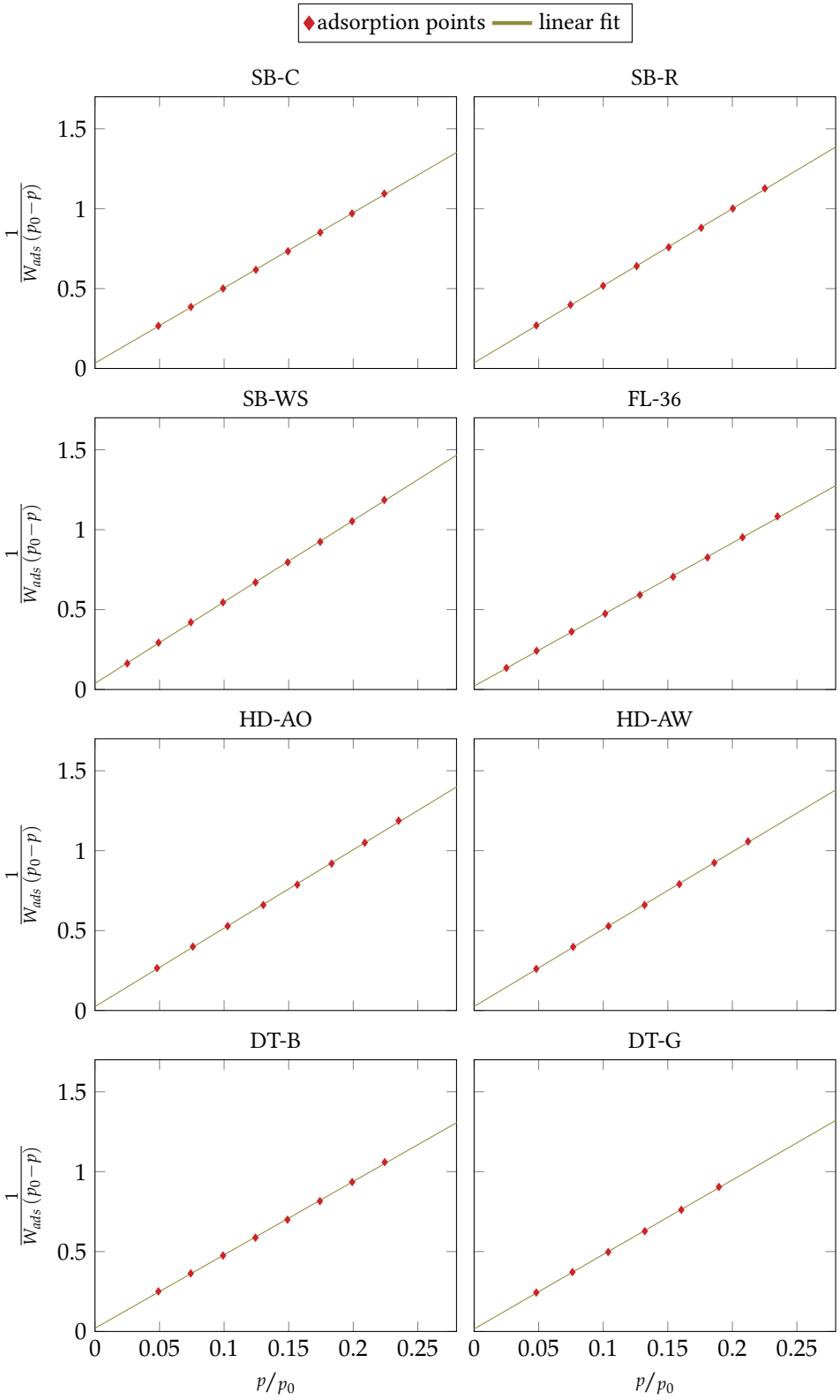

Figure 81: Compilation of the BET plots used for surface area calculation.

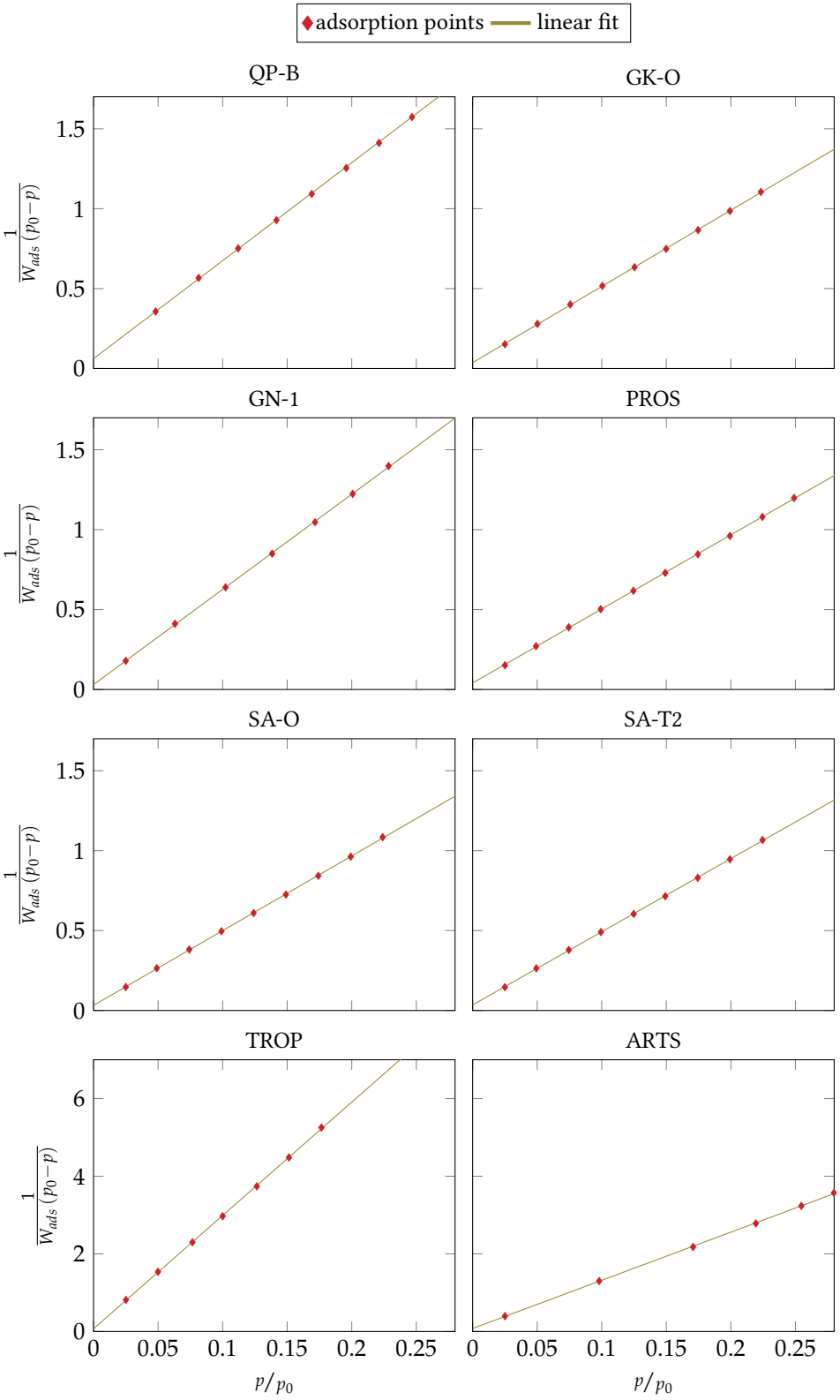

Figure 82: Compilation of the BET plots used for surface area calculation.

A.4 TGA-MS PLOTS

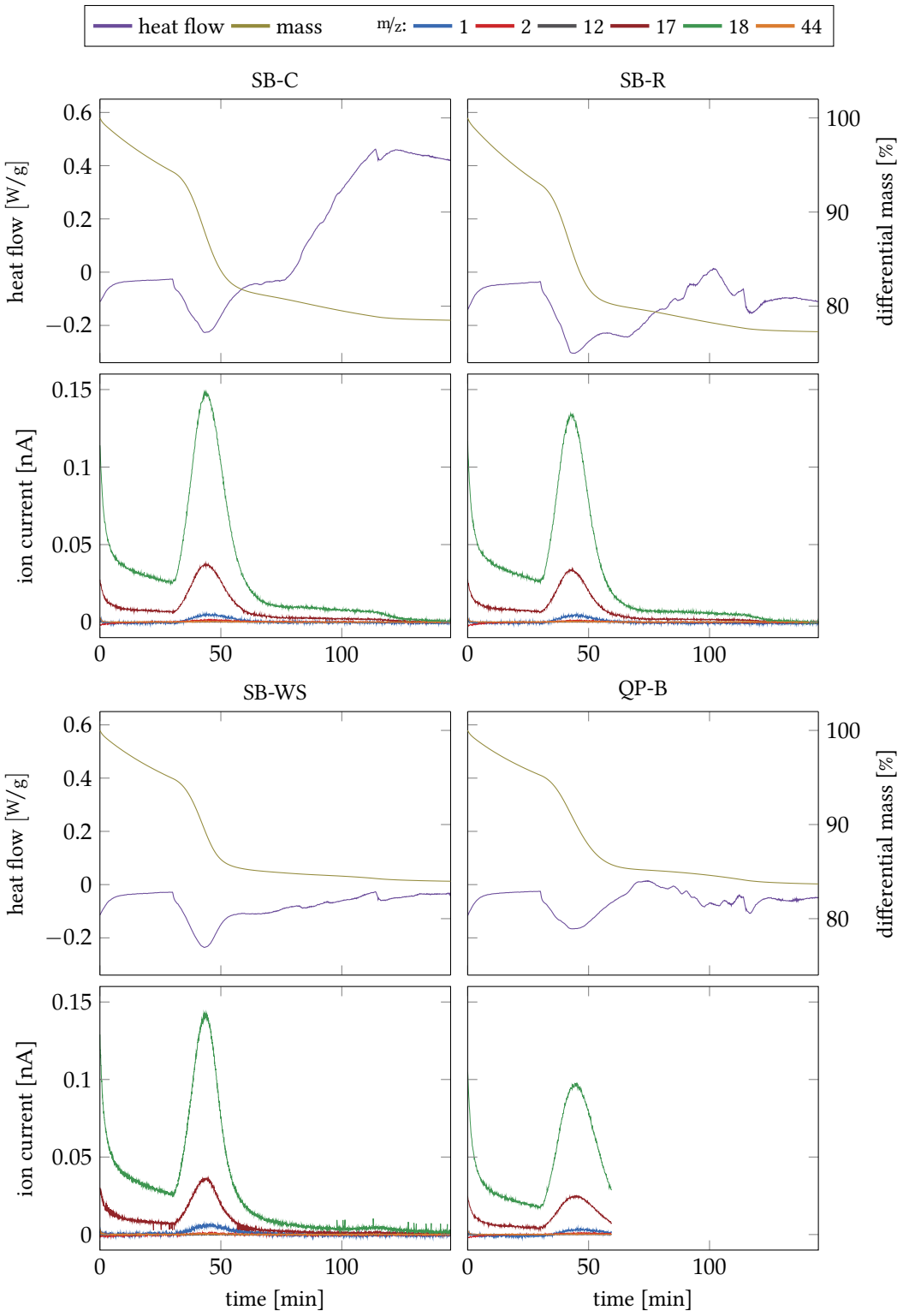

Figure 83: Thermal analysis of commercial silica gel samples, heating profile: P2

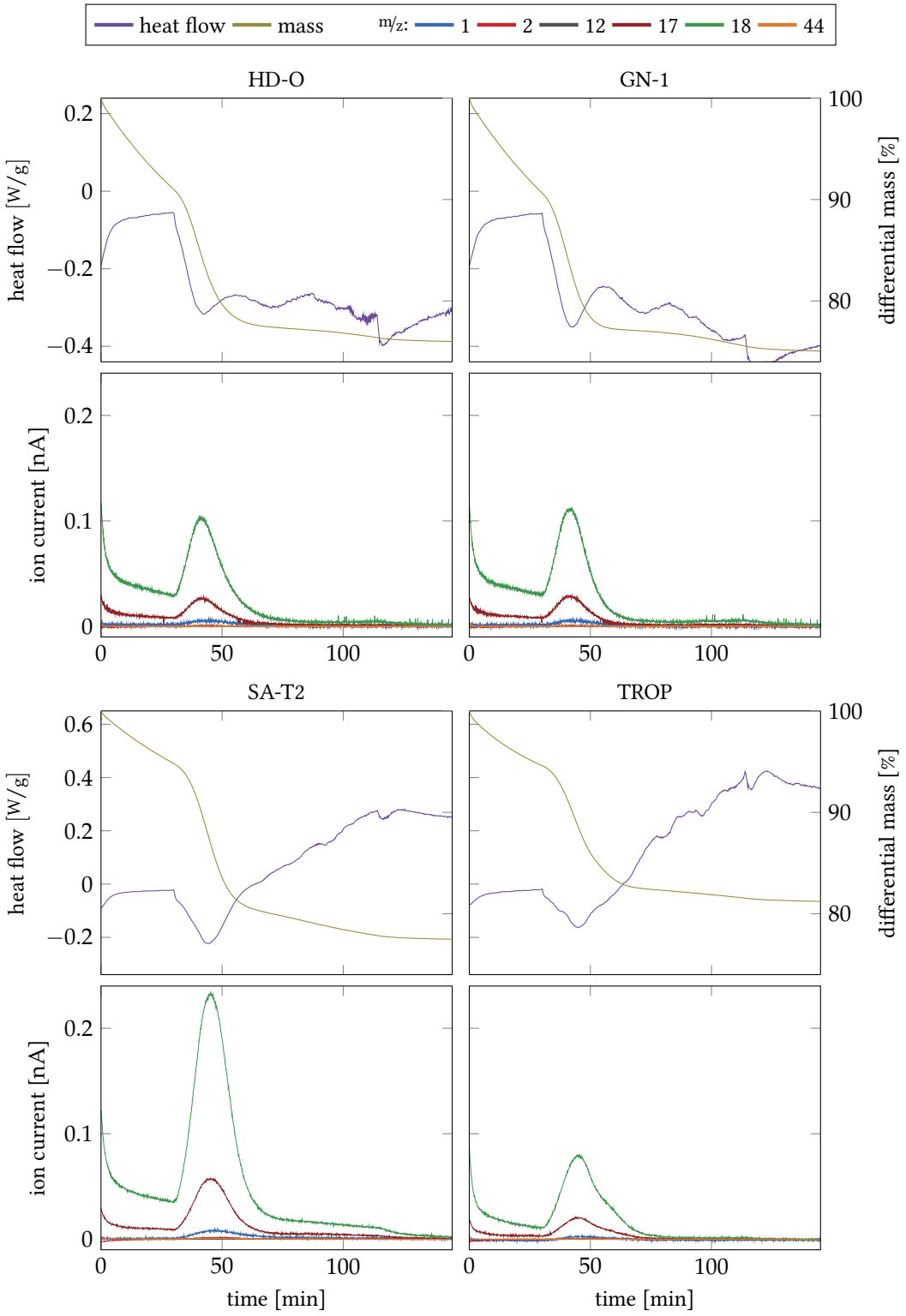

Figure 84: Thermal analysis of commercial silica gel samples, heating profile: P2

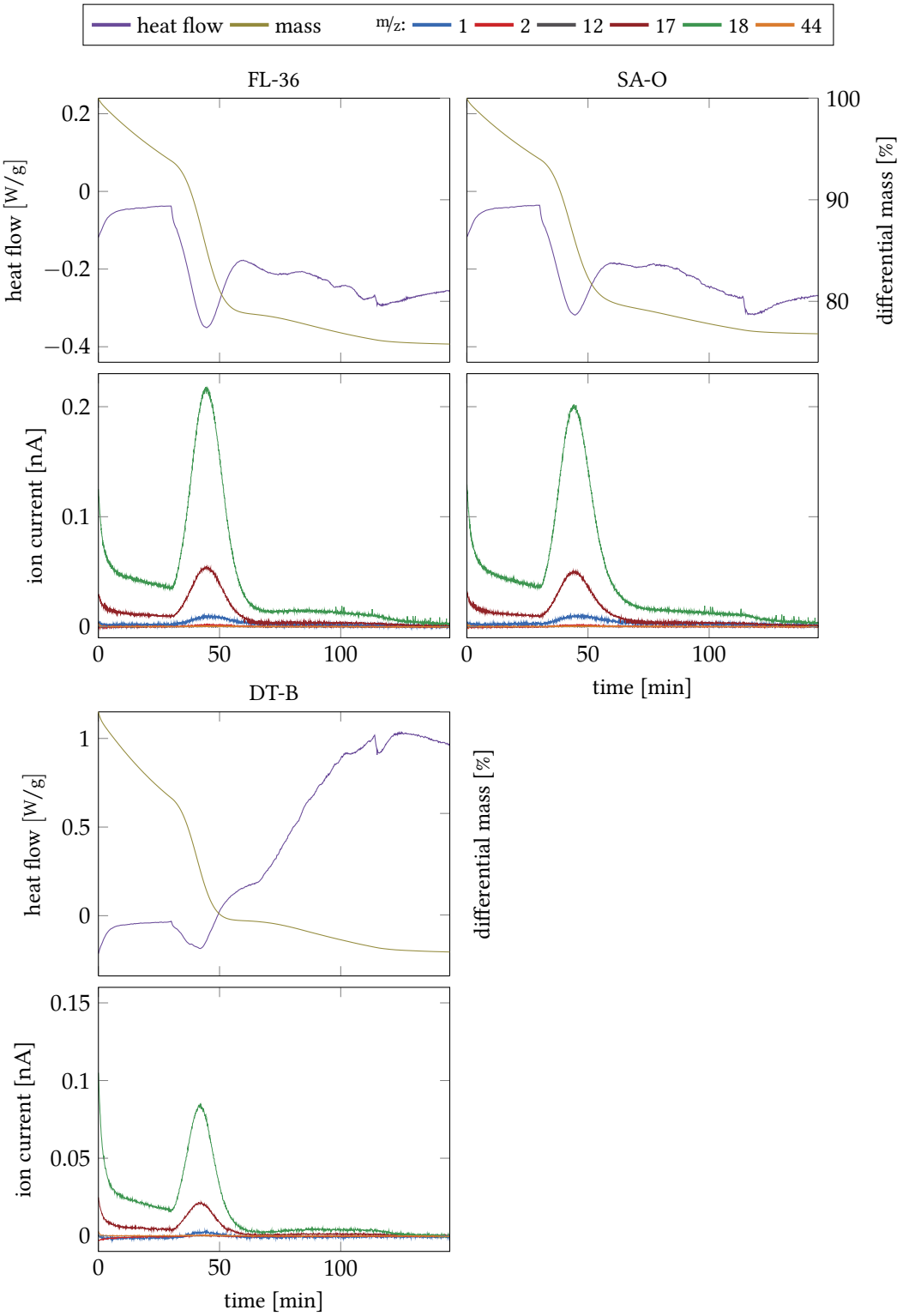

Figure 85: Thermal analysis of commercial silica gel samples, heating profile: P2

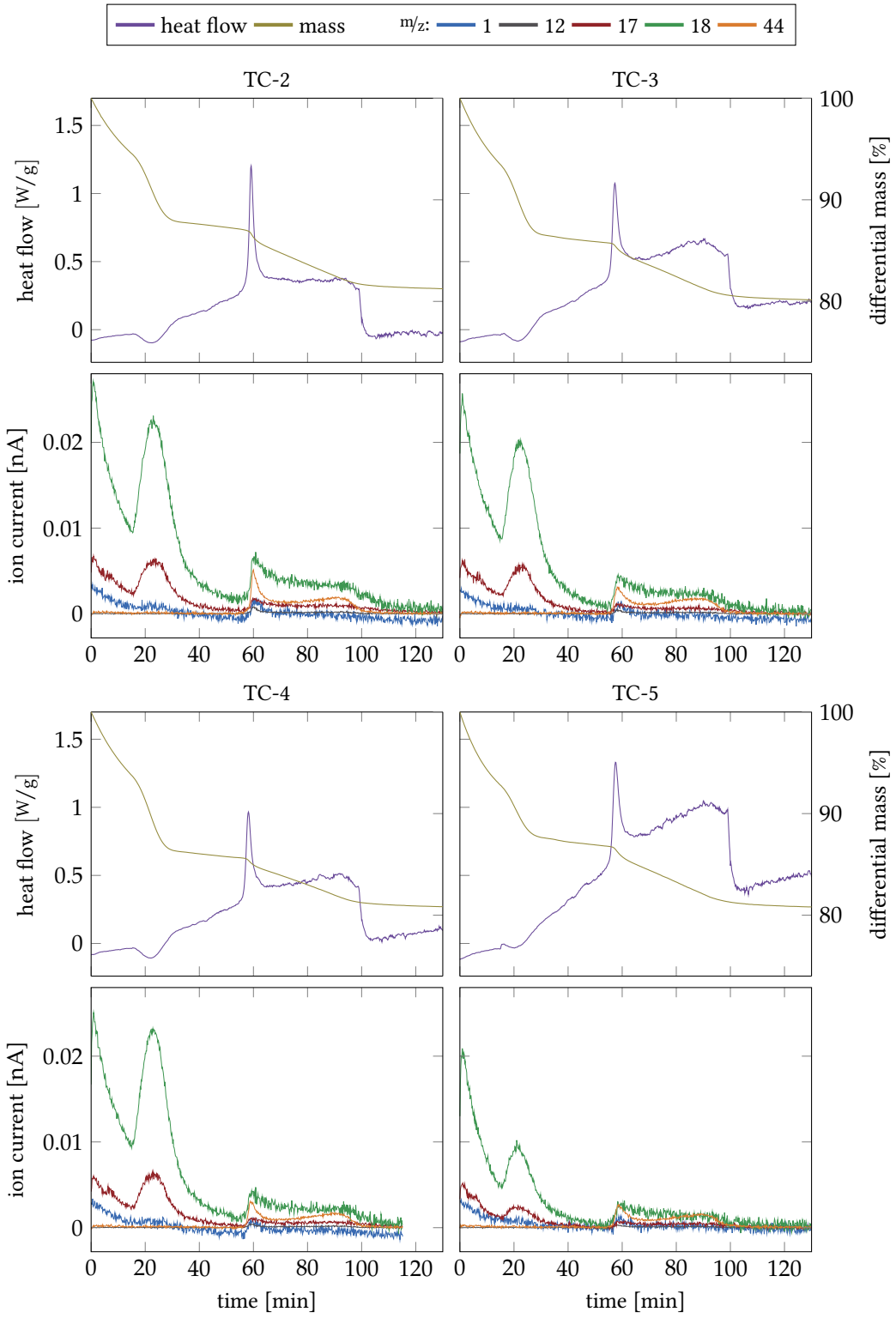

Figure 86: Thermal analysis of *SBA-15* samples, heating profile: P1.

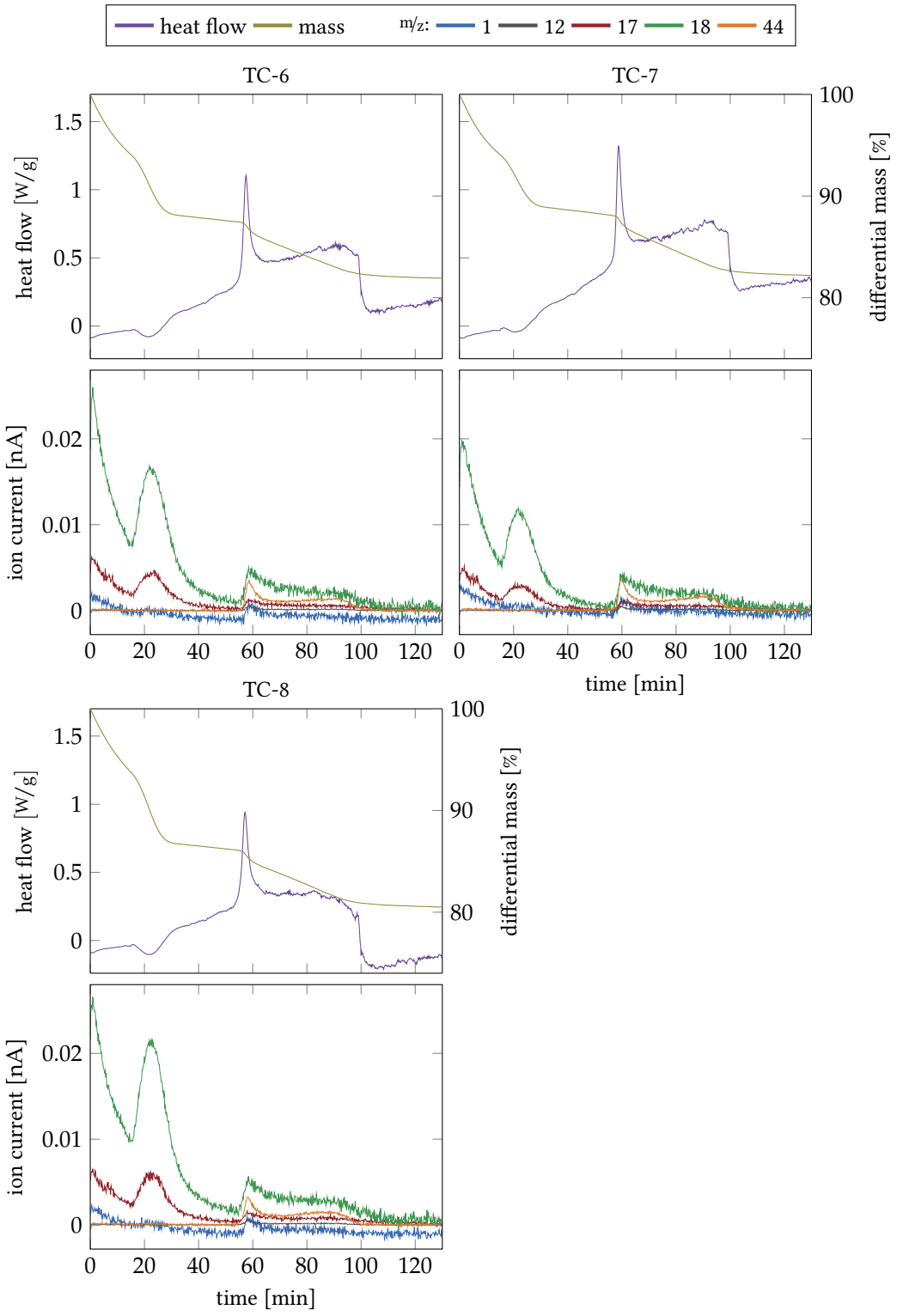

Figure 87: Thermal analysis of *SBA-15* samples, heating profile: P1.

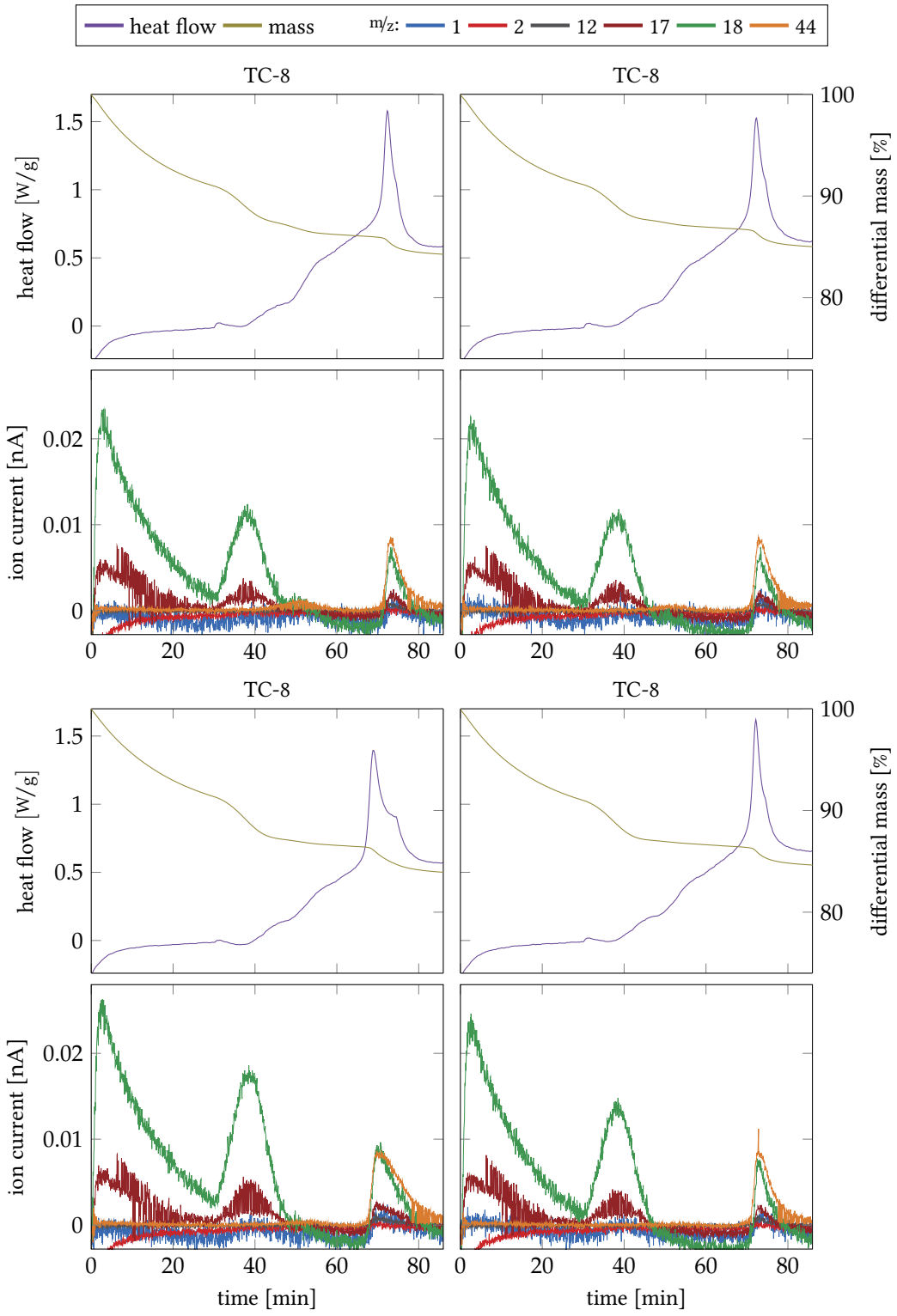

Figure 88: Thermal treatment of four parts of a *TC-8* sample.

A.5 OPEN SYSTEM PLOTS

A.5.1 *Results from Adsorber Box 1*

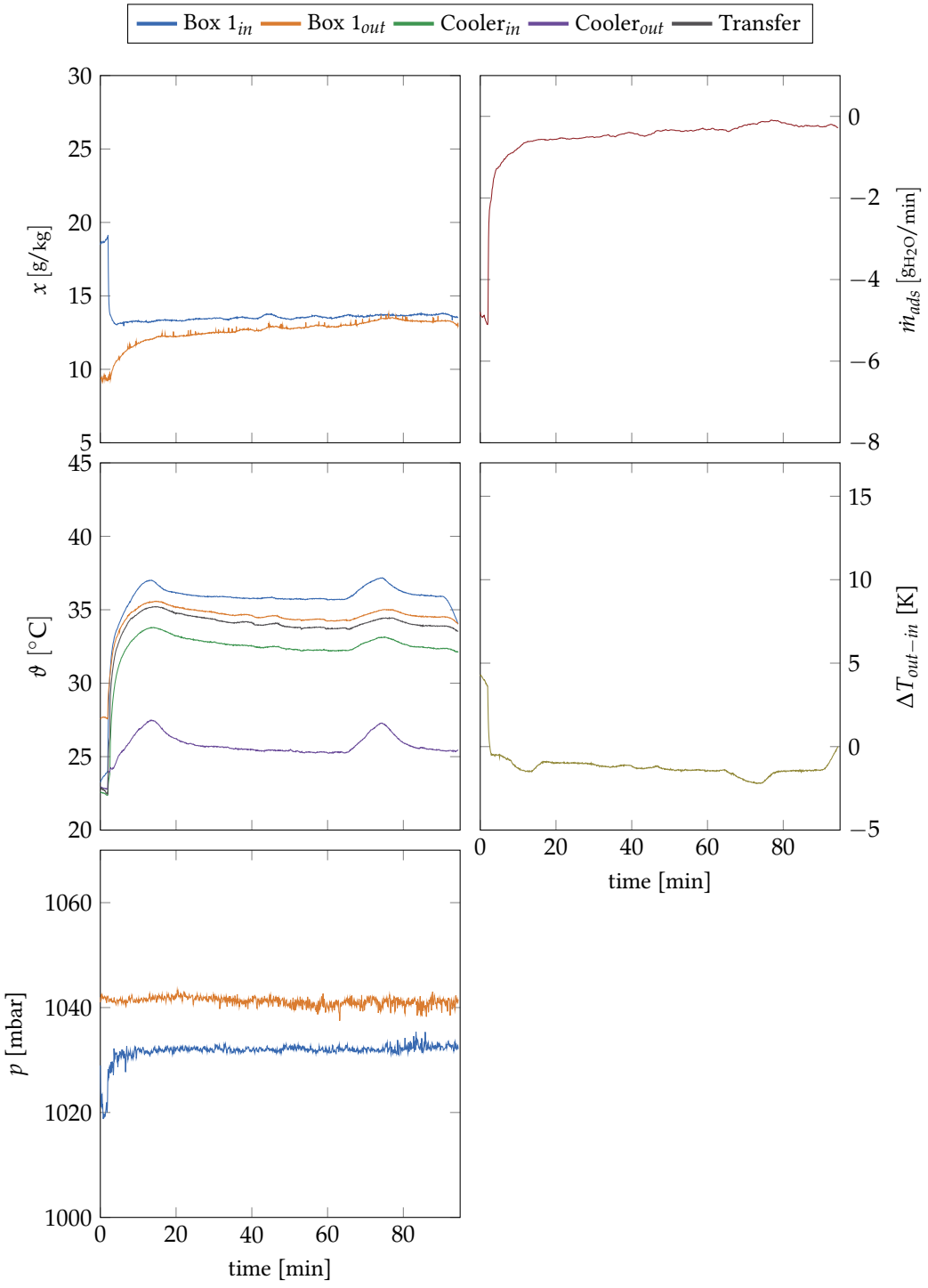

Figure 89: *Box 1* in adsorption mode at 100 % fan power. Loaded sample: *FL-36*

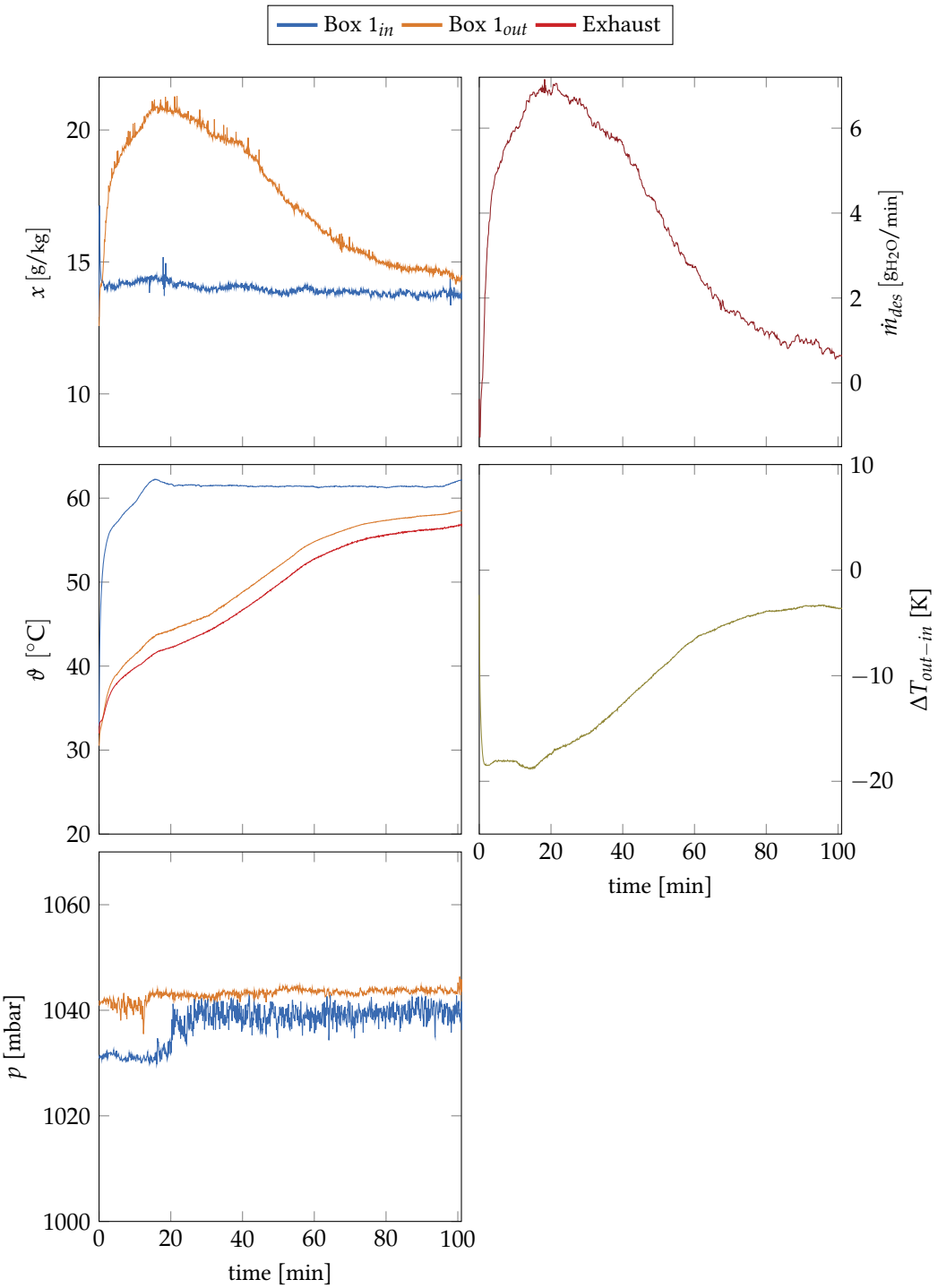

Figure 90: *Box 1* in desorption mode. Loaded sample: *FL-36*

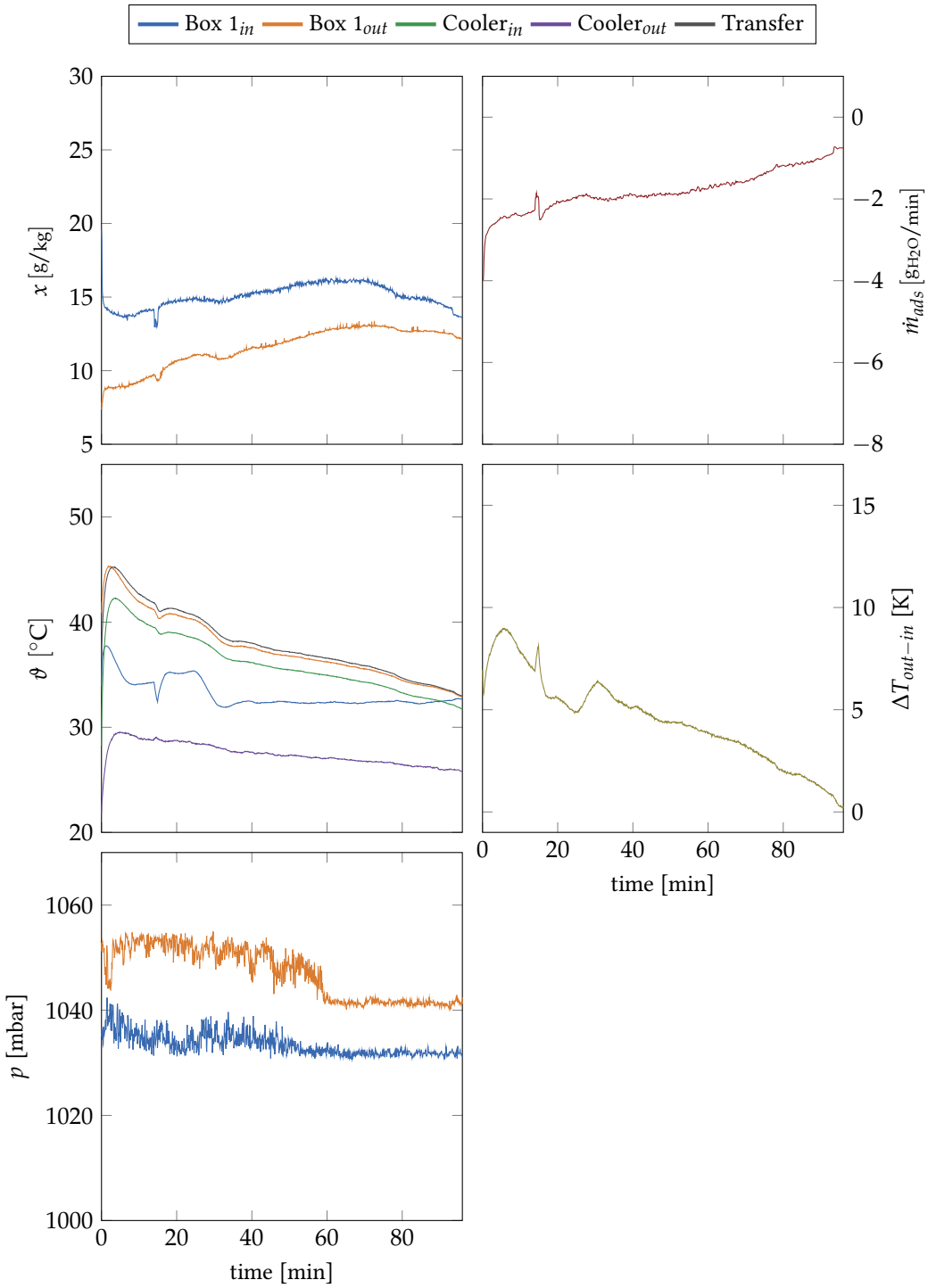

Figure 91: *Box 1* in adsorption mode at 100 % fan power. Loaded sample: *SB-R*

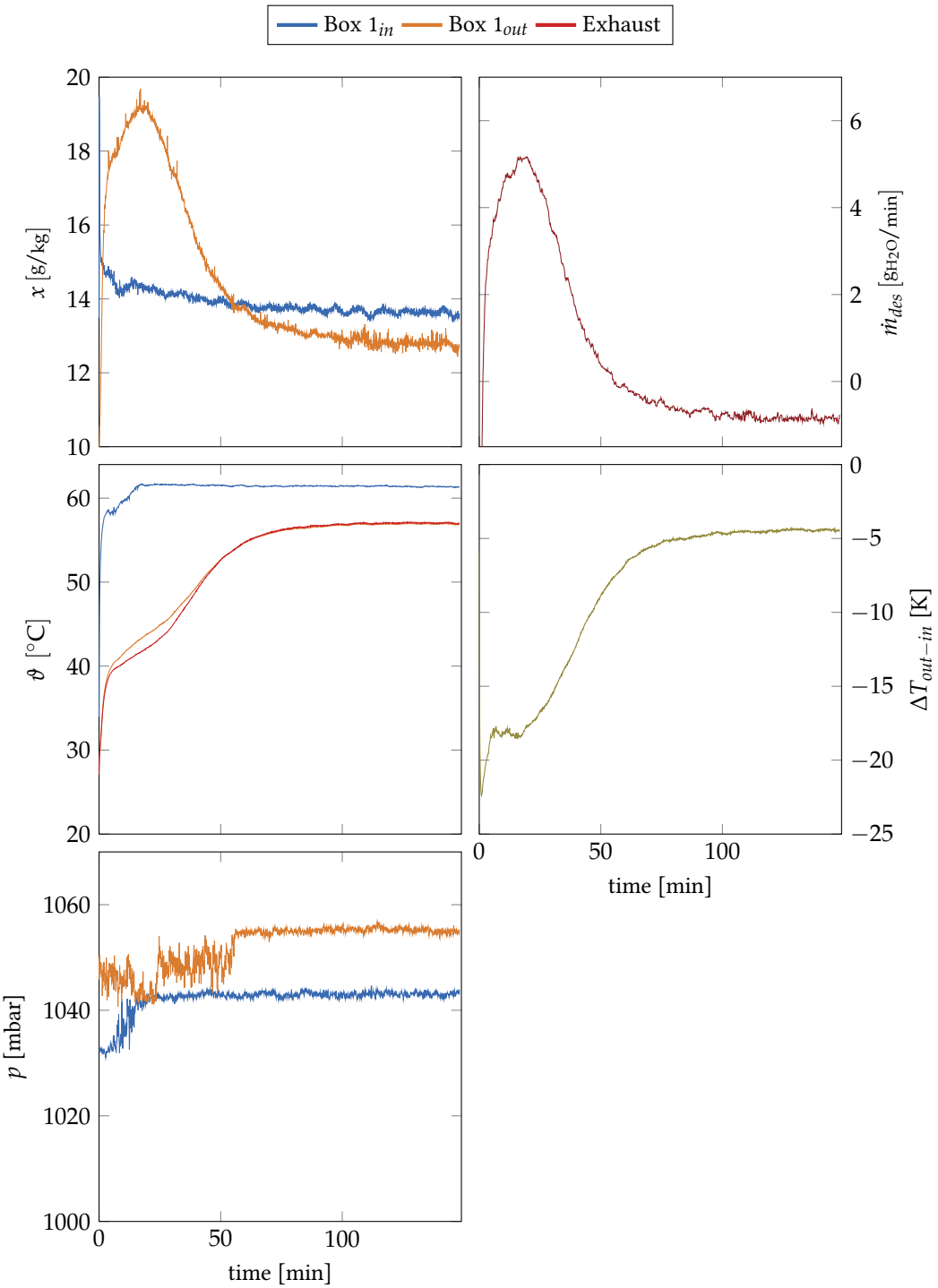

Figure 92: *Box 1* in desorption mode. Loaded sample: *SB-R*

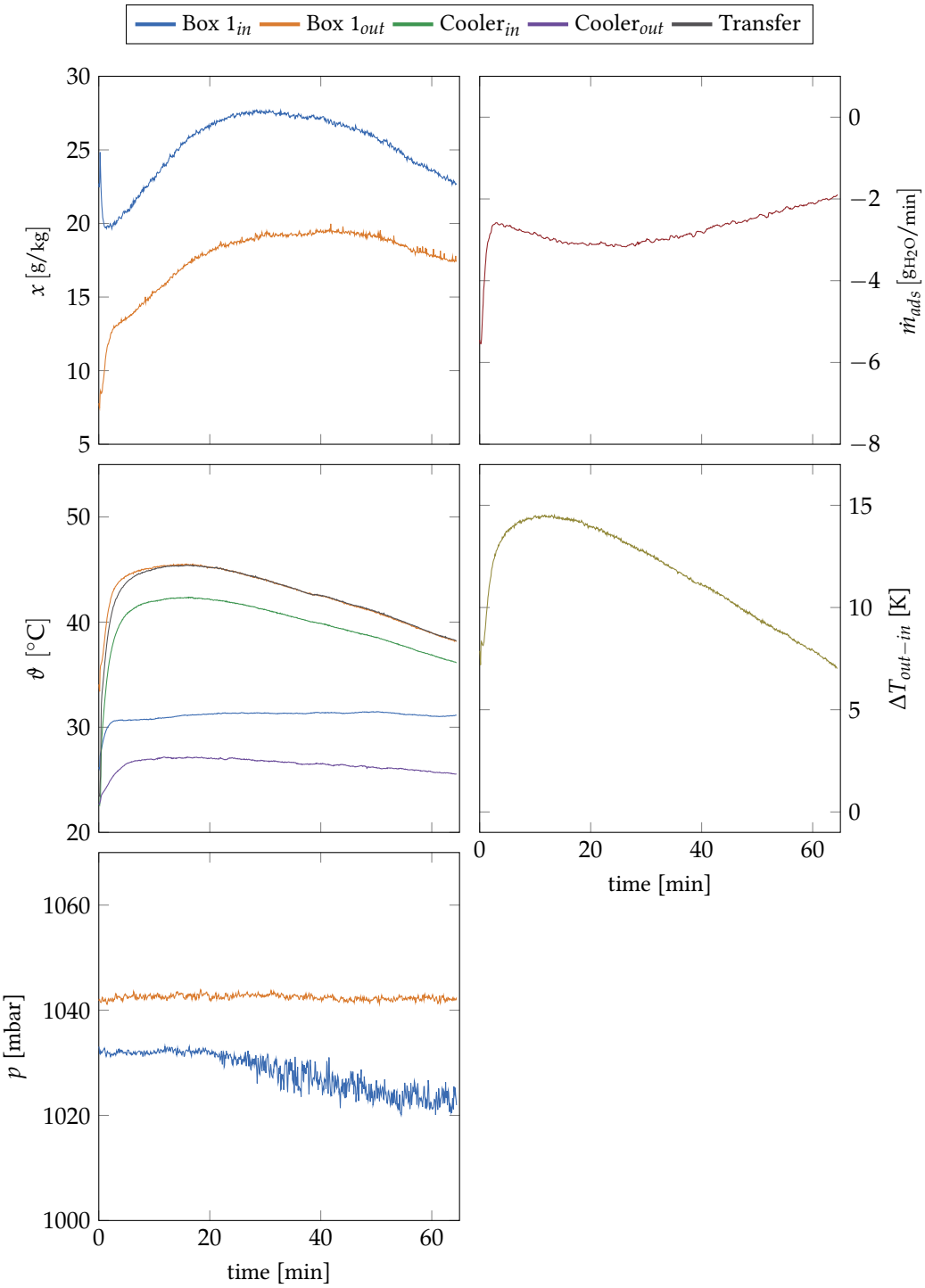

Figure 93: *Box 1* in adsorption mode at 50 % fan power. Loaded sample: *SB-R*

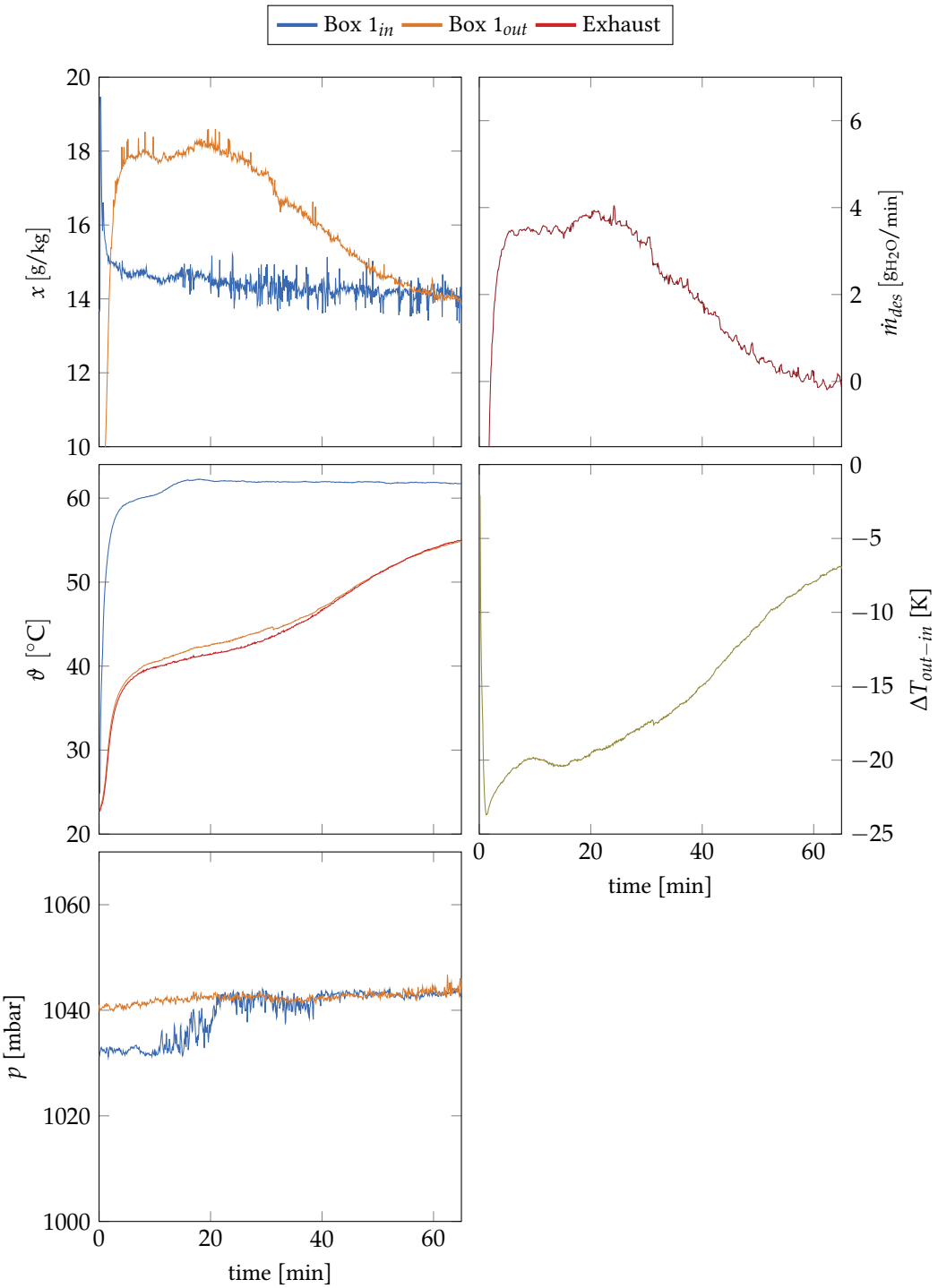

Figure 94: *Box 1* in desorption mode. Loaded sample: *SB-R*

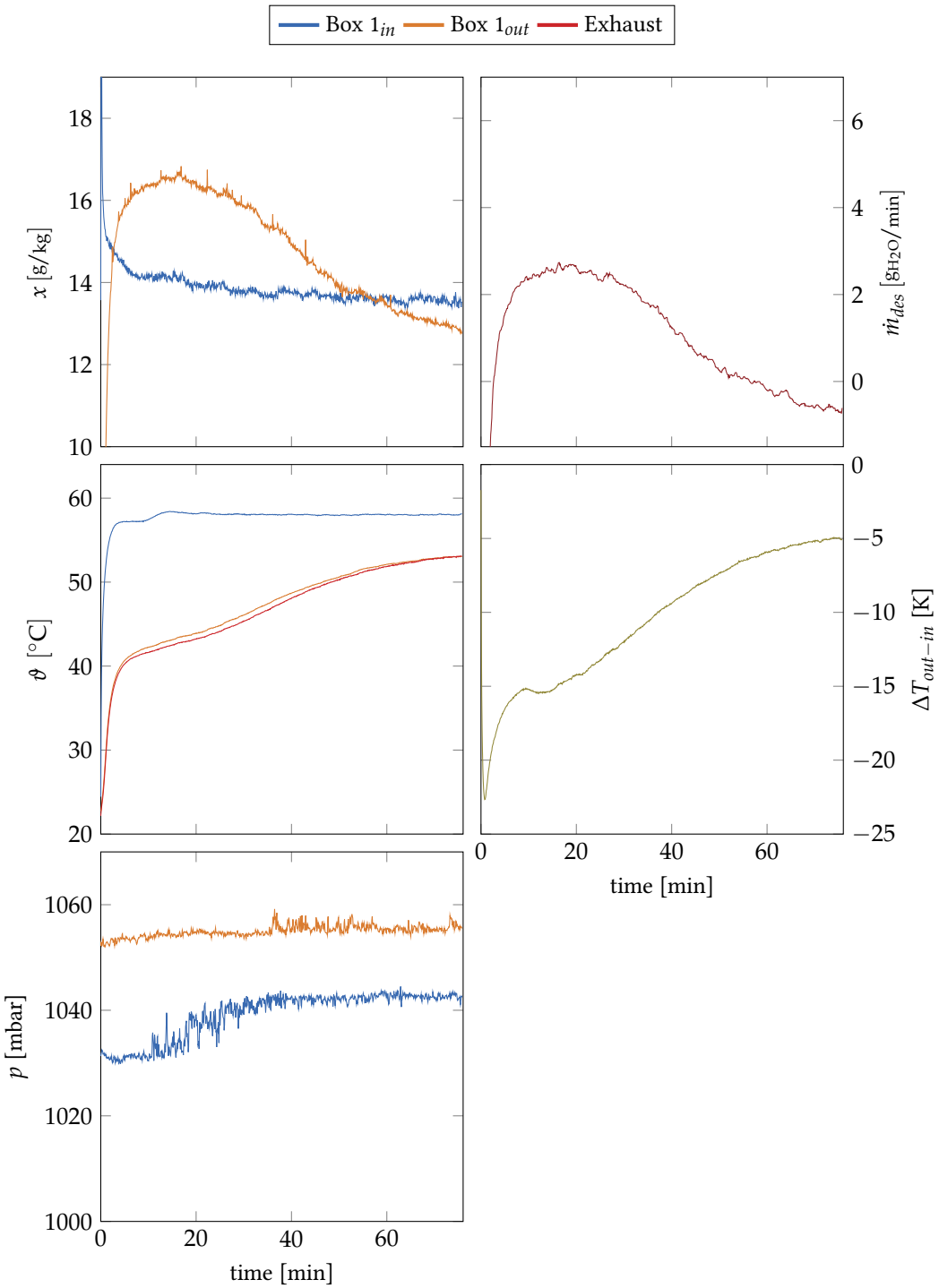

Figure 95: *Box 1* in desorption mode. Loaded sample: *SA-T2*

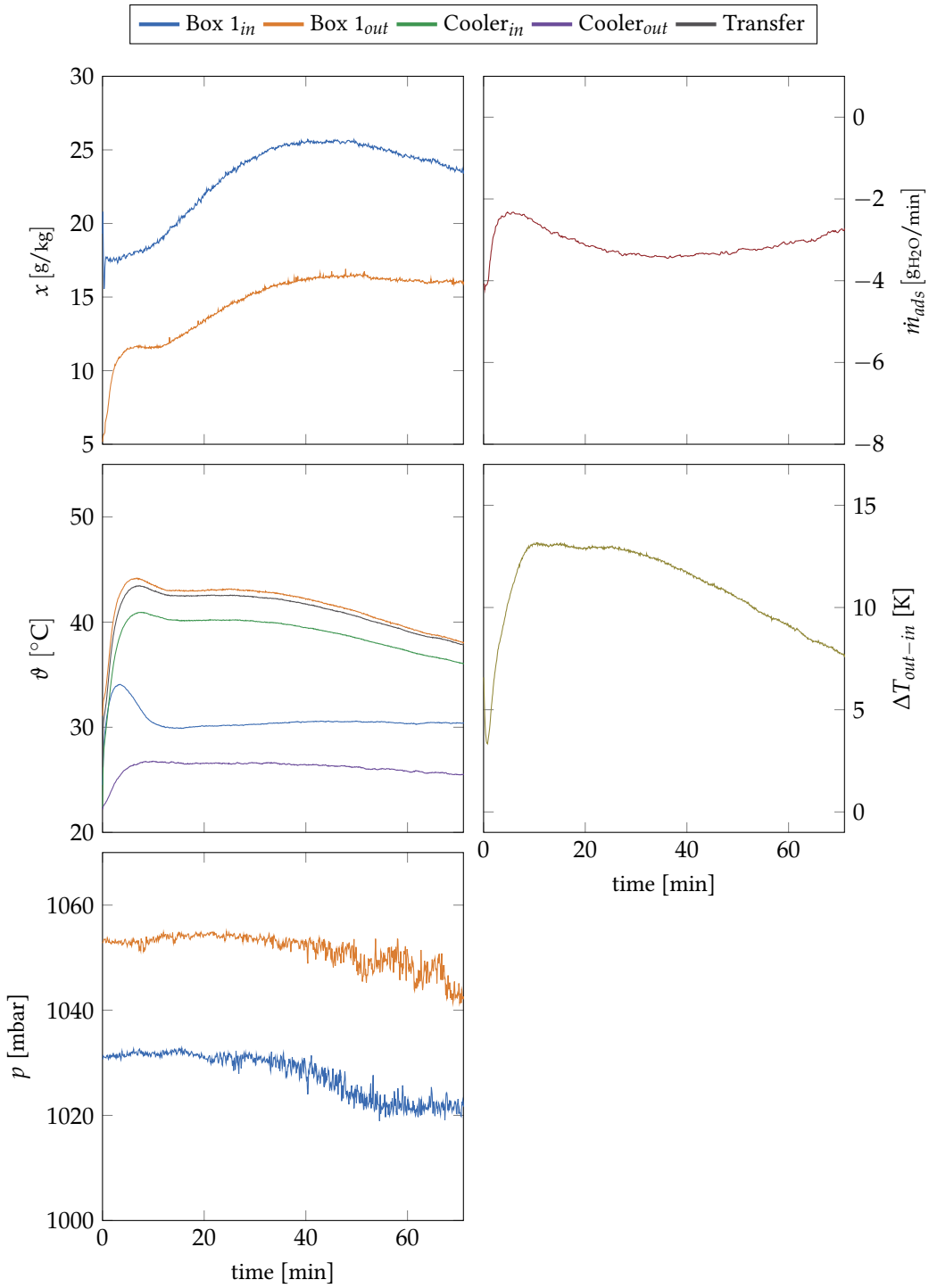

Figure 96: *Box 1* in adsorption mode at 50 % fan power. Loaded sample: *SA-T2*

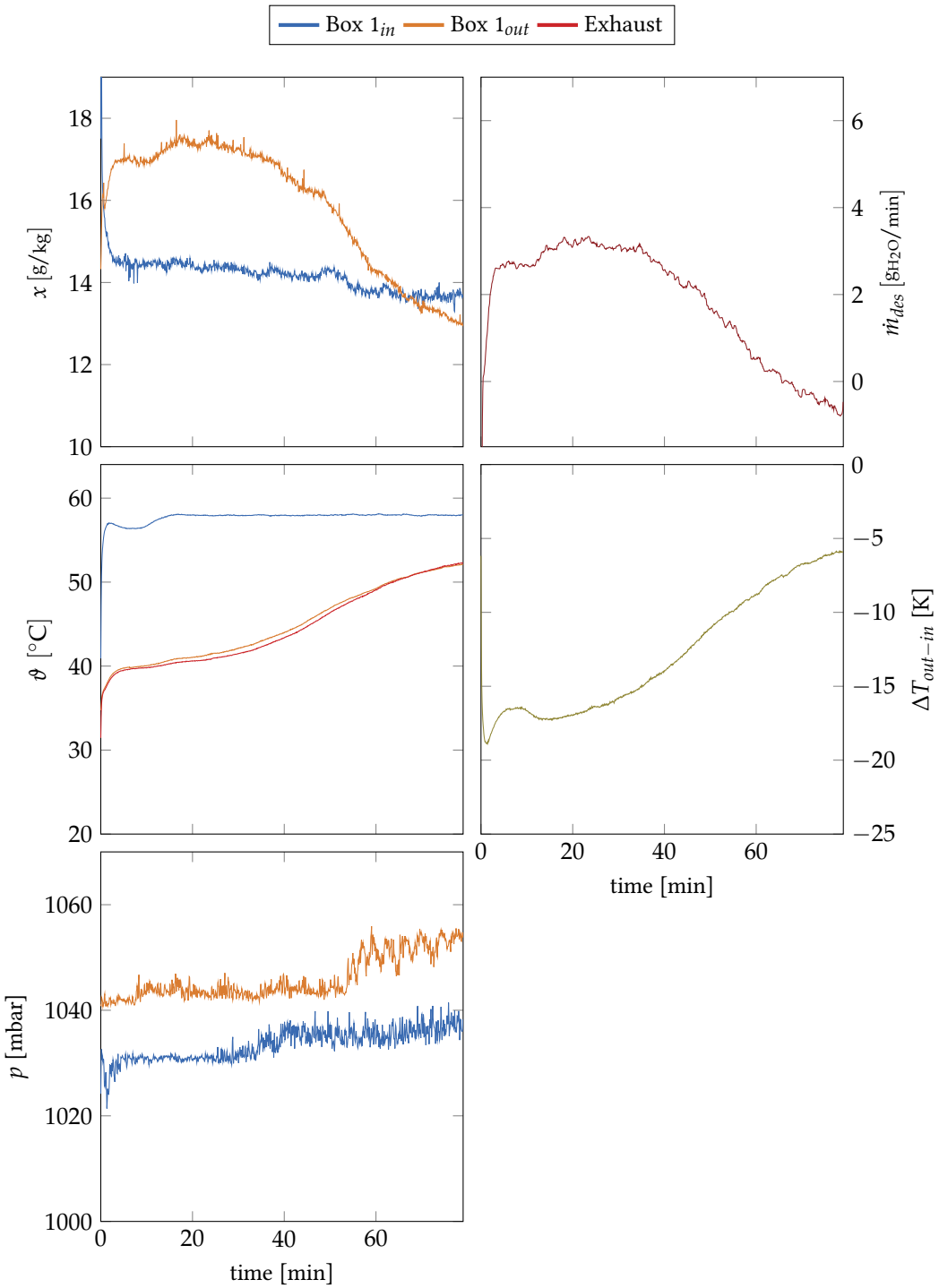

Figure 97: *Box 1* in desorption mode. Loaded sample: *SA-T2*

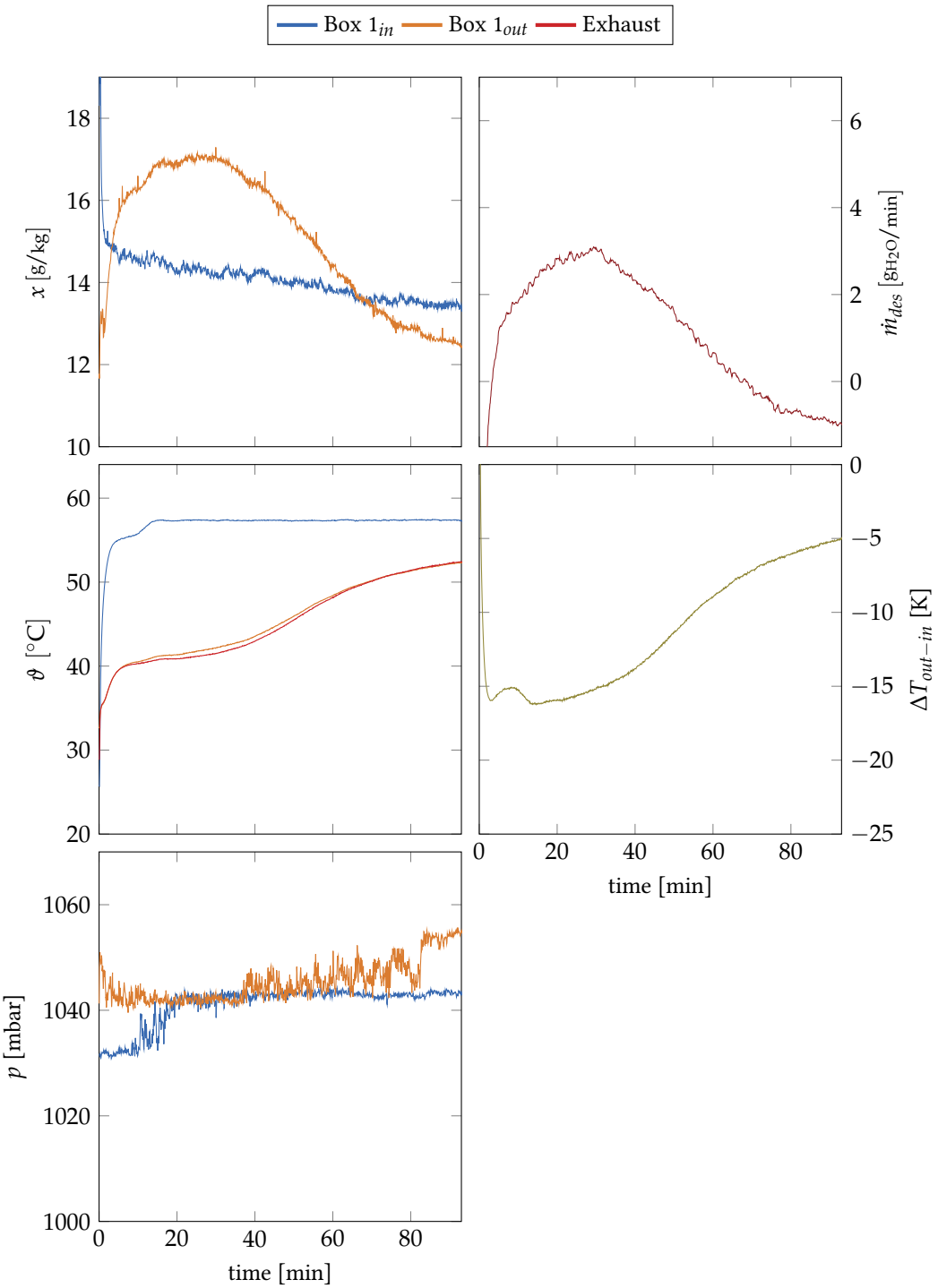

Figure 98: *Box 1* in desorption mode. Loaded sample: *SA-T2*

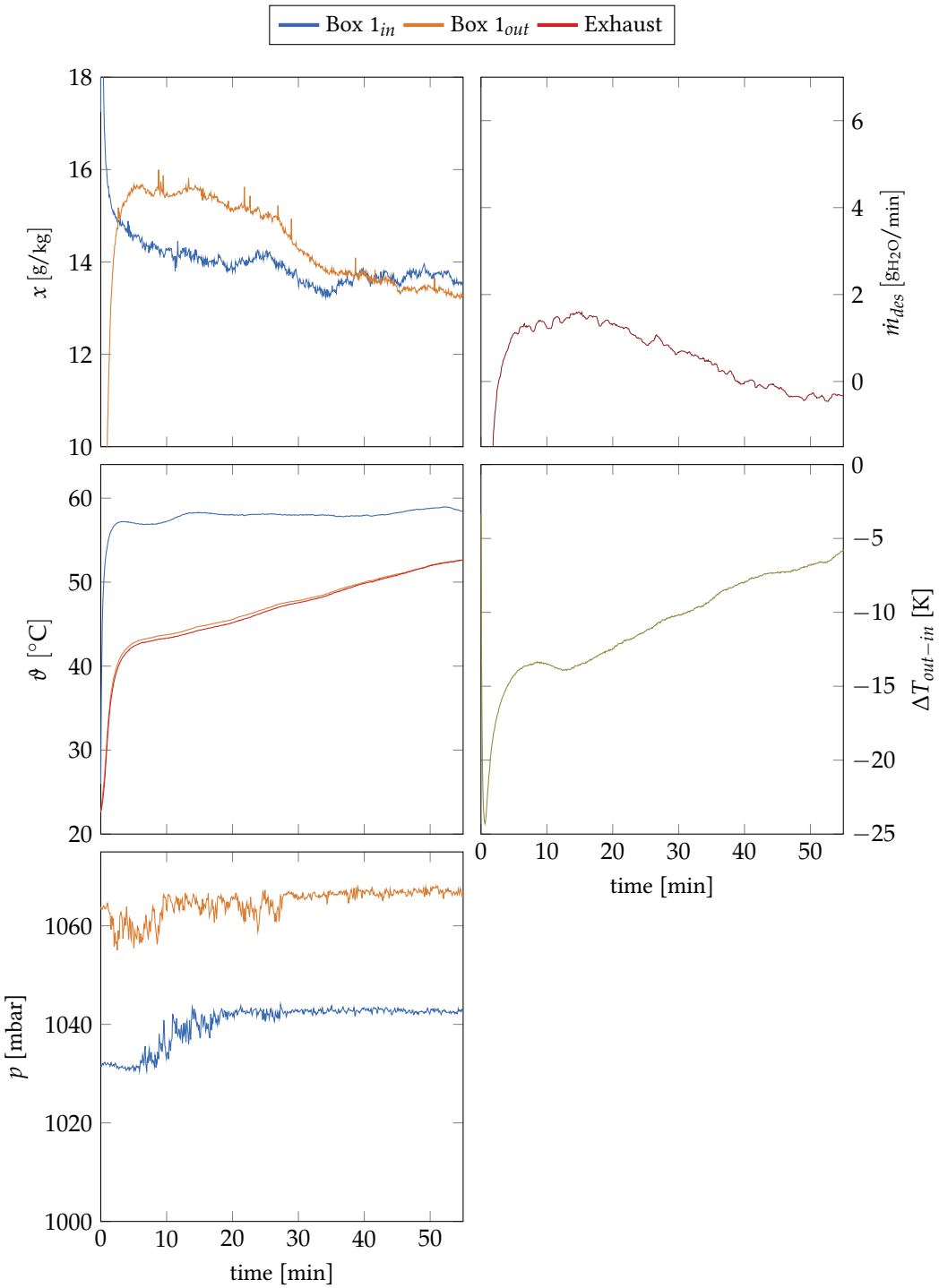

Figure 99: *Box 1* in desorption mode. Loaded sample: *SA-O*

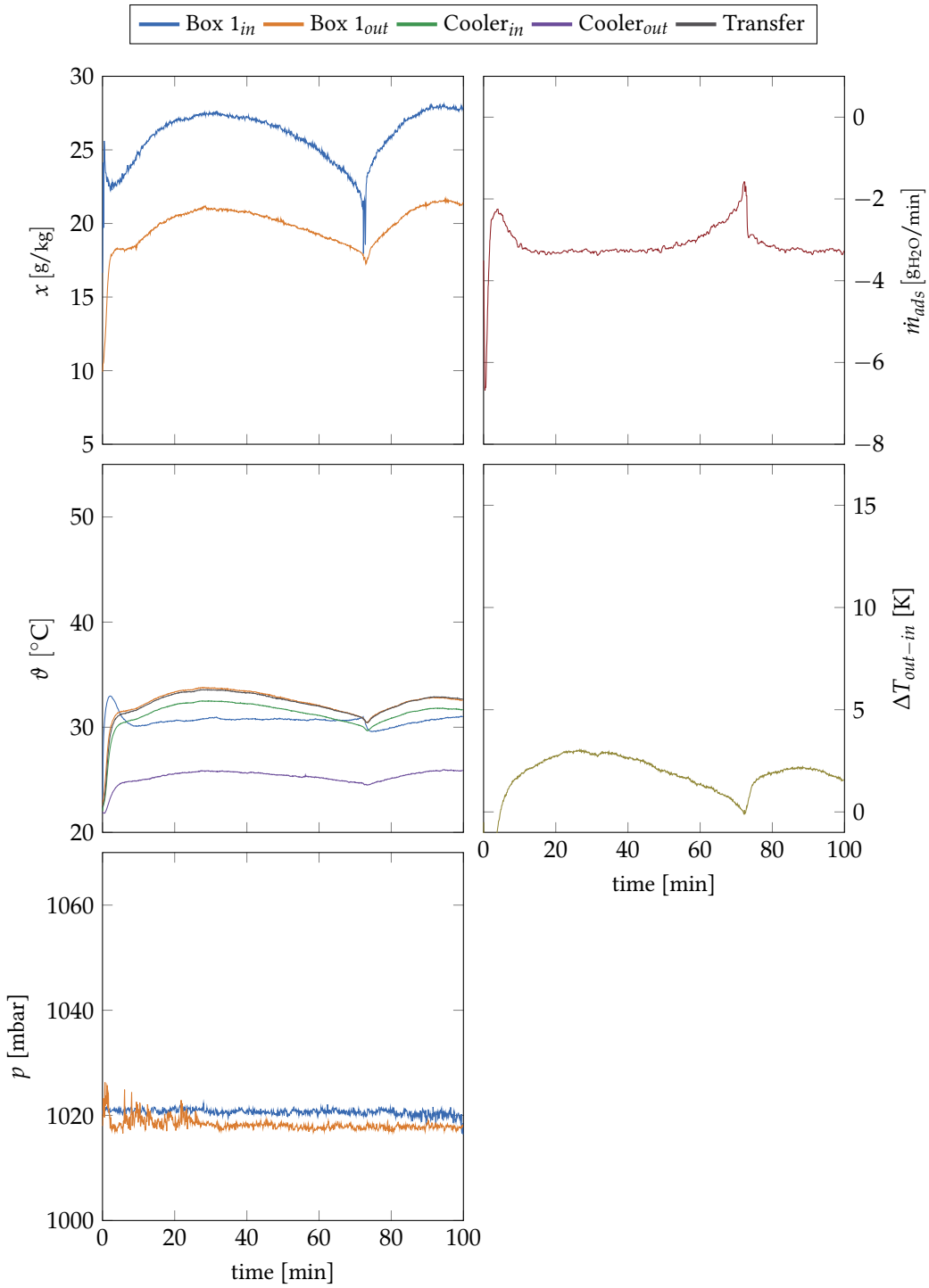

Figure 100: *Box 1* in adsorption mode at 100 % fan power. Loaded sample: *PROS*

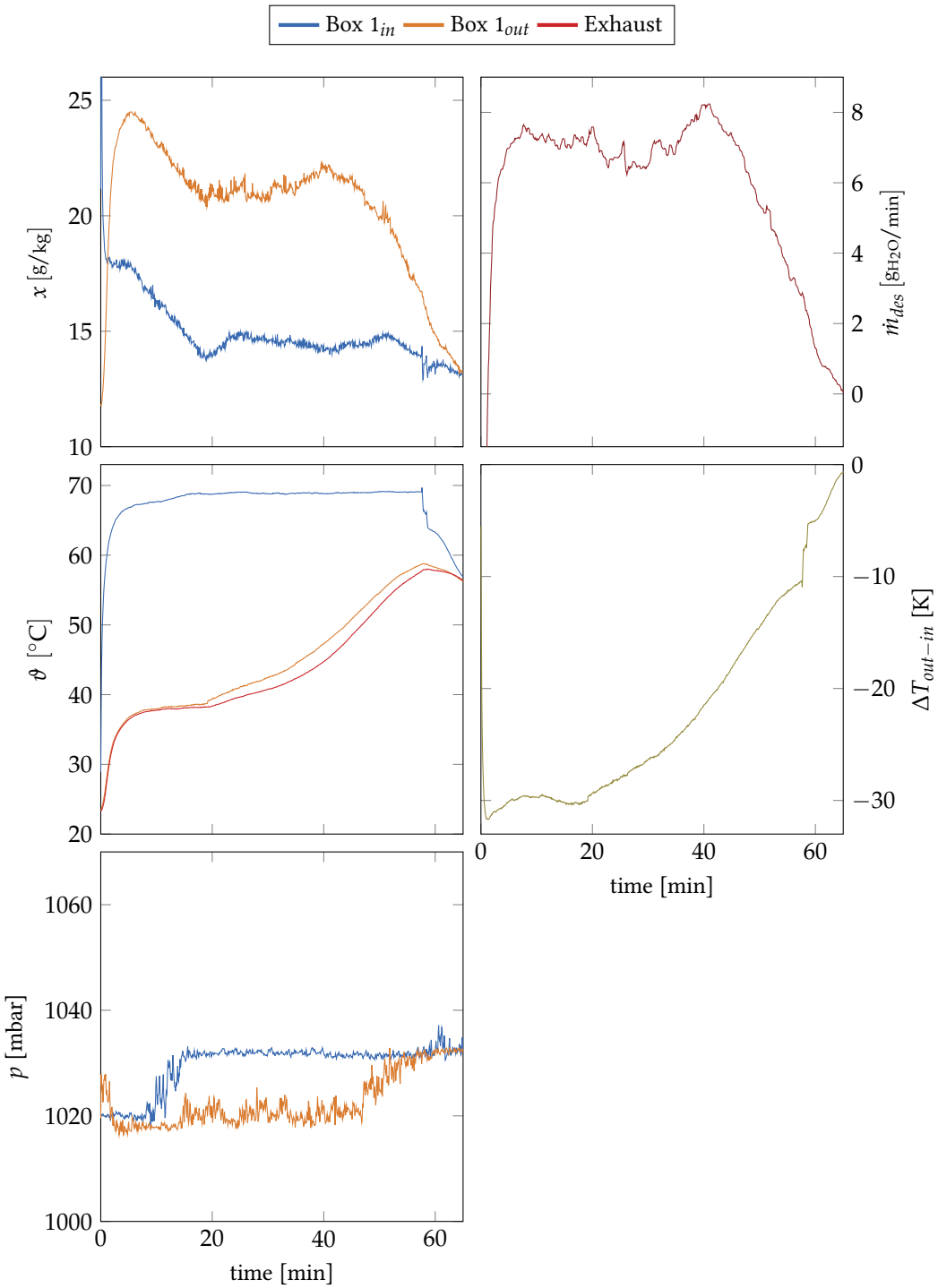

Figure 101: *Box 1* in desorption mode. Loaded sample: *PROS*

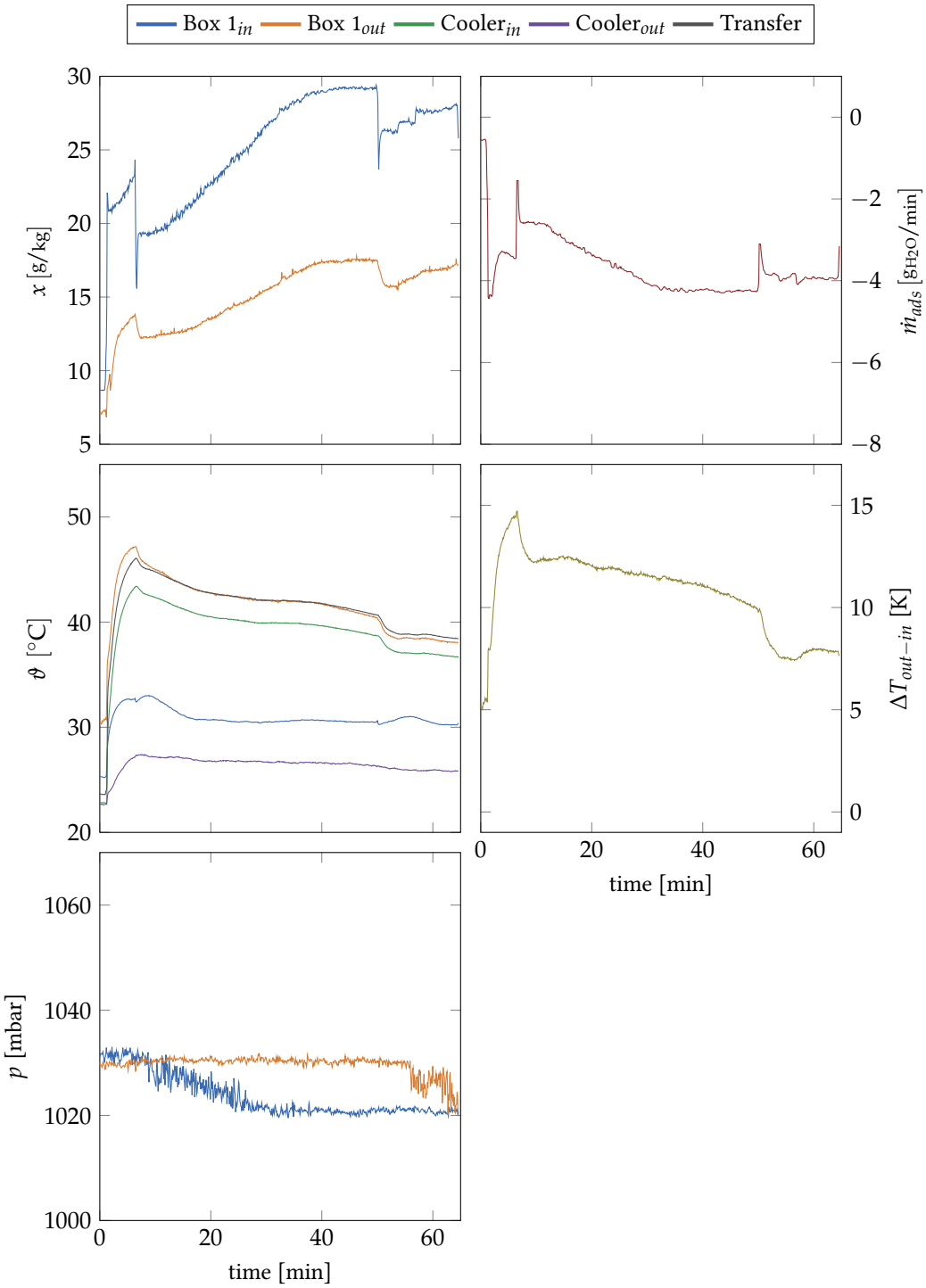

Figure 102: *Box 1* in adsorption mode at 50 % fan power. Loaded sample: *PROS*

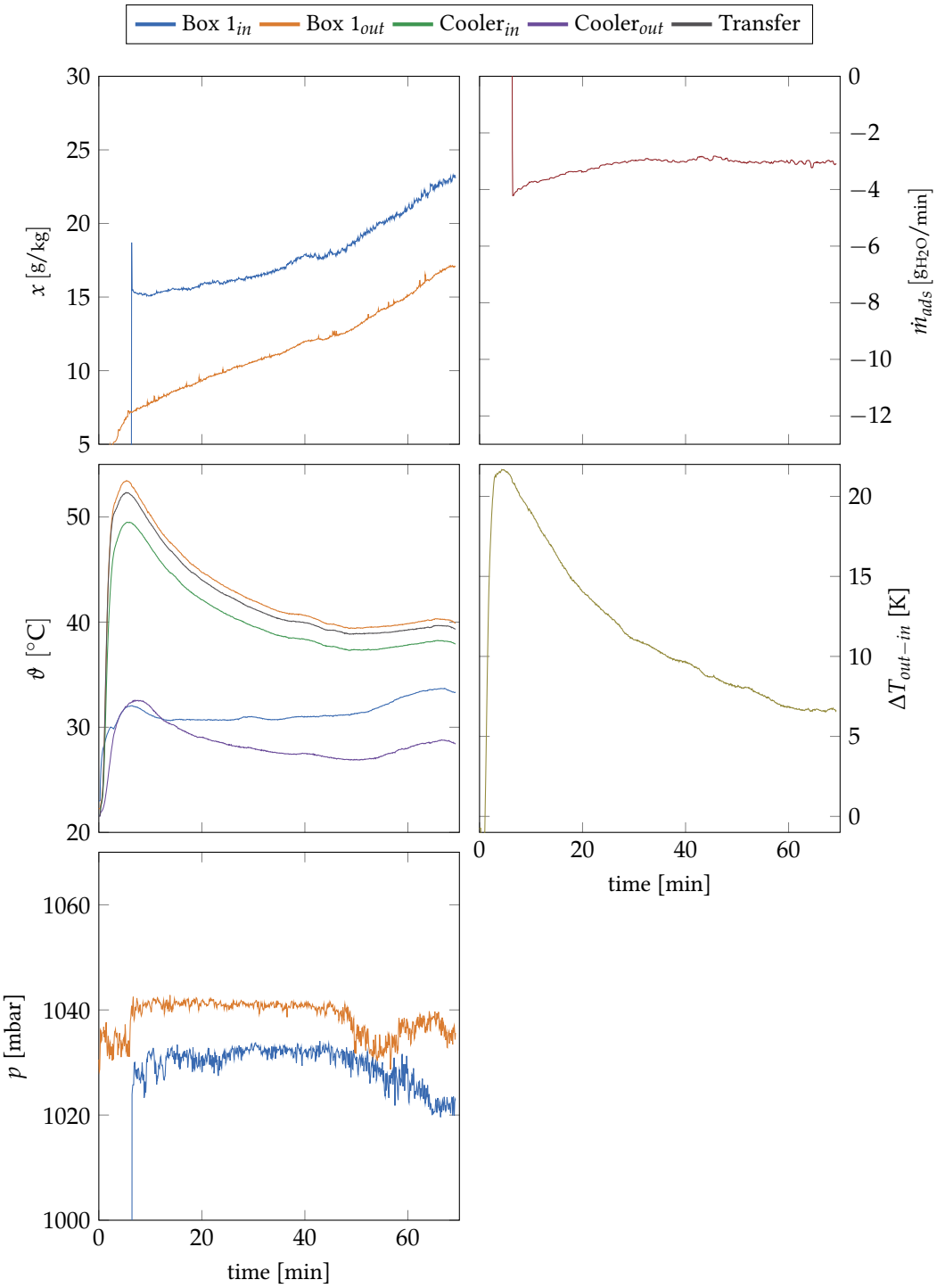

Figure 103: *Box 1* in adsorption mode at 100 % fan power. Loaded sample: *DT-G*

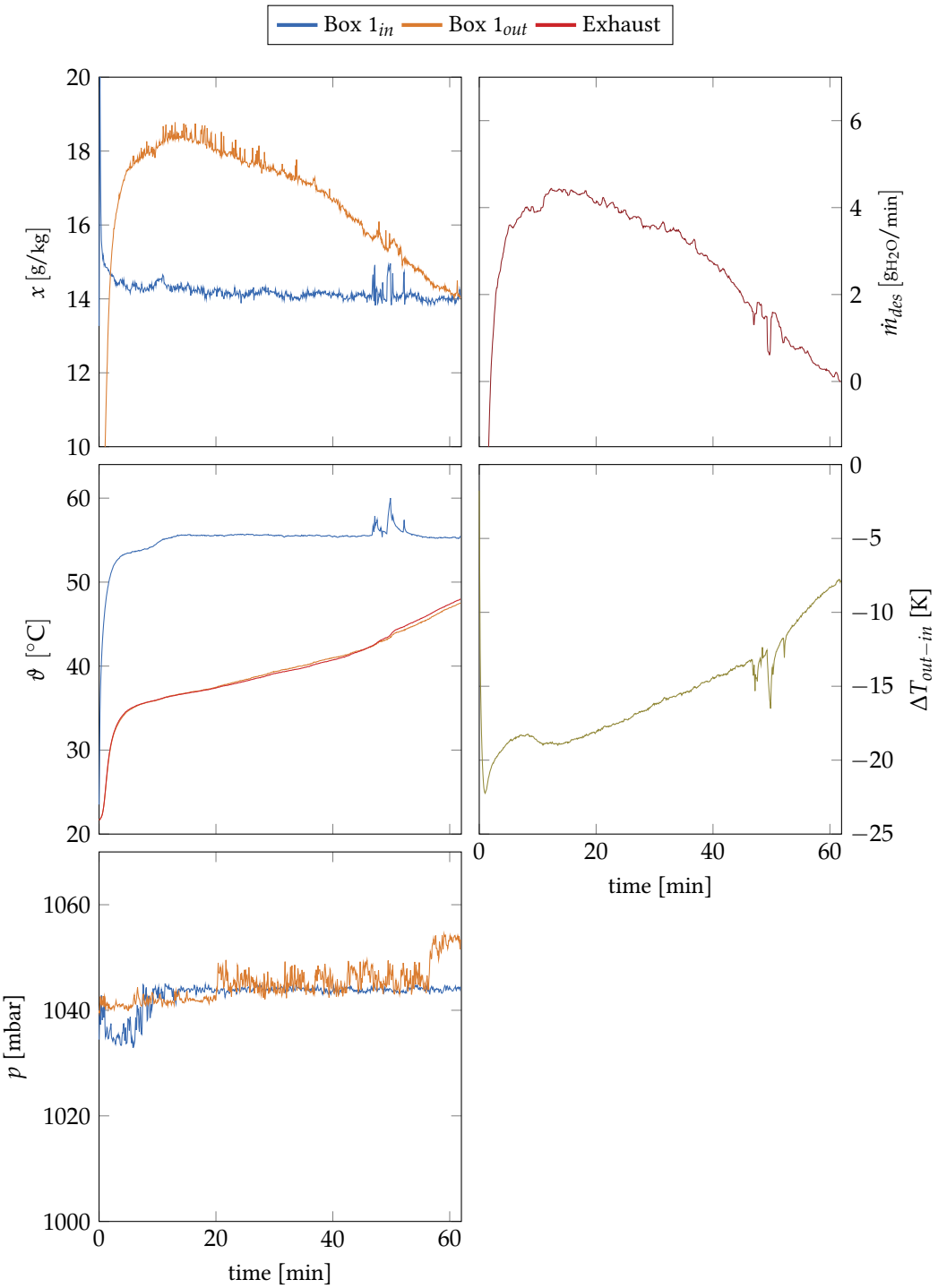

Figure 104: *Box 1* in desorption mode. Loaded sample: *DT-G*

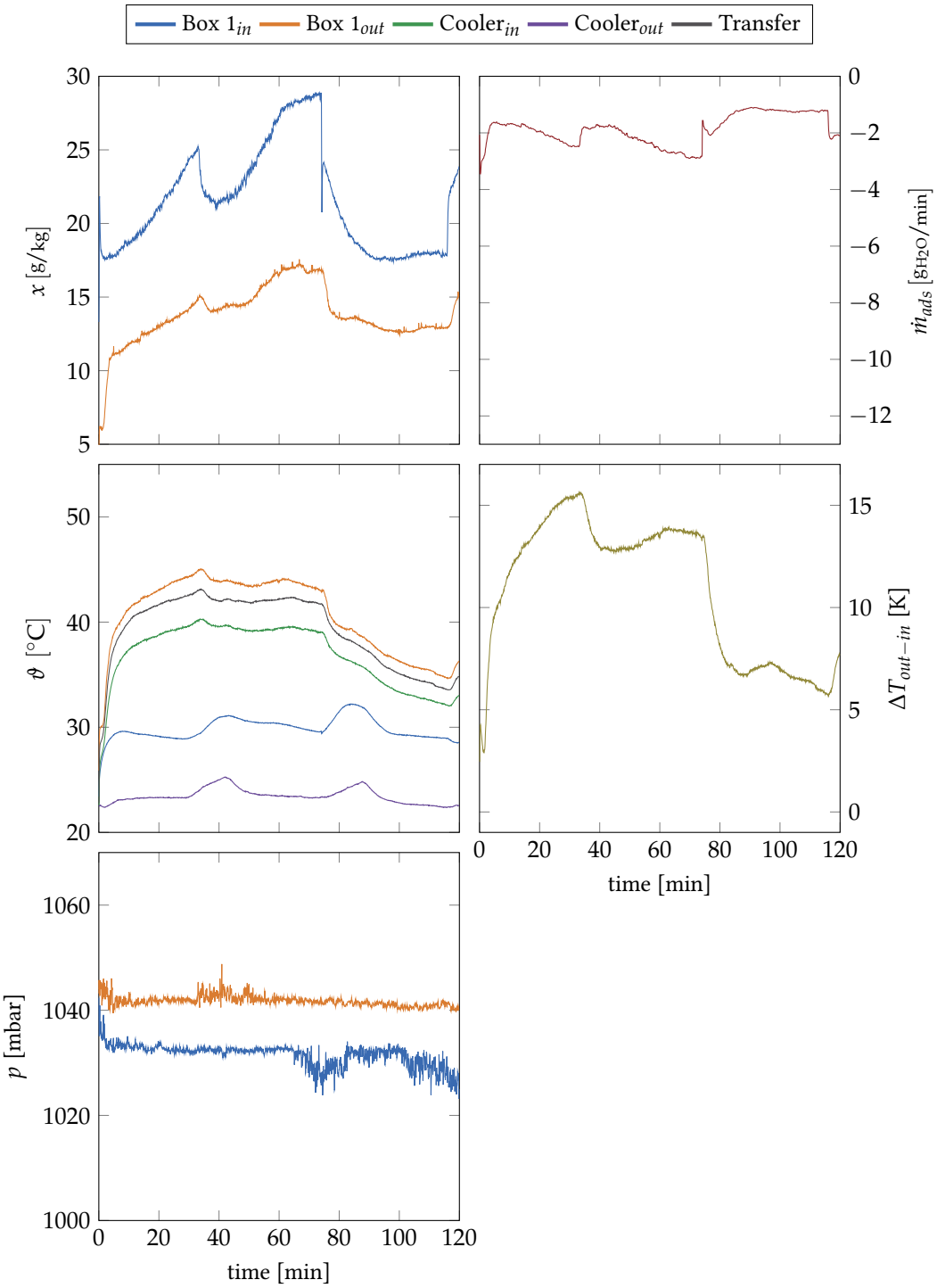

Figure 105: *Box 1* in adsorption mode at 25 % fan power. Loaded sample: *DT-G*

A.5.2 *Results from Adsorber Box 2*

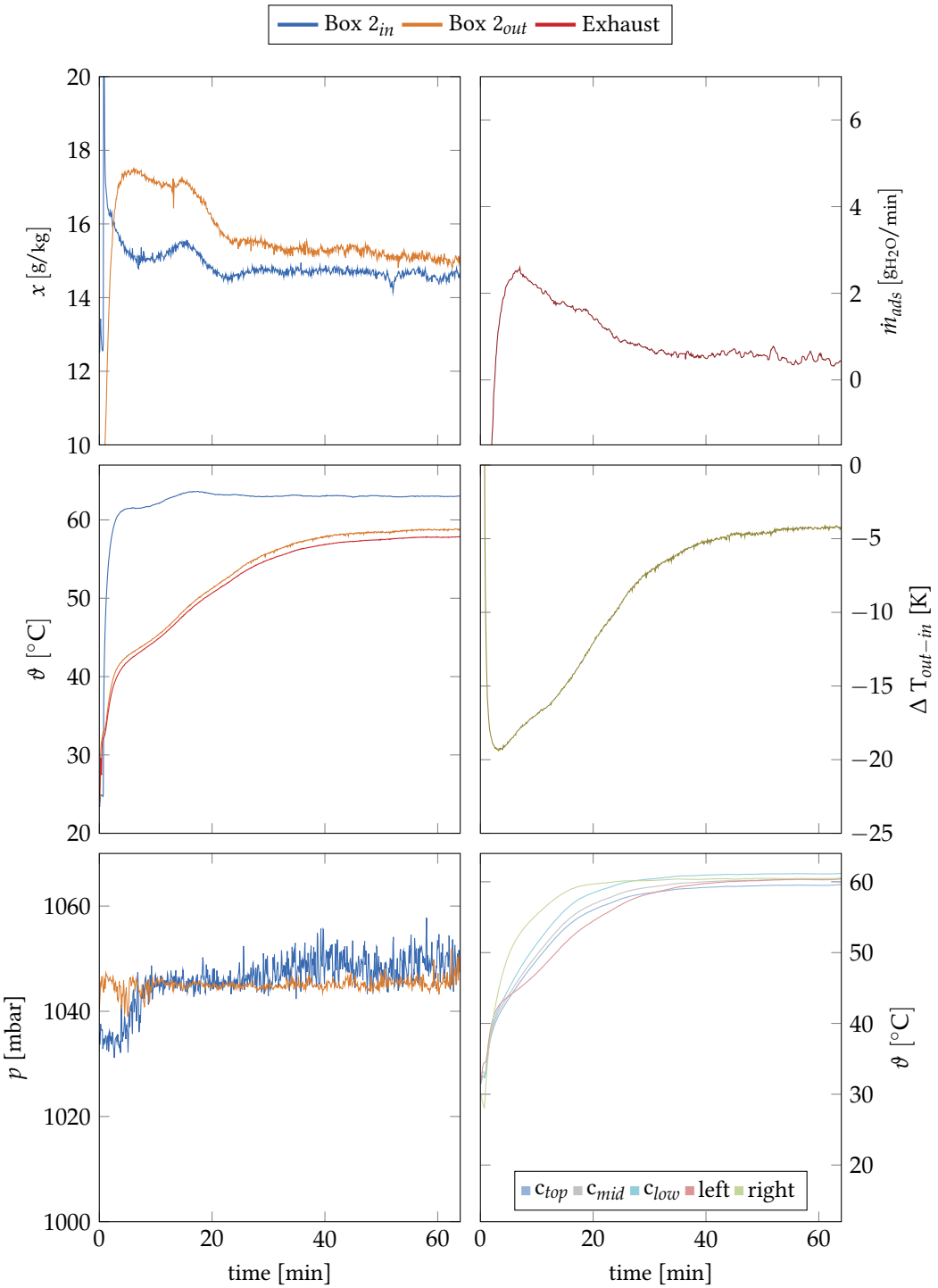

Figure 106: *Box 2* in desorption mode. Loaded sample: *SB-WS*

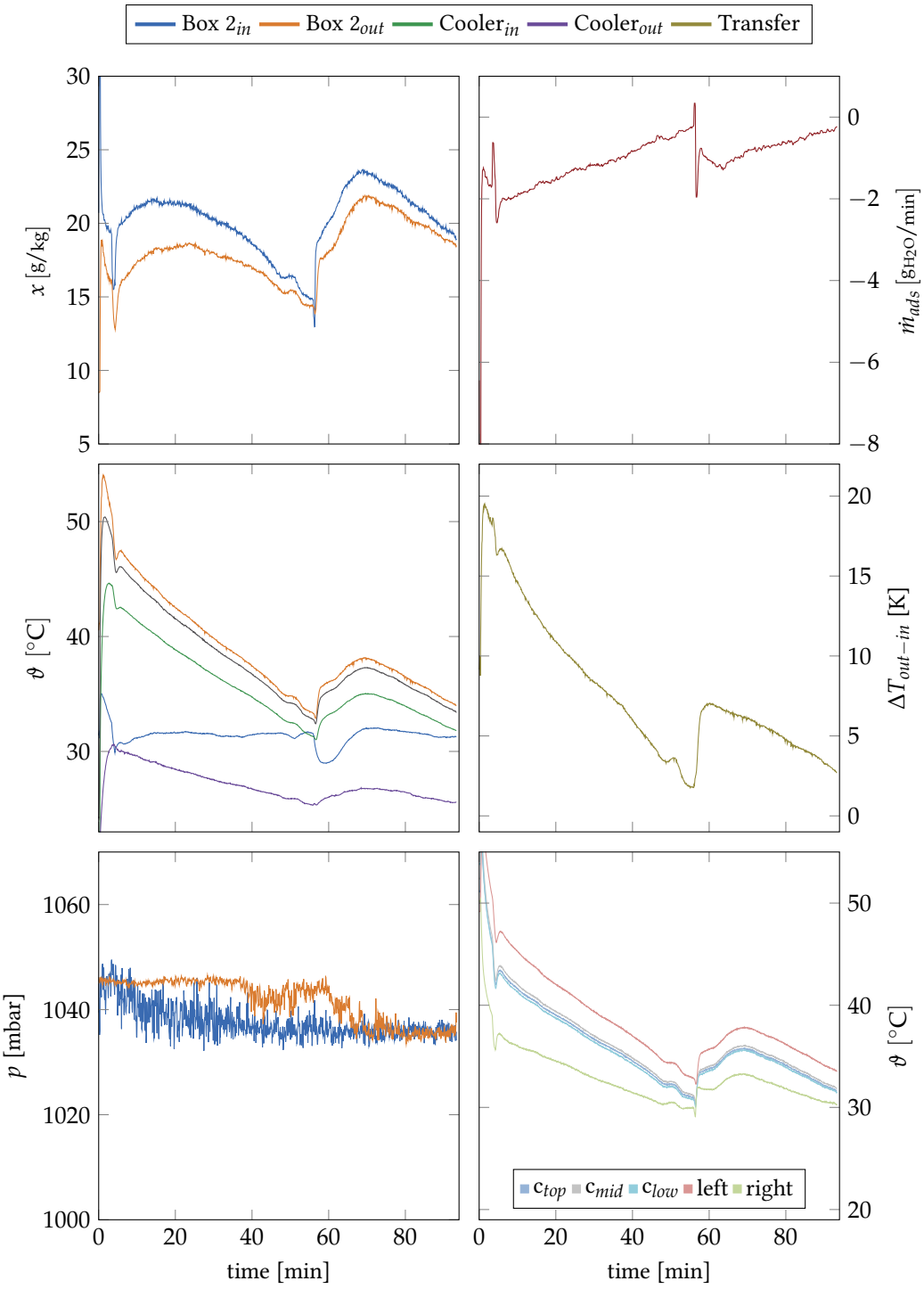

Figure 107: *Box 2* in adsorption mode at 100 % fan power. Loaded sample: *SB-WS*

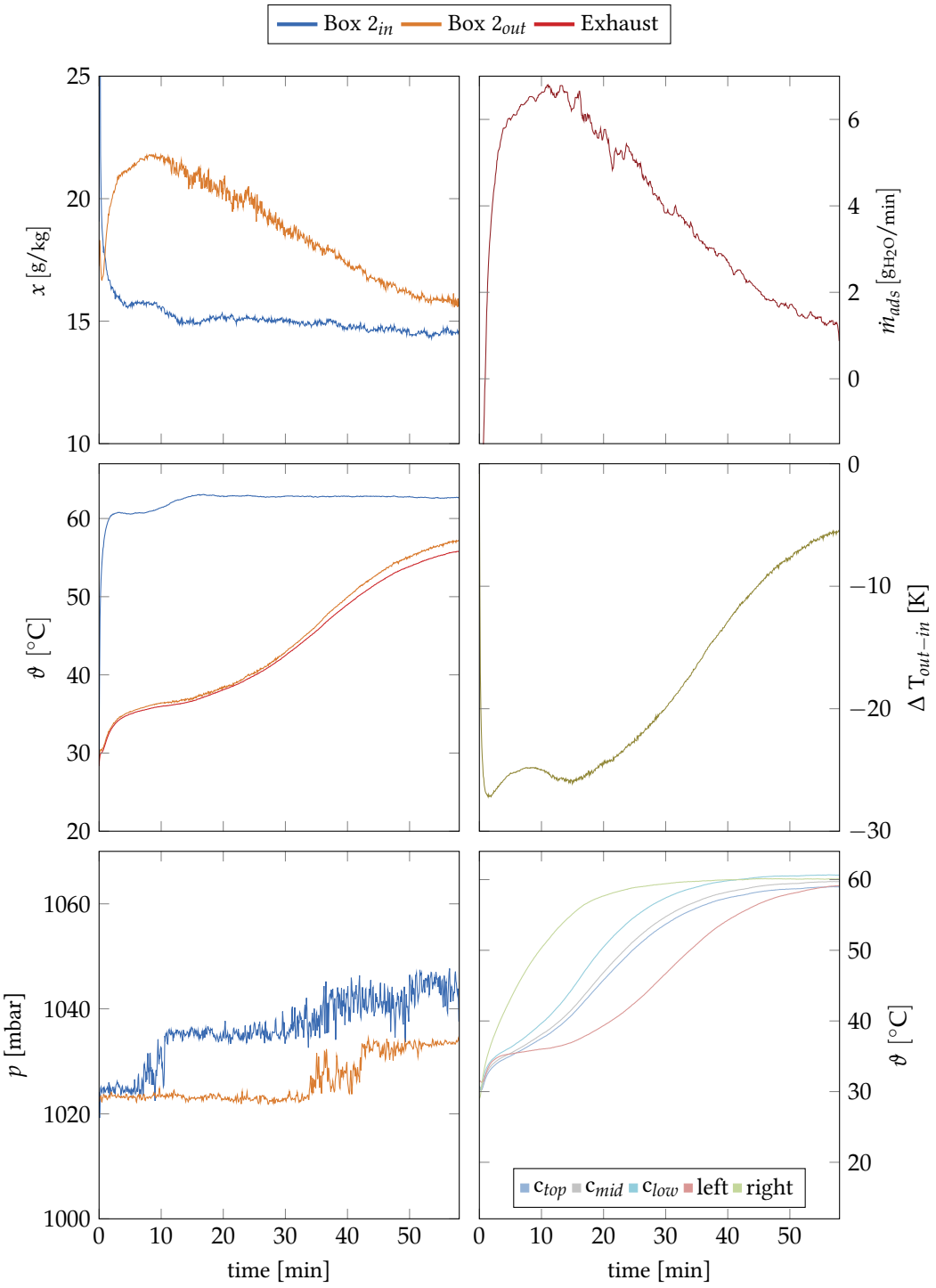

Figure 108: *Box 2* in desorption mode. Loaded sample: *SB-WS*

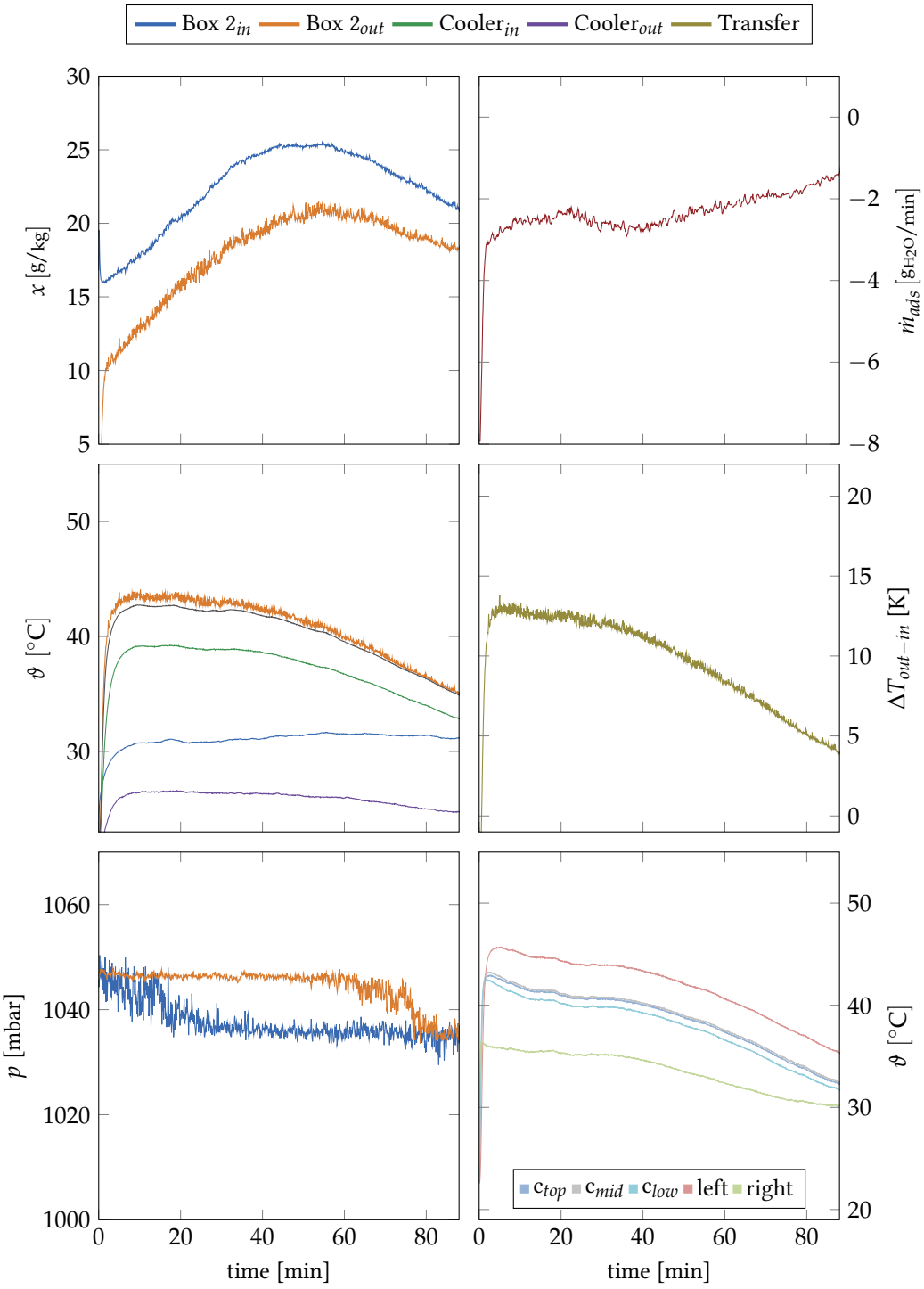

Figure 109: *Box 2* in adsorption mode at 50 % fan power. Loaded sample: *SB-WS*

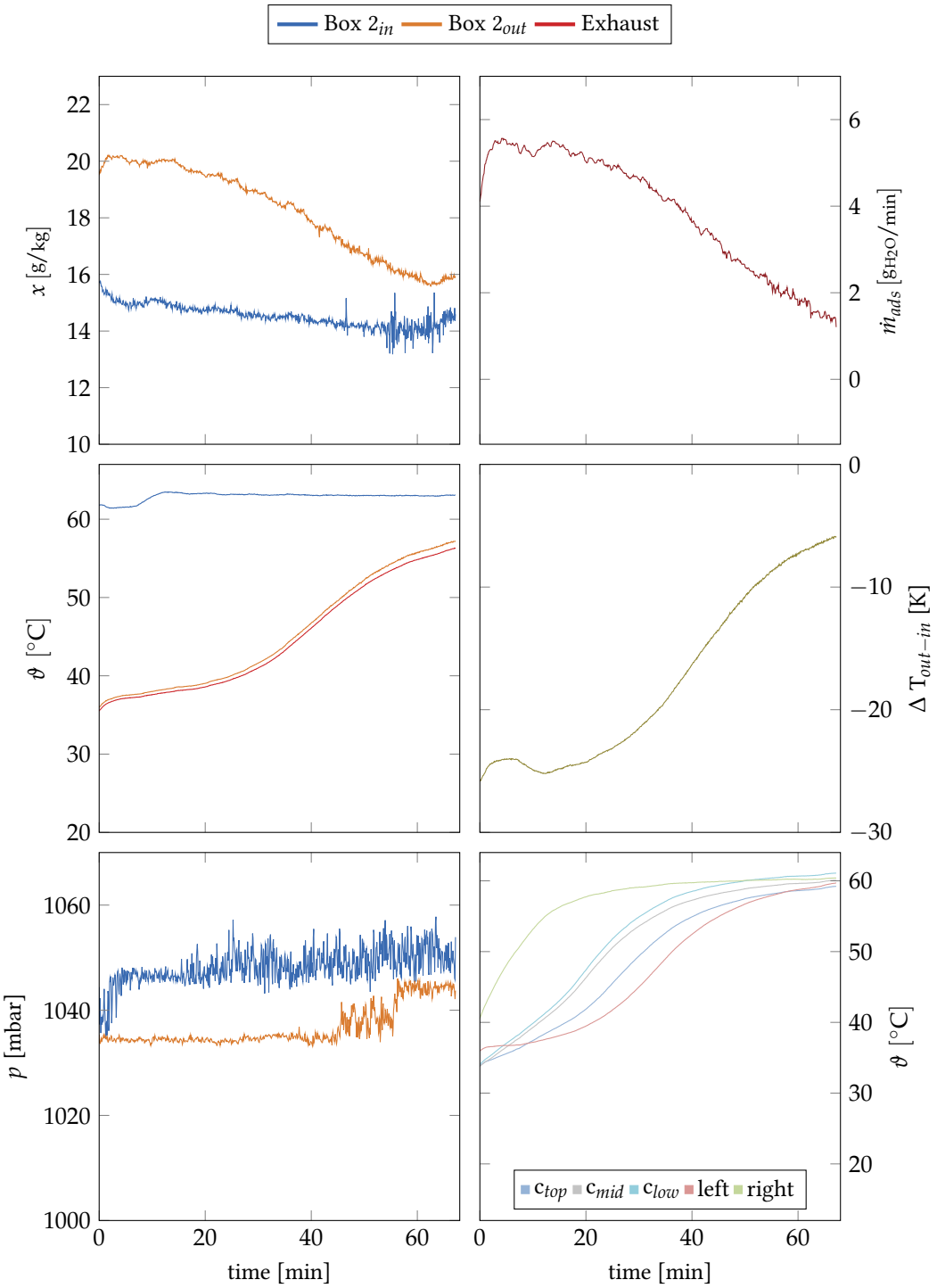

Figure 110: *Box 2* in desorption mode. Loaded sample: *QP-B*

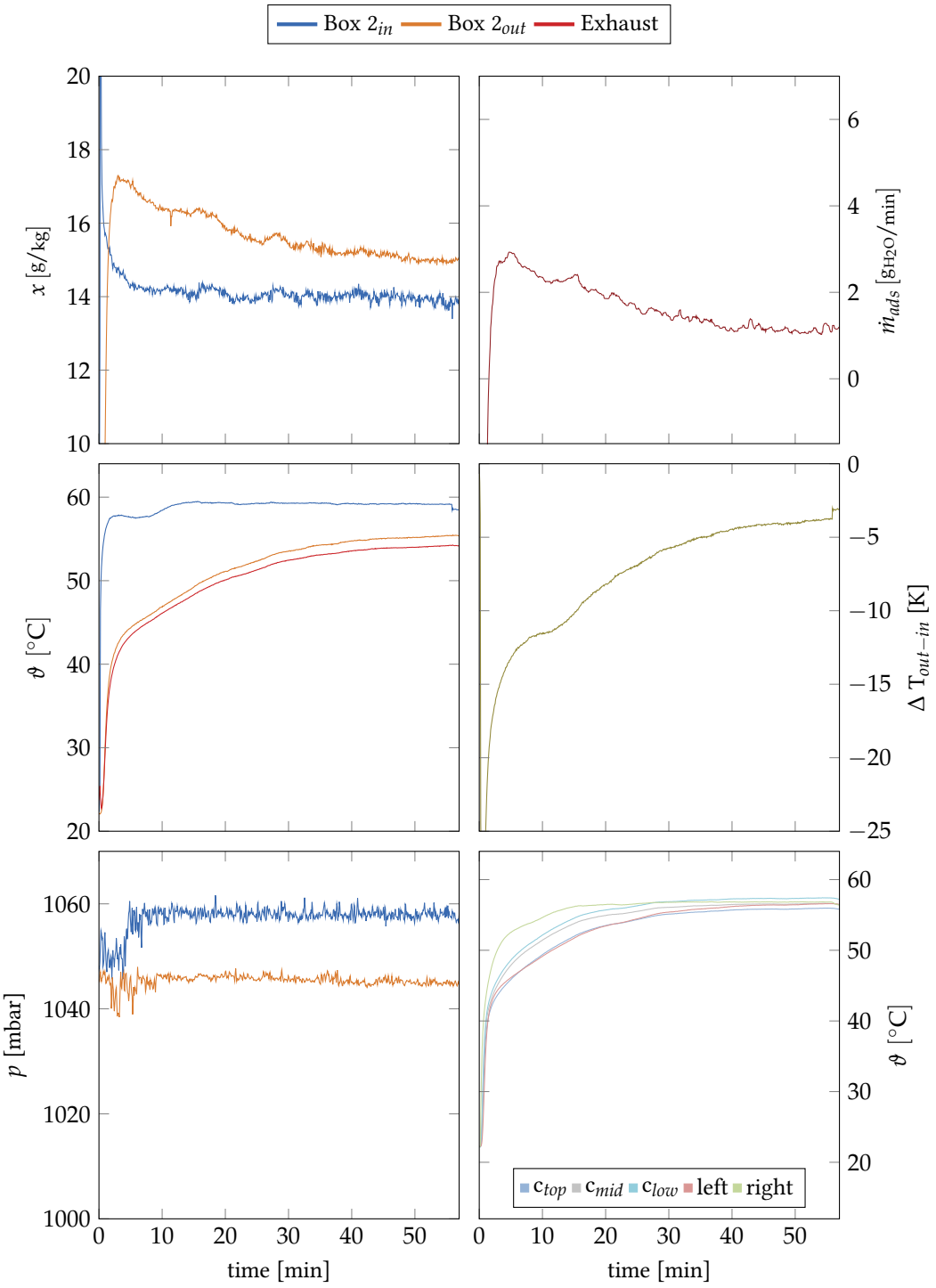

Figure 111: *Box 2* in desorption mode. Loaded sample: *QP-B*

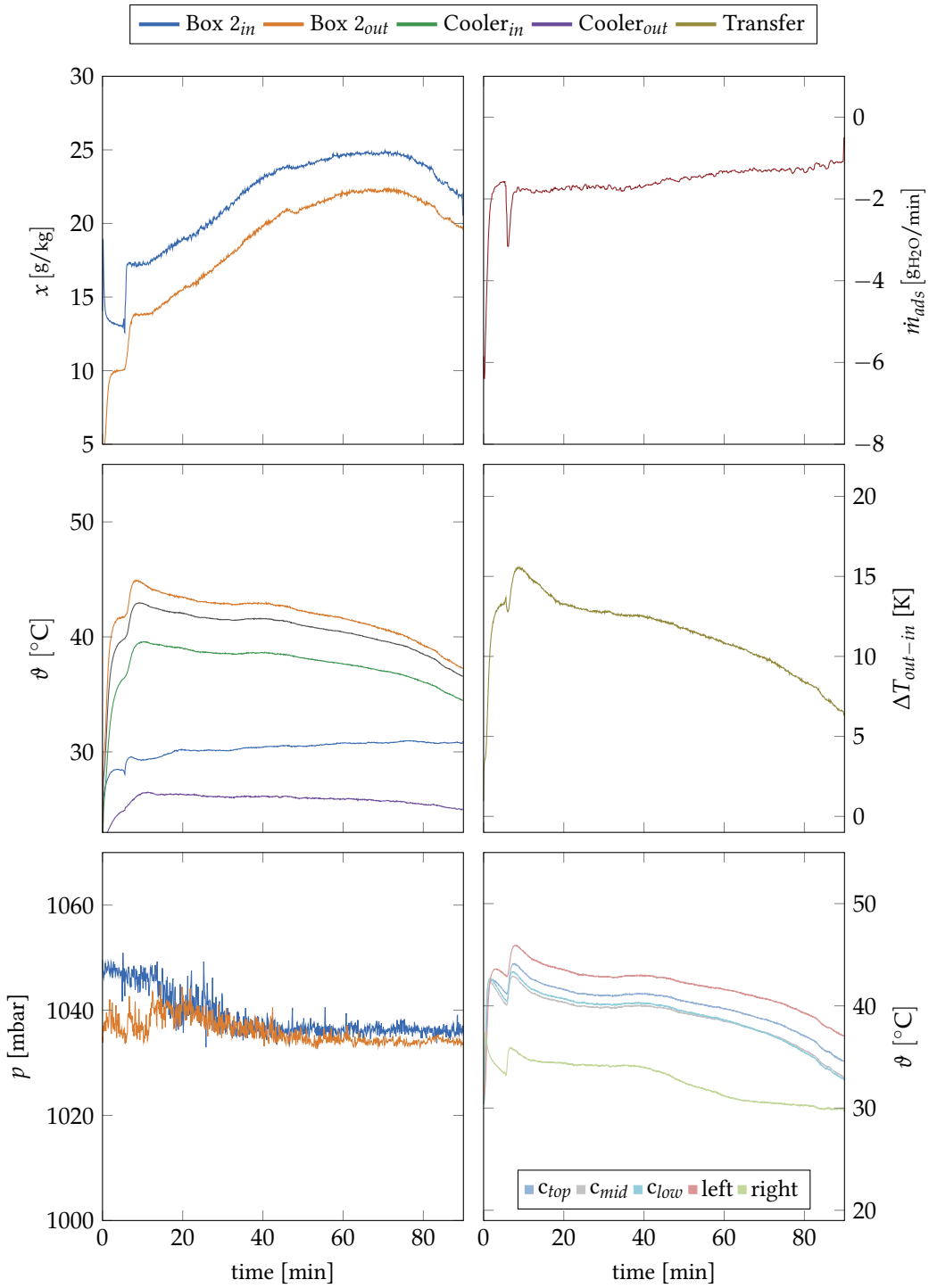

Figure 112: *Box 2* in adsorption mode at 50 % fan power. Loaded sample: *QP-B*

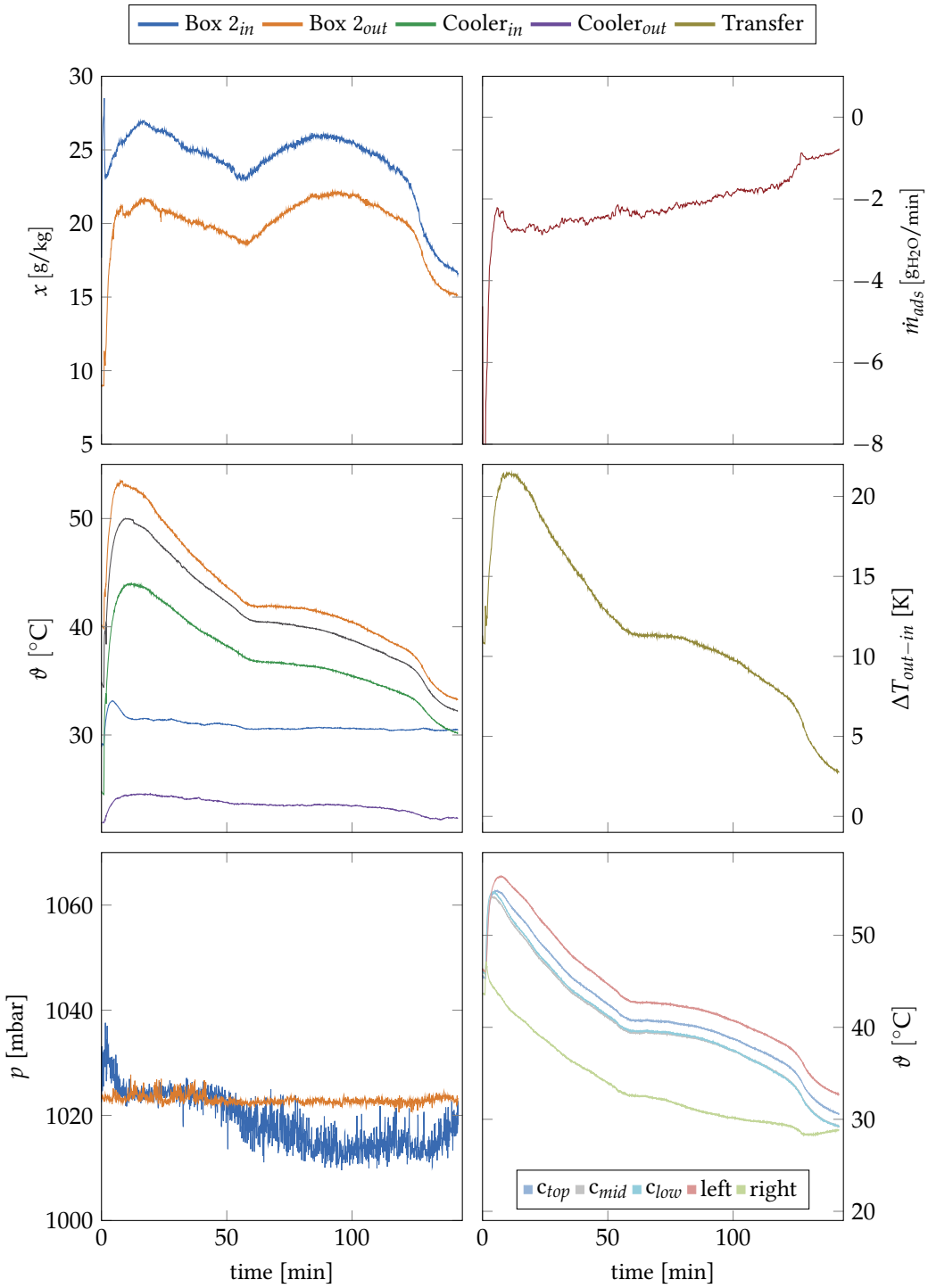

Figure 113: *Box 2* in adsorption mode at 25 % fan power. Loaded sample: *QP-B*

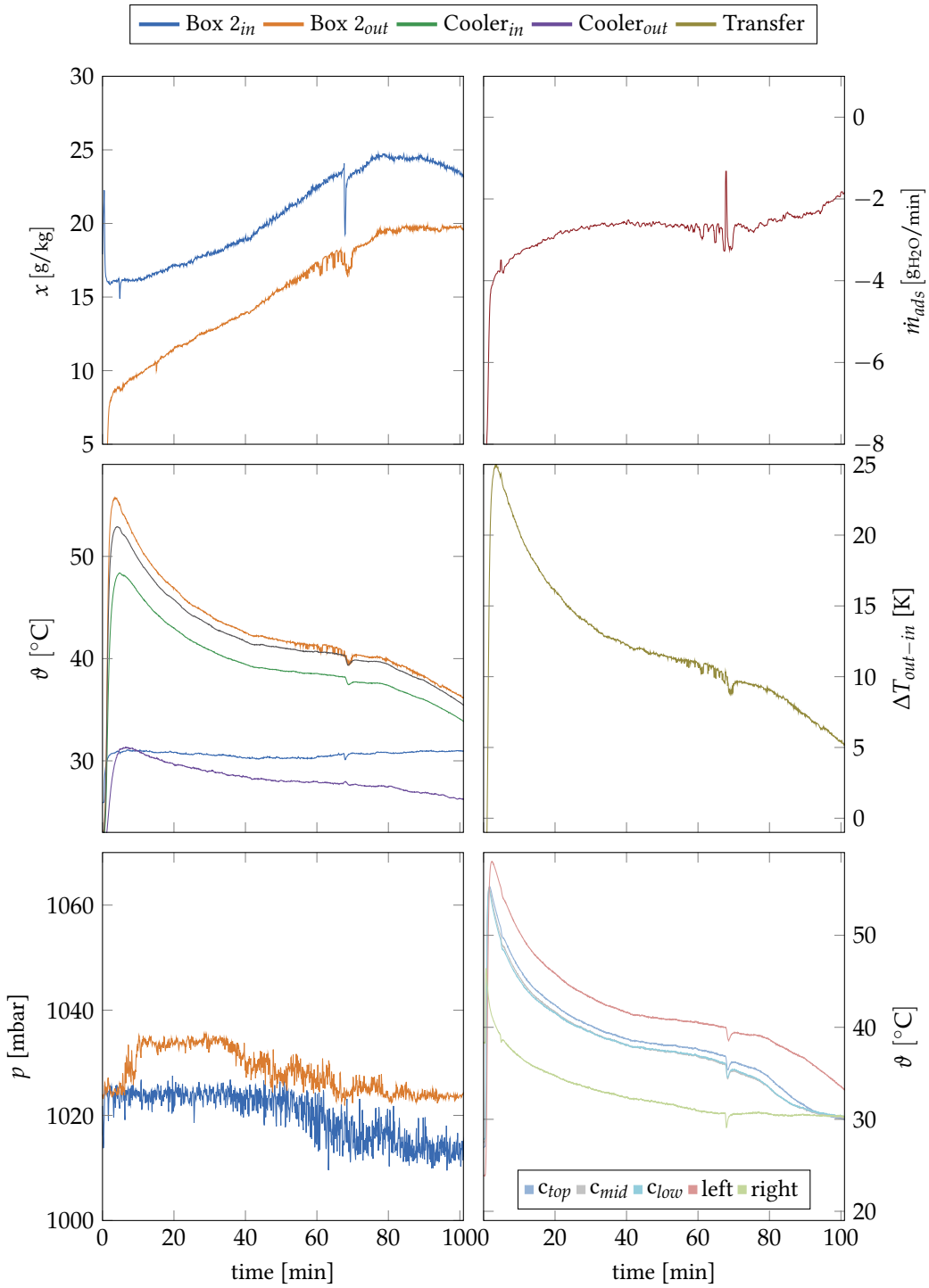

Figure 114: *Box 2* in adsorption mode at 100 % fan power. Loaded sample: *HD-W*

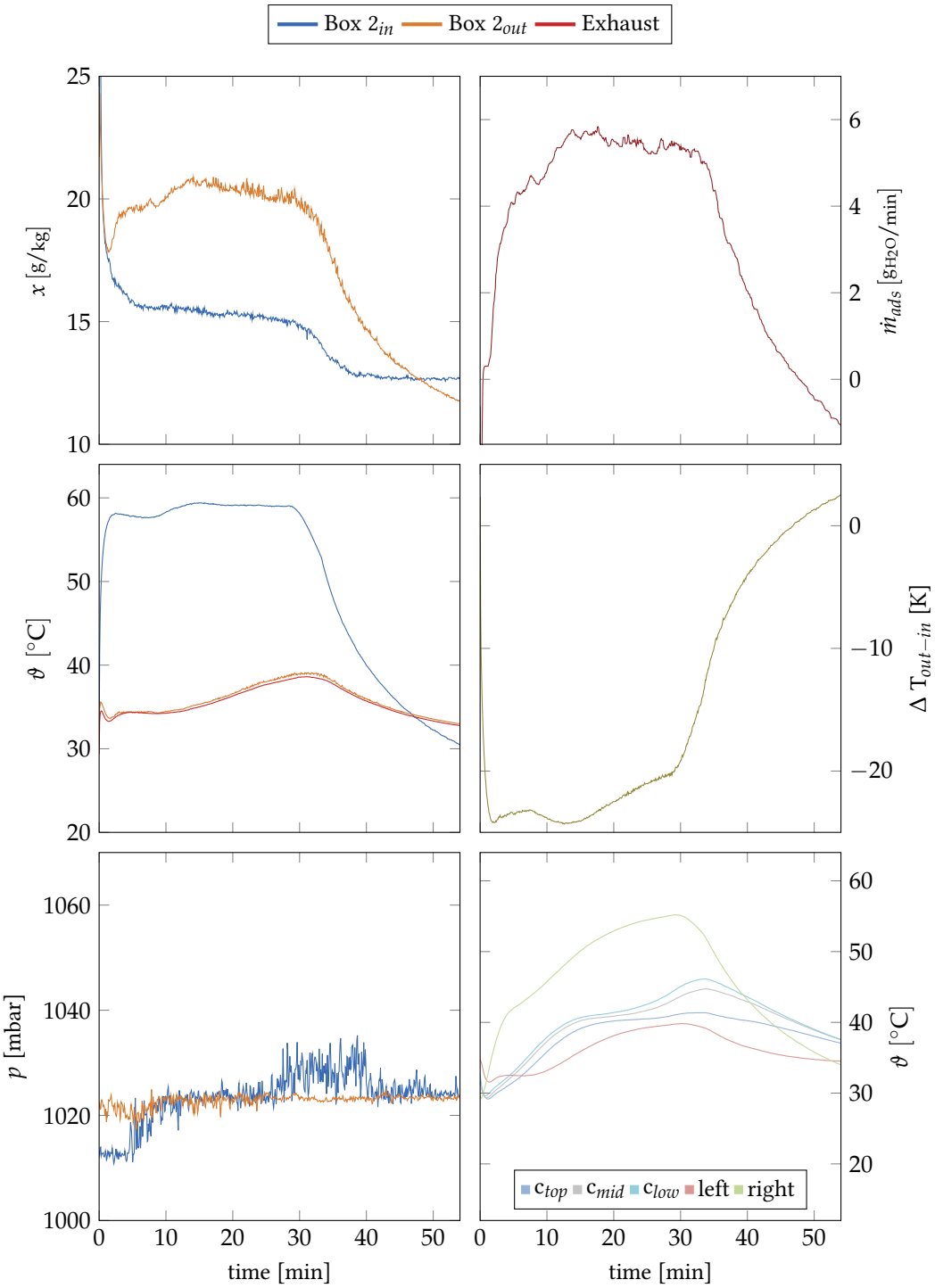

Figure 115: *Box 2* in desorption mode. Loaded sample: *HD-W*

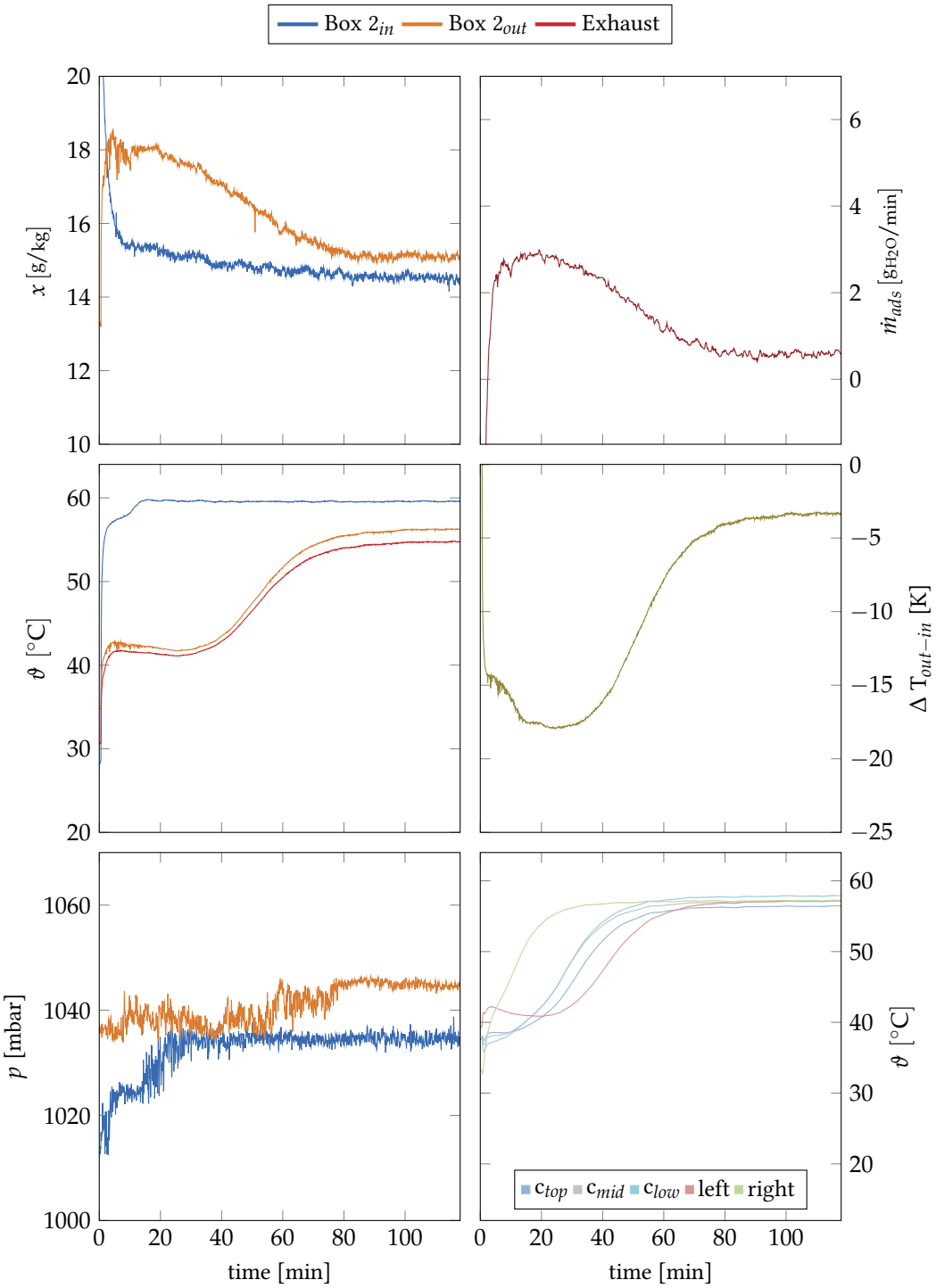

Figure 116: *Box 2* in desorption mode. Loaded sample: *HD-W*

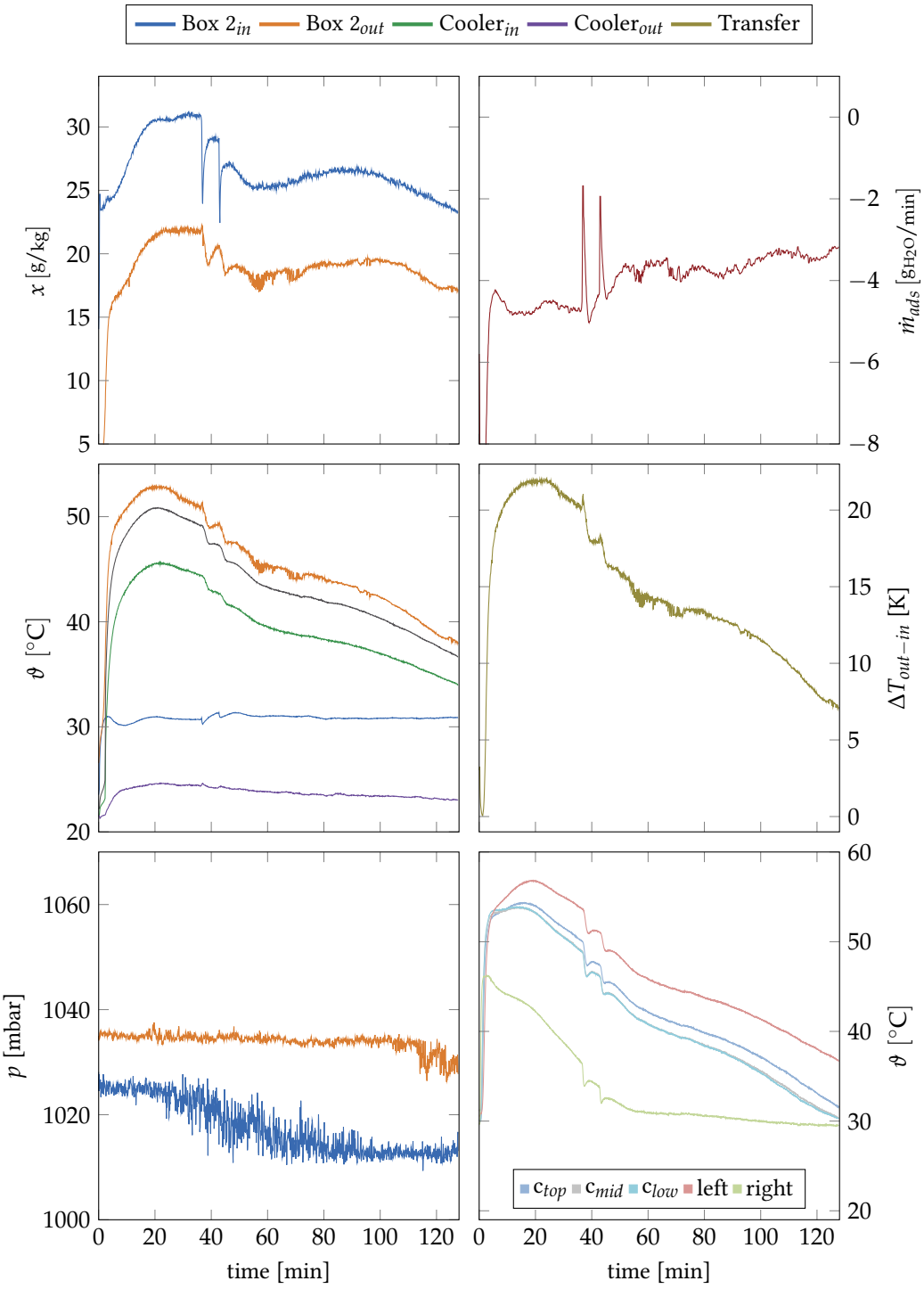

Figure 117: *Box 2* in adsorption mode at 25 % fan power. Loaded sample: *HD-W*

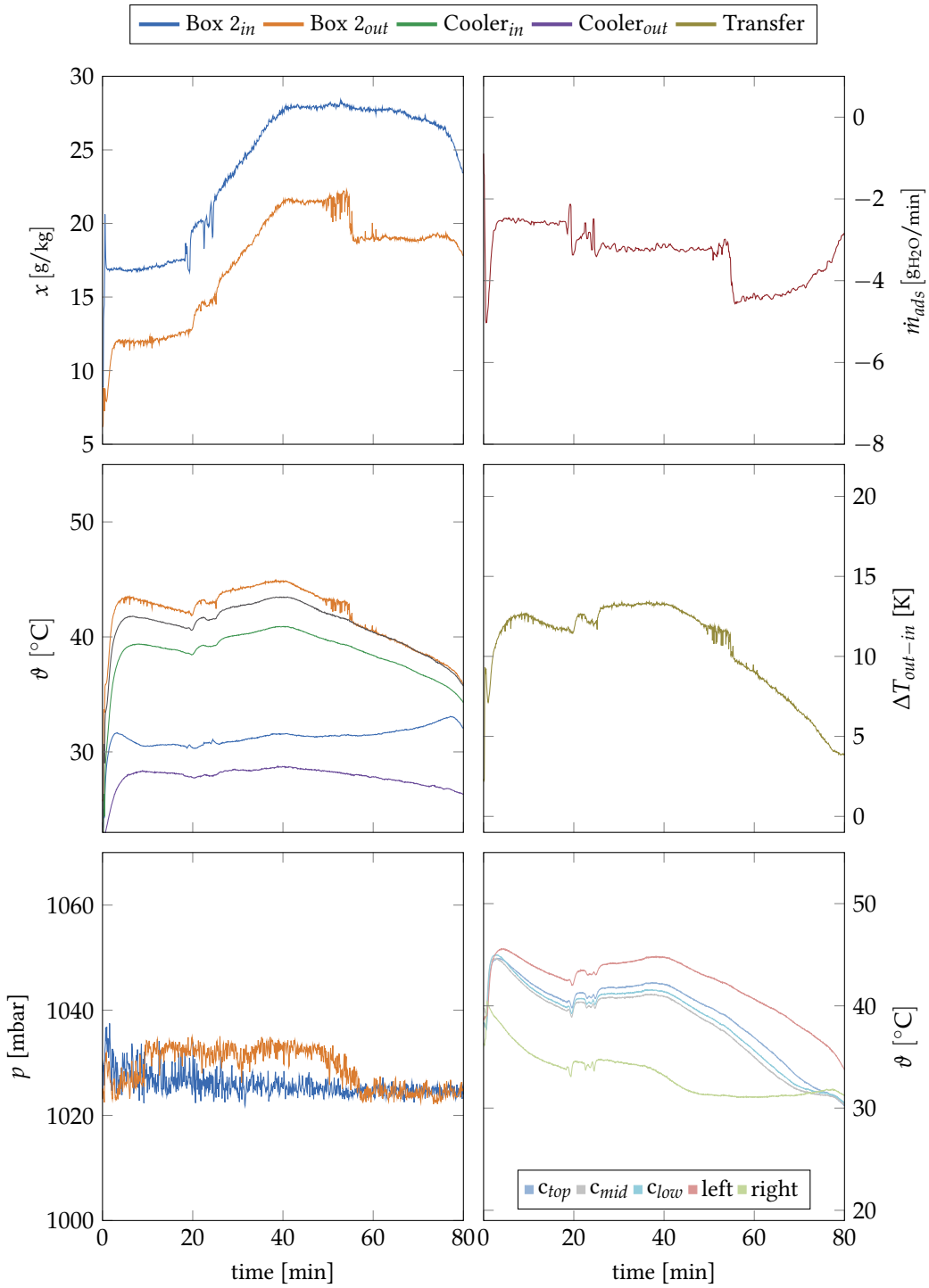

Figure 118: *Box 2* in adsorption mode at 100 % fan power. Loaded sample: *HD-W*

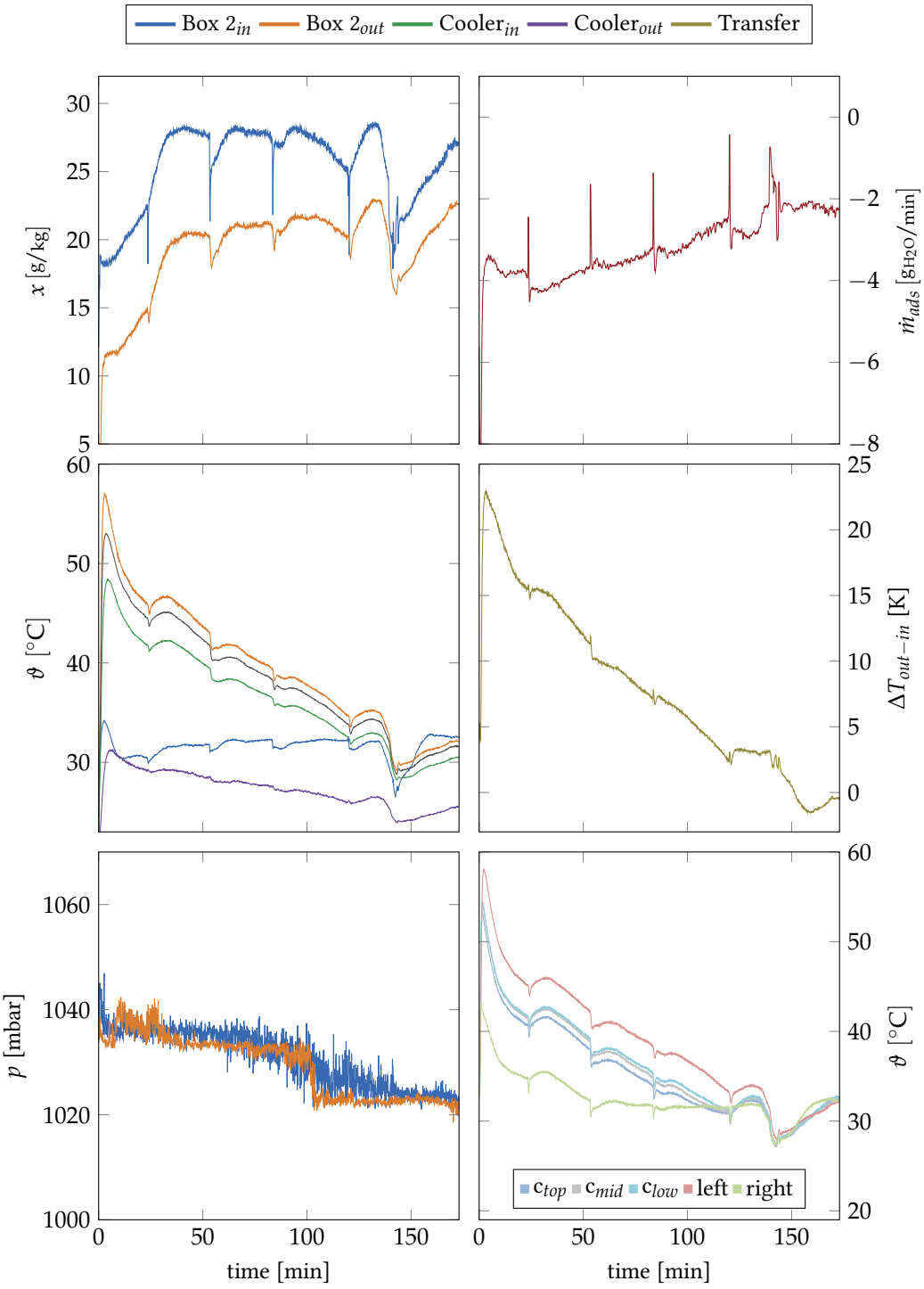

Figure 119: *Box 2* in adsorption mode at 100 % fan power. Loaded sample: *SB-C*

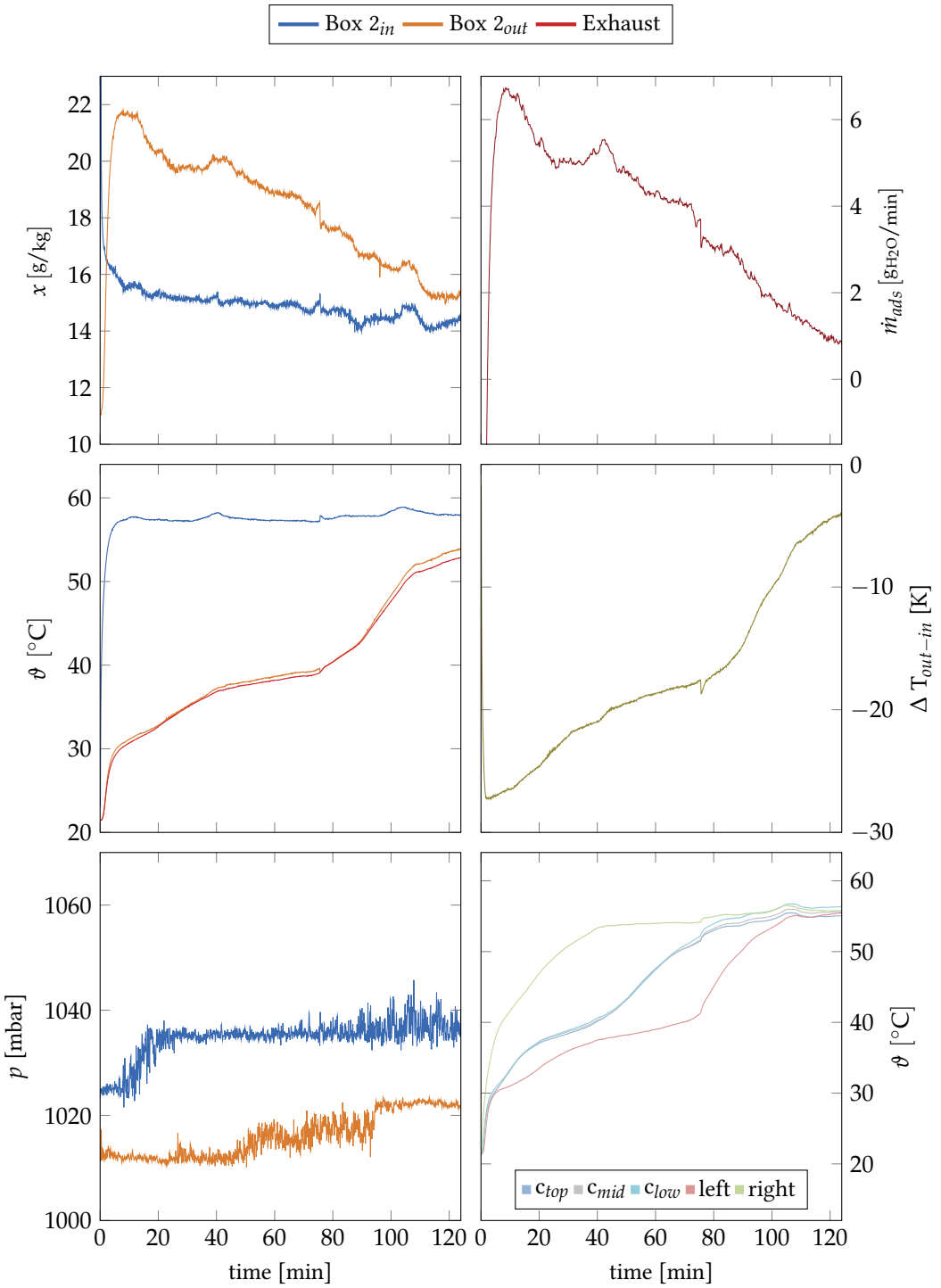

Figure 120: *Box 2* in desorption mode. Loaded sample: *SB-C*

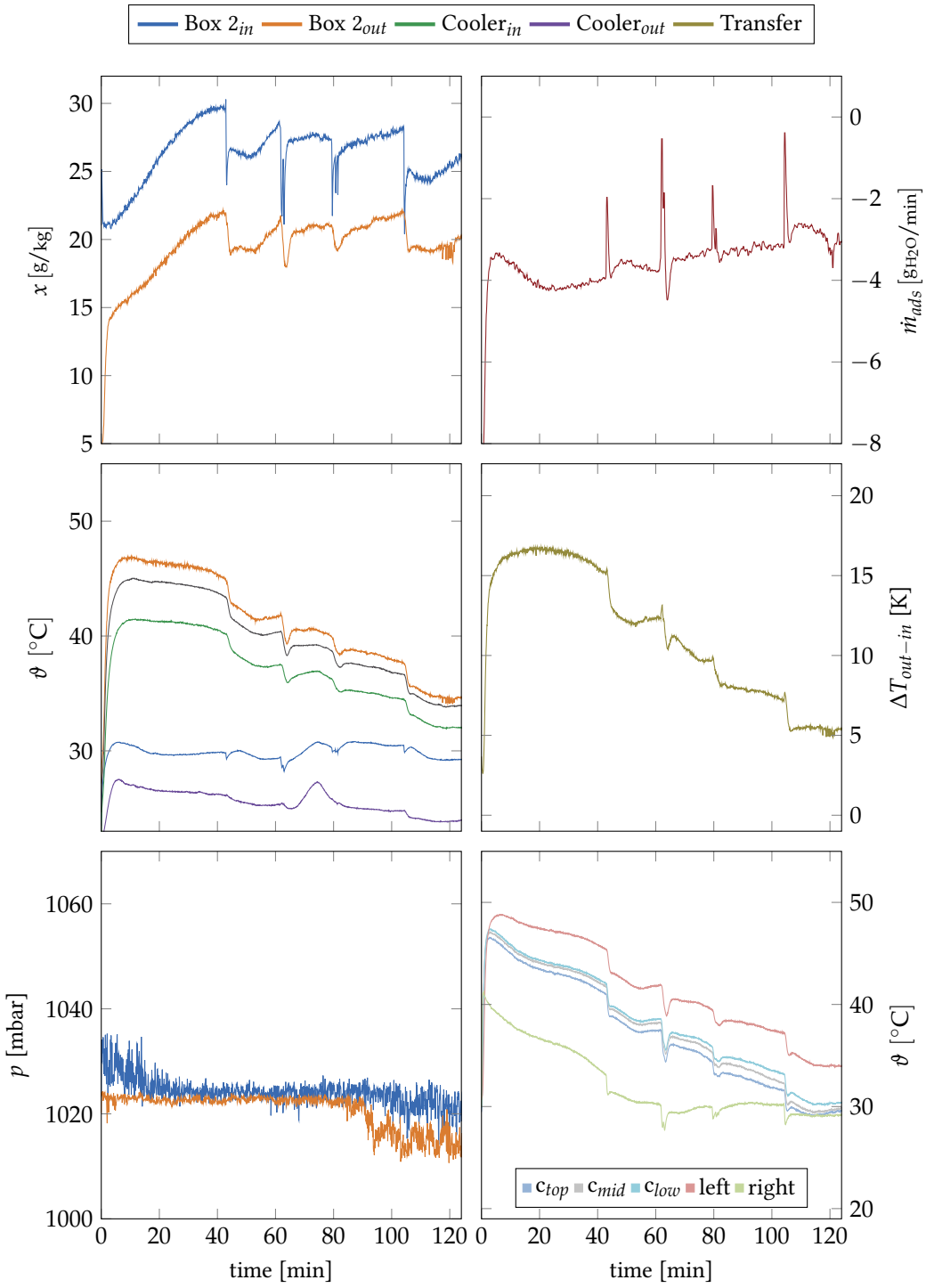

Figure 121: *Box 2* in adsorption mode at 50 % fan power. Loaded sample: *SB-C*

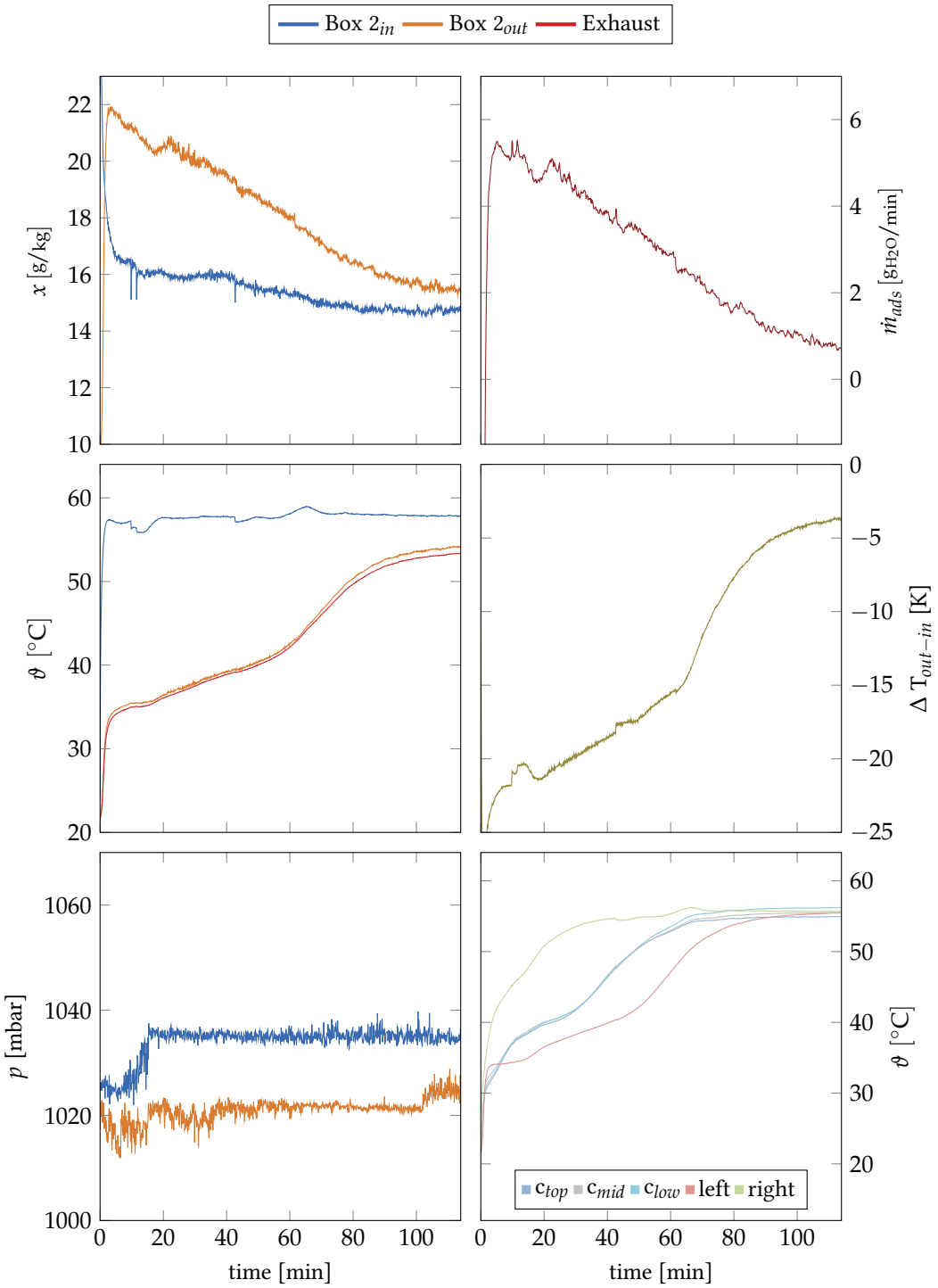

Figure 122: *Box 2* in desorption mode. Loaded sample: *SB-C*

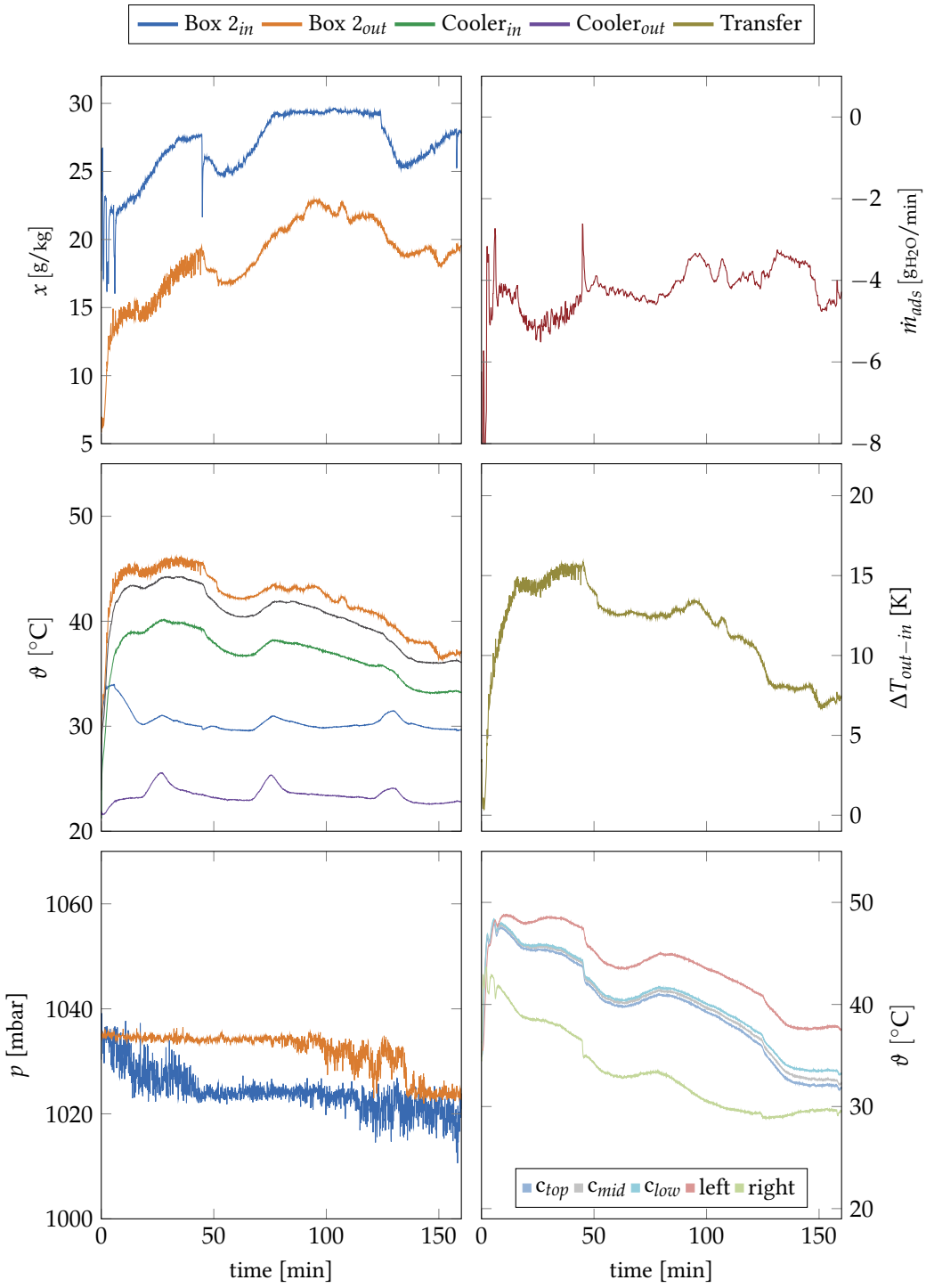

Figure 123: *Box 2* in adsorption mode at 25 % fan power. Loaded sample: *SB-C*

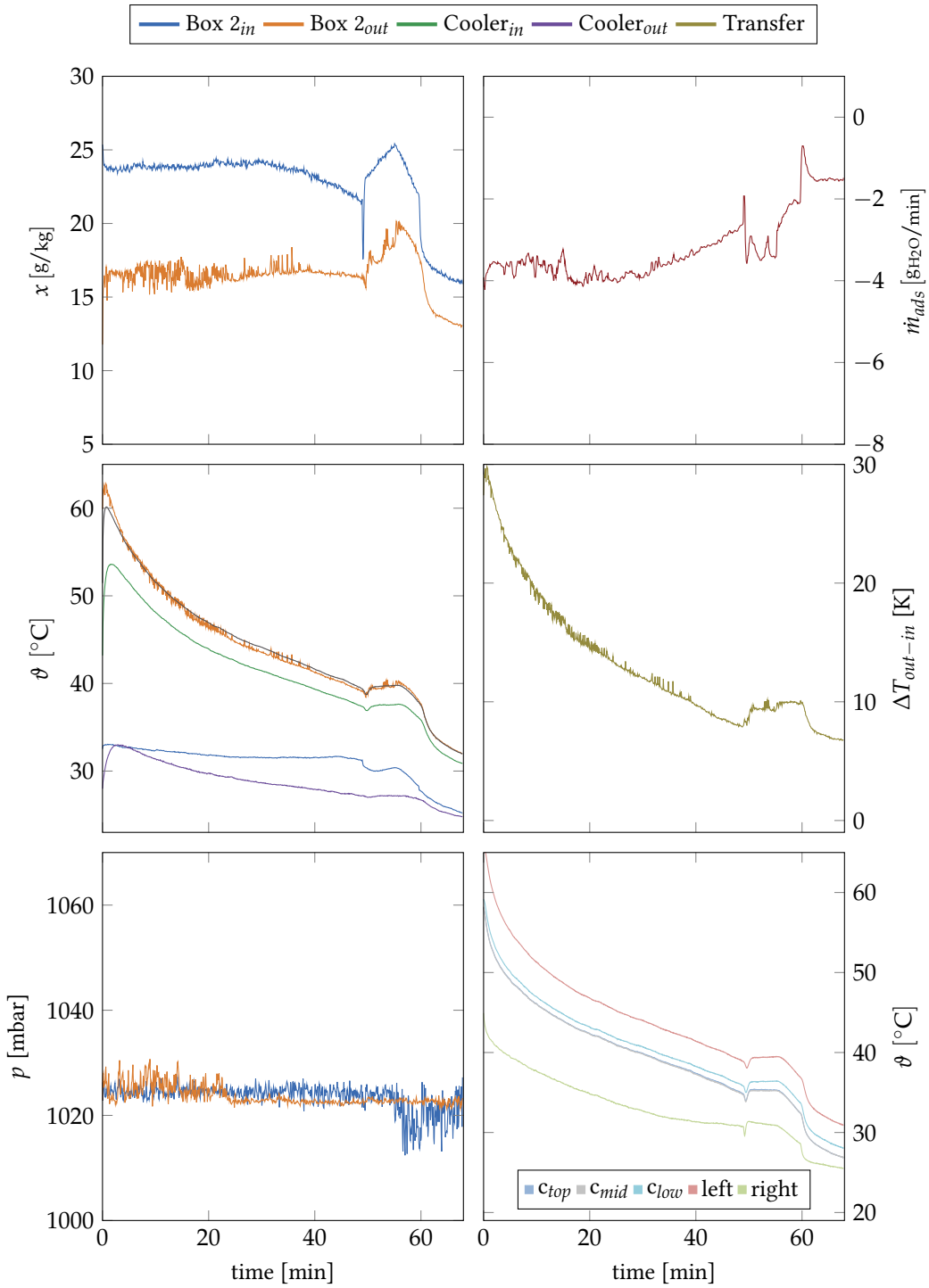

Figure 124: *Box 2* in adsorption mode at 100 % fan power. Loaded sample: *DT-B*

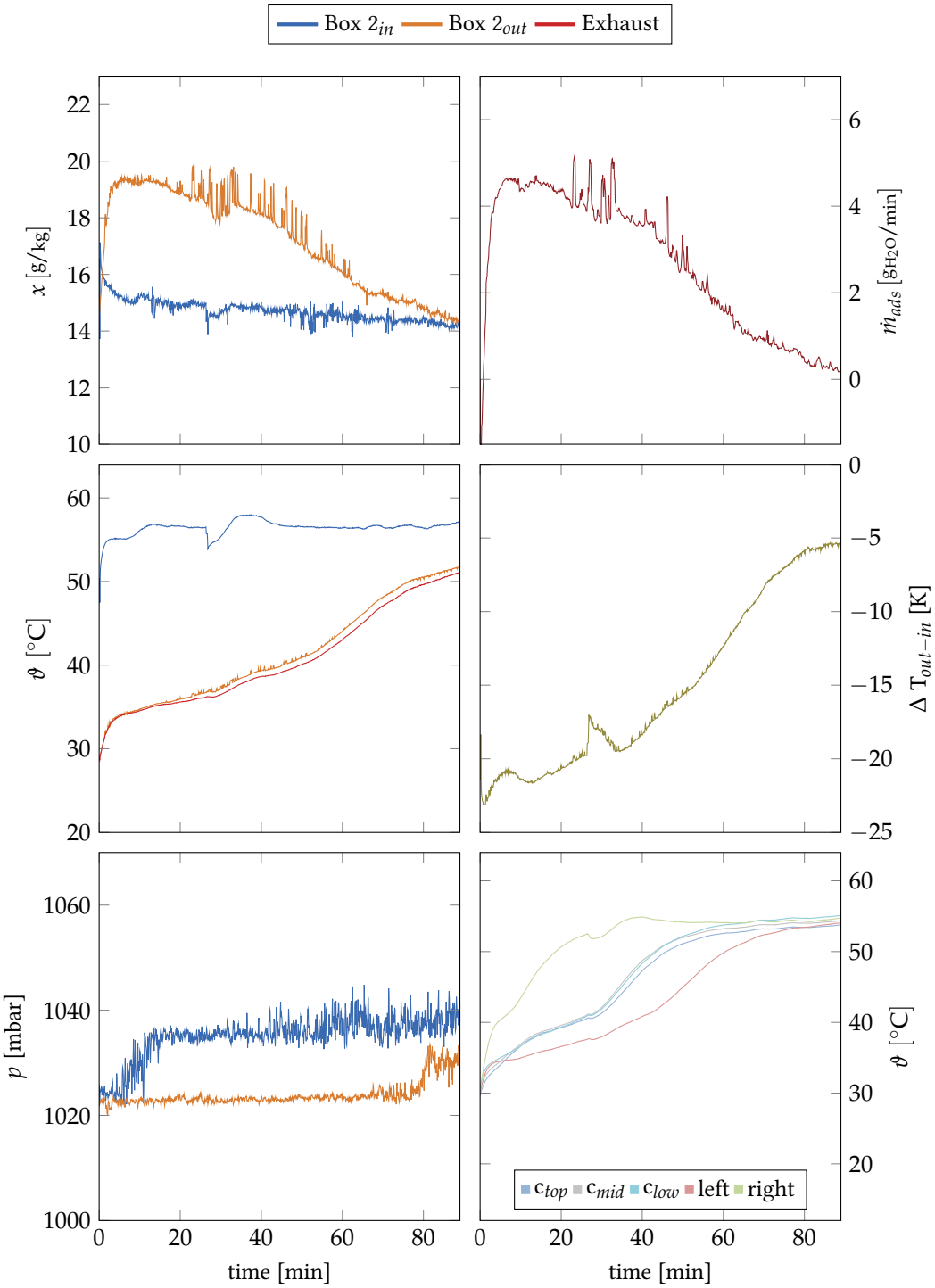

Figure 125: *Box 2* in desorption mode. Loaded sample: *DT-B*

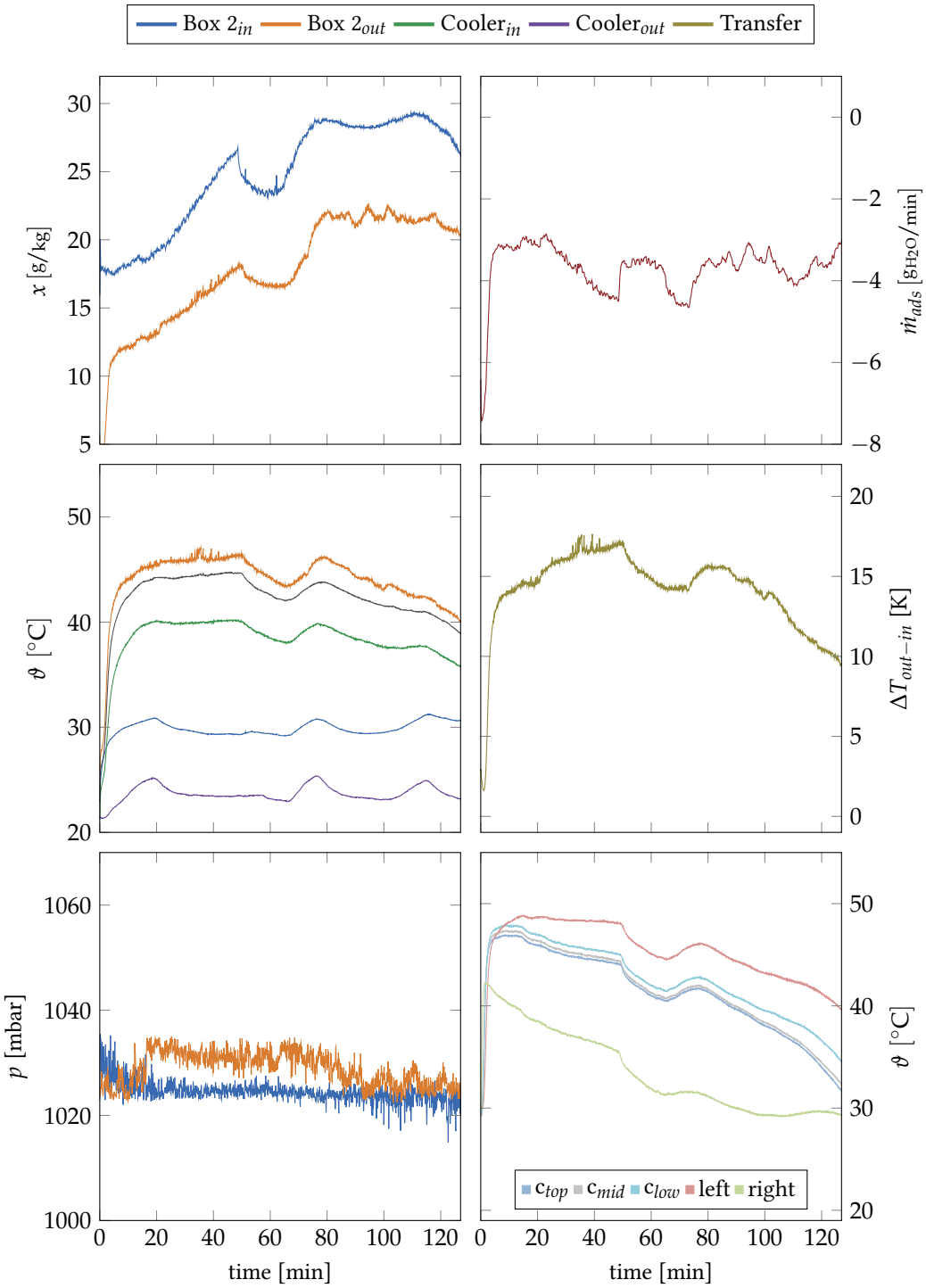

Figure 126: *Box 2* in adsorption mode at 25 % fan power. Loaded sample: *DT-B*

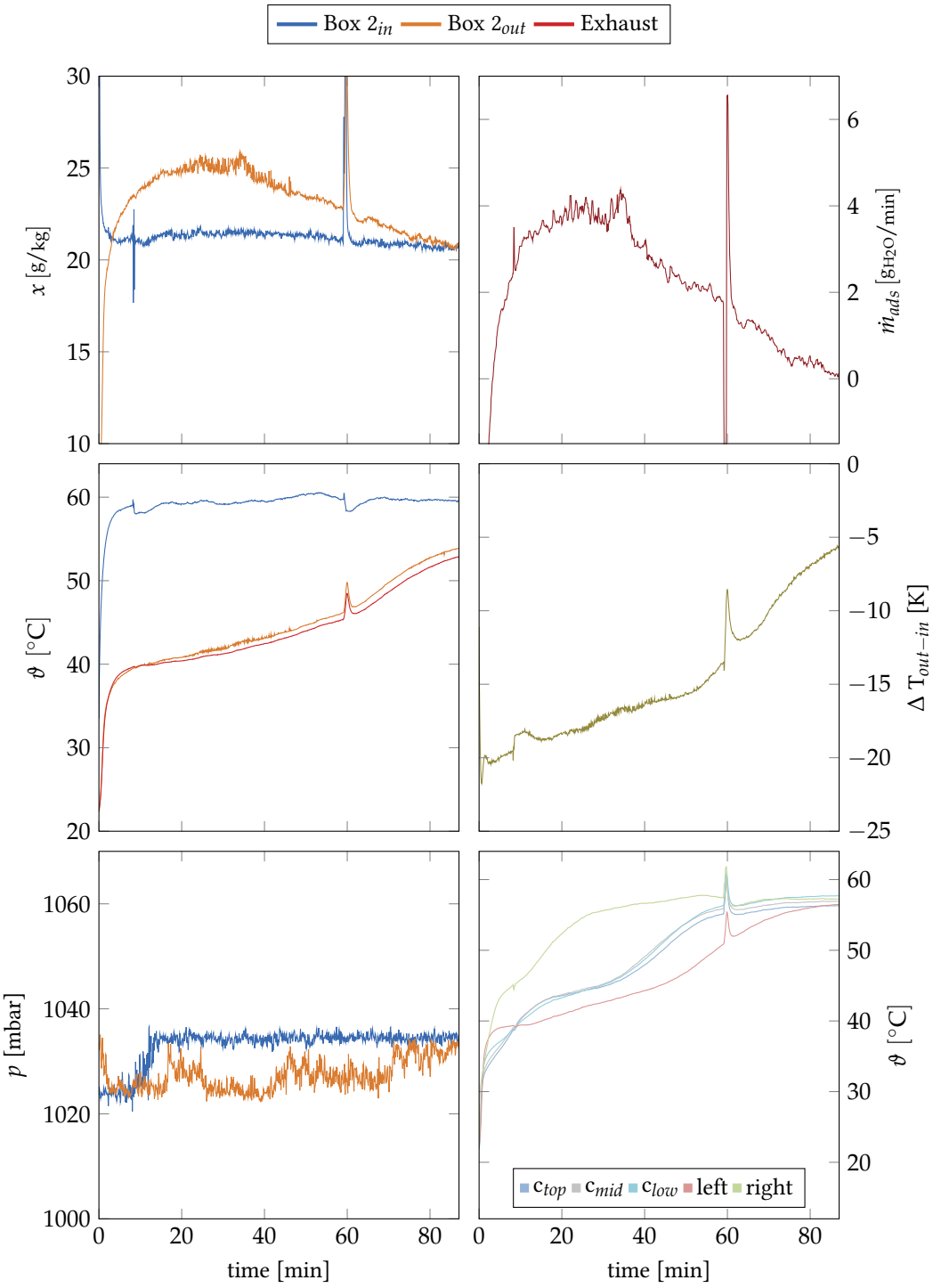

Figure 127: *Box 2* in desorption mode. Loaded sample: *DT-B*

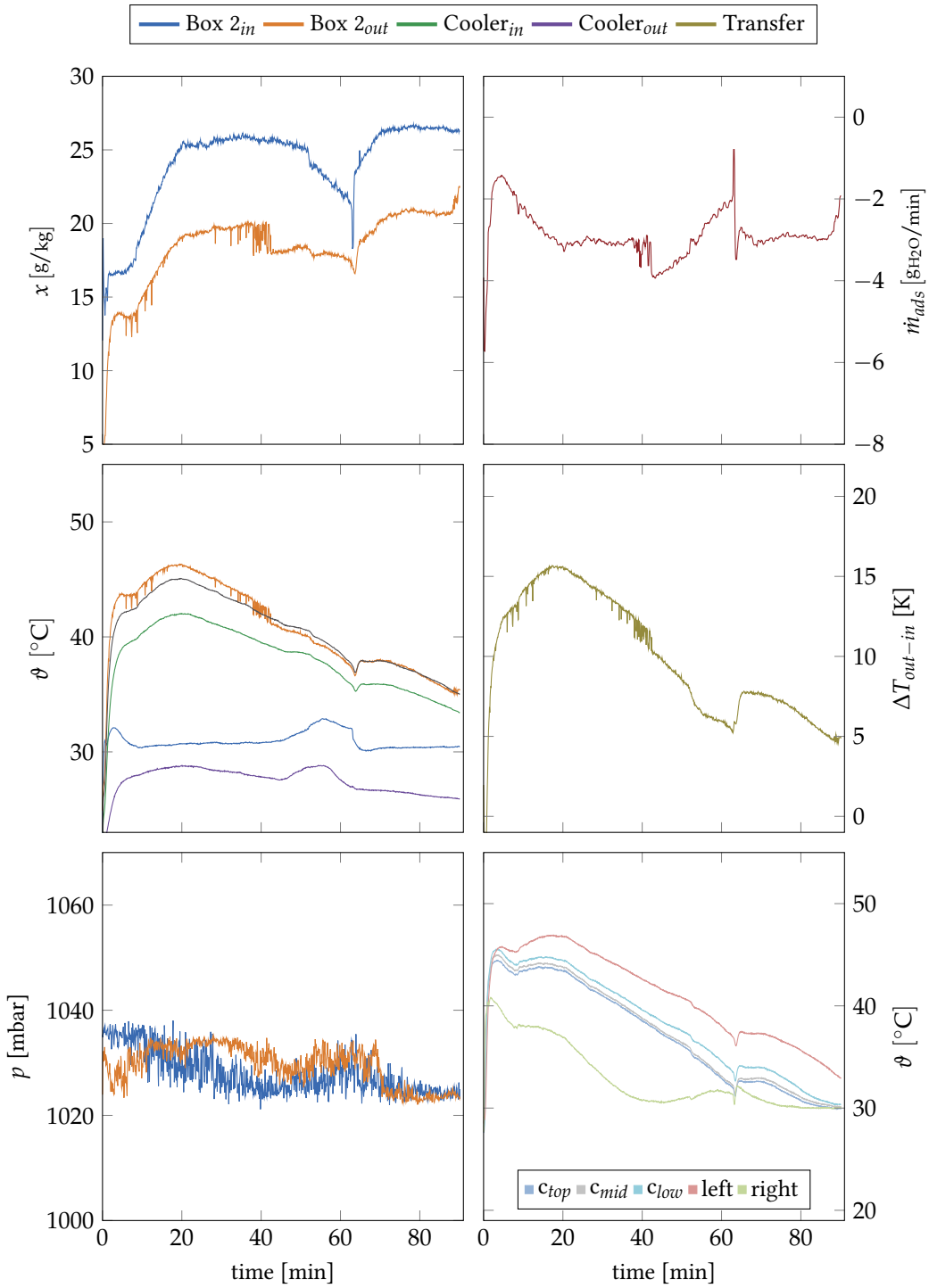

Figure 128: *Box 2* in adsorption mode at 100 % fan power. Loaded sample: *DT-B*

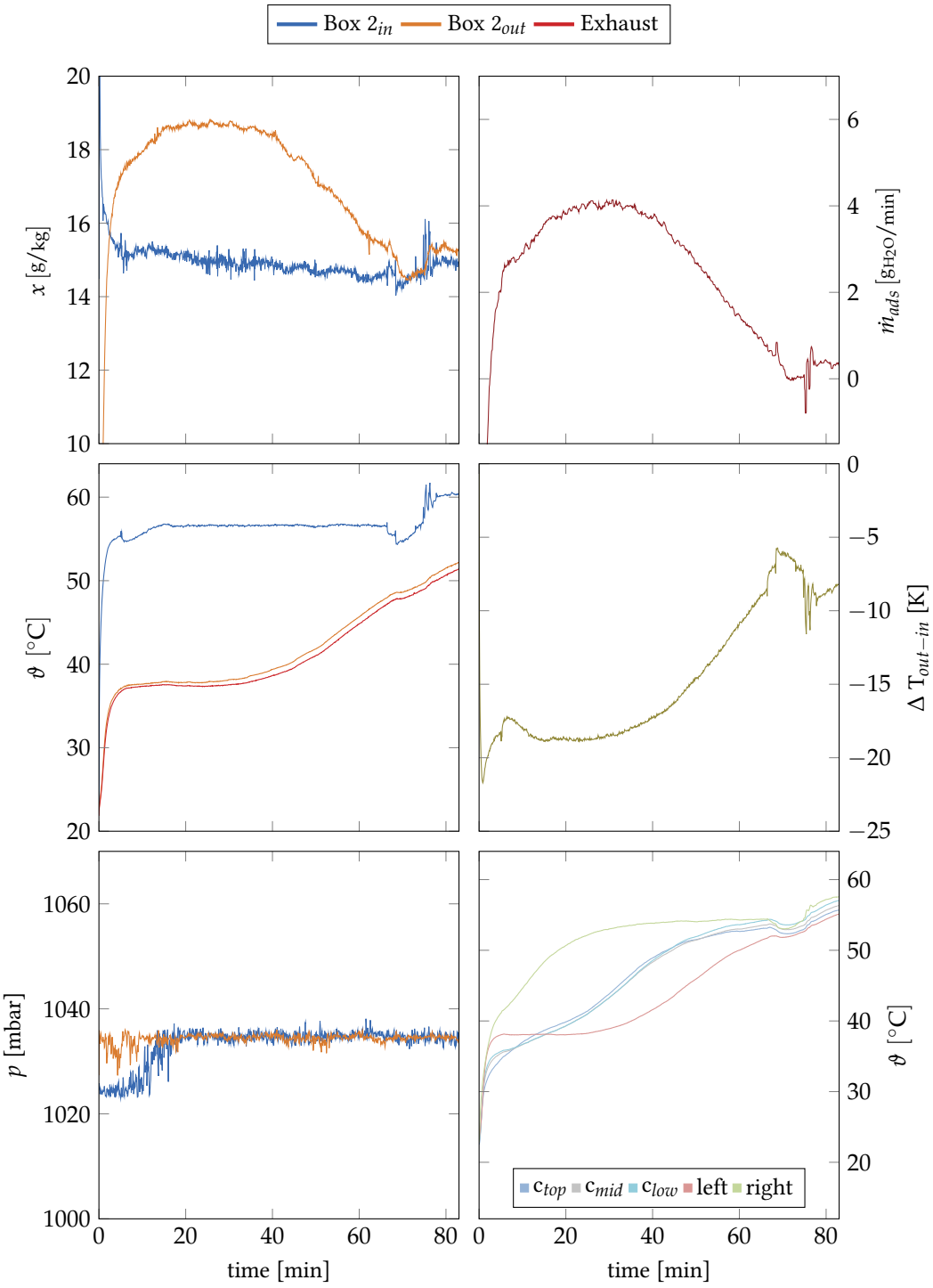

Figure 129: *Box 2* in desorption mode. Loaded sample: *HK-O*

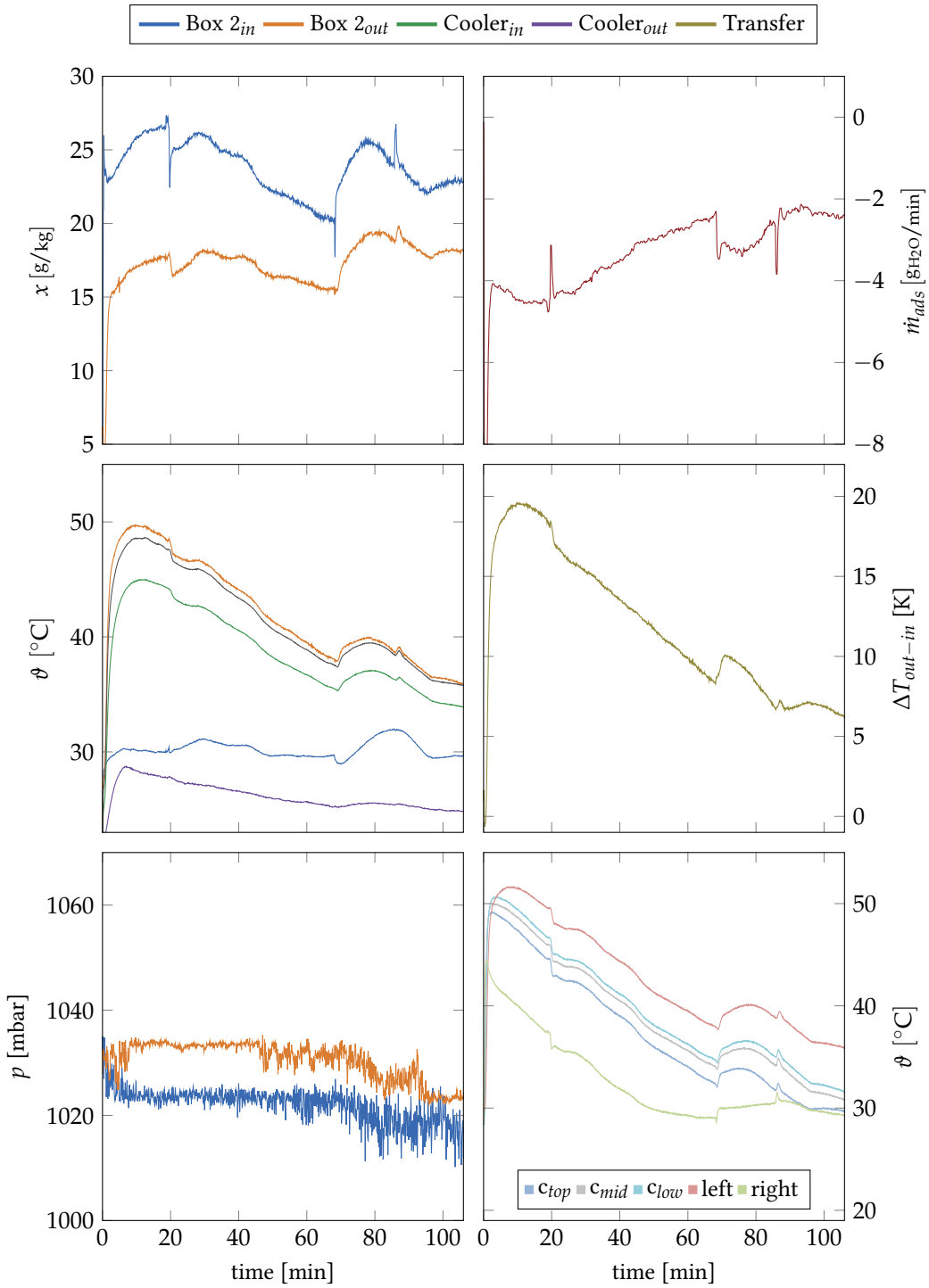

Figure 130: *Box 2* in adsorption mode at 50 % fan power. Loaded sample: *HK-O*

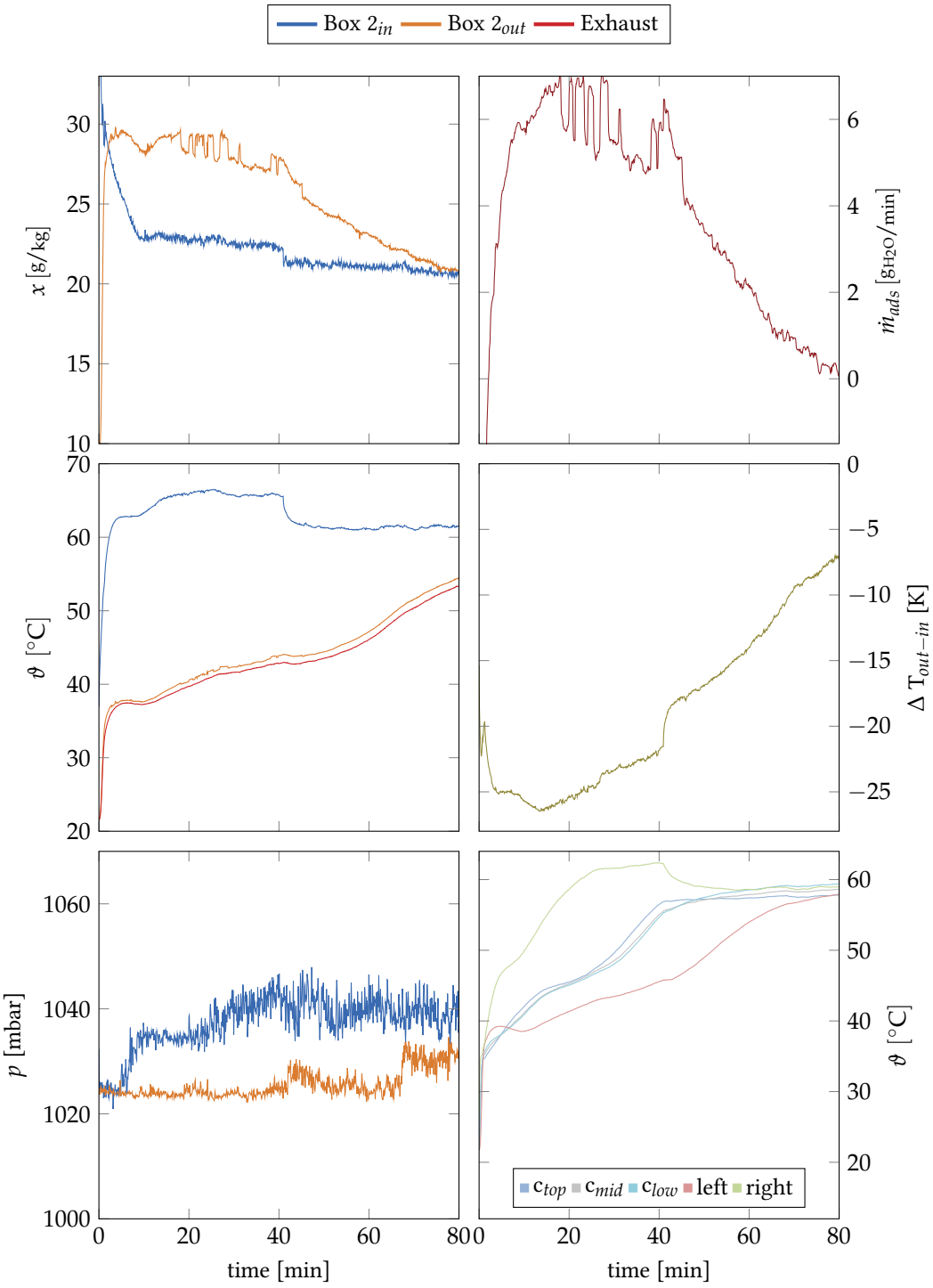

Figure 131: *Box 2* in desorption mode, with increased regeneration air humidity. Loaded sample: *HK-O*

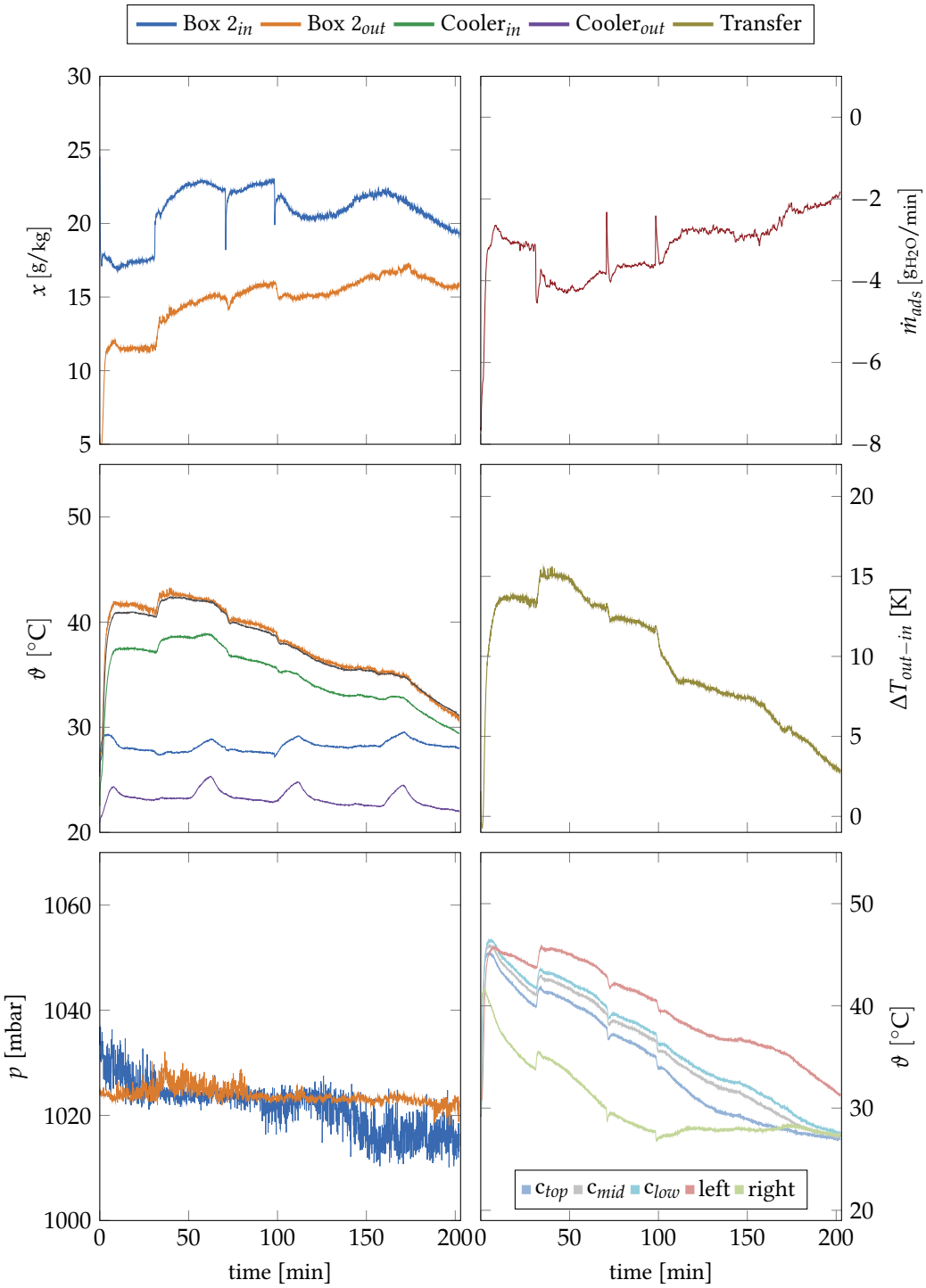

Figure 132: *Box 2* in adsorption mode at 25 % fan power. Loaded sample: *HK-O*

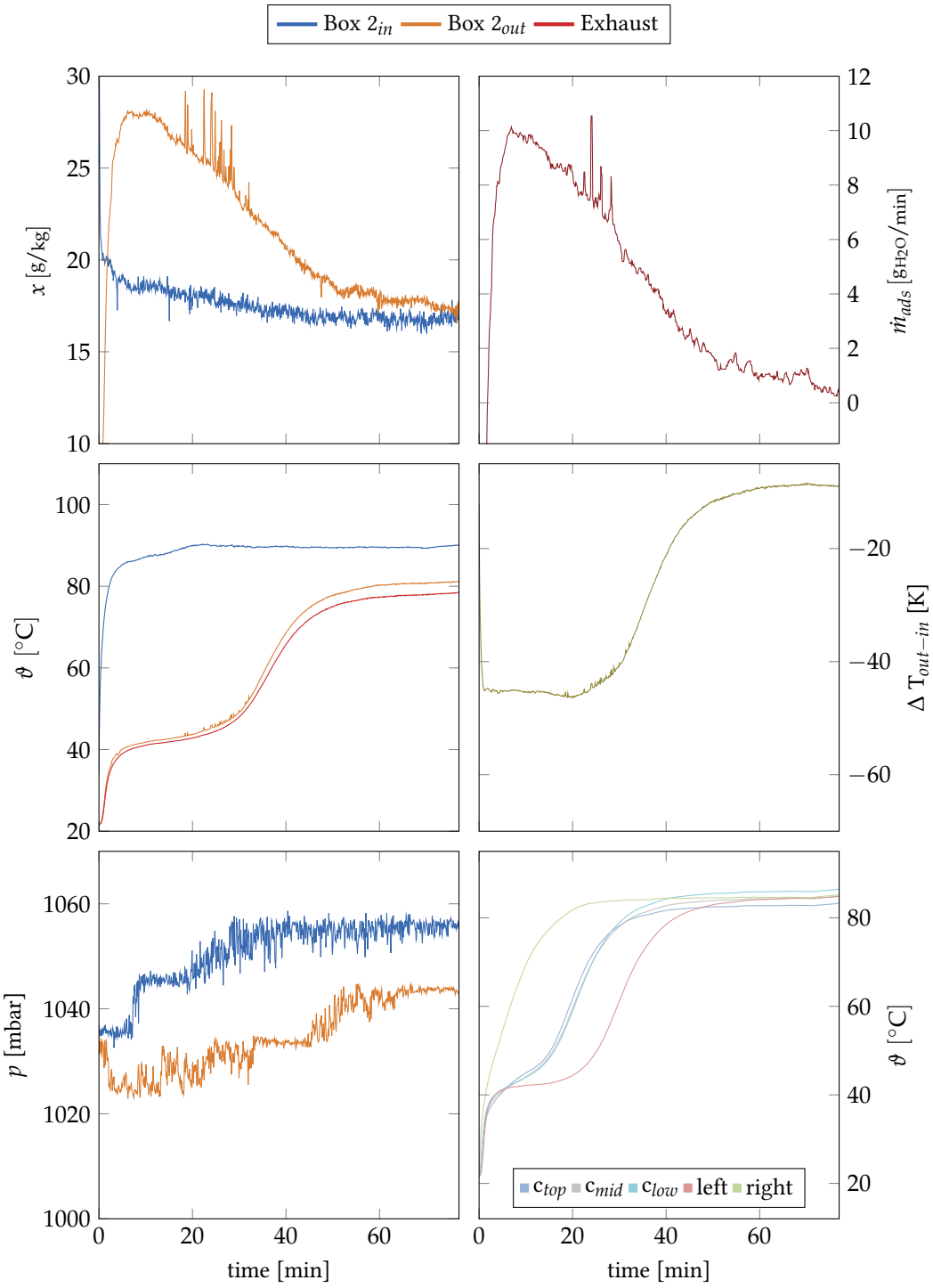

Figure 133: *Box 2* in desorption mode, with increased regeneration temperature. Loaded sample: *HK-O*

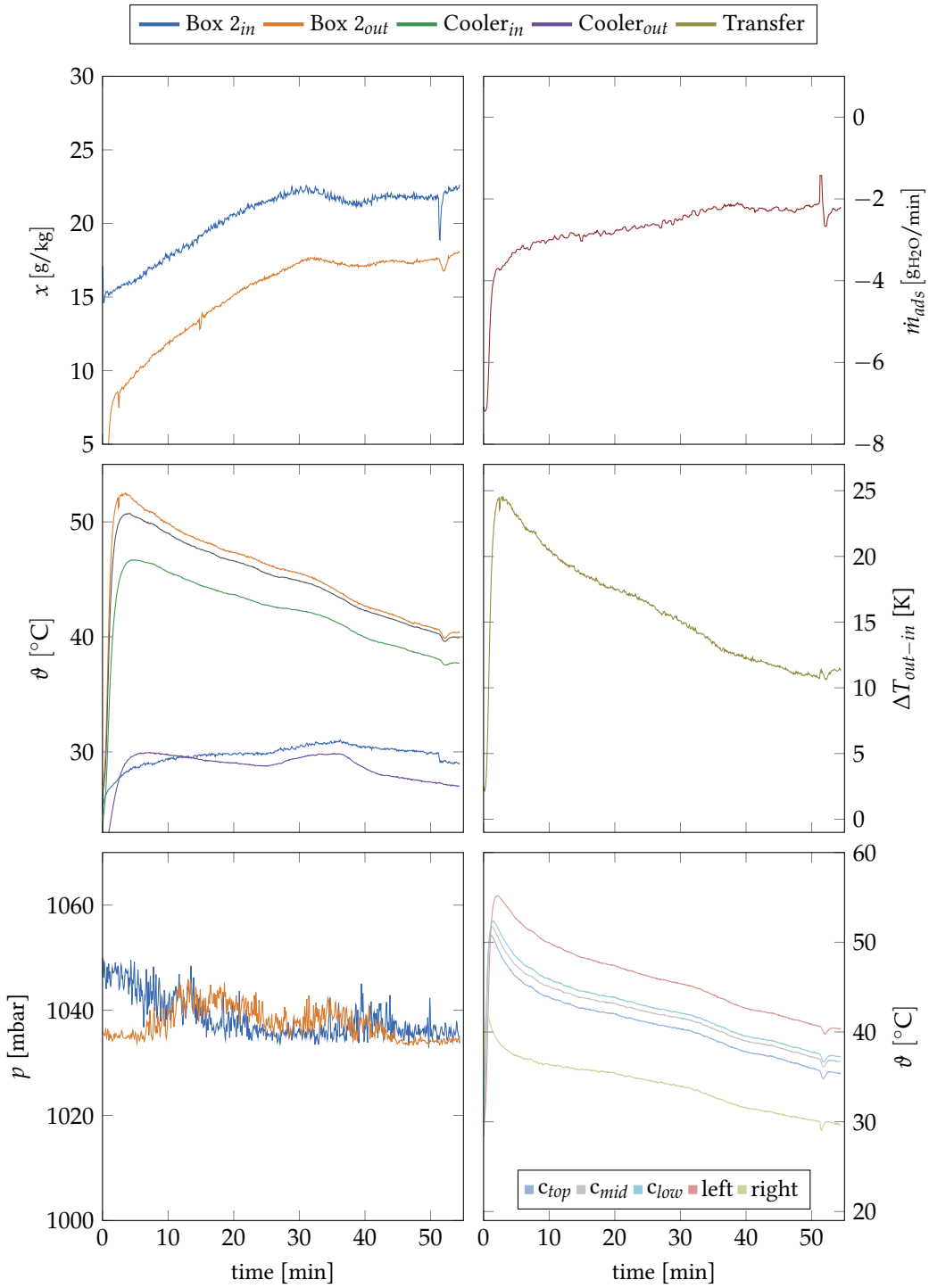

Figure 134: *Box 2* in adsorption mode at 100 % fan power. Loaded sample: *HK-O*

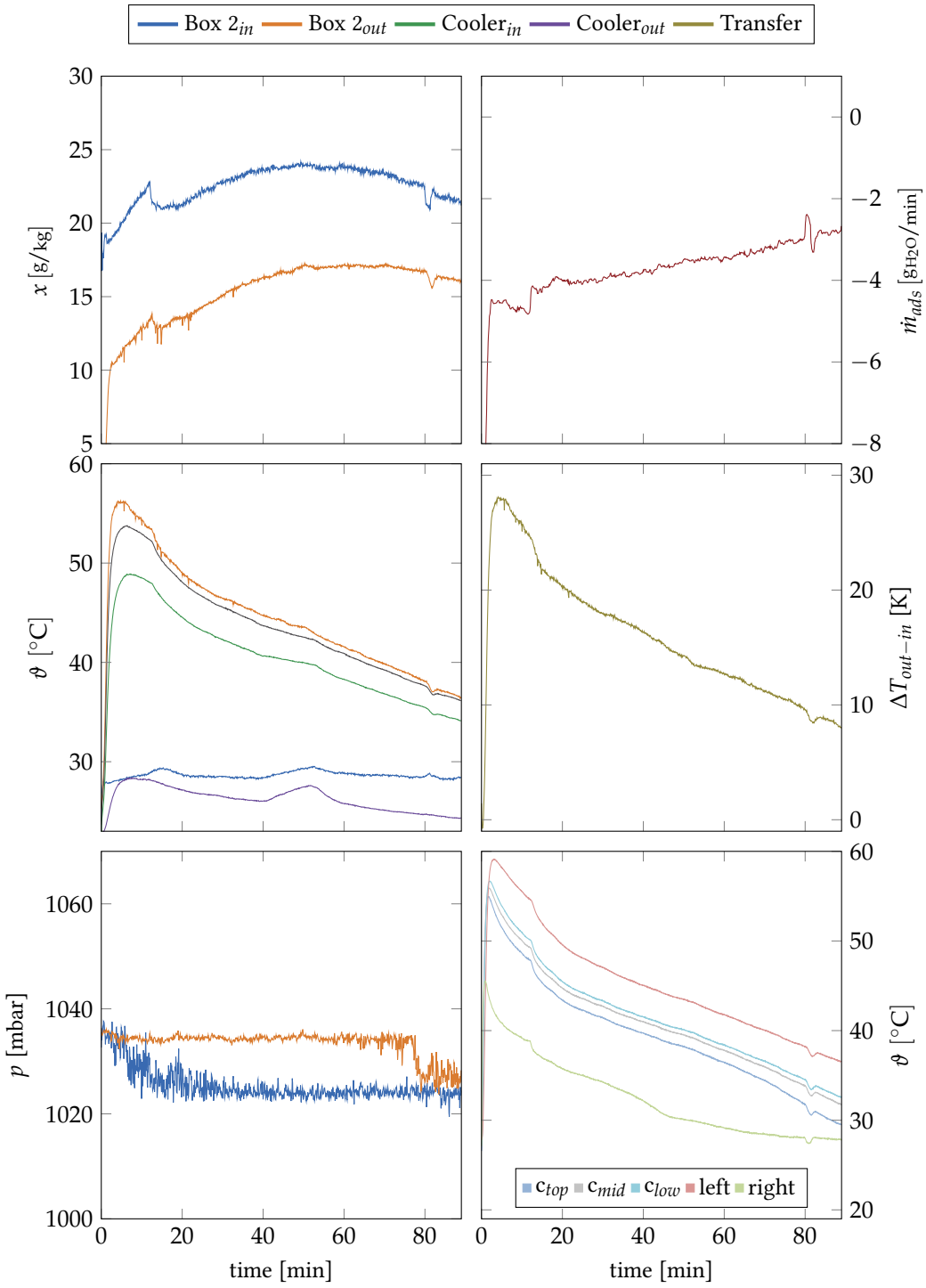

Figure 135: *Box 2* in adsorption mode at 100 % fan power. Loaded sample: *HK-O*

B

COMPUTER PROGRAMS

In this appendix, the computer program for the open system test stand is documented. The following MATLAB code was used to evaluate the raw instrument data.

```
% This program reads the .mat data file from the Agilent device.
% It performs signal treatment, then calculates the amount of water from rh
% values and outputs a pgfplots-friendly .dat-file for the active box.
%% create dialog window to select measurement file
d = dir;
str = {d.name};
[s,v] = listdlg('Name','Measurement files',...
    'PromptString','Select a file:',...
    'SelectionMode','single',...
    'ListSize', [400 400],...
    'ListString',str);
s_initial = s;
foldersize = input('\nHow many files to process?\n\n');
for k = 0:foldersize-1
    str = {d.name};
    s = s_initial + k;
    filename = str{1,s};
    load(filename);
%% convert Agilent time stamp to standard Unix epoch
% deduct internal offset and convert to Unix epoch in microseconds
time_unix = (Time_Sec(:,1)- 116444448*10^9) ./ 10^4;
% convert to relative time in seconds
time_rel_sec = (time_unix(:,1) - time_unix(1,1))./10^3;
% convert to relative time in minutes
time_rel_min = (time_unix(:,1) - time_unix(1,1))./ (60*10^3);

%% assign ambient pressure
p_amb = 1009;

%% sensor calibration functions
Trace_101_RH_corr = 0.999728558 .* (Trace_101_RH + 26.9355) - 26.91994886;
Trace_102_RH_corr = 1.000563640 .* (Trace_102_RH + 27.0323) - 27.04258854;
Trace_103_RH_corr = 1.003203163 .* (Trace_103_RH + 27.1290) - 27.20279224;
Trace_104_RH_corr = 0.996200331 .* (Trace_104_RH + 26.9677) - 26.85945692;
Trace_105_RH_corr = 1.005142862 .* (Trace_105_RH + 27.0323) - 27.16006255;
Trace_106_RH_corr = 1.002118900 .* (Trace_106_RH + 27.0323) - 27.10165911;
Trace_107_RH_corr = 1.003836339 .* (Trace_107_RH + 27.0323) - 27.12547125;
Trace_108_RH_corr = 1.002566181 .* (Trace_108_RH + 27.0645) - 27.12885873;
```

```
Trace_109_RH_corr = 1.000563317 .* (Trace_109_RH + 27.0000) - 27.00710823;
Trace_110_RH_corr = 1.001003619 .* (Trace_110_RH + 26.9355) - 26.96445426;

Trace_111_MBA_corr = sgolayfilt(4309.23037/4055.84257 * (Trace_111_MBA(:,1) +
    3035.29285) - 3295.69939,3,11);
Trace_112_MBA_corr = sgolayfilt(4309.23037/4055.84257 * (Trace_112_MBA(:,1) +
    3052.16285) - 3295.69939,3,11);
Trace_113_MBA_corr = sgolayfilt(4309.23037/4055.84257 * (Trace_113_MBA(:,1) +
    3050.75285) - 3295.69939,3,11);
Trace_114_MBA_corr = sgolayfilt(4309.23037/4055.84257 * (Trace_114_MBA(:,1) +
    3047.89285) - 3295.69939,3,11);

%% filter Box 1 out humidity sensor
% apply only to measurements of more than 500 samples
file_dimension = size(Trace_101_RH,1);
if file_dimension > 500
    % identify outliers as values that deviate more than 2.5 percent from
    % median in 50 sample interval
    % Trace_101_RH_filtered = Trace_101_RH;
    I = abs(medfilt1(Trace_101_RH_corr(:,1),50) - Trace_101_RH_corr(:,1))...
        > 0.025 * medfilt1(Trace_101_RH_corr(:,1),50);
    outliers = excludedata(time_rel_min,Trace_101_RH_corr(:,1),'indices',I);
    f2 = fit(time_rel_min,Trace_101_RH_corr(:,1),'nearestinterp','Exclude',
        outliers);
    Trace_101_RH_filtered = feval(f2,time_rel_min);
else
    Trace_101_RH_filtered = Trace_101_RH_corr;
end

%% create structs, assign the appropriate measurement site names as ID
agilent(1) = struct ('ID', 'Box1in',...
    'RH', Trace_105_RH_corr,...
    't', Trace_216_C,...
    'p', Trace_112_MBA_corr);
agilent(2) = struct ('ID', 'Box1out',...
    'RH', Trace_101_RH_filtered,...
    't', Trace_203_C,...
    'p', Trace_113_MBA_corr);
agilent(3) = struct ('ID', 'Box2in',...
    'RH', Trace_103_RH_corr,...
    't', Trace_204_C,...
    'p', Trace_114_MBA_corr);
agilent(4) = struct ('ID', 'Box2out',...
    'RH', Trace_107_RH_corr,...
    't', Trace_202_C,...
    'p', Trace_111_MBA_corr);
agilent(5) = struct ('ID', 'HotAir',...
    'RH', Trace_106_RH_corr,...
    't', Trace_205_C,...
    'p', '');
agilent(6) = struct ('ID', 'FreshAir',...
```

```
    'RH', Trace_102_RH_corr,...
    't', Trace_215_C,...
    'p', '');
agilent(7) = struct ('ID', 'Exhaust',...
    'RH', Trace_108_RH_corr,...
    't', Trace_206_C,...
    'p', '');
agilent(8) = struct ('ID', 'Transfer',...
    'RH', Trace_109_RH_corr,...
    't', Trace_201_C,...
    'p', '');
agilent(9) = struct ('ID', 'CoolerIn',...
    'RH', Trace_104_RH_corr,...
    't', Trace_207_C,...
    'p', '');
agilent(10) = struct ('ID', 'CoolerOut',...
    'RH', Trace_110_RH_corr,...
    't', Trace_213_C,...
    'p', '');
agilent(11) = struct ('ID', 'Oven',...
    'RH', '',...
    't', Trace_217_C,...
    'p', '');
agilent(12) = struct ('ID', 'Leister',...
    'RH', '',...
    't', Trace_214_C,...
    'p', '');
agilent(13) = struct ('ID', 'Box2b',...
    'RH', '',...
    't', Trace_208_C,...
    'p', '');
agilent(14) = struct ('ID', 'Box2r',...
    'RH', '',...
    't', Trace_211_C,...
    'p', '');
agilent(15) = struct ('ID', 'Box2c',...
    'RH', '',...
    't', Trace_210_C,...
    'p', '');
agilent(16) = struct ('ID', 'Box2l',...
    'RH', '',...
    't', Trace_209_C,...
    'p', '');
agilent(17) = struct ('ID', 'Box2t',...
    'RH', '',...
    't', Trace_212_C,...
    'p', '');

%% select active box
% box =  input('\nActive Box:\n\n1\n2\n');
box = 1;
```

```
%box = 2;
fprintf('\nActive Box: %g', box);

%% calculate water content at different measurement sites
switch box
    % temperature and water content at all humidity measurement sites
    case 1
        i=0;
        for z = [1,2,5:10]
            i = i + 1;
            T = agilent(z).t + 273.15;
            tau = 1 - T / 647.096 ;
            %saturation pressure in mbar (Wagner & Pru{\ss}, IAPWS-95)
            p_s = 220640 * exp(647.096 ./ T .* ((-7.85951783 .* tau +...
                1.84408259 .* tau .^1.5 - 11.7866497 .* tau.^3 +...
                22.6807411 .* tau .^3.5 - 15.9618719 .* tau .^4 +...
                1.80122502 .* tau .^7.5)));
            % temperature correction of RH according to Honeywell datasheet
            rh_corrected = agilent(z).RH ./ (1.0546 -...
                0.00216 .* agilent(z).t);
            % H2O partial pressure in mbar
            p_w = rh_corrected ./ 100 .* p_s;
            results(i) = struct ('ID', agilent(z).ID, 't', agilent(z).t,...
                'p_sat', p_s, 'p_w', p_w, 'p', agilent(z).p, 'm_w', '');
        end
        % water content as mass H2O / mass dry air (g/kg)
        % (0.62198 = molar weight ratio, factor 1000 for g/kg)
        for z = (1:2) % Box 1 in & out
            m_w = 621.98 .* results(z).p_w ./ (results(z).p - results(z).p_w);
            results(z).m_w = m_w;
        end
        for z = [3:5,8] % Hot Air, Fresh Air, Exhaust & Cooler out
            m_w = 621.98 .* results(z).p_w ./ (p_amb - results(z).p_w);
            results(z).m_w = m_w;
        end
        for z = (6:7) % Transfer & Cooler in
            m_w = 621.98 .* results(z).p_w ./ (results(2).p - results(z).p_w);
            results(z).m_w = m_w;
        end
    case 2
        i=0;
        for z = [3,4,5:10]
            i = i + 1;
            T = agilent(z).t + 273.15;
            tau = 1 - T / 647.096 ;
            % saturation pressure in mbar (Wagner & Pru{\ss}, IAPWS-95)
            p_s = 220640 * exp(647.096 ./ T .* ((-7.85951783 .* tau +...
                1.84408259 .* tau .^1.5 - 11.7866497 .* tau.^3 +...
                22.6807411 .* tau .^3.5 - 15.9618719 .* tau .^4 +...
                1.80122502 .* tau .^7.5)));
            % temperature correction of RH according to Honeywell datasheet
```

```
            rh_corrected = agilent(z).RH ./ (1.0546 -...
                0.00216 .* agilent(z).t);
            % H2O partial pressure in mbar
            p_w = rh_corrected ./ 100 .* p_s;
            results(i) = struct ('ID', agilent(z).ID, 't', agilent(z).t,...
                'p_sat', p_s, 'p_w', p_w, 'p', agilent(z).p, 'm_w', '');
        end
        % mass H2O / dry air (g/kg) (0.62198 = molar weight ratio)
        for z = (1:2) % Box 2 in & out
            m_w = 621.98 .* results(z).p_w ./ (results(z).p - results(z).p_w);
            results(z).m_w = m_w;
        end
        for z = [3:5,8] % Hot Air, Fresh Air, Exhaust & Cooler out
            m_w = 621.98 .* results(z).p_w ./ (p_amb - results(z).p_w);
            results(z).m_w = m_w;
        end
        for z = (6:7) % Transfer & Cooler in
            m_w = 621.98 .* results(z).p_w ./ (results(2).p - results(z).p_w);
            results(z).m_w = m_w;
        end
    otherwise
        fprintf('\nPlease choose a valid option\n');
        return;
end

%% create array from temp, m_w and p vectors
M = cell(1,18);
for z = 0:1
    z = z + 1;
    o = 3*z - 2;
    p = 3*z - 1;
    q = 3*z;
    M(:,o) = {results(z).t};
    M(:,p) = {results(z).m_w};
    M(:,q) = {results(z).p};
end
for z = 2:7
    z = z + 1;
    o = 2*z + 1;
    p = 2*z + 2;
    M(:,o) = {results(z).t};
    M(:,p) = {results(z).m_w};
end
% if box 2 is active, include temperature profile
if box == 2
    for z = 12:16
        z = z + 1;
        o = z + 6;
        M(:,o) = {agilent(z).t};
    end
else
```

```
end


%% switch between ads / des mode
% mode =  input('\nSelect operating mode:\n\n1 = Adsorption\n2 = Desorption\n
    ');
% mode = 1;
mode = 2;
fprintf('\nSelected Mode: %g', mode);

%% create ID vector for .dat file header
% if box 2 is active, include temperature profile
if box == 1
    header = cell(1,22);
    header(:,20) = {'delta_x'};
    if mode == 1
        header(:,21) = {'m_dot_ads'};
    else
        header(:,21) = {'m_dot_des'};
    end;
    header(:,22) = {'delta_t'};
else
    header = cell(1,27);
    header(:,25) = {'delta_x'};
    if mode == 1
        header(:,26) = {'m_dot_ads'};
    else
        header(:,26) = {'m_dot_des'};
    end;
    header(:,27) = {'delta_t'};
end;
for z = 0:1
    z = z + 1;
    o = 3*z - 1;
    p = 3*z;
    q = 3*z + 1;
    header(:,1) = {'time'};
    header(:,o) = {[results(z).ID,'_t']};
    header(:,p) = {[results(z).ID,'_m_w']};
    header(:,q) = {[results(z).ID,'_p']};
end
for z = 2:7
    z = z + 1;
    o = 2*z + 2;
    p = 2*z + 3;
    header(:,o) = {[results(z).ID,'_t']};
    header(:,p) = {[results(z).ID,'_m_w']};
end
% if box 2 is active, include temperature profile
if box == 2
    for z = 12:16
```

```
        z = z + 1;
        o = z + 7;
        header(:,o) = {[agilent(z).ID,'_t']};
    end
else
end

%% create a matrix of measurement values, rounded to three decimals and
% add calculated quantities
Q1 = cell2mat(M);
% add difference between output and input water content
delta_X = Q1(:,5) - Q1(:,2);
delta_X_filt = medfilt1(delta_X,19);
% add difference between output and input temperature
delta_t = Q1(:,4) - Q1(:,1);

%% calculate adsorbed mass
if mode == 1
    air_flow = 0.45;
else
    air_flow = 0.98;
end;
% calculate integrated value of delta x per volume [\unitfrac{g}{m^3}]
% fluid flow densities
rho_air_exhaust = 100 .* ((p_amb - results(5).p_w) .* 0.028965) ./ (8.314 *(
    results(5).t + 273.15));
rho_air_cooler_out = 100 .* ((p_amb - results(8).p_w) .* 0.028965) ./ (8.314
    *(results(8).t + 273.15));
rho_w_exhaust = 100 .* (results(5).p_w .* 0.018016) ./ (8.314 *(results(5).t +
     273.15));
rho_w_cooler_out = 100 * (results(8).p_w .* 0.018016) ./ (8.314 *(results(8).t
     + 273.15));
rho_ges_exhaust = 100 .* ((p_amb - results(5).p_w) .* 0.028965 + results(5).
    p_w .* 0.018016) ./ (8.314 * (results(5).t + 273.15));
rho_ges_cooler_out = 100 * ((p_amb - results(8).p_w) .* 0.028965 + results(8).
    p_w .* 0.018016) ./ (8.314 * (results(8).t + 273.15));
m_dot_ges_exhaust = 0.98 .* 100 .* ((p_amb - results(5).p_w) .* 0.028965 +
    results(5).p_w .* 0.018016) ./ (8.314 * (results(5).t + 273.15));
m_dot_ges_cooler_out = 0.45 .* 100 .* ((p_amb - results(8).p_w) .* 0.028965 +
    results(8).p_w .* 0.018016) ./ (8.314 * (results(8).t + 273.15));
rho_in = 100 .* ((results(1).p - results(1).p_w) .* 0.028965 + results(1).p_w
    .* 0.018016) ./ (8.314 * (results(1).t + 273.15));
rho_out = 100 .* ((p_amb - results(2).p_w) .* 0.028965 + results(2).p_w .*
    0.018016) ./ (8.314 * (results(2).t + 273.15));
% input per volume [\unitfrac{g}{m^3}]
delta_X_filt_vol_ads = delta_X_filt .* rho_air_cooler_out;
delta_X_filt_vol_des = delta_X_filt .* rho_air_exhaust;
% adsorbed mass H2O [g/min]
m_dot_adsorbed = air_flow .* delta_X_filt_vol_ads;
m_dot_desorbed = air_flow .* delta_X_filt_vol_des;
% integration
```

```
int_time_1 = 60;
int_time_2 = 30;
int_domain_max_1 = find(time_rel_min >= int_time_1,1)-1;
int_domain_max_2 = find(time_rel_min >= int_time_2,1)-1;
int_vector_1a = time_rel_min(1:int_domain_max_1,1);
int_vector_1b = delta_X_filt(1:int_domain_max_1,1);
int_vector_1b_vol_ads = delta_X_filt_vol_ads(1:int_domain_max_1,1);
int_vector_1b_vol_des = delta_X_filt_vol_des(1:int_domain_max_1,1);
int_vector_2a = time_rel_min(1:int_domain_max_2,1);
int_vector_2b = delta_X_filt(1:int_domain_max_2,1);
int_vector_2b_vol_ads = delta_X_filt_vol_ads(1:int_domain_max_2,1);
int_vector_2b_vol_des = delta_X_filt_vol_des(1:int_domain_max_2,1);
dehum_cap_total = round(trapz(time_rel_min,delta_X_filt),2);
dehum_cap_t1 = round(trapz(int_vector_1a,int_vector_1b),2);
dehum_cap_t2 = round(trapz(int_vector_2a,int_vector_2b),2);
dehum_cap_total_vol_ads = round(trapz(time_rel_min,delta_X_filt_vol_ads),2);
dehum_cap_t1_vol_ads = round(trapz(int_vector_1a,int_vector_1b_vol_ads),2);
dehum_cap_t2_vol_ads = round(trapz(int_vector_2a,int_vector_2b_vol_ads),2);
dehum_cap_total_vol_des = round(trapz(time_rel_min,delta_X_filt_vol_des),2);
dehum_cap_t1_vol_des = round(trapz(int_vector_1a,int_vector_1b_vol_des),2);
dehum_cap_t2_vol_des = round(trapz(int_vector_2a,int_vector_2b_vol_des),2);

if mode == 1
    Q = round([Q1,delta_X_filt,m_dot_adsorbed,delta_t],3);
else
    Q = round([Q1,delta_X_filt,m_dot_desorbed,delta_t],3);
end;

%% reduce dataset options
% reduces all datasets to the same fraction of the initial values
% r = input('\nReduce to every n-th values (1 = unreduced)\n');
r = 1;

% dataset reduction dialog
switch r
    case 1
        fprintf('\nCreating unreduced file\n');
    case 11
        fprintf('\nReducing to every %gth value\n', r);
    case 12
        fprintf('\nReducing to every %gth value\n', r);
    case 13
        fprintf('\nReducing to every %gth value\n', r);
    otherwise
        rs = mod(r,10);
        switch rs
            case 1
                fprintf('\nReducing to every %gst value\n', r);
            case 2
                fprintf('\nReducing to every %gnd value\n', r);
            case 3
```

```
                fprintf('\nReducing to every %grd value\n', r);
            otherwise
                fprintf('\nReducing to every %gth value\n', r);
        end
end

rows = size(Q,1);
time_rel_min(mod(r:(rows+r-1),r)>0,:) = [];
Q(mod(r:(rows+r-1),r)>0,:) = [];

% combine with header vector
S = array2table([time_rel_min , Q],'VariableNames',header);
integrated_deltax = array2table([dehum_cap_total,dehum_cap_t1,dehum_cap_t2,...
    dehum_cap_total_vol_ads,dehum_cap_t1_vol_ads,dehum_cap_t2_vol_ads,...
    dehum_cap_total_vol_des,dehum_cap_t1_vol_des,dehum_cap_t2_vol_des],...
    'VariableNames',{'total','sixty','thirty','total_vol_ads',...
    'sixty_vol_ads','thirty_vol_ads','total_vol_des','sixty_vol_des','
        thirty_vol_des'});

%% export to .dat files
% t and m_w table
% fname = strrep(filename,'.mat','.dat');
% writetable(S,fname,'Delimiter','\t');
fname_int = strrep(filename,'.mat','.dat');
writetable(integrated_deltax,fname_int,'Delimiter','\t');
fprintf('\n.dat file created\n')
files_proc = k + 1;
fprintf('Files processed: %g\n', files_proc)

end
```

C

LITERATURE VALUES

The following air change rates were used as references for the calculation of air flow rates. Some values from the original publications are omitted as they were measured under conditions irrelevant in this context (open windows). Vehicle volumes are given as geometric calculations *(meas.)* and gas concentration decay measurements *(gas)*, respectively. v refers to the speed of the moving vehicle, where applicable. In cases where the original publication used imperial units (mph), they have been rounded to $^{km}/_{h}$.

Table 34: Vehicles used in ACH studies from Table 35.

Study	Vehicle	Type	Year
Ott et al. [35]	A	Toyota Corolla	2005
	B	Ford Taurus	2005
	C	Lexus RX-300	1999
	D	Jeep Grand Cherokee Limited	1999
Rodes et al. [158]	E	Chevrolet Caprice	1991
	F	Ford Explorer	1997
	G	Ford Taurus	1997
Offermann et al. [159]	H	Minivan	1996
Knibbs et al. [160]	I	Mazda 121	1989
	J	Mitsubishi Magna	1998
	K	Subaru Liberty	2000
	L	Toyota HiLux	2005
	M	VW Rabbit	2005
	N	Subaru Legacy Outback	2007
Engelmann et al. [161]	O	Plymouth Reliant	1988
Park et al. [162]	P	unknown	unknown

Table 35: Values of air change rates found in previous studies.

		Volume [m^3]					
Study	Vehicle	Meas.	Gas	v [km/h]	Vents	Fan	ACH [1/h]
Ott	A	2.6	2.7	0	closed	off	0.92
et al. [35]	A	2.6	2.7	32	closed	off	2.4
	A	2.6	2.7	32	open	off	12
	A	2.6	2.7	32	open	low	35
	B	2.2	2.4	32	closed	low	1.9
	B	2.2	2.4	32	open + A/C	low	29.4
	B	2.2	2.4	32	open	low	30.3
	B	2.2	2.4	40	open	low	35.0
	B	2.2	2.4	80	closed	low	4.1
	B	2.2	2.4	97	open	low	35.6
	B	2.2	2.4	97	open + A/C	low	28.7
	B	2.2	2.4	97	closed	low	5.6
	B	2.2	2.4	116	closed	low	5.0
	B	2.2	2.4	116	open	low	32.9
	B	2.2	2.4	116	open + A/C	low	29.9
	B	2.2	2.4	116	closed + A/C	low	6.6
	C	4.7	5.5	10	closed	off	$0.6\,v^{1.25}$
	D	2.6	3.0	100	closed	off	6.0
	D	2.6	3.0	100	closed + A/C	off	8.2
	D	2.6	3.0	100	open + A/C	off	28.4
	D	2.6	3.0	97	open + A/C	off	23.4
Rodes	E	-	-	89	-	low	39
et al. [158]	E	-	-	89	-	medium	98
	E	-	-	89	-	high	160
	F	-	-	56	-	low	14
	F	-	-	56	-	medium	76
	G	-	-	0	-	low	1.8
	G	-	-	56	-	low	5.6
	G	-	-	89	-	low	13.5
	G	-	-	0	-	medium	20.7
	G	-	-	56	-	medium	35.7
	G	-	-	89	-	medium	55.5
Offermann	H	-	2.0	30	closed	off	4.9

et al. [159]	H	-	2.0	30	open	medium	60
Knibbs	I	-	3.32	0	closed	off	0.2
et al. [160]	I	-	3.32	0	open	low	28.9
	I	-	3.32	60	closed	off	35.6
	I	-	3.32	60	open	low	57.1
	J	-	3.72	0	closed	off	3.3
	J	-	3.72	0	open	low	40.0
	J	-	3.72	60	closed	off	8.2
	J	-	3.72	60	open	low	65.9
	K	-	4.65	0	closed	off	0.5
	K	-	4.65	0	open	low	28.5
	K	-	4.65	60	closed	off	4.1
	K	-	4.65	60	open	low	32.6
	L	-	3.33	0	closed	off	0.7
	L	-	3.33	0	open	low	39.5
	L	-	3.33	60	closed	off	4.8
	L	-	3.33	60	open	low	46.5
	M	-	3.88	0	closed	off	0.1
	M	-	3.88	0	open	low	40.0
	M	-	3.88	60	closed	off	1.3
	M	-	3.88	60	open	low	44.9
	N	-	4.43	0	closed	off	0.3
	N	-	4.43	0	open	low	29.6
	N	-	4.43	60	closed	off	4.0
	N	-	4.43	60	open	low	33.2
Engelmann	O	-	-	-	closed	off	0.38 - 1.15
et al. [161]	O	-	-	-	closed	on	1.56 - 2.90
	O	-	-	-	closed + A/C	-	1.96 - 3.41
Park	P	-	-	-	closed	off	1.0 - 3.0
et al. [162]	P	-	-	-	closed	on	1.8 - 3.7
	P	-	-	-	open	on	36.2 - 47.5